



SAIMM

JOURNAL OF THE SOUTHERN AFRICAN INSTITUTE OF MINING AND METALLURGY

VOLUME 116 NO. 10 OCTOBER 2016



advanced metals initiative

All papers featured in this edition were presented at the
Ferrous and Base Metals Development Network Conference

19–21 October 2016



ADVANCED METALS INITIATIVE

The Advanced Metals Initiative (AMI) was established by the Department of Science and Technology to facilitate research, development and innovation across the advanced metals value chain.

GOAL

To target significant export income and new industries for South Africa by 2020 through the country becoming a world leader in sustainable metals production and manufacturing via technological competence and optimal, sustainable local manufacturing of value-added products, while reducing environmental impact.

STRATEGY

The AMI takes an integrated approach across the entire value chain from resource development to metal production and the manufacture of end-products, to achieve its goal, through:

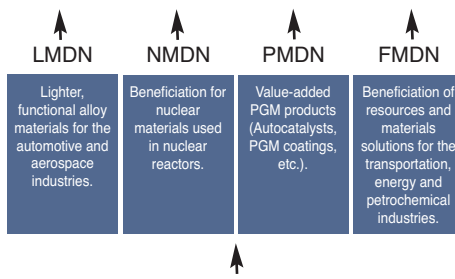
- Reducing the energy required to produce metals by 30%;
- Increasing asset productivity by 30%;
- Developing technologies that can enable new industries for South Africa; and,
- Reducing the full life cycle environmental impact of metals products by 50%.

TECHNOLOGY NETWORKS

The AMI's technology networks include:

- the Light Metals Development Network (LMDN) for titanium and aluminium co-ordinated by the Council for Scientific and Industrial Research (CSIR);
- the Precious Metals Development Network (PMDN) for gold and the platinum group metals (PGMs), co-ordinated by Mintek;
- the Nuclear Materials Development Network (NMDN) for hafnium, zirconium and monazite co-ordinated by The South African Nuclear Energy Corporation of SOC Ltd. (Necsa).
- the Ferrous Metals Development Network (FMDN) for ferrous and base metals, co-ordinated by Mintek.

Metals generating significant export income and new industries for South Africa while reducing environmental impact.



The AMI promotes collaborative research between the science councils, higher education institutions and industry.

Human resource development is critical for the networks to:

- expand the country's technical capacity;
- develop the use of metals in new applications and more diverse industries; and
- develop industrial localisation.

LIGHT METALS DEVELOPMENT NETWORK

- Global demand for ultralight, ultrastrong, recyclable metals is growing as the world switches to low-emission vehicles, energy-saving devices and sustainable products.
- Aluminium demand is forecast to increase by 30% in the near future, while for the emerging industrial light metal, titanium, the sky is the limit.
- For its part, South Africa has a mature aluminium industry, which is among the country's top exporters, and one of the world's richest titanium resources on which to build a new industry.

The LMDN sees South Africa becoming a world leader in light metals.

The LMDN conducts scientific research activities along the entire value chain, from resource development to primary metal production, fabrication, casting, joining technologies and manufactured products.

The aim is to create a globally competitive integrated light metals industry, to develop superior cost-effective technologies and manufacturing systems, and to reduce energy use, greenhouse emissions and environmental impact.

CONTACT DETAILS

Llanley Simpson
Tel: +27 12 843 6436
Fax: +27 86 681 0242
Cell: +27 83 408 6910
Email: llanley.simpson@dst.gov.za



advanced metals initiative

NUCLEAR MATERIALS DEVELOPMENT NETWORK

- The global upsurge in energy demand has led to a renewed focus on nuclear energy and related nuclear materials like zirconium and hafnium.
- Zirconium is used as cladding in nuclear reactors and zirconium carbide has applications in future nuclear reactors.
- South Africa has a vast resource of zircon and supplies 30% of the world market.

The NMDN seeks to benefit from zirconium and hafnium across the value chain through the preparation and purification of intermediate metal salts, metal manufacturing and optimum zirconium-alloys.

The NMDN targets alternative, novel, economic and environmentally friendly manufacturing processes for the metal pair zirconium/hafnium via existing plasma and fluorochemical expertise.

PRECIOUS METALS DEVELOPMENT NETWORK

Precious metals are characterised by their high density and cost, which make them less attractive for use in bulk components and more viable in coating/deposition technologies (chemical and physical) for various applications in which the unique properties of these high-value metals are beneficial.

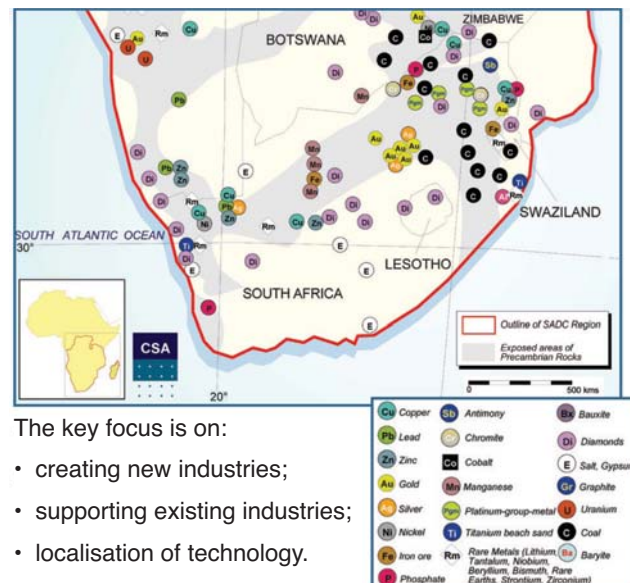
The PMDN assists South Africa in retaining the precious metals value matrix through the identification, research and promotion of new technologies and applications to support the long-term development of the mining industry.

FERROUS METALS DEVELOPMENT NETWORK

The FMDN presents a unique opportunity to simultaneously add value to several minerals that South Africa possess in large quantities such as iron, chromium, manganese, vanadium, etc. while addressing key material challenges experienced by strategic sectors of the economy such as the transportation, energy and petrochemical industries. The FMDN R&D programmes are done within a tripartite collaborative framework involving industry, academia and science councils. The broad objectives of the FMDN can thus be summarised as follows:

- Beneficiation of South Africa's ferrous resources to stages 3 and 4 undefined.

- Improvement of the country's capability to produce high-end ferrous products, especially those that are needed by other critical sectors of the economy, such as petrochemical, energy generation, transportation, etc.
- Generation of local know-how (innovation).
- Human Capital Development which will alleviate the shortage in scientific and technological qualifications and skills in these sectors and thereby ensuring the sustainability and the competitiveness of the local industry. This will also improve SA's attractiveness as an investment destination.
- Promotion of local and international collaboration in the field of ferrous metallurgy.



The key focus is on:

- creating new industries;
- supporting existing industries;
- localisation of technology.

supported by



The Southern African Institute of Mining and Metallurgy

OFFICE BEARERS AND COUNCIL FOR THE 2016/2017 SESSION

Honorary President

Mike Teke
President, Chamber of Mines of South Africa

Honorary Vice-Presidents

Mosebenzi Zwane
Minister of Mineral Resources, South Africa

Rob Davies
Minister of Trade and Industry, South Africa

Naledi Pandor
Minister of Science and Technology, South Africa

President

C. Musingwini

President Elect

S. Ndlovu

Senior Vice-President

A.S. Macfarlane

Junior Vice-President

M. Mthenjane

Immediate Past President

R.T. Jones

Honorary Treasurer

J. Porter

Co-opted Member

Z. Botha

Ordinary Members on Council

V.G. Duke	A.G. Smith
I.J. Geldenhuys	M.H. Solomon
M.F. Handley	M.R. Tlala
W.C. Joughin	D. Tudor
M. Motuku	D.J. van Niekerk
D.D. Munro	A.T. van Zyl
G. Njowa	

Past Presidents Serving on Council

N.A. Barcza	S.J. Ramokgopa
R.D. Beck	M.H. Rogers
J.R. Dixon	D.A.J. Ross-Watt
M. Dworzanowski	G.L. Smith
H.E. James	W.H. van Niekerk
G.V.R. Landman	R.P.H. Willis
J.C. Ngoma	

Branch Chairmen

Botswana	L.E. Dimbungu
DRC	S. Maleba
Johannesburg	J.A. Luckmann
Namibia	N.M. Namate
Northern Cape	C.A. van Wyk
Pretoria	P. Bredell
Western Cape	C.G. Sweet
Zambia	D. Muma
Zimbabwe	S. Matutu
Zululand	C.W. Mienie

Corresponding Members of Council

Australia:	I.J. Corrangs, R.J. Dippenaar, A. Croll, C. Workman-Davies
Austria:	H. Wagner
Botswana:	S.D. Williams
United Kingdom:	J.J.L. Cilliers, N.A. Barcza
USA:	J-M.M. Rendu, P.C. Pistorius

PAST PRESIDENTS

- *Deceased
- * W. Bettel (1894–1895)
 - * A.F. Crosse (1895–1896)
 - * W.R. Feldtmann (1896–1897)
 - * C. Butters (1897–1898)
 - * J. Loevy (1898–1899)
 - * J.R. Williams (1899–1903)
 - * S.H. Pearce (1903–1904)
 - * W.A. Caldecott (1904–1905)
 - * W. Cullen (1905–1906)
 - * E.H. Johnson (1906–1907)
 - * J. Yates (1907–1908)
 - * R.G. Bevington (1908–1909)
 - * A. McA. Johnston (1909–1910)
 - * J. Moir (1910–1911)
 - * C.B. Saner (1911–1912)
 - * W.R. Dowling (1912–1913)
 - * A. Richardson (1913–1914)
 - * G.H. Stanley (1914–1915)
 - * J.E. Thomas (1915–1916)
 - * J.A. Wilkinson (1916–1917)
 - * G. Hildick-Smith (1917–1918)
 - * H.S. Meyer (1918–1919)
 - * J. Gray (1919–1920)
 - * J. Chilton (1920–1921)
 - * F. Wartenweiler (1921–1922)
 - * G.A. Watermeyer (1922–1923)
 - * F.W. Watson (1923–1924)
 - * C.J. Gray (1924–1925)
 - * H.A. White (1925–1926)
 - * H.R. Adam (1926–1927)
 - * Sir Robert Kotze (1927–1928)
 - * J.A. Woodburn (1928–1929)
 - * H. Pirow (1929–1930)
 - * J. Henderson (1930–1931)
 - * A. King (1931–1932)
 - * V. Nimmo-Dewar (1932–1933)
 - * P.N. Lategan (1933–1934)
 - * E.C. Ranson (1934–1935)
 - * R.A. Flugge-De-Smidt (1935–1936)
 - * T.K. Prentice (1936–1937)
 - * R.S.G. Stokes (1937–1938)
 - * P.E. Hall (1938–1939)
 - * E.H.A. Joseph (1939–1940)
 - * J.H. Dobson (1940–1941)
 - * Theo Meyer (1941–1942)
 - * John V. Muller (1942–1943)
 - * C. Biccard Jeppe (1943–1944)
 - * P.J. Louis Bok (1944–1945)
 - * J.T. McIntyre (1945–1946)
 - * M. Falcon (1946–1947)
 - * A. Clemens (1947–1948)
 - * F.G. Hill (1948–1949)
 - * O.A.E. Jackson (1949–1950)
 - * W.E. Gooday (1950–1951)
 - * C.J. Irving (1951–1952)
 - * D.D. Stitt (1952–1953)
 - * M.C.G. Meyer (1953–1954)
 - * L.A. Bushell (1954–1955)
 - * H. Britten (1955–1956)
 - * Wm. Bleloch (1956–1957)
- * H. Simon (1957–1958)
 - * M. Barcza (1958–1959)
 - * R.J. Adamson (1959–1960)
 - * W.S. Findlay (1960–1961)
 - D.G. Maxwell (1961–1962)
 - * J. de V. Lambrechts (1962–1963)
 - * J.F. Reid (1963–1964)
 - * D.M. Jamieson (1964–1965)
 - * H.E. Cross (1965–1966)
 - * D. Gordon Jones (1966–1967)
 - * P. Lambooy (1967–1968)
 - * R.C.J. Goode (1968–1969)
 - * J.K.E. Douglas (1969–1970)
 - * V.C. Robinson (1970–1971)
 - * D.D. Howat (1971–1972)
 - J.P. Hugo (1972–1973)
 - * P.W.J. van Rensburg (1973–1974)
 - * R.P. Plewman (1974–1975)
 - * R.E. Robinson (1975–1976)
 - * M.D.G. Salamon (1976–1977)
 - * P.A. Von Wielligh (1977–1978)
 - * M.G. Atmore (1978–1979)
 - * D.A. Viljoen (1979–1980)
 - * P.R. Jochens (1980–1981)
 - G.Y. Nisbet (1981–1982)
 - A.N. Brown (1982–1983)
 - * R.P. King (1983–1984)
 - J.D. Austin (1984–1985)
 - H.E. James (1985–1986)
 - H. Wagner (1986–1987)
 - * B.C. Alberts (1987–1988)
 - C.E. Fivaz (1988–1989)
 - O.K.H. Steffen (1989–1990)
 - * H.G. Mosenthal (1990–1991)
 - R.D. Beck (1991–1992)
 - * J.P. Hoffman (1992–1993)
 - * H. Scott-Russell (1993–1994)
 - J.A. Cruise (1994–1995)
 - D.A.J. Ross-Watt (1995–1996)
 - N.A. Barcza (1996–1997)
 - * R.P. Mohring (1997–1998)
 - J.R. Dixon (1998–1999)
 - M.H. Rogers (1999–2000)
 - L.A. Cramer (2000–2001)
 - * A.A.B. Douglas (2001–2002)
 - S.J. Ramokgopa (2002–2003)
 - T.R. Stacey (2003–2004)
 - F.M.G. Egerton (2004–2005)
 - W.H. van Niekerk (2005–2006)
 - R.P.H. Willis (2006–2007)
 - R.G.B. Pickering (2007–2008)
 - A.M. Garbers-Craig (2008–2009)
 - J.C. Ngoma (2009–2010)
 - G.V.R. Landman (2010–2011)
 - J.N. van der Merwe (2011–2012)
 - G.L. Smith (2012–2013)
 - M. Dworzanowski (2013–2014)
 - J.L. Porter (2014–2015)
 - R.T. Jones (2015–2016)

Honorary Legal Advisers

Van Hulsteyns Attorneys

Auditors

Messrs R.H. Kitching

Secretaries

The Southern African Institute of Mining and Metallurgy

Fifth Floor, Chamber of Mines Building

5 Hollard Street, Johannesburg 2001 • P.O. Box 61127, Marshalltown 2107

Telephone (011) 834-1273/7 • Fax (011) 838-5923 or (011) 833-8156

E-mail: journal@samm.co.za

Editorial Board

- R.D. Beck
J. Beukes
P. den Hoed
M. Dworzanowski
B. Genc
M.F. Handley
R.T. Jones
W.C. Joughin
J.A. Luckmann
C. Musingwini
S. Ndlovu
J.H. Potgieter
T.R. Stacey
D.R. Vogt

Editorial Consultant

- D. Tudor

Typeset and Published by

The Southern African Institute of Mining and Metallurgy
P.O. Box 61127
Marshalltown 2107
Telephone (011) 834-1273/7
Fax (011) 838-5923
E-mail: journal@saimm.co.za

Printed by

Camera Press, Johannesburg

Advertising Representative

Barbara Spence
Avenue Advertising
Telephone (011) 463-7940
E-mail: barbara@avenue.co.za
The Secretariat
The Southern African Institute of Mining and Metallurgy
ISSN 2225-6253 (print)
ISSN 2411-9717 (online)



THE INSTITUTE, AS A BODY, IS NOT RESPONSIBLE FOR THE STATEMENTS AND OPINIONS ADVANCED IN ANY OF ITS PUBLICATIONS.

Copyright© 1978 by The Southern African Institute of Mining and Metallurgy. All rights reserved. Multiple copying of the contents of this publication or parts thereof without permission is in breach of copyright, but permission is hereby given for the copying of titles and abstracts of papers and names of authors. Permission to copy illustrations and short extracts from the text of individual contributions is usually given upon written application to the Institute, provided that the source (and where appropriate, the copyright) is acknowledged. Apart from any fair dealing for the purposes of review or criticism under *The Copyright Act no. 98, 1978, Section 12*, of the Republic of South Africa, a single copy of an article may be supplied by a library for the purposes of research or private study. No part of this publication may be reproduced, stored in a retrieval system, or transmitted in any form or by any means without the prior permission of the publishers. **Multiple copying of the contents of the publication without permission is always illegal.**

U.S. Copyright Law applicable to users in the U.S.A.

The appearance of the statement of copyright at the bottom of the first page of an article appearing in this journal indicates that the copyright holder consents to the making of copies of the article for personal or internal use. This consent is given on condition that the copier pays the stated fee for each copy of a paper beyond that permitted by Section 107 or 108 of the U.S. Copyright Law. The fee is to be paid through the Copyright Clearance Center, Inc., Operations Center, P.O. Box 765, Schenectady, New York 12301, U.S.A. This consent does not extend to other kinds of copying, such as copying for general distribution, for advertising or promotional purposes, for creating new collective works, or for resale.



SAIMM

JOURNAL OF THE SOUTHERN AFRICAN INSTITUTE OF MINING AND METALLURGY

VOLUME 116 NO. 10 OCTOBER 2016

Contents

Journal Comment by M.J. Papo	iv
Support from Mintek by A. Mngomezulu	v
President's Corner—Relevance or Extinction? by C. Musingwini	vi-vii
Exploring differences in various Nb(V)- and Ta(V) tropolonato complexes by a solid-state structural comparison study by R. Koen, A. Roodt and H.G. Visser	895
High-temperature thermal plasma treatment of monazite followed by aqueous digestion by D. Kemp and A.C. Cilliers	901
Investigation of the 'tiger skin' defect on indefinite chill rolls by J. Jonck, J.S. Moema, J. Jooste and P. van Tonder	907
The separation of zirconium and hafnium from $(\text{NH}_4)_3\text{Zr}(\text{Hf})\text{F}_7$ using amine-based extractants by E.W. Conradie, D.J. van der Westhuizen, J.T. Nel and H.M. Krieg	915
Corrosion characteristics of mild steel storage tanks in fluorine-containing acid by R. van der Merwe, L.A. Cornish and J.W. van der Merwe	921
Cold-spray coating of an Fe-40 at.% Al alloy with additions of ruthenium by R.A. Couperthwaite, L.A. Cornish and I.A. Mwamba	927
The influence of particle size distribution on the properties of metal-injection-moulded 17-4 PH stainless steel by M. Seerane, P. Ndlangamandla and R. Machaka	935
Spheroidisation of iron powder in a microwave plasma reactor by J.H. van Laar I.J. van der Walt, H. Bissett, J.C. Barry and P.L. Crouse	941
Effect of yield strength on wear rates of railway wheels by V.J. Matjeke J.W. van der Merwe, M.J. Phasha, A.S. Bolokang and C. Moopanar	947
Premature failure of re-sulphurized steel studs by E. Molobi	957
Deformation behaviour of aluminium low-micron MMCs and MMNCs at warm working temperatures (0.3–0.5 T_m) by Z. Gxowa, L.H. Chown, G. Govender and U. Curle	963
Grain refinement of 25 wt% high-chromium white cast iron by addition of vanadium by L.A. Mampuru, M.G. Maruma and J.S. Moema	969
X-ray computed microtomography studies of MIM and DPR parts by N.S. Muchavi, L. Bam, F.C. De Beer, S. Chikosha and R. Machaka	973
Effect of niobium on the solidification structure and properties of hypoeutectic high-chromium white cast irons by M.E. Maja, M.G. Maruma, L.A. Mampuru and S.J. Moema	981

International Advisory Board

- R. Dimitrakopoulos, *McGill University, Canada*
D. Dreisinger, *University of British Columbia, Canada*
E. Esterhuizen, *NIOSH Research Organization, USA*
H. Mitri, *McGill University, Canada*
M.J. Nicol, *Murdoch University, Australia*
E. Topal, *Curtin University, Australia*



Journal Comment

The Advanced Metals Initiative (AMI) programme was established in 2003 by the Department of Science and Technology (DST) and the Science Councils, namely, the CSIR, Mintek and NECSA. The objective of establishing this initiative was to research, develop and innovate across the advanced metals value chain. In this context, the advanced metals are defined as all metals that provide opportunities for creating new products and utilising advanced properties through the application of new technologies. From the DST's strategic consideration, the AMI's outputs must enable the following: the creation of new industries, improving the competitiveness of old and existing industries and the promotion of technology localisation.

In order to realise these ambitious goals, four networks were created at the CSIR, NECSA and Mintek. The CSIR is responsible for the Light Metals Development Network (LMDN), which coordinates research on aluminium and its alloys, as well as hosting the Titanium Centre of Competence (TiCoC). NECSA was tasked with the coordination of the Nuclear Materials Development Network (NMDN) with the aim of developing novel, environmentally-friendly, cost-effective processes for the manufacturing and beneficiation of zirconium, hafnium and monazite. Mintek coordinates both the Precious Metals Development Network (PMDN), which focuses on the precious metals gold and the platinum group metals (PGMs), and the Ferrous and Base Metals Development Network (FMDN).

At the FMDN's maiden conference in 2012, the R&D efforts in the network narrowly focused on three strategic sectors of the economy – the transportation, energy and petrochemical industries. However, as part of its evolution and growth since then, the R&D focus has now been extended to include pervasive material challenges in other key industrial sectors such as automotive, medical, construction, aerospace, logistics and mining. It is our wish, therefore, that the conference will provide a forum for brainstorming

and proposing other relevant R&D areas that can be included in an effort to further strengthen the FMDN for the future. The FMDN continues to support postgraduate students at various higher education institutions (HEIs) as part of its mandate towards human capital development (HCD).

The Ferrous 2016 Conference Organising Committee takes this opportunity to welcome all delegates to the conference and extends its appreciation for your attendance. We are looking forward to your technical contributions and value-adding debates that will unfold during this conference with the ultimate goal of ensuring that the eventual outcomes out of this network, and other AMI networks, benefit the broader South African community. The Committee also thanks Raymond van der Berg and his dedicated team at the SAIMM for their excellent organisation of the conference. Finally, we thank the Department of Science and Technology (DST) and the officials responsible for the AMI Programme, Llanley Simpson and Wilna du Plessis, for their expert guidance of the programme and for funding the Ferrous 2016 Conference.

Thank you.

M.J. Papo
Conference Convener

Support from Mintek

Mintek is a Science Council that is established in terms of the Mineral Technology Act, No. 30 of 1989. Its core function is to undertake research, development and technology transfer in connection with better utilisation of the mineral resources of the Republic of South Africa; the improvement of technical processes and methods for mineral production; the promotion and expansion of existing industries; and the establishment of new industries in the field of minerals and mineral products. These functions, as encapsulated in the Act, are very similar to the goal of the Department of Science and Technology's (DST's) Advanced Metals Initiative (AMI), which is to facilitate research, development and innovation across the metals value chain.

As part of the implementation of the National System of Innovation (NSI), Mintek's institutional review covered three broad categories, namely, the quality of output and outcomes from a scientific and technical perspective, the contribution of the output of Mintek to the realisation of national goals and the quality of the management of the institution.

The outcomes of the review showed that Mintek's core competencies are supported by world-class and unique laboratory-, pilot-scale and demonstration-scale facilities. Mintek was commended as a centre of excellence with significant multidisciplinary skills, particularly in the areas of pyrometallurgy, advanced materials, mining economics and strategy and hydrometallurgy. The review also indicated that internationally, Mintek has a reputation as a world-class research organisation in minerals processing and value addition. The review further found that Mintek's initiatives in support of the national priorities are aimed at addressing the triple challenges of inequality, poverty and unemployment facing South Africa. The review panel endorsed Mintek's relationships with higher education institutions as sound and commended Mintek on its strides on the transformation front, especially on attracting persons with disabilities.

The two Advanced Metals Initiative (AMI) networks that Mintek is currently hosting, namely the Ferrous and Base Metals Development Network (FMDN) and the Precious Metals Development Network (PMDN), continue to play a vital role towards fulfilling Mintek's mandate as a Science Council and an implementation agency of the South African government's National Priorities.

On behalf of Mintek, I would like to thank all the presenters who have contributed with papers that support our goal of knowledge transfer. I am confident that the knowledge you have shared with our delegates will contribute towards promoting sustainable metal production and manufacturing and sustainable local manufacturing of value-added products, while reducing environmental impact. I would also like to thank all delegates and exhibitors for their participation at the Ferrous 2016 Conference.

A. Mngomezulu
President & CEO, Mintek



Relevance or Extinction?

'An economist is an expert who will know tomorrow why the things he predicted yesterday didn't happen today.'

This quote has been attributed to several sources, including Evan Esar in 1968, Kirk Kirkpatrick in 1973, Laurence J. Peter in 1977, and James R. Faulkner in 1983.

Irrespective of the source, the key question is 'what does it have to do with the SAIMM and more specifically, with the President's Corner?' It is my view that the President's Corner is a succinct opportunity for the SAIMM membership to obtain a bird's-eye view of its leadership's vision, while the leadership is able to engage and challenge its membership and readership on strategic and operational perspectives over a quick cup of coffee. What would make you invite the President over and over again for the next 11 months for a discussion over a quick cup of coffee in the President's Corner? I think the attraction lies in building an interface that pops out engaging and probing questions.

I have been doing some crystal-ball gazing into the future of our Institute. Are we strategically positioned to continue being relevant, or is there a risk of us becoming extinct because we may cease to be relevant? Before we can answer this question, I would like us to turn to the stories and theories that have been put forward on the extinction of the dominant group of species during the Jurassic and Cretaceous periods – the dinosaurs.

Some palaeontologists believe that the extinction of dinosaurs was caused by changes in climatic and geological conditions. Another storyline is that starvation was a possibility that led to dinosaurs becoming extinct because, due to their sheer size, dinosaurs required vast amounts of food and stripped bare all the vegetation in their habitat. An alternative theory is that dinosaurs overfed themselves and their bodies became too big to be operated by their small brains, leading to terminal physiological malfunctioning. Others believe that small mammals ate dinosaur eggs as these were very delicious, causing the dinosaur population to decline to unsustainable levels and extinction. Another theory is that about 65.5 million years ago, there was a Cretaceous-Tertiary (K-T) extinction event when a comet struck the earth at a speed of about 70 000 km/h, releasing 2 million times more energy than the most powerful nuclear bomb ever detonated. The comet impact caused wildfires and tsunamis that destroyed many forms of life. The dust from the impact clouded the atmosphere, plunging the Earth into darkness and causing temperatures to drop drastically to levels unbearable for animal and plant life. In the 1980s, father-and-son scientists Luis and Walter Alvarez discovered a distinct layer of iridium – an element found in abundance only in space – that has been dated to a time that corresponds to that when the dinosaurs died, thus corroborating the K-T extinction event. In the 1990s, scientists located a massive 10 km diameter crater in Mexico, which also dates to the same period, further corroborating this theory of dinosaur extinction. These stories and theories suggest that external and internal factors can be causes of extinction. External factors are beyond our control, so we need strategies robust enough to cope with internal factors and prepare for unforeseen external events.

Relevance or Extinction? (*continued*)

The parallel of the K-T extinction event for our minerals industry is the 2008 Global Financial Crisis (GFC). The GFC is considered to be one of the worst economic crises since the Great Depression of the 1930s. It threatened to cause the collapse of large financial institutions, which was largely prevented by the bailout of banks by national governments, but stock markets dropped worldwide. The GFC forced our minerals industry into contraction and we are still reeling from its effects, as mineral commodity prices struggle to recover. Professional associations such as the SAIMM, whose financial health is greatly influenced by the performance of our minerals industry, have not been spared either. No one can predict Black Swan events such as the GFC, but good strategies ensure that we can ride out the tide. Unlike the dinosaurs that overfed, we have over time developed the capability to carefully manage our growth by stowing away for lean times. By continuing to enhance closer collaboration with sister institutes or associations, most of them much smaller than us, we can preserve our pedigree eggs for future growth of the Institute.

At more than 120 years old, having been founded in 1894 and with a current membership close to 5000, the SAIMM is like a dinosaur of professional organizations in our local minerals industry, but a smart one with a very efficient machinery to deliver on its mandate to our membership. We are well-known for being one of the oldest professional associations in the local minerals industry, hosting the highest number of excellent conferences annually, publishing an internationally accredited technical journal every month, and having functional branches locally and in neighbouring countries. Our Office Bearers and committee Chairpersons meet once a year to review our strategy. Can we grow in the coming years to possibly reach a 10 000 membership base, but without outgrowing our capacity to deliver on our mandate? Will we be able to de-risk our income through significant diversification? Will we still be well positioned to ride out any rough tide? Instead of stripping bare our habitat, how can we grow the cake so that there is enough for everyone? I can now share with you a helicopter view of your leadership's vision arising out of our strategy session this year.

Back to the quote. My ethics as a minerals engineering professional preclude me from practising prediction like the 'expert economist' as indicated in the quote, as I cannot claim competence in that space, but I am convinced that our current long-term strategy centred on regional development, enhancing collaboration with sister institutes, diversifying our income stream, and the Young Professionals Council (YPC) will ensure that the SAIMM remains relevant into the future and we can continue to be the great institute that we are – not a dinosaur facing down the barrel of extinction. But, is this sufficient? Only history will be our judge as I cannot risk acting the 'expert economist'. By way of this message I therefore invite you for the next quick cup of coffee in the next issue of the journal.

C. Musingwini
President, SAIMM



You'll find the experts work at Mintek

Mintek, centre of technological excellence, with its teams of highly trained and experienced scientists, engineers, researchers and specialists, continues to develop and provide advanced technology for the more effective extraction, utilisation and beneficiation of our mineral wealth.

We have the most extensive data resources on minerals and mining in Southern Africa.

Experience. Research. Innovation.

Mintek provides expertise in all commodities and metallurgical fields:

- One of the world's longest-running and largest minerals technology facilities based in Johannesburg, SA.
- Metallurgical support throughout all stages of project development.
- Unique, proprietary technologies and products.
- 250 engineers and scientists, and 500 support staff.
- Very large integrated test and pilot plant facilities.
- Comprehensive accredited analytical and mineralogical services - spanning all metallurgical disciplines.
- Extensive knowledge database of Southern African and worldwide mineral resources.
- 82-year track record in providing quality work.
- Library subscription available to the public
- Mintek conferencing facilities

200 Malibongwe Drive, Randburg, South Africa

Private Bag X3015, Randburg 2125, South Africa

PHONE: +27 (011) 709 4111

E-MAIL: Info@Mintek.co.za

www.mintek.co.za



DST PROFILE

The vision of the Department of Science and Technology (DST) is to create a prosperous society that derives enduring and equitable benefits from science and technology. Its mission is to develop, coordinate and manage a national system of innovation that will bring about maximum human capital, sustainable economic growth and improved quality of life for all.

When the DST was established in 2004, it was assigned a leading role in modernising South Africa's economy.

The 2002 National Research and Development Strategy (NRDS) was well received in the science system, and substantial financial resources invested by the government, partners and stakeholders have seen significant progress in the attainment of the strategy's objectives. These include an integrated approach to human capital development, investment in science and technology infrastructure, and improving the strategic management of the public science and technology system to optimise its contribution to wealth creation and an improved quality of life.

Another important DST strategy, the Ten-Year Innovation Plan (2008-2018) was developed to help drive South Africa towards sustained economic growth and a knowledge-based economy. The Plan introduces five "grand challenges" that continue to receive priority attention from government and researchers, to find ways of bridging the "innovation chasm" between research results and socio-economic benefits. For this to be achieved, government through the DST has been making important investments in human capital development, knowledge production, and the exploitation of such knowledge for commercial purposes.

The five "grand challenges" include strengthening the bioeconomy, growing space science and technology, assuring energy security, responding to global change (with a focus on climate change), and contributing to a global understanding of shifting social dynamics in development.

A quick look at the events and milestones of the past few years reveal that the country is positioning itself among global leaders in innovation, science and technology. One of the most iconic indicators in this regard is the country's remarkable work as

part of the global science project to build the world's largest radio telescope, the Square Kilometre Array, much of which is being hosted in the Northern Cape. The project has attracted considerable financial investment in infrastructure and skills advancement.

In additive manufacturing, DST-funded work is driving and funding the national development and adoption of metal and polymer additive manufacturing technology to position South Africa as a competitor in the global market. Through the Collaborative Programme in Additive Manufacturing and the Aeroswift Technology Platform, it is developing and improving design capabilities specifically for the additive manufacturing industry, as well as building a platform for the production of large titanium structures, with a very specific focus on the aerospace industry.

With science and technology critical elements in the growth and development of Africa, the DST is also playing a leading role in the development, integration and unification of the continent. The Department continues to strengthen its science, technology and innovation relations through a diverse portfolio of bilateral and multilateral relations, including with the BRICS grouping (Brazil, Russia, India, China and South Africa) and the European Union.

South Africa is also building muscle in the areas of health research, earth observation, renewable energy and the beneficiation of metals. Information and communication technology are being used in pilot projects to show how technologies can benefit South Africans, especially in previously marginalised communities, in respect of education needs, among others. The DST's Technology Localisation Programme is being used to improve the competitiveness of small and medium enterprises.

As required by the National Development Plan, the DST will continue its efforts to provide South Africa with enduring benefits from science, technology and innovation.

For more information contact Zama Mthethwa, Account Executive. Zama.Mthethwa@dst.gov.za or www.dst.gov.za



science
& technology

Department:
Science and Technology
REPUBLIC OF SOUTH AFRICA



Department:
Science and Technology
REPUBLIC OF SOUTH AFRICA



Precious Metals 2017

THE PRECIOUS METALS DEVELOPMENT NETWORK (PMDN)

20–24 November 2017

North West Province, South Africa

BACKGROUND

The Precious Metals Development Network (PMDN) of the DST's Advanced Metals initiative (AMI) programme will host the AMI's annual conference in 2017. This conference presents a forum where scientists and technologists can come together to learn and discuss the latest advances in precious metals (platinum group metals and gold) science and technology, under the broad themes of:

- ◀ Catalysis
- ◀ Materials
- ◀ Chemistry

OBJECTIVES

- ◀ To bring together researchers, industry and government stakeholders to share and debate the latest trends, research and innovation in the precious metals field.
- ◀ To provide a forum for researchers and industry to present progress made over the past few years on precious metal R&D and applications.
- ◀ To promote the activities of the AMI's PMDN.
- ◀ To network and share information.

WHO SHOULD ATTEND

- ◀ Platinum group metals and gold mining houses
- ◀ Precious metal industrial players
- ◀ Government departments
- ◀ Science Councils
- ◀ Higher Educational Institutes
- ◀ Anyone involved or interested in precious metals' R&D

EXHIBITION/SPONSORSHIP

Sponsorship opportunities are available. Companies wishing to sponsor or exhibit should contact the Conference Co-ordinator.

For further information contact:

Head of Conferencing, Raymond van der Berg
SAIMM, P O Box 61127, Marshalltown 2107
Tel: +27 11 834-1273/7 · Fax: +27 11 833-8156 or +27 11 838-5923
E-mail: raymond@saimm.co.za · Website: <http://www.saimm.co.za>





Exploring differences in various Nb(V)- and Ta(V) tropolonato complexes by a solid-state structural comparison study

by R. Koen*, A. Roodt* and H.G. Visser*

Synopsis

An in-depth crystallographic comparison of the crystal structures of *tetrakis*(tropolonato- κ^2 O,O')niobium(V) chloride ($[Nb(Trop)_4]Cl$) and *tetrakis*(tropolonato- κ^2 O,O')tantalum(V) chloride ($[Ta(Trop)_4]Cl$) was undertaken in an attempt to relate differences in complex stability previously noted in solution with solid-state characteristics such as coordination geometry, ligand bite angles and bond lengths. Significant differences of these parameters for the complexes of the two metal centres could translate to an ideal starting point for improved separation of tantalum and niobium. It was noted that the less stable Nb(V) compound, experiences a higher average degree of strain (71.39(2)°) within the bidentate chelate rings *vs.* the Ta(V) analogue (72.04(2)°). When considering the higher degree of strain, the Nb(V) complex more readily offers up one of its tropolone ligands to yield the more stable $[NbO(Trop)_3]$. The $[Ta(Trop)_4]^+$ cation also exhibits a more distorted square antiprismatic geometry than $[Nb(Trop)_4]^+$. This coordination geometry is quite distorted and could be a reason that $[Ta(Trop)_4]^+$ is inclined towards an energetically favourable dodecahedral geometry, contributing to a more stable conformation.

Keywords

tropolone, stability, geometry, tantalum, niobium.

Introduction

Niobium and tantalum are chemical ‘twins’ of the vanadium triad of the periodic table and are notoriously difficult to separate from one another and from their naturally occurring ores, due to their near-identical physical and chemical properties (Agulyansky, 2004). This similarity in behaviour has been ascribed mainly to the lanthanide contraction of the elements and also their comparable ionization energies (Hubert-Pfalzgraf, Postel and Reiss, 1987). Although the separation methods currently applied on an industrial scale, such as solvent extraction and chlorination, have been successful, these techniques remain very laborious, expensive and evolve significant chemical waste (Bose and Gupta, 2001). Accordingly, there is substantial scope for improvements in the metallurgical methods of purification of niobium and separation from tantalum.

The key to the effective and simplified separation of these elements could possibly be found in the differences in the chemical properties of two similar organic chelated

mieties of these metals. Interestingly, a detailed literature review revealed a considerable shortage of knowledge in relation to the chelation behaviour of tantalum and niobium with different organic bidentate or multidentate ligands (Allen, 2002). In fact, only a single study by Muetterties and Wright (1965) revealed successful O,O'-bidentate ligand (tropolone = tropH) coordination to Ta(V) and Nb(V) metal centres using the unmodified synthons ($[NbCl_5]_2/[TaCl_5]_2$) in atmospheric conditions, which significantly reduces the cost of upscaling for industrial application.

In Muetterties and Wright's investigation, niobium(V) and tantalum(V) pentachlorides were reacted with acidic aqueous solutions of tropolone to form the *tetrakis*-tropolonato cations $[Nb(Trop)_4]^+$ and $[Ta(Trop)_4]^+$, with near-quantitative yields. The focus of their investigation was to determine the effect of pH and temperature on the hydrolytic stabilities of the Ta(V)- and Nb(V)- tropolonato analogues. From the preliminary 1H -NMR kinetic investigation, it was found that in strongly acidic media both $[Nb(Trop)_4]^+$ and $[Ta(Trop)_4]^+$ species are stable. With increasing temperature or pH, the niobium chelate undergoes hydrolysis to the neutral $[NbO(Trop)_3]$ and separates from solution. This difference in coordinative behaviour is an ideal starting point for use in a potential separation strategy.

The solution-state investigation of the formation of these compounds was quite thorough, but not much attention was given to the solid-state characteristics of the compounds (Muetterties and Wright, 1965). With this in mind, a detailed, low-temperature crystallographic investigation of the coordi-

* Department of Chemistry, University of the Free State, Bloemfontein, South Africa.

© The Southern African Institute of Mining and Metallurgy, 2016. ISSN 2225-6253. This paper was first presented at the AMI Ferrous and Base Metals Development Network Conference 2016 19–21 October 2016, Southern Sun Elangeni Maharani, KwaZulu-Natal, South Africa.

Exploring differences in various Nb(V)- and Ta(V) tropolonato complexes

nation modes and intermolecular interactions could shed even more light on this nuance between Ta(V) and Nb(V) behaviour. Accordingly, the crystal structures of $[\text{Ta}(\text{Trop})_4]\text{Cl}$ and $[\text{Nb}(\text{Trop})_4]\text{Cl}$, as obtained following the above strategy, will be discussed in this study.

Experimental

Chemicals and instruments

All chemicals used for the preparation of the compounds were of a high analytical grade and were acquired from Sigma-Aldrich (South Africa).

The ^1H - and ^{13}C NMR solution-state spectra were acquired on a Bruker AVANCE II 600 MHz (^1H : 600.28 MHz; ^{13}C : 150.96 MHz) nuclear magnetic resonance spectrometer using an appropriate deuterated solvent (acetonitrile- d_3 [$\text{CD}_3\text{CN} = 1.94(5)$ ppm]), with all chemical shifts (δ) reported in ppm. The ^1H NMR spectra were referenced within the sample using residual protons from the deuterated acetonitrile- d_3 . The ^{13}C NMR spectra were similarly referenced internally to the solvent resonance [$\text{CD}_3\text{CN} = 1.39(4)$ ppm and 118.69(8) ppm], with all reported values noted relative to tetramethylsilane ($\delta = 0.0$ ppm).

The X-ray crystallographic data was obtained from a Bruker X8 ApexII 4K κ -CCD area detector diffractometer, specially equipped with a graphite monochromator and a MoK α fine-focus sealed tube ($T = 100(2)$ K, $\lambda = 0.71069$ Å), which operates at 2.0 kW (40 mA, 50 kV). Preliminary unit cell predictions, as well as data collections, were done by the SMART (Bruker, 1998a) refinement program. The raw frameset data was integrated using a narrow-frame integration algorithm and reduced using Bruker SAINT-Plus and XPREP (Bruker, 1999). This reduced data was corrected for the various absorption effects using the SADABS multi-scan technique (Bruker, 1998b) and the structure solved by using direct methods on the SIR97 package (Altomare *et al.*, 1999). Final refinement was completed using the WinGX (Farrugia, 1999) software, incorporating the SHELXL (Sheldrick, 1997) package (anisotropic full-matrix least-squares refinement was done on F^2). Aromatic protons were placed in geometrically idealized positions ($\text{C}-\text{H} = 0.93 - 0.98$ Å) and crystallographically constrained to ride on the host atoms with $U_{\text{iso}}(\text{H}) = 1.2U_{\text{eq}}(\text{C})$. All non-hydrogen atoms were refined with anisotropic displacement parameters. Graphics were obtained with DIAMOND (Brandenburg, 2006) (50% probability ellipsoids for non-hydrogen atoms).

Synthesis of tetrakis(tropolonato- $\kappa^2\text{O},\text{O}'$)niobium(V) chloride ($[\text{Nb}(\text{Trop})_4]\text{Cl}$) (1)

A solution of $[\text{NbCl}_5]_2$ (0.270 g, 1.001 mmol) in a mixture of dichloromethane (200 cm 3) and ether (30 cm 3) was added to a tropolone (0.489 g, 4.004 mmol) and dichloromethane (200 cm 3) mixture to produce a light orange solution from which a solid precipitated. The excess solvent was removed under reduced pressure. Acetonitrile (400 cm 3) was added to the residual powder and heated until dissolution was complete. Bright orange crystals separated on cooling. This compound was recrystallized from acetonitrile and vacuum-dried (120 °C, 3 hours) (0.409 g, yield 76%). IR (ATR, cm $^{-1}$): $\nu = 723, 876, 965, 1078, 1221, 1265, 1331, 1426, 1530, 1584$. ^1H NMR (300.13 MHz, acetonitrile- d_3 , ppm): $\delta = 7.11$ (d, 2H), 7.18 (t, 2H), 7.55 (t, 1H). ^{13}C NMR (300.13 MHz, acetonitrile- d_3 , ppm): $\delta = 87.8, 91.6, 101.3, 133.8$.

Synthesis of tetrakis(tropolonato- $\kappa^2\text{O},\text{O}'$)tantalum(V) chloride ($[\text{Ta}(\text{Trop})_4]\text{Cl}$) (2)

A solution of $[\text{TaCl}_5]_2$ (0.3582 g, 1.000 mmol) in concentrated hydrochloric acid (40 cm 3) and methanol (40 cm 3) was added to a mixture of tropolone (0.489 g, 4.004 mmol) in concentrated hydrochloric acid (20 cm 3) and methanol (320 cm 3) forming a yellow precipitate. This mixed slurry was refluxed (15 minutes) until a translucent yellow solution was observed with yellow crystalline $[\text{Ta}(\text{Trop})_4]\text{Cl}$ forming on cooling. The compound was recrystallized from a hot methanol-water solution and vacuum-dried (120°C, 3 hours) (0.394 g, yield 63 %). IR (ATR, cm $^{-1}$): $\nu = 721, 830, 1225, 1353, 1431, 1534, 1591, 1633, 3349$. ^1H NMR (300.13 MHz, acetonitrile- d_3 , ppm): $\delta = 7.18$ (d, 2H), 7.32 (t, 2H), 7.87 (t, 1H). ^{13}C NMR (300.13 MHz, acetonitrile- d_3 , ppm): $\delta = 89.2, 94.3, 103.6, 127.2$.

Results and discussion

A systematic comparison of the solid-state $[\text{Nb}(\text{Trop})_4]\text{Cl}$ and $[\text{Ta}(\text{Trop})_4]\text{Cl}$ structures is the main focal point of this investigation, with specific emphasis on bond angles and distances as well as the basic coordination geometry. This could give a clue as to why the coordination of tropolone is influenced so significantly by pH and temperature in solution (Muettteries and Wright, 1965) Figure 1 illustrates the crystal structures and coordination polyhedra of $[\text{Nb}(\text{Trop})_4]\text{Cl}$ (1) and $[\text{Ta}(\text{Trop})_4]\text{Cl}$ (2) and Table I compares selected crystallographic parameters of the compounds.

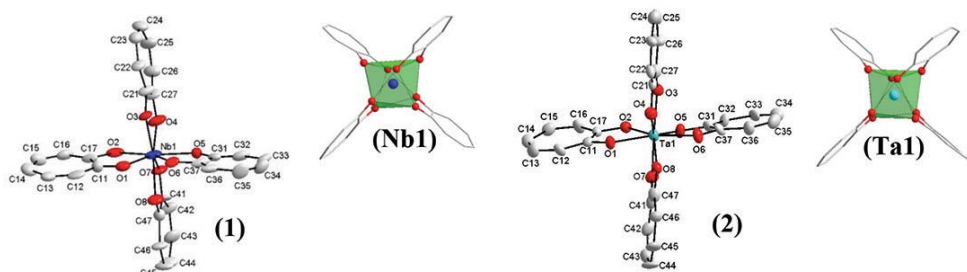


Figure 1—Illustration of the structures and coordination polyhedron of $[\text{Nb}(\text{Trop})_4]^+$ (1) and $[\text{Ta}(\text{Trop})_4]^+$ (2) showing general numbering scheme. (Note that for (2) an observed coordination configuration for Ta2 (omitted for clarity) was nearly identical with that illustrated for Ta1). Atomic displacement ellipsoids are drawn at 50% probability displacement level. Hydrogen atoms, counter-ion and Ta2 were omitted for clarity

Exploring differences in various Nb(V)- and Ta(V) tropolonato complexes

Table I

Crystallographic and refinement detail of compounds discussed in this investigation

Crystal formula	[Nb(Trop) ₄]Cl (1)	[Ta(Trop) ₄]Cl (2)
Empirical formula	C ₂₈ H ₂₀ NbO ₈	C ₂₈ H ₂₀ O ₈ Ta
Formula weight (g.mol ⁻¹)	537.80	625.55
Crystal system, space group	Triclinic, P ̄1	Monoclinic, C2/c
a, b, c (Å)	10.027(3), 12.907(3), 14.750(4)	19.626(3), 20.360(3), 22.446(3)
α, β, γ (°)	68.776(4), 78.141(3), 81.860(4)	90, 96.050(3), 90
Volume (Å ³), Z	1778.3(1), 2	2919.3(4), 4
Density (calculated, Mg/m ³)	1.371	1.506
Crystal colour, crystal size (mm ³)	Orange, 0.53 × 0.13 × 0.09	Yellow, 0.25 × 0.18 × 0.10
Absorption coefficient μ (mm ⁻¹)	0.399	3.802
F(000), theta range	583, 2.45–27.70°	3828, 1.35–28.00°
Reflections collected,independent reflections, R _{int}	6119, 3518, 0.1556	4792, 6477, 0.1617
Completeness to 2θ (°, %)	28.00, 97.6	28.00, 100
Data, restraints, parameters	20299, 0, 370	10753, 0, 240
Goodness-of-fit on F ²	1.106	1.152
Final R indices [I>2sigma(I)]	R ₁ = 0.1995 wR ₂ = 0.2956	R ₁ = 0.1131 wR ₂ = 0.3584
R indices (all data)	R ₁ = 0.2586 wR ₂ = 0.3470	R ₁ = 0.1803 wR ₂ = 0.4097
Largest diff. peak and hole (e.Å ⁻³)	0.40, -1.04	3.31, -2.15

The Nb(V) (1) compound crystallizes in the triclinic space group, P1, with one independent molecule in the asymmetric unit. For this molecule, a Nb(V) metal centre is coordinated to four independent tropolonato ligands arranged in a distorted D_2 -square antiprismatic geometry. This type of arrangement is extremely rare and has hardly ever been observed for 8-coordinated Nb(V) complexes (Booyens and Oglvie, 2008).

The Ta(V) (2) compound crystallizes in the monoclinic space group, C2/c, with one full [Ta(Trop)₄]⁺ cation (Ta1) and half of another [Ta(Trop)₄]⁺ (Ta2) moiety in the asymmetric unit. In the case of Ta1, a metal centre is surrounded by four independent tropolonato ligands arranged in a distorted D_2 -square antiprismatic geometry. In contrast, for Ta2, the Ta2 atom is located on a special position and is coordinated to two tropolonato ligands with the other half of the cation being generated through the mirror plane. Ta2 also illustrates a distorted D_2 -square antiprismatic coordination geometry. In spite of the two different crystallization modes of the two independent Ta(V) complexes, the average bite angles stay comparable with each other and typically 1° greater than for the Nb(V) complex. This type of arrangement has never been noted for a Ta(V) structure and only on one occasion in the structure of *tetrakis*(oxalato)tantalum(IV) for the Ta(IV) species (Cotton, Diebold and Roth, 1987).

A large residual electron density of 3.31 was located at a distance of 3.48 Å from C14 for compound 2 (see Table I). Although this value is very significant, it is isolated from the coordination sphere and need not be assigned for this investigation as it has minimal effect with relation coordination geometry around the metal centre.

When comparing the various bond distances and angles listed in Tables II and III, several trends are noticed. These tendencies are now discussed and compared systematically.

Nb-O and Ta-O bond distances

As expected, the average Nb-O (2.083(1) Å) and Ta-O (2.092(1) Å) bond distances correlate very well with each other. Similar average metal-oxido distances have been noted on several occasions in past studies (Allen, 2002; Davies and Jones, 2005; Peric, Brnjevic and Juric, 2009; Calderazzo and Englert, 1998; Roodt, Otto and Steyl, 2003; Schutte, Roodt and Visser, 2012). This phenomenon can probably be attributed to the near-identical covalent radii of both Ta and Nb. Although not much in relation to separation studies can be derived from this, it indicates that the assumption made – that the inferior crystal quality would not significantly influence coordinative crystal data – is acceptable.

O-metal-O bond angles and O...O bite distances

Interestingly, a substantial difference (max. 1.38°) in bidentate bite angle is noted between 1 and 2. From this it can be concluded that the chelate ring of the Nb(V) compound is significantly more strained. This could also give a clue as to why a decrease in pH has a different effect on each metal. As the pH of the solution increases, conditions become less advantageous for *tetrakis*-coordination, preferring the more stable *tris*-coordinated oxido species (if an oxygen-donating substance is available). The smaller steric demand of the four tropolone ligands in the Nb(V) case will promote nucleophilic attack by OH⁻ to the metal centre. Due to the fact that the chelate ring in the Nb(V) compound is more strained it could more readily sacrifice one of its tropolone ligands for increased stability.

Bite distances are fairly well correlated to ligand bite angle and, as expected, the average distances for 2 (2.447(1) Å) and 1 (2.431(1) Å) differ quite significantly.

Exploring differences in various Nb(V)- and Ta(V) tropolonato complexes

Table II

Selected bond lengths and bite distances for $[Nb(Trop)_4]Cl$ and $[Ta(Trop)_4]Cl$

$[Nb(Trop)_4]Cl$		$[Ta(Trop)_4]Cl$ (Ta1)		$[Ta(Trop)_4]Cl$ (Ta2)	
Atoms	Bond length (\AA)	Atoms	Bond length (\AA)	Atoms	Bond length (\AA)
Nb1-O1	2.094(1)	Ta1-O1	2.098(1)	Ta2-O9	2.087(1)
Nb1-O2	2.099(1)	Ta1-O2	2.068(1)	Ta2-O10	2.095(1)
Nb1-O3	2.092(1)	Ta1-O3	2.098(1)	Ta2-O11	2.076(1)
Nb1-O4	2.087(1)	Ta1-O4	2.093(1)	Ta2-O12	2.073(1)
Nb1-O5	2.021(1)	Ta1-O5	2.088(1)		
Nb1-O6	2.096(1)	Ta1-O6	2.091(1)		
Nb1-O7	2.085(1)	Ta1-O7	2.063(1)		
Nb1-O8	2.089(1)	Ta1-O8	2.134(1)		
O1···O2	2.454(1)	O1···O2	2.459(1)	O9···O10	2.431(1)
O3···O4	2.426(1)	O3···O4	2.456(1)	O11···O12	2.445(1)
O5···O6	2.401(1)	O5···O6	2.439(1)		
O7···O8	2.442(1)	O7···O8	2.452(1)		

Table III

Selected bond and plane angles for $[Nb(Trop)_4]Cl$ and $[Nb(Trop)_4]Cl$

$[Nb(Trop)_4]Cl$		$[Ta(Trop)_4]Cl$ (Ta1)		$[Ta(Trop)_4]Cl$ (Ta2)	
Atoms	Angle ($^\circ$)	Atoms	Angle ($^\circ$)	Atoms	Angle ($^\circ$)
O1-Nb1-O2	71.34(1)	O1-Ta1-O2	72.34(2)	O9-Ta2-O10	71.09(2)
O3-Nb1-O4	70.96(2)	O3-Ta1-O4	71.74(1)	O11-Ta2-O12	72.22(1)
O5-Nb1-O6	71.63(1)	O5-Ta1-O6	72.40(2)		
O7-Nb1-O8	71.60(2)	O7-Ta1-O8	71.69(1)		
Out-of-plane distortion (O1-O2-O3-O4)	28.46(3)	Out-of-plane distortion (O1-O2-O3-O4)	31.01(1)	Out-of-plane distortion (O9-O10-O11-O12)	26.99(2)
Out-of-plane distortion (O5-O6-O7-O8)	27.47(2)	Out-of-plane distortion (O5-O6-O7-O8)	27.61(2)		
Trop1/Trop3	174.34(2)	Trop1/Trop3	171.54(1)	Trop5/Trop5'	167.06(1)
Trop2/Trop4	174.71(3)	Trop2/Trop4	169.05(1)	Trop6/Trop6'	173.81(1)

Coordination geometry

Table III highlights the fact that the degree of distortion from D_2 -square antiprismatic (D_2 -SAP) geometry towards dodecahedral geometry is much more pronounced for 2. For ideal SAP geometry the ligand planes would have to lie opposite each other at an ideal 180° angle. When considering the 'ligand planes' as described in Table III, it is obvious that the distortion from ideal 180° is much more pronounced in the case of the 2 compound, although a significant distortion is also noted for 1. Figure 2 further illustrates this distortion by illustrating the outward bends of the various OA-OB-OC-OD planes for both complexes. Again, this is independent of the two different crystallization modes of Ta1 and Ta2.

Some correlation can be drawn between the observations by Muetteries and Wright in solution and this distortion noted in solid state (Muetteries and Wright, 1965). From basic crystallography it is known that dodecahedral geometry is an energetically favourable coordination mode, affording a more stable compound. It might then seem that the robustness of 2 vs. 1 in solution could also be ascribed to the more energetically favourable coordination mode (Hutchings *et al.*, 2014). Accordingly, an argument can be proposed that the 2 has dodecahedral geometry and is significantly distorted towards the D_2 -SAP geometry. Although this notion is not irrefutably conclusive, it cannot be ignored.

Conclusions

Some interesting observations were made from the comparison of the $[Ta(Trop)_4]Cl$ and $[Nb(Trop)_4]Cl$ solid-state crystal structures. The bite angles of both compounds revealed that the $[Nb(Trop)_4]Cl$ compound experiences a higher degree of strain within the chelate ring but less steric repulsion, thus is more prone to nucleophilic attack. This could have interesting implications for complex stability. When considering the higher degree of strain (less energetically favourable) within the Nb(V) chelate ring, this complex could more readily sacrifice one of its tropolone ligands for the sake of obtaining the more stable $[NbO(Trop)_3]$ complex (average bite angle $71.39(2)^\circ$).

Secondly, the $[Ta(Trop)_4]^+$ cation exhibits a more distorted square antiprismatic geometry compared with $[Nb(Trop)_4]^+$. In fact, the coordination geometry is so distorted that $[Ta(Trop)_4]^+$ might favour the more energetically favourable dodecahedral geometry. This might further contribute to the Ta(V) complex stability.

These observations from this crystallographic study of Nb(V) and Ta(V) tropolones substantiate the results noted from the solution-state investigation (Muetteries and Wright, 1965). With this enhanced knowledge of the intricacies of these systems, it is possible to investigate separation methods such as separation by ionic resins (in solution:

Exploring differences in various Nb(V)- and Ta(V) tropolonato complexes

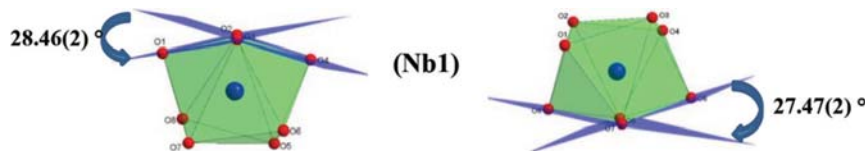
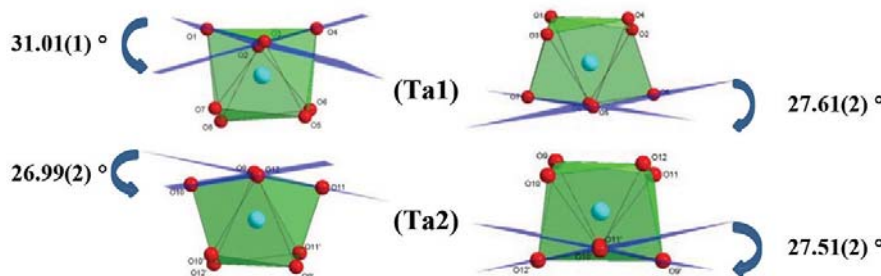


Figure 2—Illustration of the distortion of the SAP coordination polyhedron found in 1. (Left) Outward bend of the top-most atoms; 28.46(2)° (right) 27.47(2)° for bottom plane



Ta1: Outward bend of the top-most plane of 31.01(1)° and 27.61(2)° for the bottom plane
Ta2: Outward bend of the top-most plane of 26.99(2)° and 27.51(2)° for the bottom plane

Figure 3—Illustration of the distortion of the SAP coordination polyhedron found in 2

neutral $[NbO(Trop)_3]$ vs. cationic $[Ta(Trop)_4]^+$ at slightly acidic pH values), sublimation (differences in solid-state stability should cause differences of the sublimation temperatures of these Nb(V) and Ta(V) analogues) as well as fractional crystallization, which could be upscaled for industrial use.

Although comparison of reaction properties in solution with solid-state crystal structures should be done with care, this solid-state investigation has already shed some more light as to why the properties of the Nb(V) and Ta(V) compounds differ significantly.

Acknowledgements

Financial support from the Advanced Metals Initiative (AMI) of the Department of Science and Technology (DST) of South Africa, through the Nuclear Metals Development Network (NMDN) managed by the South African Nuclear Energy Corporation SOC Ltd (Necsa) is gratefully acknowledged. Appreciation is also expressed towards the University of the Free State and PETLabs Pharmaceuticals for financial provision of research initiative outputs. This work is based on research supported in part by the National Research Foundation of South Africa (UIDs 71836 and 84913).

References

- AGULYANSKY, A. 2004. The Chemistry of Tantalum and Niobium Fluoride Compounds. Elsevier, Amsterdam.
- ALLEN, F.H. 2002. The Cambridge Structural Database: a quarter of a million crystal structures and rising. *Acta Crystallographica*, B58, vol. 3. pp. 380–388.
- ALTOMARE, A., BURLA, M.C., CAMALLI, M., CASCARANO, G.L., GIACOVAZZO, C., COTTON, F.A., DIEBOLD, M.P. and ROTH, W.J. 1987. Variable stereochemistry of the eight-coordinate *Tetrakis*(oxalato)niobate(IV), $Nb(C_2O_4)_4^{4-}$. *Inorganic Chemistry*, vol. 26. pp. 2889–2901.
- ALTOMARE, A., BURLA, M.C., CAMALLI, M., CASCARANO, G.L., GIACOVAZZO, C., GUAGLIARDI, A., MOLITERNI, A.G.G., POLIDORI, G. and SPAGNA, R. 1999. SIR97: a new tool for crystal structure determination and refinement. *Journal of Applied Crystallography*, vol. 32. pp. 115–119.
- BOOVENS, J.C.A. and OGLVIE, J.F. 2008. Models, Mysteries and Magic of Molecules. Elsevier Netherlands.
- BOSE, D.K. and GUPTA, C.K. 2001. Extractive metallurgy of tantalum. *Mineral Processing and Extractive Metallurgy Review*, vol. 22. pp. 389–412.
- BRANDENBURG, K. 2006. DIAMOND, Release 3.0e. Crystal Impact GbR, Germany.
- BRUKER AXS Inc. 1998a. Bruker SMART-NT Version 5.050, Area-Detector Software Package. Madison, WI, USA.
- BRUKER AXS Inc. 1998b. Bruker SADABS Version 2004/1, Area Detector Absorption Correction Software. Madison, WI, USA.
- BRUKER AXS Inc. 1999. Bruker SAINT-Plus Version 6.02 (including XPREP), Area-Detector Integration Software. Madison, WI, USA.
- CALDERAZZO, F. and ENGLERT, U. 1998. Eight-coordinate chelate complexes of Zr(IV) and Nb(IV): X-ray diffractometric and EPR investigations. *Inorganica Chimica Acta*, vol. 270. pp. 17–7191.
- DAVIES, H.O. and JONES. 2005. Synthesis and structure of a tantalum(V) *Tetrakis*-O,O chelate: $[Ta(tmhd)_4][TaCl_6]$. *Inorganic Chemistry Communications*, vol. 8. pp. 585–592.
- FARRUGIA, L.J. 1999. WinGX Suite for small-molecule single-crystal crystallography. *Journal of Applied Crystallography*, vol. 32. pp. 837–838.
- HUBERT-PFALZGRAF, L.G., POSTEL, M. and REISS, J.G. (1987). *Comprehensive Coordination Chemistry*. Elsevier Pergamon, Oxford, UK.
- HUTCHINGS, A., HABIB, F., HOLMBERG, R.J. and KOROBKOV, I. 2014. Structural rearrangement through lanthanide contraction in dinuclear complexes. *Inorganic Chemistry*, vol. 53. pp. 2102–2112.
- MUETTERIES, E.L. and WRIGHT, C.M. 1965. Chelate chemistry. III. Chelates of high coordination number. *Journal of the American Chemical Society*, vol. 87, no. 21. pp. 4706–4717.
- PERIC, B., BRNICEVIC, N. and JURIC, M. (2009). $[NH_4]_4[(CH_3)_2NH_2]_2[Ta(C_2O_4)_4] \cdot 2H_2O$: the first (oxalato)tantalate(v) complex structurally characterized. *Structural Chemistry*, vol. 20. pp. 933–941.
- ROODT, A., OTTO, S. and STEYL, G. 2003. Structure and solution behaviour of rhodium(I) Vaska-type complexes for correlation of steric and electronic properties of tertiary phosphine ligands. *Coordination Chemistry Reviews*, vol. 245. pp. 125–142.
- SCHUTTE, M., ROODT, A. and VISSER, H.G. 2012. Coordinated aqua vs methanol substitution kinetics in fac-Re(I) tricarbonyl tropolonato complexes. *Inorganic Chemistry*, vol. 51. pp. 11996–12006.
- SHELDRICK, G.M. 1997. SHELXL97. Program for crystal structure refinement, University of Göttingen, Germany. ♦

The SAIMM Journal all you need to know!

- ★ Less 15% discount to agents only
- ★ PRE-PAYMENT is required
- ★ The Journal is printed monthly
- ★ Surface mail postage included
- ★ ISSN 2225-6253

The SAIMM Journal gives you the edge!

- ★ with cutting-edge research
- ★ new knowledge on old subjects
- ★ in-depth analysis

SUBSCRIBE TO 12 ISSUES
January to December 2017

of the SAIMM Journal

R2025.00

LOCAL



US\$520.00

OVERSEAS

per annum per subscription



For more information please contact: Kelly Mathee
The Journal Subscription Department

Tel: 27-11-834-1273/7 • e-mail: kelly@saimm.co.za or journal@saimm.co.za
Website: <http://www.saimm.co.za>

A serious, 'must read' that equips you for your industry—Subscribe today!

PARTS FOR EVERY PROCESS.

Quality Components Technical Expertise Superior Service | PART OF THE PROCESS



In your endless campaign to perfect operational efficiencies, BMG stands out as a partner who can truly make a difference.

Supported by the world's premium manufacturers, BMG's relentless expansion of product and service offerings continue to evolve, providing real opportunities to boost productivity in mining across the continent.

For more information
contact your nearest BMG branch.

www.bmgworld.net

facebook.com/bmgworld

ISO 9001 Certified

BEE 3



BEARINGS • SEALS • POWER TRANSMISSION • DRIVES & MOTORS • MATERIALS HANDLING
FASTENERS & TOOLS • HYDRAULICS • PNEUMATICS • FILTRATION • LUBRICATION • VALVES
TECHNICAL RESOURCES • FIELD SERVICES



High-temperature thermal plasma treatment of monazite followed by aqueous digestion

by D. Kemp* and A.C. Cilliers*

Synopsis

Monazite is a chemically inert, radioactive phosphate mineral that contains the light rare earth metals (Ce, La, Nd, Pr and Y), thorium and uranium. A new process, which improves the extraction efficiency of monazite, is under development. The equilibrium mole composition, in conjunction with the Gibbs free energy, indicates that as monazite is heated in the presence of carbon to a temperature above 1400°C, it decomposes into the rare earth oxides. These temperatures are within the operational limits of a thermal plasma. When monazite is fed to a DC plasma it forms amorphous plasma-treated monazite (PTM), which is more susceptible to chemical attack. This increased chemical reactivity permits dilute mineral acids to digest the PTM, which leads to higher extraction efficiencies of the rare earth elements than when monazite is digested using the conventional processes. When the conventional process for digestion of monazite is adapted to PTM, the extraction of rare earth elements, thorium and uranium is increased significantly.

Keywords

monazite, rare earth elements, thermal plasma.

Introduction

South Africa is a resource-based economy with an estimated *in situ* mineral wealth of US\$2.5 trillion. This makes South Africa one of the wealthiest mining jurisdictions in the world. However, considerable amounts of South Africa's minerals are exported as raw or partially processed ore. South Africa has embraced a mineral beneficiation strategy to develop the value chain for various minerals. One such mineral is monazite (South Africa, 2011) which, until now, underwent minimal industrial beneficiation in South Africa (Kemp and Cilliers, 2014).

Monazite is a chemically inert, radioactive phosphate mineral and is considered to be one of the most important rare earth minerals in the world (Hassan *et al.*, 1997; Amaral and Morais, 2010; Dill *et al.*, 2012). Monazite is a component of 'black sand' found in various beach deposits worldwide (Dilorio *et al.*, 2012) in combination with varying concentrations of ilmenite, magnetite, zircon, rutile and garnet (Ashry *et al.*, 1995; Sroor, 2003). Monazite contains the light rare earth elements (LREE) Ce, La, Pr, Nd and Y, which are in high demand and the radioactive elements thorium and uranium (Kim *et al.*, 2009). Conventional

monazite processing is a complicated, laborious and expensive process (Hurst, 2010) that utilizes highly corrosive media like concentrated sulphuric acid or sodium hydroxide, at elevated temperatures for extended periods of time (Zhu *et al.*, 2015). This process produces large volumes of radioactive and acidic effluents (Xie *et al.*, 2014). For these reasons, China, which produces 97% of the world's rare earth elements (Hurst, 2010), has prohibited the exploitation of monazite deposits (Zhu *et al.*, 2015). This opens the market for new and innovative technologies for the processing of monazite.

Zircon (ZrSiO_4) is a mineral with a chemically inert crystal structure, which requires harsh alkaline treatment to extract the zirconium metal (Biswas *et al.*, 2010). To overcome the chemical inertness of zircon sand, the South African Nuclear Energy Corporation SOC Ltd (Necsa) has developed a process using a DC non-transferred plasma to convert zircon into plasma-dissociated zircon ($\text{PDZ} - \text{ZrO}_2\text{SiO}_2$). PDZ is chemically more reactive than zircon and can be processed more efficiently (Havenga and Nel, 2012; Rendtorff *et al.*, 2012). The high temperatures (10 000°C), good thermal conductivities and high heat contents of thermal plasmas make them ideal for the processing of materials like zircon (Toumanov, 2003; Rendtorff *et al.*, 2012). It is hypothesized that a similar process could increase the chemical reactivity of monazite in order to improve downstream processing efficiency. This would increase the output of the REE, thorium and uranium while simultaneously permitting the use of less aggressive chemical processes (Toumanov, 2003).

* North-West University, Potchefstroom Campus, Potchefstroom, South Africa.

© The Southern African Institute of Mining and Metallurgy, 2016. ISSN 2225-6253. This paper was first presented at the AMI Ferrous and Base Metals Development Network Conference 2016 19–21 October 2016, Southern Sun Elangeni Maharani, KwaZulu-Natal, South Africa.

High-temperature thermal plasma treatment of monazite

If plasma-treated monazite (PTM) can be processed using less harsh chemicals, as hypothesized, it would create a unique competitive advantage for future rare earth and thorium developers. The new process reduces the environmental and radioactive hazards of monazite processing by treating monazite in a high-temperature thermal plasma followed by low-temperature mineral acid leaching. This paper provides a summary of the current development of this process.

Experimental procedure

Thermodynamic data from HSC version 6.1, developed by Outotec, was used to evaluate the Gibbs free energy, the equilibrium composition of the dissociation of monazite and to present alternative chemical processes that could require further investigation, or need to be avoided. Monazite is represented as the rare earth (RE) phosphate (REPO_4 , with RE = Ce, La, Pr, Nd and Y).

We treated monazite in a DC direct arc plasma batch reactor with the monazite housed in a graphite crucible. The reactor produces a high-temperature electric arc which is used to treat the monazite and produce PTM. The PTM product was heated in a high-temperature oven at 650°C for 24 hours to drive off excess graphite formed during the plasma processing.

Crushed monazite (MzC) was produced by hand-crushing 10 g of monazite for 10 minutes. Heat-treated monazite (HTM) was produced by heating 20 g of monazite in an alumina crucible at 1000°C for 3 hours, then rapidly cooling the product with water. Inductive monazite (IMz) was produced by heating 20 g of monazite in a graphite vessel to 1800°C in an induction oven. The product was cooled naturally and removed.

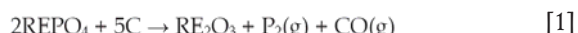
Monazite and PTM were leached with various commercially available mineral acids (32% HCl, 65% HNO_3 and 10% H_2SO_4) at 80°C for 1 hour; concentrated H_2SO_4 at 230°C for 4 hours, or by alkaline leaching (60% NaOH) at 140°C for 3 hours followed by mineral acid digestion (HCl or HNO_3) at 80°C for 1 hour. The concentrations of the individual REE in the leachate samples were determined by ICP analysis at an external laboratory. These values were used to calculate the extraction efficiency of the process.

Results and discussion

Theoretical decomposition of monazite

In order to evaluate whether monazite (rare earth phosphates) would dissociate in a plasma, its physical properties were compared to values from the literature and theoretical simulations for a known mineral, zircon (ZrSiO_4). Monazite has a physically weaker crystal lattice than zircon due to its lower chemical bond strength (Cottrell, 1958) and melting point (Table I) (Pirkle and Podmeyer, 1988; Hikichi and Nomura, 1987). From a physical strength perspective, the monazite crystal is weaker and could be destroyed more easily using less energy than required for zircon. As the plasma can destroy the zircon crystal lattice, (Kock *et al.*, 2011; Havenga and Nel, 2012) it is probable that the monazite crystal could be destroyed in a similar manner.

The temperature at which monazite dissociates without the use of a reagent is unknown at present. Monazite in the presence of excess carbon dissociates into the rare earth oxide, phosphor and carbon monoxide at a temperature between 1200 and 1400°C (Equation [1]) (Peng-fei *et al.*, 2010). According to the literature, zircon dissociates into PDZ at 1673 ± 10°C. The dissociation temperature can be lowered by 250°C when excess carbon is added in the presence of oxygen (Kaiser *et al.*, 2008; Telle, n.d.; Yugeshwaran *et al.*, 2015).



It is anticipated that the presence of carbon in the plasma could have a similar effect on monazite, which would lower its dissociation temperature by a few hundred degrees Celsius. To determine the potential dissociation temperature of monazite, the Gibbs free energy was used to estimate the temperature at which the individual rare earth (RE = Ce, La, Nd, Pr and Y) phosphates dissociate into the rare earth oxides and a phosphor-oxygen complex.

The dissociation temperature of zircon without excess carbon was accurately plotted using the Gibbs free energy at 1600–1700°C. Similarly, the Gibbs free energy of the dissociation of monazite in the presence of excess carbon was plotted for a dissociation temperature between 1100 and 1300°C. The Gibbs free energy of the dissociation of the rare earth phosphates (Equation [2]) indicates that CePO_4 dissociates at 1700°C, as predicted. However the remaining rare earth phosphates dissociate between 2500 and 3000°C (Figure 1), which is beyond the anticipated temperature range compared to zircon and CePO_4 . This dissociation will be investigated further.



Table I
Physical properties of monazite and zircon in relation to crystal strength

	Zircon	Monazite
Melting point (°C)	2100–2300	2057
Chemical bond strength (kJ/mol)	Si—O: Zr—O:	P—O: RE—O: (av.)

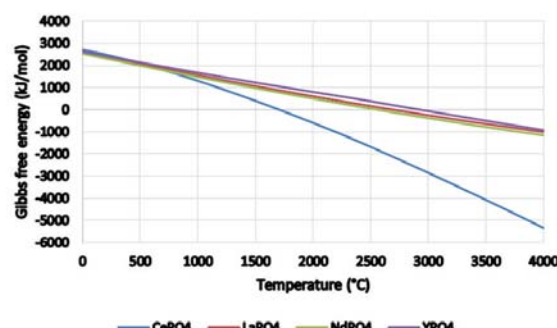


Figure 1—Gibbs free energy of the dissociation of monazite (rare earth phosphate) into the rare earth oxides and phosphor dioxide

High-temperature thermal plasma treatment of monazite

The formation of the rare earth oxides from monazite would improve the leachability of the plasma-treated monazite (PTM). This is because the highly inert monazite crystal would have been destroyed enabling the rare earth oxides to be leached using a diluted mineral acid, unlike the rare earth phosphates (Peelman *et al.*, 2014).

Plasma treatment of monazite

The starting material for all plasma cycles was monazite sand obtained from an external source. The sand consisted of 69.55% monazite, 17.67% zircon and 4.85% ilmenite with the remaining 7.93% consisting of other materials. Examination of the monazite sand by optical microscopy revealed a number of oval-shaped brown, red, white and black particles (Figure 2). These oval-shaped particles are reminiscent of this monazite sample and may differ from other monazite samples.

X-ray diffraction (XRD) analysis of monazite sand (Figure 3) and PTM was used to determine whether plasma treatment induces any structural or compositional changes in monazite. The XRD pattern of this monazite (Figure 3) shows peaks at $2\theta = 26.5^\circ$, 28° , 35° and 47° , along with a number of smaller peaks. The peak at $2\theta = 26.5^\circ$ was positively identified as that of the rare earth phosphates,

which are components of monazite. No further analysis for this study was completed.

We produced PTM by placing monazite sand in a graphite crucible and treating it in a DC direct arc plasma. We removed the PTM graphite layer after plasma treatment by heating the PTM in a conventional oven at 650°C for 24 hours, producing plasma-treated monazite heated (PTMH). We found that when monazite is treated incorrectly it behaves and looks like monazite when viewed under an optical microscope and analysed using XRD. If monazite is heated in the plasma for too long it melts and forms larger, more inert monazite particles. When monazite is treated correctly in the plasma then the changes to the physical structure of the particles are visible under an optical microscope, as all of the oval-shaped particles are destroyed (Figure 4). For this reason, it can be concluded that the proper treatment of monazite can be verified partially through the use of an optical microscope. Elemental X-ray fluorescence analysis on all PTM samples indicated no statistical difference in the elemental composition compared with the original monazite.

XRD analysis of PTMH confirmed the destruction of the monazite crystal structure. The absence of the monazite peaks (Figure 5) indicates that a completely amorphous powder has been produced. This indicates that the inert



Figure 2—Optical micrograph of monazite

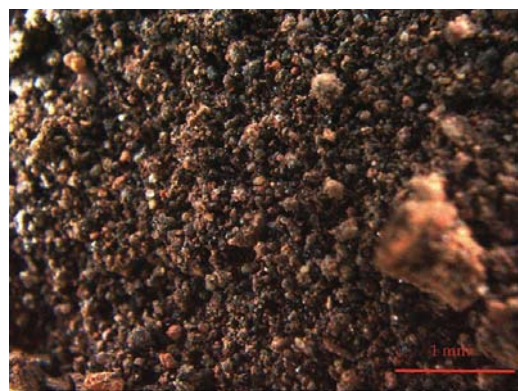


Figure 4—Optical micrograph of plasma-treated monazite

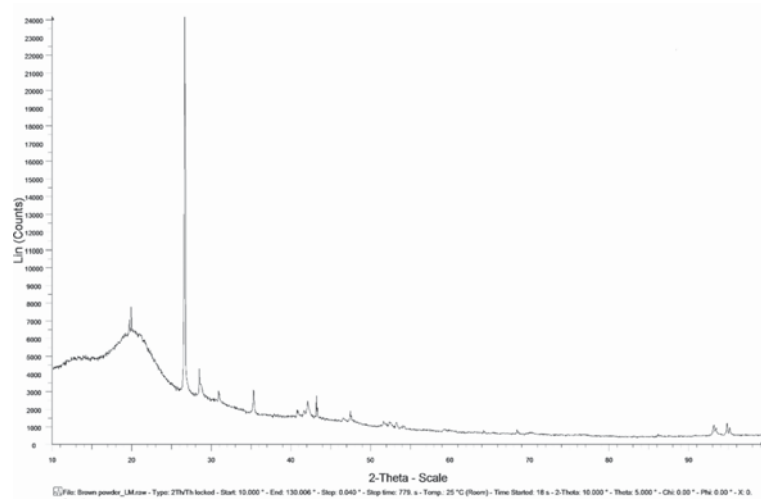


Figure 3—XRD analysis of monazite sand

High-temperature thermal plasma treatment of monazite

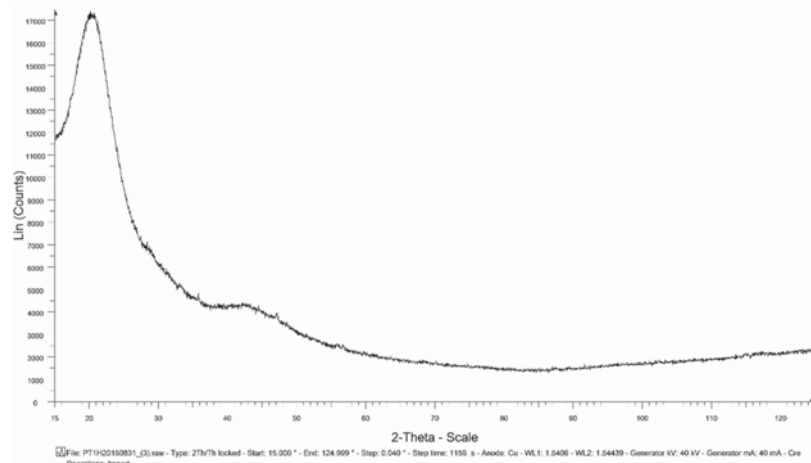


Figure 5—XRD pattern of amorphous plasma-treated monazite

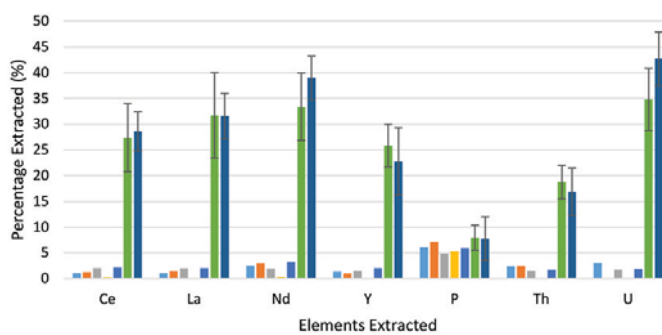


Figure 6—Extraction efficiency from various forms of monazite using 32% HCl at 80°C for 1 hour

phosphate crystal matrix, which is responsible for the inert nature of monazite (El-Nadi *et al.*, 2005), has been destroyed. The disadvantage of the formation of the amorphous substance is that the presence of the more reactive rare earth oxides cannot be confirmed. Other minerals, like zircon, have also been destroyed.

Chemical reactivity of plasma-treated monazite

In order to confirm the hypothesis that the plasma treatment of monazite delivers a more reactive product, PTM and PTMH were digested using a variety of different lixivants multiple times. The results indicate the quantity of the specific element extracted, as a percentage of the original amount of that element in the starting material. The standard deviation is shown as error bars. In order to obtain a proper comparison of the reactivity, additional samples were tested, like monazite (Mz), crushed monazite (Mzc), heat-treated monazite (HTM) and inductive monazite (IMz).

Digestion of PTM extracted on average 20 times more of the REE, 7 times more thorium and up to 11 times more uranium compared with untreated samples. Comparison of the extraction efficiency from Mz, Mzc, HTM, IMz, PTM and PTMH with 32% HCl (Figure 6) shows that simply heating the monazite (HTM and IMz) in a graphite crucible, even to a temperature above 1800°C, does not result in a more reactive product. The phosphor content remained reasonably constant throughout and cannot be used as an accurate indicator of the efficiency of the extraction process.

The results demonstrate the importance of using an appropriate temperature and treatment time period in order to increase the chemical reactivity of monazite. The plasma treatment of monazite is the predominant reason for improved REE and thorium extraction, as the plasma treatment destroys the monazite crystal matrix and produces amorphous PTM (Kemp and Cilliers, 2016a). Comparing the REE extraction efficiencies between heat-treated (PTM_H) and non-heat-treated PTM reveals a small but significant increase in the extraction efficiency. The multiple experiments conducted for this study were not optimized and the potential advantage gained by removing graphite from PTM requires further investigation.

In order to develop the process, the digestion of monazite and PTMH with various reagents was compared. Each experiment was repeated several times until a satisfactory standard deviation was achieved. These reagent included 65% HNO₃ (HNO₃) and 10% H₂SO₄ (H₂SO₄d) at 80°C for 1 hour, 98% H₂SO₄ at 230°C for 4 hours (H₂SO₄c) and 60% NaOH at 140°C for 3 hours followed by either 32% HCl (NaOH/HCl) or 65% HNO₃ (NaOH/HNO₃) at 80°C. The average extraction efficiencies of the various digestion processes over multiple experiments for monazite (Figure 7) and PTM_H (Figure 8) show clearly that PTM_H is more reactive than monazite. The optimum REE extraction using aqueous digestion from PTM_H was obtained using 32% HCl, which resulted in an average extraction efficiency of 38.44%. Alkaline digestion followed by HNO₃ yielded the highest

High-temperature thermal plasma treatment of monazite

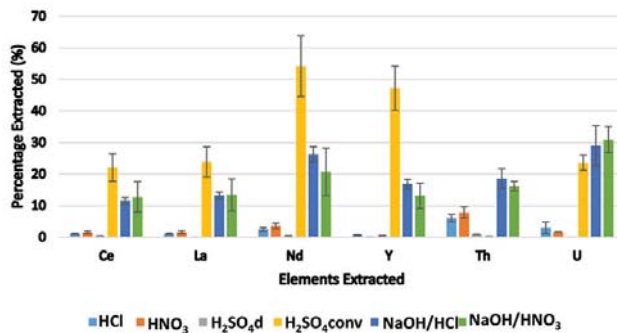


Figure 7—Extraction efficiencies of the rare earths, thorium and uranium from monazite for each reagent

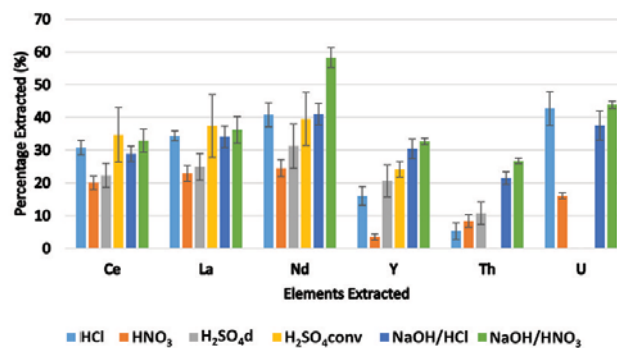


Figure 8—Extraction efficiencies of the rare earths, thorium and uranium from PTM_H for each reagent

possible extraction efficiency of 38.56% for the REE. Digestion using concentrated H₂SO₄ did not result in any vast improvement on the process, but did indicate that thorium was not extracted. Phosphor, which is still present in the PTM_H, is a contaminant that reduces the percentage of material extracted from the process (Kemp and Cilliers, 2016b).

The simpler diluted mineral acid digestion delivered higher extraction efficiency values for the REE, thorium and uranium from PTM_H – within 30% of those obtained using the conventional process – and has the distinct advantage of being simpler, easier to work with and potentially more economical. The conventional monazite digestion processes is more efficient at extracting the REE from PTM_H than the diluted mineral acids, with varying degrees of success for thorium and uranium. The extraction values obtained for Nd and Y by the conventional H₂SO₄ process were consistently high. No explanation can be given at this time and this phenomenon will be investigated further.

Thorium is found in monazite worldwide and can be used as fuel in a nuclear reactor (Greeneche *et al.*, 2007). 32% HCl extracted 16.89 % of the available thorium from monazite, PTM and PTM_H. The digestion of PTM_H with 60% NaOH followed by HNO₃ obtained the highest extraction efficiency for thorium along with the REE. This is surprising, as the thorium should have been at a minimum due to it precipitating out as Th(OH)₄. This phenomenon will be investigated further.

To produce PTM the monazite sample must be rapidly heated to allow it to properly dissociate and cooled rapidly to prevent the monazite particles from fusing together to form

larger, more inert particles. This can be accomplished with the use of an in-flight RF induction plasma or a DC non-transferred arc plasma, whereby the monazite would be subjected to the required rapid heating rate. After the rapid heating of the monazite particles, the design of the in-flight plasma would allow the particles to cool fast enough to prevent the formation of excessively large particles or recombination as a rare earth phosphate (Boulos, 1985).

Conclusion

The objective of this study was to treat monazite in a plasma in order to extract the rare earths, thorium and uranium more efficiently. Theoretically, when monazite, as a rare earth phosphate, is treated in a thermal plasma at 1600°C, it decomposes into chemically more reactive rare earth oxides. XRD analysis of plasma-treated monazite (PTM) indicated that the monazite crystal matrix was destroyed to produce an amorphous substance. It was determined that in order for the monazite to become more reactive the temperature and duration of the plasma treatment are crucial, otherwise, there would only be a minimal increase in chemical reactivity. PTM can be leached using a dilute mineral acid at a lower temperature and in less time, than in the conventional monazite processes, while obtaining similar extraction values. The overall conclusion of the study is that the plasma treatment of monazite increases its chemical reactivity. This knowledge can now be used to develop a more efficient and economical process than the comparable conventional chemical digestion methods currently employed to process monazite.

High-temperature thermal plasma treatment of monazite

Acknowledgements

The authors thank the South African Nuclear Energy Corporation SOC Ltd (Necsa) and the Nuclear Materials Development Network of the Advanced Metals Initiative of the Department of Science and Technology of South Africa for financial support.

References

- AMARAL, J.C.B.S. and MORAIS, C.A. 2010. Thorium and uranium extraction from rare earth elements in monazite sulfuric acid liquor through solvent extraction. *Minerals Engineering*, vol. 23, no. 6. pp. 498–503.
- ASHRY, H.A., KHAZBAK, A.E., SOLIMAN, F.A.S. and IBRAHIM, M.A. 1995. Determination of uranium and thorium content in the various stages of monazite upgrading. *Applied Radiation and Isotopes*, vol. 46, no. 8. pp. 735–739.
- BISWAS, R.K., HABIB, M.A., KARMAKAR, A.K. and ISLAM, M.R. 2010. A novel method for processing of Bangladeshi zircon: Part I: Baking and fusion with NaOH. *Hydrometallurgy*, vol. 103, no. 1–4. pp. 124–129.
- BOULOS, M.I. 1985. Inductively coupled R.F. (radio frequency) plasma. *Pure and Applied Chemistry*, vol. 57, no. 9. pp. 1321–1352.
- COTTRELL, T.L. 1958. The Strengths of Chemical Bonds. 2nd edn. Butterworth, London.
- DILL, H.G., WEBER, B. and KLOSA, D. 2012. Morphology and mineral chemistry of monazite-zircon-bearing stream sediments of continental placer deposits (SE Germany): Ore guide and provenance marker. *Journal of Geochemical Exploration*, vol. 112. pp. 322–346.
- DILORIO, C.L., KNIGHT, D.J. and MANCUSO, M.P. 2012. Adoption of thorium power. Project Number IQP-BJS-TP11. Worcester Polytechnic Institute, Worcester, MA.
- EL-NADI, Y.A., DAOUD, J.A. and ALY, H.F. 2005. Modified leaching and extraction of uranium from hydrous oxide cake of Egyptian monazite. *International Journal of Mineral Processing*, vol. 79. pp. 101–110.
- GRENECHE, D., SZYMCZAK, W.J., BUCHHEIT, J.M., DELPECH, M., VASILE, A. and JOLFIER, H. 2007. Rethinking the thorium fuel cycle: an industrial point of view. *Proceedings of the International Congress on Advances in Nuclear Power Plants*, Nice, Paper 7367.
- GUPTA, C.K. and KRISHNAMURTHY, N. 2005. Extractive Metallurgy of Rare Earths. CRC Press, Boca Raton, FL.
- HASSAN, A.M., ABDEL-WAHAB, M., NADA, A., WALLEY EL-DINE, N. and KHAZBAK, A. 1997. Determination of uranium and thorium in Egyptian monazite by gamma-ray spectrometry. *Applied Radiation and Isotopes*, vol. 48, no. 1. pp. 149–152.
- HAVENGA, J.L. and NEL, J.T. 2012. The manufacture of plasma-dissociated zircon (PDZ) via a non-transferred arc process utilizing three 150 kW DC plasma torches. *Journal of the Southern African Institute of Mining and Metallurgy*, vol. 112, no. 7. pp. 12–14.
- HIKICHI, Y. and NOMURA, T. 1987. Melting temperatures of xenotime and monazite. *Journal of the American Ceramic Society*, vol. 70, no. 10. pp. C252–C253.
- HURST, C. 2010. China's rare earth elements industry: what can the West learn? Institute for the Analysis of Global Security, Potomac, MD. <http://www.iags.org/rareearth0310hurst.pdf>
- KAISER, A., LOBERT, M. and TELLE, R. 2008. Thermal stability of zircon ($ZrSiO_4$). *Journal of the European Ceramic Society*, vol. 28, no. 11. pp. 2199–2211.
- KEMP, D. and CILLIERS, A.C. 2014. Fluorination of rare earth, thorium and uranium oxides and phosphates from monazite a theoretical approach, *Proceeding of the 2014 AMI Light Metals Development Network Conference*, Pilanesberg, South Africa. pp. 439–445.
- KEMP, D. and CILLIERS, A.C. 2016a. High temperature plasma treatment of monazite. *International Journal of Mineral Processing*. [Under review].
- KEMP, D. and CILLIERS, A.C. 2016b. Theoretical and experimental evaluation of the digestion of plasma treated monazite with diluted HCl and HNO_3 . *International Journal of Mineral Processing*. [Under Review].
- KIM, W., BAE, I., CHAE, S. and SHIN, H. 2009. Mechanochemical decomposition of monazite to assist the extraction of rare earth elements. *Journal of Alloys and Compounds*, vol. 486, no. 1–2. pp. 610–614.
- KOCK, L.D., LEKGOTHI, M.D.S., SNYDERS, E., WAGENER, J.B., NEL, J.T. and HAVENGA, J.L. (2011). The determination of percentage dissociation of zircon ($ZrSiO_4$) to plasma-dissociated zircon ($ZrO_2 \cdot SiO_2$) by Raman spectroscopy. *Journal of Raman Spectroscopy*, vol. 43, no. 6. pp. 769–773.
- PEELMAN, S., SUN, Z.H.I., SIETSMAN, J. and YANG, Y. 2014. Leaching of rare earth elements: Past and present, *Proceeding of the ERE2014L 1st European Rare Earth Resources Conference*, Milos, Greece, 4–7 September 2014. pp. 446–456.
- PIRKLE, F.L. and PODMEYER, D.A. 1988. Zircon: origin and uses. *Transactions of the Society for Mining, Metallurgy and Exploration*, vol. 292. pp. 1–20.
- RENDTORFF, N.M., SUÁREZ, G., CONCONI, M.S., SINGH, S.K. and AGLIETTI, E.F. (2012). Plasma dissociated zircon (PDZ) processing; influence of the Zr:Si ratio in the composition, microstructure and thermal re-crystallization. *Procedia Materials Science*, vol. 1. pp. 337–342.
- RUSSIAN FOUNDATION OF BASIC RESEARCH. 2008. Mincryst. http://database.iem.ac.ru/mincryst/s_lattice.php?ZIRCON [accessed 16 Mar. 2016].
- SOUTH AFRICA. 2011. A beneficiation strategy for the minerals industry of South Africa June 2011. Department of Mineral Resources.
- SROOR, A. 2003. Passive and active measurements of Egyptian monazite samples. *Applied Radiation and Isotopes*, vol. 58, no. 2. pp. 281–285.
- TELLE, R. (Not dated) Thermal stability of zircon ($ZrSiO_4$) and its dependence on natural impurities in the raw materials. Institut für Gesteinshüttenkunde, RWTH Aachen University.
- TOUMANOV, I.N. 2003. Plasma and High Frequency Processes for Obtaining and Processing Materials in the Nuclear Fuel Cycle. Nova Science Publishers, New York.
- XIE, F., AN ZHANG, T., DREISINGER, D. and DOYLE, F. 2014. A critical review on solvent extraction of rare earths from aqueous solutions. *Minerals Engineering*, vol. 56. pp. 10–28.
- XING, P., ZHUANG, Y., TU, G. and GUO, J. 2010. High temperature dephosphorization behavior of monazite concentrate with charred coal. *Transactions of Nonferrous Metals Society of China*, vol. 6326, December 2009. pp. 2392–2396.
- YUGESWARAN, S., ANANTHAPADMANABHAN, P.V., THIYAGARAJAN, T.K. and RAMACHANDRAN, K. 2015. Plasma dissociation of zircon with concurrent in-flight removal of silica. *Ceramics International*, vol. 41, no. 8. pp. 9585–9592.
- ZHU, Z., PRANOLO, Y. and CHENG, C.Y. 2015. Separation of uranium and thorium from rare earths for rare earth production – a review. *Minerals Engineering*, vol. 77. pp. 185–196. ♦



Investigation of the 'tiger skin' defect on indefinite chill rolls

by J. Jonck*, J.S. Moema*†, J. Jooste‡ and P. van Tonder§

Synopsis

Hot strip mills (HSMs) are used to roll steel slabs down from their initial size to plate or sheet, which are then used to manufacture a wide variety of goods for various industrial markets. The surface quality of the rolls that contact and deform the strip must be maintained during rolling, as roll imperfections can be imposed onto the strip, affecting the quality. For many years various roll producers have experienced the occurrence of a surface defect, commonly referred to as 'tiger skin' (TS), on indefinite chill (IC) work rolls, but the cause of the defect has not been thoroughly investigated. The characteristics of the TS defects on the roll surface were studied in an attempt to identify the cause and prevent its occurrence. In this paper, the characterization results of the defects are highlighted. Various techniques were utilized in the analysis: visual inspection, chemical analysis, optical microscopy, hardness testing, scanning electron microscopy and X-ray diffraction. The purpose of the testing was to identify any variations in the roll microstructure that could give rise to the surface variation. The results confirmed that the TS defects appeared as a pattern that is not related to a variation in the surface profile, surface cracking, chemical segregation, graphite characteristics, carbide characteristics, primary phase characteristics, bulk hardness, or microhardness. Further investigations are recommended.

Keywords

rolling, mills, hot strip, surface defects, 'tiger skin'.

Introduction

Hot strip mills (HSMs) are used to roll cast steel slabs from their initial size to plate or sheet, which is then used to manufacture a wide variety of goods for various industrial markets. The working rolls that contact and deform the strip are arguably the primary element of the HSM. The surface quality of the rolls must be maintained during rolling as imperfections are imposed onto the strip, affecting the quality. Among these rolls are indefinite chill (IC) work rolls. The general IC roll chemistry and microstructure compares well with traditional white cast iron, except for the sulphur and phosphorus impurity elements, which are kept to lower levels and the presence of some graphite in the microstructure similar to the other cast irons such as gray and ductile cast iron.

Various roll producers have experienced the occurrence of a surface defect on IC work rolls for many years, but the root cause of the defect has not been thoroughly investigated.

The defect has been commonly referred to as 'tiger skin' (TS) or elephant skin (van Tonder, 2012). In this research, the characteristics of the TS surface defect were studied in an attempt to identify and remedy the cause.

Background

Following discussions with both HSMs and the South African Roll Company (SARCO) in February and March 2012, the opinion was that while the TS defects appeared to be limited to IC work rolls, these were sourced from various reputable global roll producers. The TS defects appear as minor variations in the surface appearance of the roll, which can be difficult to identify, as shown in Figure 1. The TS defect is transferred to the strip during rolling and is classed as an aesthetically undesirable defect by the steel mill. While in service, TS is readily detected on the product by strip surface quality monitoring systems. The TS problem occurs intermittently and does not appear to correspond to specific periods or seasons. TS has been found in both single-stand reversing Steckel mills and multiple-stand continuous mills and at both carbon steel and stainless steel mills (van Tonder, 2012).

SARCO also indicated that the TS appeared within a specific layer of the shell (the outer portion of the composite roll) thickness, which is typically at the roll surface after approximately 70% of the roll's performance life. The

* Mintek, Randburg, South Africa.

† University of Pretoria, Pretoria, South Africa.

‡ Vaal University of Technology, Vanderbijlpark, South Africa.

§ South African Roll Company Pty. Ltd., Vanderbijlpark, South Africa.

© The Southern African Institute of Mining and Metallurgy, 2016. ISSN 2225-6253. This paper was first presented at the AMI Ferrous and Base Metals Development Network Conference 2016 19–21 October 2016, Southern Sun Elangeni Maharani, KwaZulu-Natal, South Africa.

Investigation of the 'tiger skin' defect on indefinite chill rolls



Figure 1—Visual appearance of the tiger skin (TS) surface defect on an IC work roll

TS appears only within the roll area that is in contact with the strip during rolling. The surface can be ground to remove the TS, but the defect commonly reappears when the roll resumes service. If TS is detected on a roll, a sufficient amount of shell material will be removed (based on recommendations from the roll supplier), reducing the roll diameter. The roll will then be returned to service and monitored closely to detect whether the defect reappears. If the defect has not been eliminated, the procedure is repeated until the defect is no longer present. The lost roll material results in loss of production and operational expenses for the mill (Columbus Stainless Steel, 2009). It has been postulated that TS may be related to a variation in graphite distribution over the roll surface. The general assumption was that TS must be roll-related, given the characteristics of occurrence, with the mill type and conditions also contributing to the prevalence (Columbus Stainless Steel, 2009; vander Voort, 1999).

Consultation with roll producers who have experienced TS indicated that, although the source is not clear, the belief was that the TS phenomenon was inherent to the roll casting process. It has also been postulated that TS could be related to the direction of rotation during casting, which is either in, or opposite to, the rolling direction in service. However, this should not be the case in a Steckel mill where the feed direction alternates.

Experimental procedure

Samples from various industrial IC rolls were analysed, including defective newly-manufactured rolls, rolls removed from service that did not show the TS defect, rolls showing the TS defect in service and rolls that had completed their service life without showing the TS defect. Shavings were removed from the roll displaying TS at diameters of 0, 7 and 15 mm (depth below the surface) of the roll, from the drive side and the free side.

The working surface was characterized by visual examination, replication with a 0.1 µm resolution of the surfaces, optical microscopy of replicas and the cleaned surfaces. Scanning electron microscopy (SEM) and etching trials were performed to identify any variation of microstructural features on the working surface related to the TS appearance.

A variety of etchants were used for the etching trials, including 4% nital, 10% nital, 4% picral, alkaline sodium

picrate (ASP), Beaujard's solution and a four-step duplex etchant (ASTM, 2003). The optical microscope stage height was recorded to determine the average height difference between the protruding carbides and the primary phase of the light and dark TS areas.

Chemical analysis of metal shavings was done to identify any chemical segregation or differences over the shell depth. The amounts of carbon and sulphur were determined by LECO combustion analysis. The other elements of interest were determined by inductively coupled plasma optical emission spectrometry (ICP-OES) analysis.

The samples were ground and polished to a 1 µm surface finish in the transverse and radial directions at different depths for microscopy. The polished sections were used to evaluate the graphite volume fraction, distribution and morphology, to identify any variations in graphite occurrence which could be related to TS. The samples were etched with 3% nital by swabbing the surface, to reveal the general microstructure. The etchant does not attack any carbides (which then remain white), enabling good contrast between the carbides (primary and secondary carbides) and the darker phases. This ensures accurate determination of the carbide volume fraction by means of image analysis. The samples were then etched with a range of selective carbide etchants to identify the carbide type, or any variation in the carbide type that might be present (specifically related to the TS defect). The etchants considered included an ASP etchant, Murakami's reagent, Groesbeck's reagent, 1% CrO₃ and 10% ammonium persulphate (APS) solution. The samples were etched with Beraha's sulfamic acid solution and a sodium metabisulphite (SMB) tint etch in order to identify any retained austenite (RA) within the microstructure. Beraha's tint etchant selectively colours the austenite phase blue. The SMB etchant darkens martensite and does not etch all other phases, including austenite (vander Voort, 1999).

Hardness testing was performed to determine if the TS pattern was related to changes in the bulk hardness or microhardness of individual phases within the microstructure. The bulk hardness was measured using a Rockwell C tester, while the microhardnesses of the carbides and primary phase were individually measured using a Vickers microhardness tester with a load of 200 g and a holding time of 15 seconds.

SEM analysis of the polished samples was performed to identify any microstructural or chemical variations associated with the TS. The chemical analysis was performed using energy-dispersive X-ray spectrometry (EDX) at the centre of the primary phase grains, centre of the primary carbides, interface between the primary phase and the carbides and the regions isolated by the eutectic carbides.

Samples were prepared for XRD using universal sample holders under typical metallography guidelines, followed by a brief final electropolish using chromic-acetic acid and a stainless steel cathode. The samples were examined prior to XRD testing to ensure no pitting of the surface had occurred (vander Voort and Manilova, 2005; ASTM, 2003; Klimek, 1975). XRD was then done to analyse the phases present within the samples. The relative phase amounts (mass %) were estimated using the Rietveld method (Lowe-Ma and Donlon, 2001). The carbide morphologies and quantity data (as determined by microscopy) were used to ensure accurate

Investigation of the 'tiger skin' defect on indefinite chill rolls

RA peak identification to avoid erroneous overestimation. A slow scanning rate of $0.5^\circ/2\text{ min}$ was utilized as low amounts of RA were expected for all the samples.

Results and discussion

Working surface

Visual examination showed that the TS defect could be clearly identified as a pattern of alternating lighter and darker shaded areas on the working surface. The difference in surface appearance could not be properly photographed, as none of the macro etchants highlighted the TS defect. Optical microscopy of the cleaned surfaces also showed no significant variation of microstructural features (carbide exposure, carbide distribution *etc.*) on the working surface related to the TS appearance, as shown in Figure 2. The average height difference between the protruding carbides and the depressed primary phase was not consistently higher or lower when comparing the light and dark TS areas, as shown in Table I.

SEM analysis showed widespread cracking of the roll surface which appeared to propagate through the carbide networks, as indicated in Figure 3. The carbides appeared to have been crushed during rolling, as indicated by smaller cracks that were limited to the carbides (Figure 4). However, the cracking did not appear to be related to TS, as the cracking was uniform across both the light and dark areas of all the samples. Oxide was observed on the primary phase, which is expected for a roll taken from service.

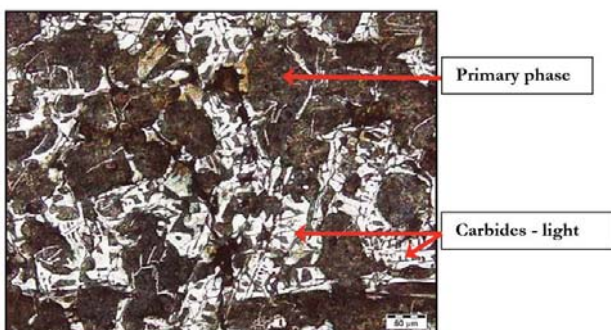


Figure 2—Micrograph showing the carbide (light) and primary phase (dark) on the working surface of a roll from service containing the TS defect

Table I Results from the height difference calculations of the working surfaces			
Height difference (μm)	Light	Dark	Overall
Minimum	3.8	3.0	3.0
Maximum	7.9	10.0	10.0
Average	5.4	6.5	5.9
Standard deviation	1.1	1.1	1.1

Chemical analysis

There was little variation in chemical composition across the shell material, except for the silicon content at both ends of the roll, which showed significant variation. The silicon decreases the stability of Fe_3C and increases the degree of graphitization of the roll, which could cause variations in graphite content (Craig, Hornung and McCluhan, 1988). However, the variation in silicon content did not appear to be more severe in the TS region compared to the other regions of the shell material and did not seem to be related to TS. No other chemical variations were identified that could give rise to the TS defect. The detailed chemical analysis may not be reported for proprietary reasons, but the typical IC composition is shown in Table II.

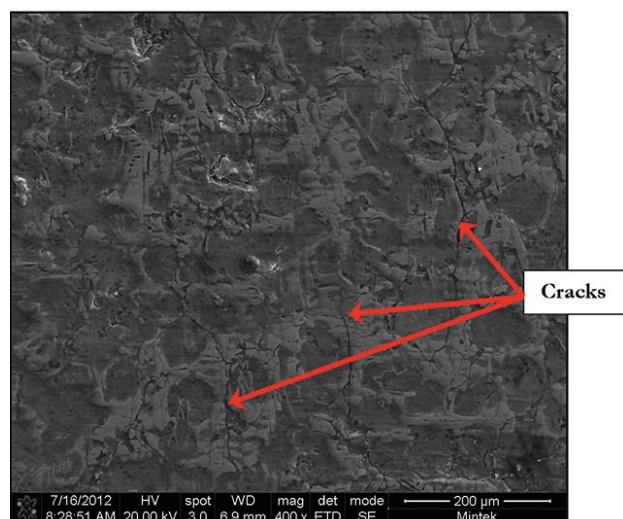


Figure 3—Secondary SEM image of the surface of a roll from service containing the TS defect, showing cracking along the carbide networks

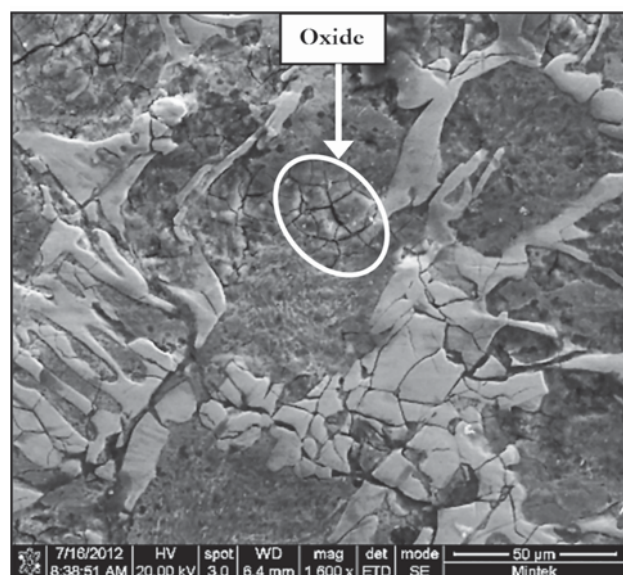


Figure 4—SEM image showing cracking of the carbides and oxide at the primary phase regions on the surface of a roll from service containing the TS defect

Investigation of the 'tiger skin' defect on indefinite chill rolls

Table II

Typical IC roll chemical composition, in mass % (Mees, 1999)

Element (mass %)	C	Mn	S	P	Si	Cr	Mo	Ni	V
Typical	Min.	3.0	0.3	0.0	0.0	0.5	0.7	0.1	3.0
	Max.	4.0	1.6	0.2	0.2	2.0	2.5	0.8	5.0

Microscopy

The polished sections showed coarse graphite with a uniform distribution and morphology on both the transverse and radial sections of most samples. The only exception was on one of the radial TS samples, where a variation between regions of predominantly fine, well-distributed graphite (Figure 5a) and coarse graphite particles (Figure 5b) was seen. These variations could influence the lubrication effect of the graphite during rolling, leading to variations in friction coefficient and slippage resistance across the roll and thereby cause a surface effect such as TS (Mees, 2002). Unfortunately, as the working surface had already been ground off on the as-received material, it could not be confirmed if the variation in graphite distribution correlated with the TS surface pattern.

Variation in the measured graphite content was observed between the transverse and radial sections of all the samples. The average graphite content showed a consistent increase with increase in depth below the surface, as shown in Figure 6. The increase in graphite content was probably due to the slower cooling rate associated with greater depths below the surface during solidification.

The general microstructures of all the samples were similar, consisting of free graphite and primary carbide networks within a martensitic primary phase. The primary carbide was found as interdendritic and eutectic structures, with the interdendritic being the most abundant. The arrangement of the two carbide structures did not correspond to the TS pattern. Figure 7 shows that the surface cracks propagated predominantly through the carbides, confirming the crushing of carbides identified during SEM analysis. The cracks were mostly limited to a depth of 100 µm below the surface.

The Nital-etched samples were used to determine the carbide area fraction. The amount of carbide was slightly higher at a depth of 7 mm and lower at a depth of 15 mm than at the surface (Figure 8). The carbide contents of the light and dark areas of the TS were found to be similar.

Only two etchants from the range tested were able to distinguish the carbides. The 10% APS etchant outlined the carbides, while the alkaline sodium picrate (ASP) etchant outlined and coloured the carbides, as shown in Figure 9. The combination of the etch response confirms that the carbides are of the M_3C type (vander Voort, 1999). The samples showed a uniform carbide type at the three depths examined

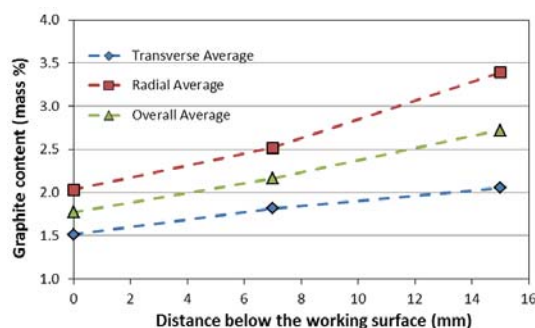


Figure 6—Variation in graphite content over the shell depth

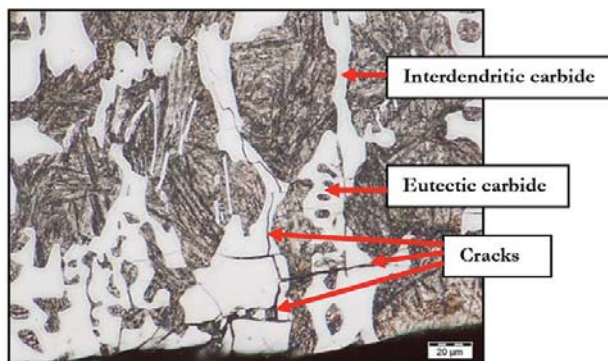


Figure 7—Micrograph showing the cracks extending along the carbides at the working surface

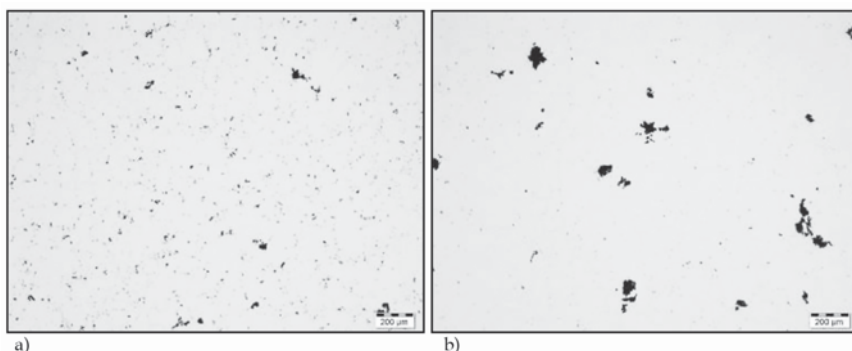


Figure 5—Micrograph of a radial sample in the polished condition, showing (a) finely distributed graphite and (b) coarse graphite

Investigation of the 'tiger skin' defect on indefinite chill rolls

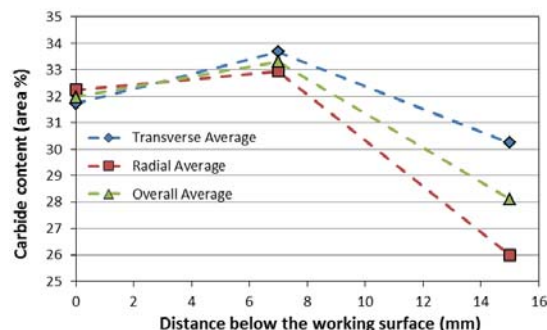


Figure 8—Variation in carbide amount (area percent) with shell depth from the surface

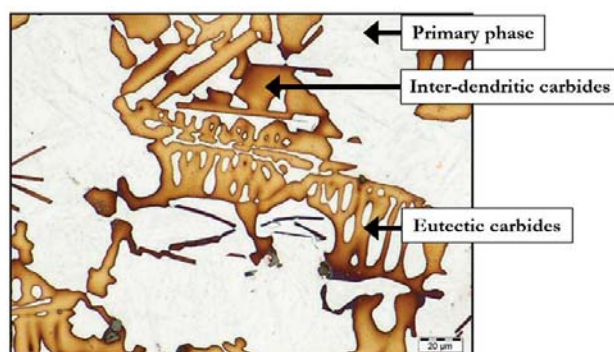


Figure 9—Micrograph of the surface sample etched with ASP

(0, 7 and 15 mm). Also, no variation in carbide type was found between the light and dark areas of the TS.

Beraha's sulfamic acid solution tinted traces of RA blue in all of the samples. However, the etchant did not show sufficient contrast between the RA and the martensite to enable accurate quantification. The RA appeared to be concentrated around the carbide networks, especially the eutectic carbides (Figure 10). There was no noticeable variation in the amount of RA between the light and dark TS areas, but quantification could not be performed to confirm the observation. In general, RA is identified only when it is in excess of approximately 10–15%, suggesting that the samples may all contain more than 10% RA (vander Voort 2009). However, it must be noted that the 10–15% RA observation was made on wrought tool steels, which have significantly more homogeneous structures than white cast iron (WCI). The more segregated and inhomogeneous cast structure of the IC rolls could lead to high local amounts of RA, despite bulk RA amounts significantly lower than 10%.

The sodium metabisulphite tint etch also confirmed the presence of RA associated with the carbide networks (Figure 11). The etchant appeared to show larger percentages of RA than Beraha's sulfamic acid etchant. The difference in etch response suggests that SMB may be more sensitive to RA than Beraha's sulfamic acid etchant and could reveal RA at smaller amounts. There appeared to be no difference in the amount of RA between the light and dark areas of the TS, similar to the response with the Beraha's sulfamic acid etchant. However, there was insufficient contrast between the

RA and the martensite and carbides to confirm this observation by quantitative phase analysis.

Hardness testing

The bulk hardness was fairly uniform and showed no notable hardness differences through the shell to a depth of 15 mm below the surface, as listed in Table III. No distinct difference in bulk hardness was found between the light and dark areas of the TS defects. The average bulk hardness was within acceptable levels for IC material.

The microhardness results of the primary phase showed a large variation ranging from 362 HV_{0.2} up to a maximum hardness of 655 HV_{0.2}. The large variation could be an indication of the lack of homogeneity of the structure. The average primary phase hardness was acceptable for IC material (Mees, 1999). No significant variation in primary phase hardness or trend between the light and dark TS regions was found.

The carbide microhardness also showed a large variation, ranging from 808 HV_{0.2} to 1319 HV_{0.2}. Many carbides cracked during the measurements, so the indentations that caused cracking were excluded from the results. The average carbide hardness of the samples was acceptable for IC material (Mees, 1999). The average carbide hardness did not show significant variation with shell depth from the surface and no significant trend or variation in carbide hardness was found between the light and dark TS regions.

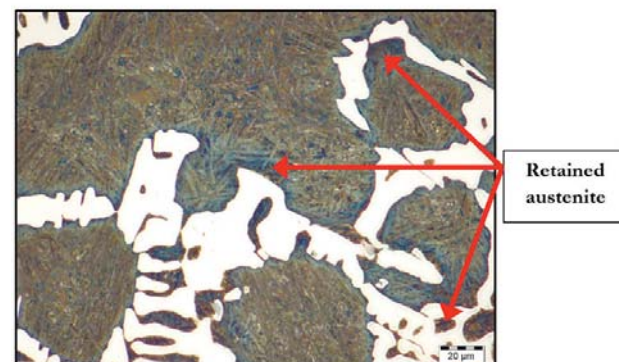


Figure 10—Micrograph of sample etched with Beraha's sulfamic acid etchant, showing RA (blue) adjacent to the carbide networks



Figure 11—Micrograph of sample etched with SMB and ASP, showing RA (light) adjacent to the carbide networks

Investigation of the 'tiger skin' defect on indefinite chill rolls

Table III

Bulk hardness testing results (Mees, 1999)

Bulk hardness (HRC)		No TS			TS defect			
		Surface	7 mm	15 mm	Dark	Light	7 mm	15 mm
Transverse	Minimum	55.2	56.7	53.0	47.4		49.0	47.9
	Maximum	58.8	59.1	57.5	57.7		59.1	56.3
	Average	57.2	57.9	55.9	53.1		53.5	52.7
	Standard deviation	1.2	0.8	1.5	1.4		1.7	1.4
Radial	Minimum	44.3	42.2	44.8	42.9	40.8	29.0	33.9
	Maximum	54.2	49.9	52.7	51.3	51.5	52.6	53.4
	Average	49.3	47.1	48.1	47.9	47.1	44.6	44.2
	Standard deviation	3.9	2.4	2.5	2.2	2.8	6.1	3.3
Typical IC hardness					45–60			

There was no marked difference in bulk hardness between the coarse graphite region at an average of 54.2 HRC and the fine graphite region at an average of 53.9 HRC. Differences in the bulk hardness across the surface also did not correspond with the areas of coarse and fine graphite. However, the primary phase hardness showed a substantial increase of approximately 300 HV associated with the fine graphite regions. It is not clear whether the increase in primary phase hardness was associated with TS. The high primary phase hardness values were not found on any other TS sample other than the specific radial sample.

SEM analysis

The SEM backscattered electron (BSE) images showed no clear distinction between the light and dark TS regions. However, in BSE mode the primary phase regions in the eutectic which were completely isolated by the eutectic carbides were a slightly lighter shade of grey compared to the darker grey remainder of the primary phase, as highlighted in Figure 12. These were the same areas identified by optical microscopy as being rich in austenite and this confirms the association of the eutectic carbides with the retained austenite. The shading variation suggests that there could be a slight compositional variation between these regions. The primary phase also showed needle-like phases, which are probably martensite and austenite, as identified during optical microscopy. The variation was found on all the samples analysed. The results from the EDS analysis showed no measurable variation in chemical composition of the primary phase between the light and dark areas of the TS. There was no measurable variation in chemical composition of the primary phase between the surface and 7 mm below the surface. There was also no measurable variation in chemical composition of the carbides or the primary phase between the light TS area, dark TS area, surface and 7 mm below the surface.

The chemical analyses also indicated that the lighter primary phase areas in the eutectic carbide regions are enriched with nickel, silicon and molybdenum compared to the general primary phase composition. Nickel is a strong austenite former and stabilizer, which typically increases the amount of retained austenite after casting and reduces the hardness (Gundlach, 1988). Enrichment in these elements will also increase the hardenability at these locations and

delay martensite formation relative to the rest of the primary phase (Craig *et al.*, 1988).

XRD analysis

The XRD results showed distinct peaks that were clearly distinguished from the background, which ensures accurate analysis. All the samples contained four phases: α' (martensite), cementite (M_3C carbide), γ -Fe (austenite) and graphite. The XRD analysis for RA is strongly affected by alloying elements and carbides. Given the high level of alloying elements in the material it should be noted that the accuracy will be less than typically achieved by XRD (vander Voort and Manilova, 2005; Lowe-Ma and Donlon, 2001).

XRD confirmed that the M_3C carbide type was in agreement with the EDX results. The amount of retained austenite was consistently above 3%, which is high and was in agreement with the microscopy observations. Higher amounts of RA will typically result in a decrease in roll performance, due to a reduction in hardness (Breyer, 2002). The typical hardness of retained austenite and martensite in IC rolls is approximately 375 HV and 600 HV, respectively (Schleiden, 2002). However, no significant variation in the distribution of RA was found between the different samples showing TS and the samples removed from deep enough below the surface that should not show any TS. Thus, the TS defect was not expected to be associated with high RA contents. However, the TS defect could be caused and/or influenced by a variation in RA content over the roll surface.

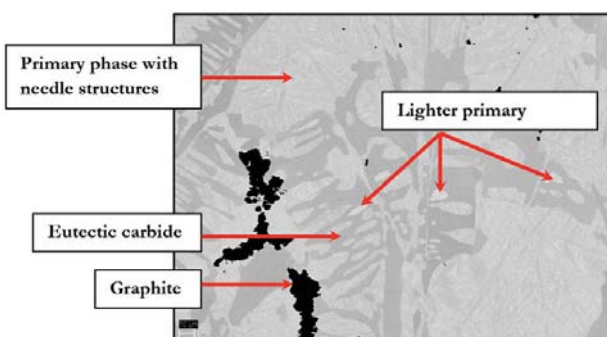


Figure 12—SEM-BSE image at 7 mm below the surface, showing lighter primary phase regions isolated by carbides

Investigation of the 'tiger skin' defect on indefinite chill rolls

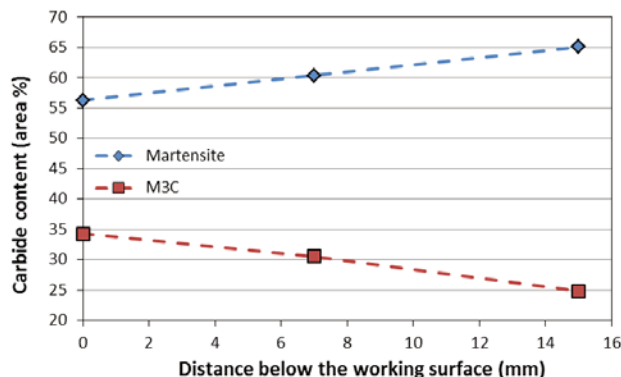


Figure 13—Variation in martensite and carbide content over the shell depth

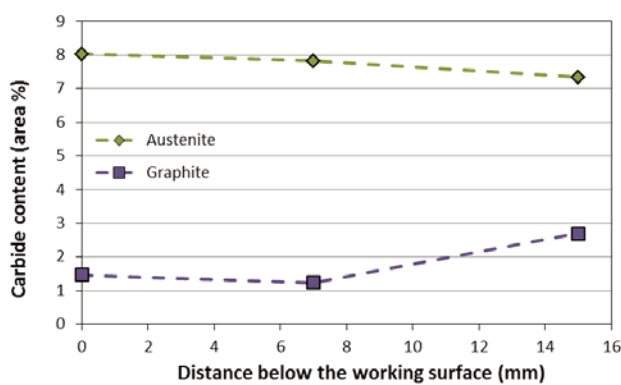


Figure 14—Variation in austenite and graphite amounts with shell depth

There should be sufficient heterogeneity within the cast structure to facilitate variations in RA content even though segregation effects could not be identified by microscopy.

It was generally found that the martensite and graphite content increased with depth below the surface, while the carbide content decreased (Figures 13 and 14). There was no significant variation in the amount of retained austenite from the surface to 15 mm below the surface.

Conclusions

The tiger skin (TS) defect appeared as a pattern of alternating lighter and darker shaded areas on visual inspection of an IC work roll at low magnification. This defect did not seem to be specifically related to variations in: the surface profile, surface cracking, chemical segregation, bulk hardness, or microhardness. There was also no correlation found between the TS defect and phase characteristics, *i.e.* amount, distribution, size and composition of: graphite, M₃C, martensite and retained austenite.

SEM analysis showed widespread cracking of the roll surface which appeared to propagate through the carbide networks. Microscopy confirmed that the carbides had been crushed during rolling, as indicated by smaller cracks which were limited to the carbides.

Further investigation of the casting parameters, solidification process and solidification front is required in order to recommend remedial action to prevent the TS formation. It is also clear that a collective effort between roll manufacturers and the mill end-user would be required in order to resolve the occurrence of TS.

References

- ASTM. 2003. Standard practise for X-ray determination of retained austenite in steel with near random crystallographic orientation. *ASTM E975-03*. ASTM International, Philadelphia, USA.
- BREYER, J.P. 2002. The metallurgy of high chromium-molybdenum white iron and steel rolls. *Rolls for the Metalworking Industries*. Lee, G.E. (ed.). Iron and Steel Society, Warrendale, PA. pp. 29–40.
- COLUMBUS STAINLESS STEEL. 2009. Tiger skin defect on SARCO roll surface. Middelburg, South Africa. Internal report.
- CRAIG, D.B., HORNUNG, M.J. and McCLUHAN, T.K. 1988. Gray iron. *ASM Handbook: Castings*. Davis, J.R., Destefani, J.D. and Zorc, T.B. (eds.). ASM International, Materials Park, OH. pp. 1365–1409.
- GUNDLACH, R.B. 1988. High-alloy white-irons. *ASM Handbook: Castings*. Davis, J.R., Destefani, J.D. and Zorc, T.B. (eds.), ASM International, Materials Park, OH. pp. 1484–1500,
- KLIMEK, E.J. 1975. A metallographic method for measuring of retained austenite. *Metals Engineering Quarterly*, vol. 15, no. 1. pp. 55–61.
- LOWE-MA, C.K. and DONLON, W.T. 2001. Comments on determining X-ray diffraction-based volume fractions of retained austenite in steels. *Powder Diffraction*, vol. 16, no. 4. pp. 198–204.
- MEES, J.B. 1999. The metallurgy of indefinite chill cast iron. *Rolls for the Metalworking Industries*. Lee, G.E. (ed.), Iron and Steel Society, Warrendale, PA. pp. 41–47.
- NUNDLALL, K. 2008. Memorandum: metallurgical analysis of elephant skin defect on Steckel mill work rolls. Report no. Met. Ref. 200807P01. Columbus Stainless Steel, Middelburg, South Africa. Internal report.
- SCHLEIDEN, R.F. 2002. The metallurgy of cast iron rolls. *Rolls for the Metalworking Industries*. Lee, G.E. (ed.). Iron and Steel Society, Warrendale, PA. pp. 20–28.
- VAN TONDER, P. 2012. Personal communication, 14 February. South African Roll Company.
- VANDER VOORT, G.F. 2009. Martensite and retained austenite. *Industrial Heating*, vol. 76, no. 4. pp. 51–54.
- VANDER VOORT, G.F. and MANILOVA, E.P. 2005. Hints for imaging phases in steels. *Advanced Materials and Processes*, vol. 163, no. 2. pp. 32–37.
- VANDER VOORT, G.F. 1999. *Metallography: Principles and Practices*. ASM International, Materials Park, OH. ◆



Terex® Minerals Processing Systems

Not just equipment. A complete solution.

ELB Equipment, the sub-Saharan Africa distributor of a complete range of Terex® Minerals Processing Systems, understands your business and with Terex® are dedicated to offering cost-effective solutions for your needs.

In today's competitive environment, you need high quality equipment backed by an outstanding support network locally and inter-nationally. Our sales and after-market teams are trained to provide customers with outstanding crushing and screening process knowledge and service.

As a member of the ELB Group, we have a century of experience in the mining industry that you can depend on. Customer satisfaction is our ultimate goal.

Distribution and Product Support by:



EQUIPMENT
A Member of the ELB Group

H/Office: Tel: (011) 306-0700
Fax: (011) 918-7208
e-mail: Elb@elbquip.co.za
Website: www.elbequipment.com

Branches and Dealers throughout
Southern Africa

6th Sulphur and Sulphuric Acid 2017 Conference

9 May 2017—WORKSHOP
10–11 May 2017—CONFERENCE
12 May 2017—TECHNICAL VISIT

Cape Town Convention Centre
Cape Town, South Africa

BACKGROUND

The production of SO₂ and Sulphuric acid remains a pertinent topic in the Southern African mining, minerals and metallurgical industry. Due to significant growth in acid and SO₂ production as a fatal product, as well as increased requirement for acid and SO₂ to process Copper, Cobalt and Uranium, the Sub Saharan region has seen a dramatic increase in the number of new plants. The design capacity of each of the new plants is in excess of 1000 tons per day.

In light of the current state of the industry and the global metal commodity prices the optimisation of sulphuric acid plants, new technologies and recapture and recycle of streams is even more of a priority and focus. The 2017 Sulphuric Acid Conference will create an opportunity to be exposed to industry thought leaders and peers, international suppliers, other producers and experts.

To ensure that you stay abreast of developments in the industry, The Southern African Institute of Mining and Metallurgy, invites you to participate in a conference on the production, utilization and conversion of sulphur, sulphuric acid and SO₂ abatement in metallurgical and other processes to be held in May 2017 in Cape Town.

OBJECTIVES

- > Expose SAIMM members to issues relating to the generation and handling of sulphur, sulphuric acid and SO₂ abatement in the metallurgical and other industries.
- > Provide opportunity to producers and consumers of sulphur and sulphuric acid and related products to be exposed to new technologies and equipment in the field.
- > Enable participants to share information and experience with application of such technologies.
- > Provide opportunity to role players in the industry to discuss common problems and their solutions.

For further information contact:

Conference Co-ordinator: Camielah Jardine

Tel: (011) 834-1273/7

E-mail: camielah@saimm.co.za

Website: <http://www.saimm.co.za>





The separation of zirconium and hafnium from $(\text{NH}_4)_3\text{Zr}(\text{Hf})\text{F}_7$ using amine-based extractants

by E.W. Conradie*, D.J. van der Westhuizen*, J.T. Nel† and H.M. Krieg*

Synopsis

The suitability of the amine-based extractants Alamine 336, Aliquat 336 and Uniquat 2280 (10 wt%) for the selective extraction of zirconium (Zr) and hafnium (Hf) from a $(\text{NH}_4)_3\text{Zr}(\text{Hf})\text{F}_7$ solution was investigated. The extractant-containing organic phase consisted of cyclohexane and 5 v/v% 1-octanol as phase modifier. The $(\text{NH}_4)_3\text{Zr}(\text{Hf})\text{F}_7$ was dissolved in either hydrochloride acid or sulphuric acid (0.01–8.0 mol/dm³). The following variables were investigated: (i) the type and concentration of the acid, (ii) the equilibrium time, (iii) the organic/aqueous phase ratio and (iv) the extractant to metal ratio. Subsequently, using the optimized extraction conditions, the stripping of extracted metals from the organic phase was investigated using sodium chloride and sulphuric acid. The metal content in the aqueous phase was determined using ICP-OES before and after extractions.

When using sulphuric acid solutions, extractions of >80% were reached both for Zr and Hf. In all cases equilibrium was achieved in less than 25 minutes of contact between the organic and the aqueous phase. Stripping of metals was achieved with >40% separation and 50% extraction using a sodium chloride (0.7 mol/dm³) stripping solution.

Keywords
zirconium, hafnium, amine extractants, $(\text{NH}_4)_3\text{Zr}(\text{Hf})\text{F}_7$.

Introduction

Zirconium (Zr) and hafnium (Hf) coexist in nature and have similar chemical properties such as ionic radii (0.074 mm for Zr^{4+} and 0.075 mm for Hf^{4+}) and valence electrons in the outer orbitals. (Xu *et al.*, 2015; Nielsen *et al.*, 2000). Although both elements can be found in group 4 of the periodic table, their properties as regards nuclear application differ, the thermal neutron capture cross-section being much higher for Hf than that for Zr. (Purohit and Devi, 1997; Yang *et al.*, 2002) Zr also has a high corrosion resistance in acid media, which improves the lifetime of cladding materials in nuclear reactors. Hence, for Zr to be used as fuel cladding material and water-cooled components in nuclear reactors, the Hf content must be reduced from the naturally occurring 3% to <100 ppm. (Li *et al.*, 2011)

There are several processes that are currently in use for the extraction and purification of Zr and Hf, such as the methyl isobutyl ketone (MIBK) process proposed by

Fischer and Chalybaeus (Overholser *et al.*, 1960). In this process, Zr and Hf form complexes with thiocyanate that have different solubilities, resulting in Hf being preferentially extracted into the organic phase. The disadvantages of this process are the high concentrations of ammonium and cyanides in the waste stream. The formation of cyanides from thiocyanate can occur in various ways, but in the case of the MIBK process the thiocyanate (SCN^-) is converted to OCN^- by the ammonium and to HCN by nitric acid solutions also present in the mixtures (Jenny *et al.*, 2001). The low flashpoint of the solvent is also a disadvantage. Other processes known to the industry are the tributyl phosphate (TBP) and Cyanex 923 processes, in which selective extraction is attained in a nitric acid solution as proposed by Taghizadeh *et al.* (2011). In 1974, Sato and Watanabe investigated the extraction of Zr in a sulphate medium using different types of amine extractants, showing that secondary amines are superior to tertiary amine extractants (Amaral *et al.*, 2013). In 2014, Wang and Lee reported on the preferential extraction of Zr in a sulphate medium using Aliquat 336, Alamine 336, Alamine 300 and Alamine 308 (Wang and Lee, 2015). All of the abovementioned methods and processes use Zr and Hf chloride salts as the starting reagent.

The South African Nuclear Energy Corporation (Necsa) has patented a plasma and fluoride process for the manufacturing of

* Chemical Resource Beneficiation, (CRB), North-West University of Potchefstroom Campus, Potchefstroom, South Africa.

† The South African Nuclear Energy Corporation (SOC) Ltd. (Necsa), Pretoria, South Africa.

© The Southern African Institute of Mining and Metallurgy, 2016. ISSN 2225-6253. This paper was first presented at the AMI Ferrous and Base Metals Development Network Conference 2016 19–21 October 2016, Southern Sun Elangeni Maharani, KwaZulu-Natal, South Africa.

The separation of zirconium and hafnium from $(\text{NH}_4)_3\text{Zr}(\text{Hf})\text{F}_7$

zirconium metal starting from the mineral zircon (ZrSiO_4) (Nel *et al.*, 2014). According to the patent, plasma-dissociated zircon is reacted with ammonium bifluoride and an $(\text{NH}_4)_3\text{Zr}(\text{Hf})\text{F}_7$ complex is formed and isolated for downstream processing, *i.e.* separation of Zr and Hf. It is the purpose of this research to determine the suitability of amine extractants (Alamine 336, Aliquat 336 and Uniquat 2280) for the separation of Zr and Hf from $(\text{NH}_4)_3\text{Zr}(\text{Hf})\text{F}_7$ (97 ppm Zr and 3 ppm Hf) in hydrochloric and sulphuric acid solutions (0.01–8 mol/dm³). Since the extraction from this salt has not been published previously, limited comparison of the data to literature data was possible. The parameters investigated were the type of acid and acid concentration, the type of extractant, extractant concentration and the effect of the two metals (Zr and Hf) on one another. Subsequently, two stripping agents (sodium chloride and sulphuric acid) were evaluated to regenerate the organic phases and to serve as possible scrubbing liquors.

Materials and methods

Tri-octyl/decyl amine (98% Alamine 336, Cognis Corporation), tricaprylmethylammonium chloride (97% Aliquat 336, Cognis Corporation) and didecyl dimethyl ammonium chloride (Uniquat 2280, 80%, Lonza) were diluted with cyclohexane (98%, Labchem) to 10 wt%. Lastly, 5 v/v% 1-octanol (98%, Sigma Aldrich) was added to the solvent to prevent the formation of a third phase. All chemicals were of analytical grade and used as received.

Fresh stock solutions of sulphuric (9% H_2SO_4 , Labchem) or hydrochloric acid (32% HCl, LabChem) were prepared containing $(\text{NH}_4)_3\text{ZrF}_7$ and $(\text{NH}_4)_3\text{HfF}_7$ obtained from Necsa. The pure Zr and Hf salts were prepared by simulating the Necsa plasma process (Nel *et al.*, 2014) using a single metal feed of zirconium oxide (99.9% ZrO_2 , Sigma-Aldrich) and hafnium oxide 99.9% HfO_2 , Sigma-Aldrich). The prepared $(\text{NH}_4)_3\text{ZrF}_7$ and $(\text{NH}_4)_3\text{HfF}_7$ were analysed at Necsa to ensure the correctness and purity (97%) of the compounds.

Pelindaba Analytical Laboratories (PAL) performed ICP analysis to verify the metal concentrations. Distillation methods were used to obtain the relevant fluoride data and an ion-selective electrode was used to analyse the ammonium content. Acid concentrations varied from 0.001–8 mol/dm³, while the metal concentrations were fixed for single salt extractions at 100 mg/dm³ Zr/Hf and for mixed salts extractions at 97 mg/dm³ and 3 mg/dm³ for Zr and Hf respectively. Aqueous phase dilutions were made with deionized water (Millipore Milli-Q Plus® Q-pack CPMQ004R1).

H_2SO_4 and sodium chloride (98% NaCl, LabChem) were diluted with deionized water to concentrations ranging from 0.001–2 mol/dm³.

The extraction and stripping experiments were done by contacting equal volumes of the organic and aqueous phase (25 mL; A/O = 1) at 25°C for 60 minutes in a rotary shaker and incubator at 310 r/min. Although equilibrium was reached after 25 minutes (data not shown), all samples were shaken for 60 minute to ensure sufficient equilibrium. After achieving equilibrium and separating the phases in standard separation funnels, inductively coupled plasma-optical

emission spectrometry (ICP-OES, Thermo Scientific iCAP 6000 SERIES ICP + CETAC ASX- 520 Auto sampler) was used to analyse the metal concentration in the aqueous phase. The concentration of the metal in the organic phases was assumed to be in accordance with the mass balance.

Results and discussion

Extraction

Influence of acid concentration on single salt extraction

The initial experiments were designed to observe the effect and correlation of single- and mixed salt extractions. Both single and binary systems were evaluated using HCl and H_2SO_4 solutions with as wide as possible concentration range for the initial screening (0.1–8 mol/dm³). In subsequent experiments more data points in narrower ranges were selected. Three different amine-based extractants were used. Alamine 336 is a tertiary amine with three carbon chains extended from the nitrogen ($\text{C}_{24}\text{H}_{51}\text{N}$). Both Aliquat 336 and Uniquat 2280 are quaternary ammonium salts with a positively charged nitrogen bonded to a methyl group and three additional carbon chains in the case of Aliquat 336 and two methyl groups and two carbon chains in the case of Uniquat 2280 (Senol, 2001; Tan *et al.*, 2007; Barnabas and Treadway, 2010)

In the single salt experiments, emulsions were observed and hence no analysis was possible when extracting with Uniquat 2280 in 4–8 mol/dm³ H_2SO_4 as well as when using Alamine 336 in 0.1 mol/dm³ H_2SO_4 . Banda *et al.* (2012) observed similar emulsions and third phase formations while using Alamine 336 in HCl.

Figure 1 and Figure 2 display data on the single metal extraction of Zr and Hf from HCl and H_2SO_4 respectively using the experimental conditions described. No significant extraction was obtained above 1 mol/dm³ acid, irrespective of the type of acid or extractant used. The highest extraction

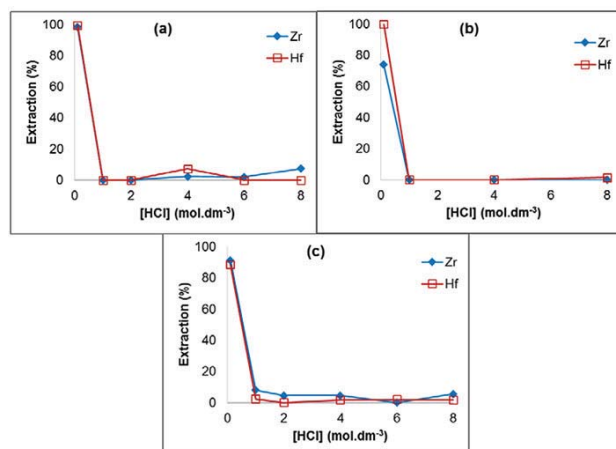


Figure 1—Effect of hydrochloric acid concentration with single salt extraction using (a) Alamine 336, (b) Aliquat 336 and (c) Uniquat 2280. Conditions: 10 wt% extractants, 100 ppm Zr, 100 ppm Hf, A/O = 1, contact time 60 minutes

The separation of zirconium and hafnium from $(\text{NH}_4)_3\text{Zr}(\text{Hf})\text{F}_7$

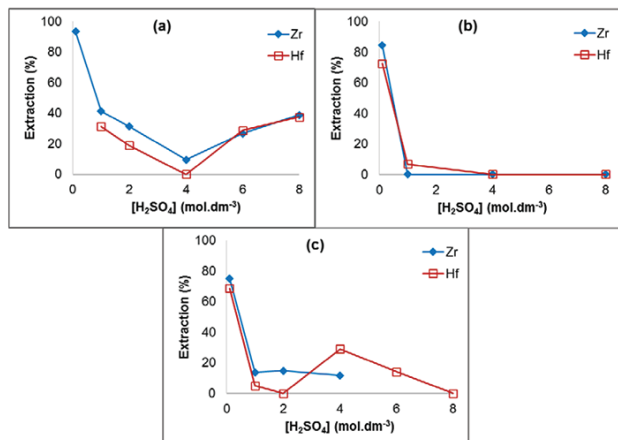


Figure 2—Effect of sulphuric acid concentration with single salt extraction using (a) Alamine 336, (b) Aliquat 336, (c) Uniquat 2280. Conditions: 10 wt% extractants, 100 ppm Zr, 100 ppm Hf, A/O = 1, contact time 60 minutes

values (>85%) were attained at 0.1 mol/dm³, with a slightly higher extraction from a HCl environment. The only noteworthy selectivity at high enough extraction values was obtained using Aliquat 336 (Figure 1b), where a 27% Hf selectivity was observed at 0.1 mol/dm³. The percentage selectivity was calculated by subtracting the lesser extracted metal from the greater extracted metal.

Influence of acid concentration on mixed salt extractions
Using the same parameters that had been used for single salts, mixed salt (97 wt% Zr and 3 wt% Hf) experiments were performed to correlate single- and mixed salt extractions, thereby determining whether the metals affected each other; for example, due to mutual inhabitation during extraction. Mixed salt extractions with the three amine-based extractants and the two acids were evaluated. HCl and H₂SO₄ solutions with a concentration range of 0.01–8 mol/dm³ were used.

Similar to the discussion in the previous section, Figure 3 and Figure 4 illustrate the data on the mixed metals extractions of Zr and Hf from an HCl and H₂SO₄ solution, respectively. When attempting extraction from HCl, no extraction was attained when using Alamine 336 between 0.1–4 mol/dm³ HCl (Figure 3a), increasing to just over 20% extraction at 6 mol/dm³ HCl. With Aliquat 336, 48% extraction was obtained at 0.1 mol/dm³ HCl with a 4% Hf selectivity (Figure 3b). Although Uniquat 2280 (Figure 3c) showed some extraction in the range of 1–8 mol/dm³ HCl, the extraction remained less than 20%. It is known that amine-based extractants can form emulsions when extracting from an HCl environment (Barnabas and Treadway, 2010); this was also observed in the present study when using Alamine 336 combined with H₂SO₄ at 0.1 mol/dm³ and Uniquat 2280 at 6–8 mol/dm³. Emulsions were observed in HCl solutions of 8 mol/dm³ for Alamine 336 and 0.1 mol/dm³ solution for Uniquat 2280.

Due to the high extraction with Alamine 336, seven extractions were completed with less than 1 mol/dm³ H₂SO₄ (0, 0.01, 0.1, 0.2, 0.4, 0.6, 0.8 mol/dm³) to obtain more comprehensive data. When considering the extraction of the mixed salts from a H₂SO₄ solution (Figure 4), significant extraction for Alamine 336 and Aliquat 336 was observed when extracting from a low acid concentration, while no significant extraction was observed when using Uniquat 2280. Extraction with both Alamine 336 and Aliquat 336 increased at high (>6 mol/dm³) and low (<2 mol/dm³) H₂SO₄ concentrations. For both Alamine 336 and Aliquat 336 the extractions decreased from above 80% to 20–30% between 0.1 and 2 mol/dm³, remained practically constant between 2 and 4 mol/dm³ and then gradually increased again from 4–8 mol/dm³ H₂SO₄. The highest extractions with Alamine 336 and Aliquat 336 were 91% and 78% respectively at

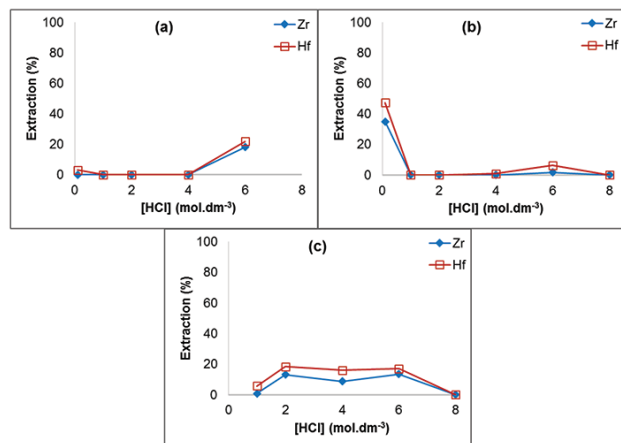


Figure 3—Effect of hydrochloric acid concentration with mixed salts using (a) Alamine 336, (b) Aliquat 336, (c) Uniquat 2280. Conditions: 10 wt% extractants, 97 ppm Zr and 3 ppm Hf, A/O = 1, contact time 60 minutes

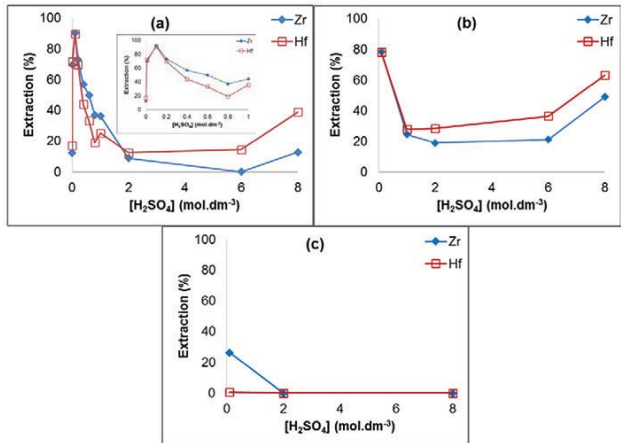


Figure 4—Effect of sulphuric acid concentration with mixed salts using (a) Alamine 336, (b) Aliquat 336, (c) Uniquat 2280. Conditions: 10 wt% extractants, 97 ppm Zr and 3 ppm Hf, A/O = 1, contact time = 60 minutes

The separation of zirconium and hafnium from $(\text{NH}_4)_3\text{Zr}(\text{Hf})\text{F}_7$

0.1 mol/dm³ H₂SO₄. This trend has been observed in previous studies – when increasing HCl above 6 mol/dm³ a similar increase in extraction took place. (Banda *et al.*, 2012; Poriel *et al.*, 2006)

When comparing the single (Figure 1 and Figure 2) and mixed salt (Figure 3 and Figure 4) extractions, both correlations and differences become apparent. In HCl (Figure 1 and Figure 3), the same negligible extraction was observed above 1 mol/dm³ HCl. However, at 0.1 mol/dm³ the extraction with Aliquat 336 was >80% for single salts, which is significantly higher than the 50% attained for mixed salts. No significant extraction was attained when using either Alamine 336 (where emulsion formation was observed above 6 mol/dm³) or Uniquat 2280 when extracting mixed salts compared to the >90% extraction achieved when using single salts. The differences in extractions for the various extractants could be related to the fact that tertiary amines (Alamine 336) have a neutral charge, whereas quaternary amines have a positive charge. The zirconium salt used for extraction ($(\text{NH}_4)_3\text{Zr}(\text{Hf})\text{F}_7$) probably has a negative charge in solution ($\text{Zr}(\text{Hf})\text{F}_7^{3-}$, or possibly $\text{Zr}(\text{Hf})\text{F}_6^{2-}$). In spite of some protonation of the tertiary amine in the acid environment, it can be assumed that this will still be less charged than the quaternary amine where all extractants remain positively charged irrespective of the acid concentration. Assuming the negatively charged Zr salt ($\text{ZrF}_6^{2-}/\text{ZrF}_7^{3-}$ anion) in solution, a higher extraction can be expected with the quaternary amine due to its positive charge. This expectation is corroborated in Figure 4 when comparing (a) (tertiary amines) and (b) (quaternary amine). While higher extraction for quaternary amine (Aliquat 336) occurred only above 2 mol/dm³ H₂SO₄, higher extraction was observed with lower acid concentrations (>1 mol/dm³) for Alamine 336. This is preferential in view of the lower amount of acid used, which has both economic as well as environmental advantages

While most data correlates between the single and mixed salts, it is clear that the two salts influence each other's extractions, specifically at low HCl concentrations (<1 mol/dm³). While the competitive behaviour is influenced by the speciation, which due to its complexity falls beyond the scope of this article, the changed extraction behaviour, specifically of Hf in the mixed salt, could be related to the change in the Hf concentration from 100 ppm to 3 ppm from the single to the mixed salts. It was shown that Cl⁻ at higher concentrations in both the single and mixed salts inhibits extraction. Hence, when the Hf concentration was decreased from the single to the mixed salt experiments, the Cl⁻ to Hf ratio increased, implying that at 3 ppm Hf the Cl⁻, even at low HCl concentrations, was sufficiently in excess to inhibit the extraction of Hf. It remains, however, unclear why this would also result in such a significant decrease in the Zr extraction.

In H₂SO₄ (Figure 2 and Figure 4) mostly similar tendencies for single and mixed salts were observed irrespective of the acid concentration (0.1–8 mol/dm³), which again confirms the role of the Cl⁻ ion during extraction from an HCl environment. Some differences were observed; for example, the Alamine 336 formed no emulsions during the

extractions with mixed salts while emulsions did occur when using single salts. A reason for this is not apparent. In addition, Aliquat 336 yielded 20% higher extraction from 1 mol/dm³ H₂SO₄, which increased gradually with the increase in acid concentration with mixed salts. Uniquat 2280, on the other hand, formed emulsions at 4 and 6 mol/dm³ (Figure 4c). Comparing the data with Figure 2b, where emulsions were formed only in the presence of Zr, it seems that the Zr is responsible for these emulsions (Nielsen *et al.*, 2000).

Influence of extractant to metal_{Zr+Hf} ratio on mixed salts extraction

According to the previous section, the best results for mixed salts were attained when extracting from a low H₂SO₄ concentration using Alamine 336 as extractant (Figure 4). Accordingly, the influence of the extractant to metal (E/M) ratio was determined by changing the Alamine 336 concentration between 0.01–10 wt% at 0.01, 0.1 and 0.5 mol/dm³ H₂SO₄.

Figure 5 illustrates the extraction behaviour of Zr and Hf with increasing Alamine 336 concentration at three different H₂SO₄ concentrations. Apart from yielding the best results in the previous section, low concentrations of acids are also more cost-effective and leave a smaller chemical footprint. It is interesting to note that the extraction curve with 0.01 and 0.5 mol/dm³ H₂SO₄ has a near S-shape, while extraction at 0.1 mol/dm³ first increases logarithmically ($R^2 = 0.9082$) before levelling off. This might be related to the change in extraction between 0 and 1 mol/dm³ H₂SO₄ (shown in the insert in Figure 4a) where the 0.01 mol/dm³ data point was to the left of the inclining slope while the 0.5 mol/dm³ data point was to the right of the descending slope with 0.1 mol/dm³ on the peak of the graph. This, however, only confirms that there is a change in the speciation in the vicinity of 0.1 mol/dm³ H₂SO₄, but not what this change might be. Irrespective of the variation in the shape of

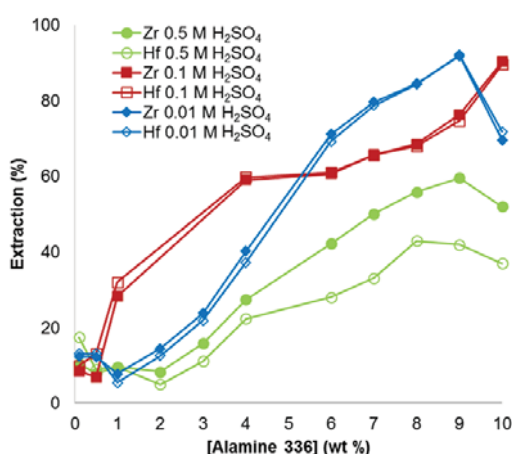


Figure 5—Effect of extractant concentration changes with mixed salts in sulphuric acid using Alamine 336. Conditions: 0.001–10 wt% extractant, [acid]: 0.01, 0.1 and 0.5 mol/dm³, 97 ppm Zr and 3 ppm Hf, A/O = 1, contact time 60 minutes

The separation of zirconium and hafnium from $(\text{NH}_4)_3\text{Zr}(\text{Hf})\text{F}_7$

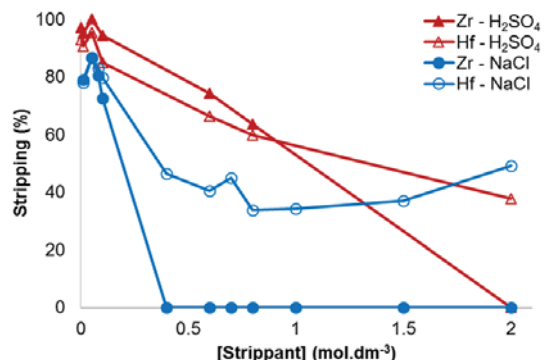


Figure 6—Effect of sodium chloride and sulphuric acid as strippers on loaded Alamine 336. Extraction conditions: 9 wt% Alamine 336, 0.5 mol/dm³ sulphuric acid, 97 ppm Zr and 3 ppm Hf, O/A = 1, contact time 60 minutes. Stripping conditions: 9 wt% Alamine loaded, [strippant] = 0–2 mol/dm³, O/A = 1, contact time 60 minutes

the curves, however, extraction increased in all cases with increasing Alamine 336 concentration from 2 to 9 wt%.

An extraction of 92% was attained at 9 wt% Alamine 336 when extracting from 0.01 mol/dm³ H₂SO₄ and 87% at 10 wt% Alamine 336 when extracting from 0.1 mol/dm³ H₂SO₄. Extraction from 0.5 mol/dm³ H₂SO₄, while also increasing with increasing extractant concentration, had the smallest gradient, resulting in the lowest extraction reaching a maximum of 60% Zr and 41% Hf at 9 wt% Alamine 336. In spite of the lower extraction, the experiment at 0.5 mol/dm³ was the only one that displayed any selectivity between the two metals, in this case favouring the extraction of Zr with a 19% selectivity at 9 wt% Alamine 336.

Stripping

In the work described in the previous sections the extractions were optimized. In order to be able to reuse the extractants for subsequent extraction in a solvent extraction process, the

stripping of the metal complexes (Zr and Hf) from the loaded Alamine 336 has to be investigated. While stripping has been demonstrated in the literature with various stripping liquors (Gefvert, 1994), in this study the best results were attained when using NaCl and H₂SO₄ (Banda *et al.*, 2012).

Figure 6 indicates the stripping of a loaded organic phase attained by a 60-minute extraction from a 0.5 mol/dm³ H₂SO₄ solution using 9 wt% Alamine 336. The stripping liquor concentrations were varied from 0–2 mol/dm³ for H₂SO₄ and NaCl. According to Figure 6, both stripping liquors achieved stripping of the Zr and Hf, with decreasing stripping with increasing strippant concentration. However, when using H₂SO₄ as stripping liquor, a 48% Hf selectivity was achieved at 2 mol/dm³. NaCl yielded favourable stripping results at 2 mol/dm³ NaCl with a 46% Hf stripping and 0% Zr stripping. Although 2 mol/dm³ NaCl was not able to strip all the Hf, it did result in a selective removal of Zr leaving pure Hf in the organic phase, which can be stripped in a second stripping step, for example using H₂SO₄.

Proposed extraction, scrubbing and stripping scheme

Using the extraction and stripping data obtained in this study a possible scheme with various stages of extraction and stripping can be proposed (Figure 7), which ultimately could lead to a process for the manufacturing of nuclear-grade Zr, if designed correctly. In the extraction step, the aqueous feed (0.5 mol/dm³ H₂SO₄) and the aqueous scrubbing liquor (2.0 mol/dm³ NaCl) are contacted with the organic solution (Alamine 336, 9 wt%) and the loaded organic solution. During this extraction an excess of Zr is extracted into the organic phase. During the scrubbing of the loaded organic phase most of the remaining extracted Hf is scrubbed to the aqueous phase. Thereafter the Zr is stripped from the organic phase using 0.05 mol/dm³ H₂SO₄. Subsequently, the solvent is regenerated, water being used to remove any residual Zr or Hf from the organic phase. Finally, the depleted solvent is recirculated to the solvent make-up where any lost extractant is replenished, completing the process.

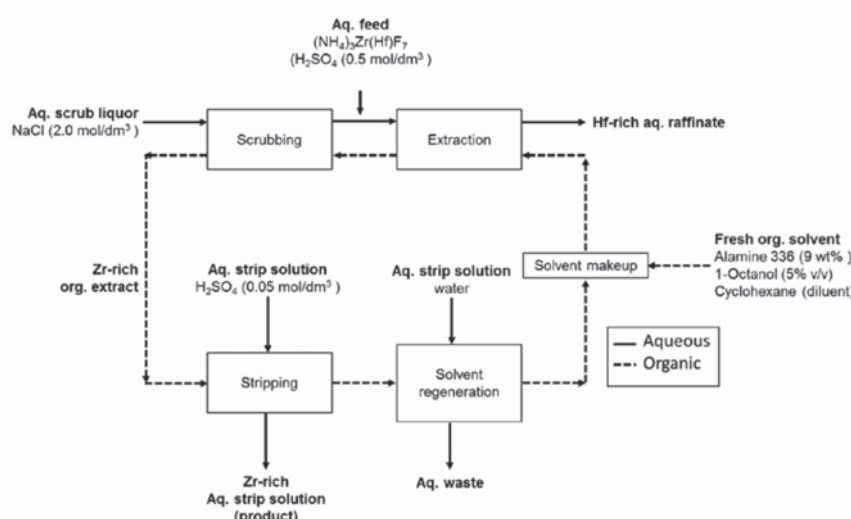


Figure 7—Proposed extraction, scrubbing and stripping scheme for Zr purification

The separation of zirconium and hafnium from $(\text{NH}_4)_3\text{Zr}(\text{Hf})\text{F}_7$

Conclusion

A solvent extraction study was done to determine the extraction and separation of Zr and Hf as $(\text{NH}_4)_3\text{Zr}(\text{Hf})\text{F}_7$ from a HCl and H_2SO_4 environment (0.01–8 mol/dm³) using three amine-based extractants (Alamine 336, Aliquat 336 and Uniquat 2280). While similar extractions were attained for single and mixed salts, both the Zr and Hf extractions were significantly lower when using mixed salts at low HCl concentrations. Of the three amines tested, Alamine 336 exhibited the best extraction and selectivity for the separation of Zr from Hf at both low (86%) and high (39%) H_2SO_4 concentrations. Varying the E/M ratio of Alamine 336 at three low H_2SO_4 concentrations (0.01, 0.1 and 0.5 mol/dm³) led to a 19% selective extraction of Zr over Hf with 9 wt% Alamine 336 in 0.5 mol/dm³ H_2SO_4 . Complete stripping of Zr and Hf from loaded Alamine 336 was achieved using 2 mol/dm³ NaCl. A proposed extraction, scrubbing and stripping scheme was presented showing the possibility for the development of a process for the separation of Zr and Hf from $(\text{NH}_4)_3\text{Zr}(\text{Hf})\text{F}_7$ in a H_2SO_4 environment using amine-based extractants such as Alamine 336. With the current data it is possible to purify Zr from 97% to 98.49%. By combining further extraction, scrubbing and stripping steps, it should be possible to reduce the Hf concentration to below 100 ppm as required by the nuclear industry.

Acknowledgements

This work was initiated by the Department of Science and Technology (DST), South Africa under its Advanced Metals Initiative (AMI). The Nuclear Energy Corporation of South Africa (NECSA) (SOC) Ltd, due to existing expertise and infrastructure, was entrusted to investigate the manufacturing of the metals Zr and Hf, thereby establishing the Nuclear Materials Development Network (NMDN) Hub of the AMI. The authors express thanks to the DST for the funding of this project. We also would like to thank Dr S.J. Lötter from NECSA for manufacturing the $(\text{NH}_4)_3\text{Zr}(\text{Hf})\text{F}_7$ salt used in this study.

References

- AMARAL, J.C., ROCHA, L.R. and MORAIS, C.A.D. 2013. Study of the separation of zirconium and hafnium from nitric solutions by solvent extraction. *Proceedings of the International Nuclear Atlantic Conference - INAC, Recife, Brazil, 24–29 November*. Brazilian Nuclear Energy Association.
- BANDA, R., LEE, H.Y. and LEE, M.S. 2012. Separation of Zr from Hf in hydrochloric acid solution using amine-based extractants. *Industrial and Engineering Chemistry Research*, vol. 51. pp. 9652–9660.
- BARNABAS, F.A. and TREADWAY, J.L. 2010. Microemulsion or protomicroemulsion cleaning composition with disrupting surfactants. US patent application 20100009888A1. January 14, 2010.
- GEFVERT, D.L. 1994. Solvent extraction of precious metals with hydroxyquinoline and stripping with acidified thiourea. US patent application 975. 504 p.
- JENNY, R., BOTZ, M.M., DIMITRIADIS, D., POLGLASE, T. and PHILLIPS, W. 2001. Processes for the regeneration of cyanide from thiocyanate. *Minerals and Metallurgical Processing*, vol. 18. pp. 126–132.
- LI, H., NERSISYAN, H. H., PARK, K.-T., PARK, S.-B., KIM, J.-G., LEE, J.-M. and LEE, J.-H. 2011. Nuclear-grade zirconium prepared by combining combustion synthesis with molten-salt electrorefining technique. *Journal of Nuclear Materials*, vol. 413. pp. 107–113.
- NEL, J.T., RETIEF, W.L., HAVENGA, J.L., DU PLESSIS, W. and ROUX, J.P. 2014. Treatment of chemical feedstocks. US patent application US 20140238195A1.
- NIELSEN, R.H., SCHLEWITZ, J.H. and NIELSEN, H. 2000. Zirconium and Zirconium Compounds. *Kirk-Othmer Encyclopedia of Chemical Technology*. Wiley.
- OVERHOLSER, L.G., BARTON, C.J. and RAMSEY, J.W. 1960. Separation of hafnium from zirconium. US patent application 301, 902.
- PORIEL, L., FAVRE RÉGUILLON, A., PELLET ROSTAING, S. and LEMAIRE, M. 2006. Zirconium and hafnium separation, part 1. Liquid/liquid extraction in hydrochloric acid aqueous solution with Aliquat 336. *Separation Science and Technology*, vol. 41. pp. 1927–1940.
- PUROHIT, R. and DEVI, S. 1997. Determination of nanogram levels of zirconium by chelating ion exchange and on-line preconcentration in flow injection UV-visible spectrophotometry. *Talanta*, vol. 44. pp. 319–326.
- SENOL, A. 2001. Extraction equilibria of nicotinic acid using Alamine 336 and conventional solvents: effect of diluent. *Chemical Engineering Journal*, vol. 83. pp. 155–163.
- TAGHIZADEH, M., GHANADI, M. and ZOLFONOUN, E. 2011. Separation of zirconium and hafnium by solvent extraction using mixture of TBP and Cyanex 923. *Journal of Nuclear Materials*, vol. 412. pp. 334–337.
- TAN, B., LUO, G. and WANG, J. 2007. Extractive separation of amino acid enantiomers with co-extractants of tartaric acid derivative and Aliquat-336. *Separation and Purification Technology*, vol. 53. pp. 330–336.
- WANG, L.Y. and LEE, M. S. 2015. Separation of Zr and Hf from sulfuric acid solutions with amine-based extractants by solvent extraction. *Separation and Purification Technology*, vol. 142. pp. 83–89.
- XU, L., XIAO, Y., VAN SANDWIJK, A., XU, Q. and YANG, Y. 2015. Production of nuclear grade zirconium: a review. *Journal of Nuclear Materials*, vol. 466. pp. 21–28.
- YANG, X.J., FANE, A.G. and PIN, C. 2002. Separation of zirconium and hafnium using hollow fibers: Part I. Supported liquid membranes. *Chemical Engineering Journal*, vol. 88. pp. 37–44. ◆



Corrosion characteristics of mild steel storage tanks in fluorine-containing acid

by R. van der Merwe*†, L.A. Cornish* and J.W. van der Merwe*

Synopsis

The hydrofluoric acid (HF) industry in South Africa uses normalized mild steel (SA 516 Gr 70) for the storage and distribution of its technical-grade product (70% HF). The technical-grade acid is split from the anhydrous hydrogen fluoride (AHF) product during distillation just after HF is produced, in a stainless-steel-lined kiln, from the reaction of calcium fluoride (CaF_2) with sulphuric acid (H_2SO_4). Uniform corrosion of the storage tanks is mitigated during commissioning by contacting the steel with 70% HF. A corrosive reaction takes place ($2\text{H}^+ + 2\text{F}^- + \text{Fe} \rightarrow \text{H}_2 + \text{FeF}_2$) to form scale inside the tank which diminishes the attack of the steel by fresh HF, thus prolonging the service life expectancy of the vessels. This iron fluoride scale in the vessel grows continually, resulting in corrosion of the vessels continuing at a predictable rate (approx. 0.5 mm/a) since the first commissioning of the tanks at Necsa in 1993.

In early 2012, an increase in the average corrosion rate of the tanks to 3 mm/a measured at and below the liquid band in the storage vessels was noted. Three months later the corrosion rate had increased to 30 mm/a, just before the first leak from the tank was detected. The tanks were decommissioned shortly afterwards and an investigation revealed that the rapid corrosion was due to the presence of increased levels (>50 ppm) of nitric acid (HNO_3) in the tanks, which attacked the fluoride layer protecting the steel.

The oxidation characteristics of high concentrations of HNO_3 with low concentrations of HF on stainless steel surface treatment are well documented. The effects of low levels of nitric acid on the corrosion of steels in sulphuric acid are also known, but no suitable published data currently exists on corrosion by high HF concentrations with low HNO_3 concentrations. Establishing the rate and mechanism of corrosion by HNO_3 (0.1 to 1%) in 70% HF is currently a high priority for the HF industry in South Africa and will become increasingly important in the near future due to depleting fluorite reserves and cheaper, but less efficient, processes producing H_2SO_4 with higher impurity levels, which were not anticipated in the original plant design. The aim of this study is to simulate the corrosion conditions in the plant on a laboratory scale in order to establish the corrosion characteristics of the steels used in the HF plant, which are increasingly exposed to the HNO_3 impurities that tend to concentrate in the final technical-grade HF acid product.

Keywords

hydrofluoric acid, mild steel, corrosion, nitric acid contamination.

Introduction

Mild steel is a relatively inexpensive material that is often effectively used for the storage and distribution of technical-grade hydrofluoric acid (70% HF). Uniform corrosion of HF storage tanks is inevitable and typically reaches 0.5 mm/a (Valkenburg, 2012). The thickness of the steel is regularly monitored ultrasonically and documented during

inspections so that the service life can be safely anticipated. However, despite the regular inspections and current contingencies in the HF plant at Necsa, an isolated case of HF leakage from two mild steel vessels during operation occurred without warning (Valkenburg, 2012). The failure of both these vessels necessitated their premature decommissioning and uncovered a real need to understand the corrosion characteristics of mild steel used in the HF industry and recommend corrosion design improvements.

The reason for the failure of the mild steel was traced to an excess of nitric acid (HNO_3) in the feedstock to the plant, which eventually concentrated in the technical-grade HF product downstream. The combined corrosion effect of HF and HNO_3 in the storage tanks led to their premature failure.

A study to simulate the corrosion conditions in the laboratory was required to better estimate the service life of the steels used in the HF plant. Understanding the effect of HNO_3 contamination on the plant's steels and the determination of corrosion inhibition strategies was essential. Laboratory immersion experiments were required to establish the corrosion characteristics of the mild steel used in a HF plant, which could be exposed to >50 ppm HNO_3 impurities. Neither published, nor quantitative, corrosion data on the corrosiveness of HF in the presence of an oxidizing agent were available at the time of the failure of the two technical-grade HF

* School of Chemical and Metallurgical Engineering, University of Witwatersrand, Johannesburg and DST-NRF Centre of Excellence in Strong Materials, hosted by the University of the Witwatersrand.

† Applied Chemistry Department, South African Nuclear Energy Corporation SOC Limited (Necsa).

© The Southern African Institute of Mining and Metallurgy, 2016. ISSN 2225-6253. This paper was first presented at the AMI Ferrous and Base Metals Development Network Conference 2016 19–21 October 2016, Southern Sun Elangeni Maharani, KwaZulu-Natal, South Africa.

Corrosion characteristics of mild steel storage tanks in fluorine-containing acid

storage tanks at Necsa (Valkenburg, 2012). In the absence of data, to understand the effects of the different concentrations and combinations of HF and HNO₃, the only option was to reproduce the unique corrosive environment in a laboratory. The initial step was to develop a safe method for conducting immersion corrosion tests using chemically pure HF. The results from these experiments would then be used as a reference to compare the findings from future corrosion tests where HNO₃ contamination was introduced. Moreover, these laboratory tests would serve to establish whether the approach used was suitable for predicting the corrosion rates of the steel tanks and components in the plant in its present condition.

To determine the necessary duration of typical HF corrosion tests, planned interval corrosion tests (PICTs), as prescribed by Wachter and Treseder in ASTM Standard G31-72 (2004), needed to be conducted safely. This work has been reported elsewhere (van der Merwe, Cornish and van der Merwe, 2016). Since safety implications when working with fuming HF (>60% HF) were a concern, initially the PICTs were used to establish the lowest HF concentration at which laboratory-scale tests could be conducted, while producing corrosion data that could be related to the corrosive conditions experienced in industry. Next, corrosion tests using the most suitable conditions could continue in which the effect of HNO₃ concentration would be the focus. However, the effect of HF concentration on mild steel corrosion was also accessible from the PICT results, which showed that varying corrosion forms and mechanisms occur at different HF concentrations. These results differed somewhat from published data (Craig and Anderson, 1994; Hansen and Puyear, 1996; Honeywell, 2002) and were therefore examined further in this study.

Materials and methods

Materials

The material was a mild steel (SA 516 Gr 70), used as construction material for 70% HF storage tanks. The steel was initially hot-rolled to a thickness of 3 mm, then cut with a waterjet to produce coupons sized 25 × 25 × 3 mm. A 7 mm hole was cut in the middle of each coupon, which effectively produced a surface area of 15.39 cm². Therefore, a total of four coupons would be allowed to hang from the corrosion

rack during a 500 mL experiment, effectively exceeding the minimum ASTM target requirement of 30 mL/cm² per immersion experiment (Baboian, 2005). Coupons were sandblasted and washed with acetone to remove mill scale prior to each experiment. All coupons were pre-passivated in HF for 24 hours at 25°C prior to each PICT. Pre-passivation was done to produce the protective scale layer essential for the use of mild steel in the HF industry (Jennings, 2007).

The HF used for the PICTs was aqueous hydrogen fluoride (70% industrial grade) collected from the Pelchem SOC Ltd fluorochemical plant, situated on the site at Necsa. The 70% HF was a high-quality product (fluorosilicic acid ≤100 ppm, sulphuric acid ≤200 ppm and nitric acid <5 ppm) received in sealed 25 L bottles, which were intended for export by Protea Chemicals (Inland). The lower concentration HF solutions (40% and 48%) were analytical grade ([NO₃⁻] <5 ppm) solutions purchased from Merck (Pty) Ltd. Corrosion solutions were analysed at Pelindaba Analytical Laboratories (PAL) using volumetric titrations and inductively coupled plasma optical emission spectrometry (ICP-OES) to determine HF and metal concentrations in corrosion solution products.

Methods

Each experiment was conducted in a 500 mL Teflon bottle which was placed in a water bath to maintain the acid at a constant temperature while corrosion of the coupons took place (Figure 1a). The coupons were assembled into a cylindrical rack (made of Teflon) which was placed upright in the bottle (Figure 1b). The HF was then poured into the bottle until the cylindrical rack holding the coupons (Figure 1c) had been completely covered. The bottle lid, with the 2 mm diameter drilled hole, was then screwed on. This allowed for the release of HF fumes in order to avoid pressure build-up in the Teflon container. The temperature was maintained at 25°C using an immersion cooler attached to the polypropylene lid, custom-made to cover the bath and which allowed the immersion cooler to hang freely in the water while being shielded from HF fumes by a polypropylene cylinder attached to the lid (Figure 1a). The lid over the water bath had a release valve in the open position, which channelled any HF fumes from the corrosion reaction to the extraction line of the fume cupboard, which led out to the KOH scrubber.



Figure 1—Experimental set-up: (a) water bath with immersion cooler, (b) corrosion reactor components: Teflon bottle, cylindrical corrosion rack and steel coupons and (c) complete assembly for safely simulating the corrosive conditions in HF

Corrosion characteristics of mild steel storage tanks in fluorine-containing acid

PICTs were allowed to run for periods of time experimentally determined by the planned interval tests of Wachter and Treseder in ASTM Standard G 31-72 (ASTM, 2009). Four coupons per bottle were introduced to a maximum of 500 mL HF. Subsequently, one coupon was removed from the corrosion rack at a specified time; this continued over the entire duration of a corrosion experiment, until all coupons had been removed. This was done to establish the metal samples' susceptibility to corrosion, the liquid's corrosiveness and the rate of the corrosion reaction under the simulated conditions. Following this standard method, the fourth coupon (B) was placed into the HF corrosion solution at the same time that the second coupon (A_t) was removed and allowed to corrode with the third coupon (A_{t+1}) for the remaining four days. In this way, comparing the corrosion rate measured for coupons 3 and 4, a change in the liquid corrosiveness could be compared to the criteria set out in the ASTM practice. In the same way, the susceptibility of the mild steel to the HF corrosion solution was determined by comparing the corrosion rate determined for coupon B to that of coupon A_2 (Tables I–III). The mass loss for coupon A_2 was determined by subtracting the mass losses of coupons A_t and A_{t-1} and the corrosion rate determined using the average density of the coupons in that batch (e.g. coupon 1–4 in Table I).

Each time a coupon was removed from the bottle, it was rinsed with water and air-dried before storage in a desiccator. After testing, the corrosion products were removed from the coupons by ultrasonic cleaning for 30 minutes, followed by mechanical cleaning with a steel brush to ensure complete removal of the scale from the coupon prior to weighing. To calculate the corrosion rate (CR) in mm/a from metal loss the following equation was used:

$$CR = 87.6 \times (W/\rho A t) \quad [1]$$

where W = weight loss (in mg), ρ = density (in g/cm³), A = area (in cm²) of the coupons exposed to HF over time (in hours) based on ASTM Standard G31-72 (2004). The convention is to measure corrosion rate in mils penetration per year (MPY) (Jones, 1996). However, the constant (in this case $K = 87.6$) is dimensionless and changes with the conversion to the desired unit (in this case mm/a) (Davis and ASM International, 2000).

In the PICTs, identical coupons were placed in the same HF solution in the 500 mL Teflon bottle. The temperature was kept constant at 25°C for the entire time ($t + 1$). The symbols A_1 , A_t , A_{t+1} and B were used to represent the corrosion damage experienced in each test (ASTM, 2009). Subsequently, A_2 was calculated by subtracting A_t from A_{t+1} .

Results

The data collected from the tests at different HF concentrations is shown in Tables I–IV and Figures 2–3.

When HF contacts mild steel, a corrosive reaction takes place:



whereby scale forms on the surface of the steel and inhibits further attack of the steel (Hansen and Puyear, 1996). Since this pre-passivation technique is applied in industry by allowing the storage tanks to be corroded by HF and HF fumes for 24 hours before commissioning (Jennings, 2007), the coupons in the PICT experiments were pre-passivated to represent the starting condition of the steel used in calculating the mass loss in each case. Equation [1] was used to calculate apparent density and the nominal density of 7.85 g/cm³ for mild steel was used throughout the study.

Table I

Planned interval corrosion test for mild steel in 40% HF

Coupon (no.)	Interval (days)	Mass loss (g)	Apparent corrosion rate (mm/a)
1) A_1	0–1	5.03	152.2
2) A_t	0–4	5.63	42.6
3) A_{t+1}	0–8	6.04	22.8
4) B	4–8	0.524	4.0
Calc. A_2	4–8	0.407	3.1
3.1 mm/a < 4.0 mm/a < 152.2 mm/a		Liquid corrosiveness:	Decreased
Therefore: $A_2 < B < A_1$		Susceptibility to corrosion:	Decreased

Table II

Planned interval corrosion test for mild steel in 48% HF

Coupon (no.)	Interval (days)	Mass loss (g)	Apparent corrosion rate (mm/a)
1) A_1	0–1	6.06	183.1
2) A_t	0–4	5.54	41.8
3) A_{t+1}	0–8	6.12	23.1
4) B	4–8	1.01	7.6
Calc. A_2	4–8	0.58	4.4
4.4 mm/a < 7.6 mm/a < 183.1 mm/a		Liquid corrosiveness:	Decreased
Therefore: $A_2 < B < A_1$		Susceptibility to corrosion:	Decreased

Corrosion characteristics of mild steel storage tanks in fluorine-containing acid

Table III

Planned interval corrosion test for mild steel in 70% HF

Coupon (no.)	Interval (days)	Mass loss (g)	Apparent corrosion rate (mm/a)
1) A ₁	0–1	0.07	2.1
2) A _t	0–4	0.20	1.5
3) A _{t+1}	0–8	0.32	1.2
4) B	4–8	0.20	1.5
Calc. A ₂	4–8	0.12	0.9
0.9 mm/a < 1.5 mm/a < 2.1 mm/a		Liquid corrosiveness:	Decreased
Therefore: A ₂ < B < A ₁		Susceptibility to corrosion:	Decreased

Table IV

Observation of corrosion products after 8 days

	40% HF	48% HF	70% HF
Visual appearance of coupons after cleaning	Pitting corrosion visible. Excessive corrosion after 8 days. (Figure 7, coupon 3)	Severe attack of entire sample surface over entire period of test. (Figure 8, coupons 1–3)	No visible corrosion. Clean surface. (Figure 9, coupons 1–4)
Colour of corrosion solution	Dark brown	Dark brown	Colourless
Appearance of precipitate	Light brown (FeF ₂)	Light brown (FeF ₂)	None
Composition of final corrosion solution	38.1% HF 1.98% Fe	46.7% HF 0.71% Fe	68.6% HF 0.0164% Fe

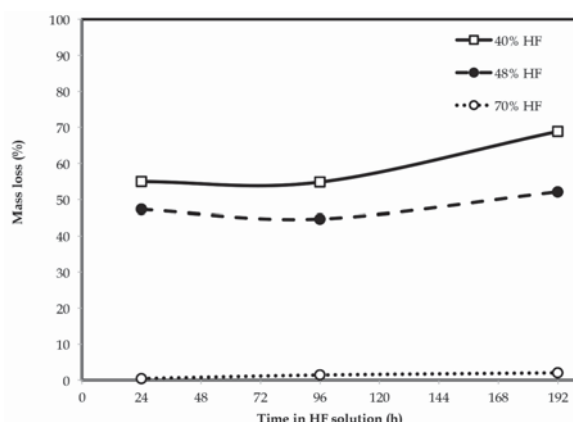


Figure 2—Mass loss of mild steel at different HF concentrations for different time intervals at 25°C

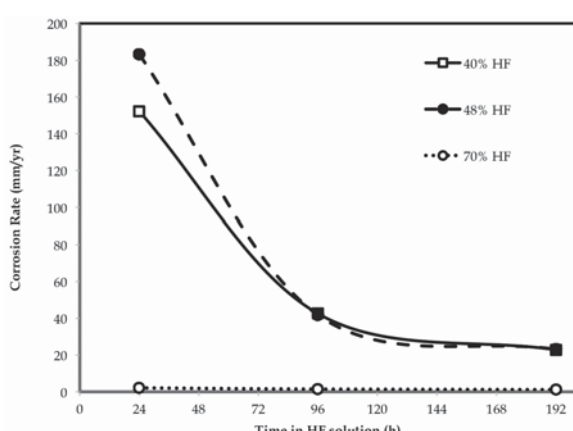


Figure 3—Corrosion rates of mild steel at different HF concentrations for different time intervals at 25°C

Honeywell Fluorine Products (Honeywell International Inc., 2014) is an HF supplier that documented the properties of HF to make technical and safety-related literature openly available in order to ensure safe usage of their products. From this literature, corrosion rates for carbon steel against HF concentration were provided and reported in MILS per year (1 MIL = 0.0254 mm). The values for average corrosion of mild steel were converted so that apparent corrosion rates from PICT tests measured after 192 hours could be compared (Figure 4).

Discussion

Planned interval corrosion tests

From the corrosion tests conducted with both 40% and 48% HF, the criteria set in ASTM Standard practice G 31-72 indicated that the corrosion rate for the calculated A₂ value

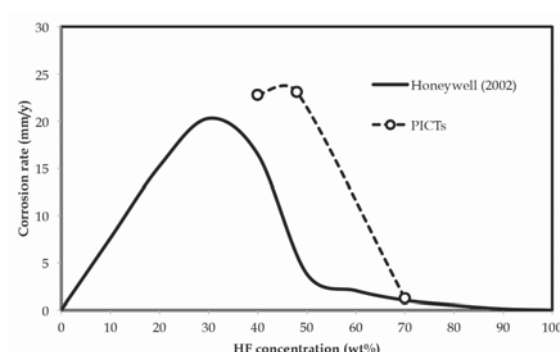


Figure 4—Corrosion rates of mild steel at 25°C after 198 hours from PICTs superimposed onto average corrosion rates of carbon steel vs. HF concentration (adapted from Honeywell, 2002)

Corrosion characteristics of mild steel storage tanks in fluorine-containing acid

was smaller than the rate measured for B, and therefore the metal's susceptibility to corrosion decreased during the test. Moreover, coupon B had a smaller corrosion rate than A₁, and therefore the liquid corrosiveness also decreased. This combined situation (A₂ < B < A₁) indicated that the 40% and 48% HF significantly decreased in corrosiveness during the test and the formation of a partially protective scale on the steel was likely (Tables I and II).

The 70% HF PICT fell under the same criteria as the 40% and 48% HF tests. However, the corrosion rates determined for A₂, B, and A1 were significantly smaller (Table II). The A₂ and B values determined for the more corrosive 48% HF (Table II) were nearly five times larger than the 0.9 and 1.5 mm/a corrosion rates determined for 70% HF under the same conditions. Therefore, the corrodibility of the metal was much lower in 70% HF than in 48% and 40% HF. Similarly, the initial corrosion rate determined for 48% HF was in excess of 180 mm/a and approximately 86 times faster than the A₁ value for the 70% HF test. Therefore, the liquid corrosiveness of 70% HF was much less than was measured for the 48% and 40% HF PICTs. Irrespective of the safety risk aspects associated with 70% HF (van der Merwe, Cornish and van der Merwe., 2016), corrosion experiments with 70% HF produced slower, more steady corrosion rates and left an adequate portion of a coupon behind (<50% mass loss) for mass loss measurements after 8 days (Figure 2) to be best relatable to what was experienced in industry.

Effect of HF concentration

The lower the concentration of HF, the faster mild steel corrodes (Honeywell, 2002). This was shown in Figure 3. Notwithstanding that 48% HF was slightly more corrosive than 40% HF, the initial corrosion rate (over the first 24 hours) was much higher than for the 70% HF (2.1 mm/a). Thus, high corrosion rates (152–183 mm/a) were measured for HF below 50% concentration, despite the formation of the protective fluoride (FeF₂) scale layer during the pre-passivation step. FeF₂ is soluble in water (Perry, 2011) and since there was a higher water balance in the low-concentration acids, the scale readily dissolved and the mild steel substrate was attacked by fresh HF. However, with increased time, the scale did stabilize and the corrosion rate decreased to below 25 mm/a. The 70% HF was more conducive to scale formation on the mild steel and corrosion rates did not exceed 2 mm/a over the entire 8-day test (Figure 3).

The effect of HF concentration on the corrosion rate of mild steel after 192 hours (Coupon B, Tables I–III) was related to average corrosion rates reported in the Honeywell (2002) special chemical edition, where hydrofluoric acid properties were summarized (Figure 4). On average, lower HF concentrations (between 5 and 50% HF) resulted in significantly higher corrosion rates (>20 mm/a), while higher HF concentrations (>50% HF) corroded mild steel significantly slower (<2 mm/a). PICTs conducted over the HF range of 40% to 70% showed a similar trend to Honeywell (2002) (Figure 4), although the peak appeared to shift to the right, with 40% to 48% HF producing the highest corrosion rates. However, corrosion experiments at HF concentrations below 40% were not conducted, therefore this peak shift could not be substantiated. Moreover, the corrosion rates measured differed significantly as the exact corrosive conditions (initial

condition of the coupons, temperature, pressure and volume of HF used) were not known and therefore could not entirely be reproduced.

Observations

The corrosion solutions and coupons were observed over 8 days. Of the corrosion products (scale layer on coupons, corrosion solution and precipitates collected at the bottom of the bottle), only the corrosion solution was analysed. The coupons showed a heavily oxidized surface after pre-passivation (Figure 6). Iron fluoride (FeF₂) has a grey colour, while the ferric hydroxide (FeF₃.3H₂O) has a recognizable yellow-brown colour (Haynes, 2016). The black colour is characteristic of oxidation (iron II/III oxide) of the steel (Haynes, 2016), as the corrosion reaction was allowed to take place in a well ventilated bottle. A combination of all these coloured substances formed the scales on the coupon surfaces and contributed to the unique colours visible when the coupons were removed and dried after pre-passivation (Figure 6).

The results in Table IV and images of the cleaned coupons after each test, differed significantly depending on the initial concentration of the HF in the corrosion solution (Figures 7–9). Pitting-type corrosion was present over the entire surface of the coupons exposed to 40% HF (Figure 7). The 48% HF resulted in a visibly more aggressive attack over the entire surface of the coupons, reminiscent of uniform corrosion. The lower iron concentration (approx. 0.7% Fe) in the 48% HF corrosion products indicated that more iron was

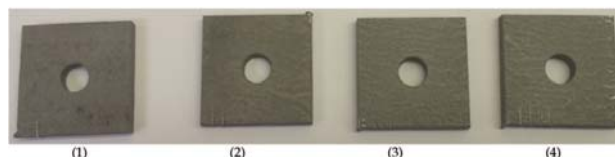


Figure 5—Mild steel coupons: (1) A₁, (2) A_t, (3) A_{t+1} and (4) B before exposure to HF corrosion solutions



Figure 6—Mild steel coupons : (1) A₁, (2) A_t, (3) A_{t+1} and (4) B after pre-passivation in HF for 24 h at 25°C

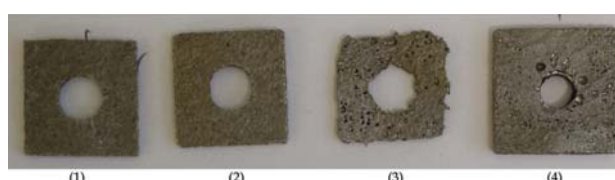


Figure 7—Mild steel coupons: (1) A₁, (2) A_t, (3) A_{t+1} and (4) B after exposure to 40% HF and removal of the scale layer

Corrosion characteristics of mild steel storage tanks in fluorine-containing acid



Figure 8—Mild steel coupons: (1) A₁, (2) A_b, (3) A_{t+1} and (4) B after exposure to 48% HF and removal of the scale layer



Figure 9—Mild steel coupons: (1) A₁, (2) A_b, (3) A_{t+1} and (4) B after exposure to 70% HF and removal of the scale layer

present in the solid scale layer and precipitate compared to the 40% test (approx. 2% Fe). Therefore, in the 48% HF test, the HF was forming more scale on the coupon surface which broke off and fell to the bottom of the reaction bottle, allowing HF to uniformly attack the freshly exposed steel surface and form scale to repeat the corrosion process (Figure 8). In contrast, the corrosion mechanism in the 40% HF was a visible pitting action (Figure 7), which penetrated through the passivation scale and aggressively kept corroding under the scale previously formed, resulting in the highest mass loss over the entire period (Figure 3).

No scales were found at the bottom of the Teflon bottles of the 70% HF tests and the colour of the corrosion solutions remaining almost unchanged from the initial HF introduced (Table IV). The iron concentration analysed in the corrosion solution was less than 0.02%, with little HF being consumed over the entire test period (<1.5% HF). Here, the scale layer formed during the pre-passivation (Figure 9) succeeded in protecting the mild steel from further corrosion and produced a surface visibly free from corrosion, once the scale had been brushed off (Figure 9).

Conclusion

Corrosion results on SA 516 Gr 70 normalized mild steel indicated that HF concentrations below 48% were capable of producing corrosion rates above 180 mm/a. Conversely, the steel coupons placed in 70% HF corroded significantly slower (<2 mm/a after 8 days) and the corrosion rates were more closely related to those experienced in industry.

Acknowledgement

The Department of Science and Technology and the National Research Foundation are thanked for financial support. The South African Nuclear Energy Corporation Ltd. is thanked for time allowed for completing this article, as well as the Nuclear Materials (NM) and the Organic Fluorine Chemistry (OFC) sections within the Applied Chemistry (AC) department, in the Research and Development Division at Necsa, for the use of their facilities.

References

- ANDERSEN, T.N., VANORDEN, N. and SCHLITT, W.J. 1980. Effects of nitrogen oxides, sulfur dioxide, and ferric ions on the corrosion of mild steel in concentrated sulfuric acid. *Metallurgical Transactions A*, vol. 11, no. 8. pp. 1421–1428.
- ASTM. 2009. G 31-72, standard practice for laboratory immersion corrosion testing of metals. *Annual Book of ASTM Standards*. ASTM International, West Conshohocken, USA.
- BABOIAN, R. 2005. Corrosion tests and standards: application and interpretation. ASTM International, West Conshohocken, USA.
- NICKEL DEVELOPMENT INSTITUTE. 1988. Cleaning and descaling stainless steels. *Designers' Handbook Series*. Toronto.
- CRAIG, B.D. and ANDERSON, D.S. 1994. *Handbook of Corrosion Data*. ASM International, Materials Park, Ohio, USA.
- DAVIS, J.R. and ASM INTERNATIONAL (eds). 2000. *Corrosion: Understanding the Basics*. ASM International, Materials Park, Ohio, USA.
- HANSEN, D.A. and PUYEAR, R.B. 1996. *Materials Selection for Hydrocarbon and Chemical Plants*. CRC Press, New York, USA.
- HAYNES, W.M. 2016. *CRC Handbook of Chemistry and Physics*, 94th edn. CRC Press.
- Honeywell. 2002. Hydrofluoric acid properties. <http://www3.imperial.ac.uk/pls/portallive/docs/1/7276108.PDF> [accessed 10 May 2016].
- HONEYWELL INTERNATIONAL INC. 2014. Honeywell hydrofluoric acid. <https://www.honeywell-hfacid.com/literature/> [accessed 3 July 2016].
- JENNINGS, H. 2007. Materials for storing and handling commercial grades of aqueous hydrofluoric acid and anhydrous hydrogen fluoride (no. 24057). *NACE International Publication 5A171* (2007 edn). Houston, TX.
- JONES, D.A. 1996. *Principles and Prevention of Corrosion*. 2nd edn. Prentice Hall, Upper Saddle River, NJ, USA.
- PERRY, D.L. 2011. *Handbook of Inorganic Compounds*. 2nd edn. CRC Press, Sound Parkway, USA.
- VALKENBURG, E.G. 2012. HF ISO tanks corrosion evaluation. Confidential internal report: Part 1: PCM-OPSA60-REP-12007. Pelchem SOC Ltd, Pelindaba, South Africa.
- VAN DER MERWE, R., CORNISH, L.A. and VAN DER MERWE, J.W. 2016. Corrosion safety risk assessment for testing in hydrofluoric acid. *[African Corrosion Journal]*, in press. ♦



Cold-spray coating of an Fe-40 at.% Al alloy with additions of ruthenium

by R.A. Couperthwaite*, L.A. Cornish†‡ and I.A. Mwamba*

Synopsis

In previous work by the authors, it was established that additions of 0.2 at.% Ru to an Fe-40 at.% Al alloy improved the corrosion and oxidation resistance of the alloy. The alloy was produced by mechanical alloying and spark plasma sintering and the work showed that non-equilibrium processing was able to significantly refine the grain size of the material. The sintered material had a higher hardness than the as-cast material and the change in grain size did not significantly affect the oxidation and corrosion. In the present research, the mechanically alloyed powder was coated onto a mild steel substrate using cold-spray coating at a gas pressure of 10 bar and a temperature of 500°C. The coatings were found to be 5–10 µm thick, although thicknesses of up to 30 µm were observed. The coated materials were subjected to oxidation and corrosion tests to determine the effectiveness of the coating in increasing the oxidation and corrosion resistance of mild steel. This was done to determine the effectiveness of cold-spray coating as a technique to coat these mechanically alloyed powders.

Keywords

Fe-Al alloy, mechanical alloying, cold-spray coating, addition, corrosion resistance.

Introduction

Previous work conducted by Mintek (Couperthwaite *et al.*, 2013, 2015) investigated the effect of precious metal additions on the structure, oxidation and corrosion properties of an Fe-40 at.% Al (Fe-Al) alloy. Initial work determined that additions of more than 0.5 at.% precious metal did not improve the oxidation and corrosion properties of the materials and in some cases even decreased the resistance to corrosion. Further work identified Pt and Ru as beneficial additions to the FeAl alloy. Four alloys were then produced by mechanical alloying and sintering (FeAl-0.2 at.% Pd, FeAl-0.2 at.% Ru, FeAl-0.5 at.% Ag, FeAl-0.5 at.% Pt). These alloys were all successfully produced by melting and casting and mechanical alloying sintering and it was found that the non-equilibrium processing greatly decreased the grain size of the materials compared to the as-cast materials. It was found that the additions of Ru and Pt were still the most beneficial to the oxidation and corrosion properties, with Ru being considered the most beneficial.

This report details the results from the initial spray testing work done with the FeAl-0.2 at.% Ru alloy powder produced by mechanical alloying. There are several options for powder coating onto substrates; thermal-spray techniques, which include high-velocity oxy-fuel (HVOF) coating and plasma coating, or cold-spray (also known as supersonic-spray) techniques. Cold-spray techniques have attracted a lot of interest lately and as a system is available at University of the Witwatersrand, it was decided to use cold spraying in the current work. This work was done to determine the effectiveness of cold-spray coating of these mechanically alloyed powders.

Fe-Al Alloys

The iron-aluminium system has attracted a large amount of research due to the fact that Fe-Al intermetallic compounds possess good mechanical properties, along with low density and low cost, as well as easy access to the raw materials (Ji *et al.*, 2006; Montealegre *et al.*, 2000). Arzhnikov *et al.* (2008) found that the Fe-Al alloys are promising, due to their good refractoriness, oxidation and corrosion resistance and good ductility at room temperature. In comparison to conventional alloys, Fe-Al alloys perform much better at higher temperatures, due to the stability of the

* Advanced Materials Division, Mintek, Randburg, South Africa.

† School of Chemical and Metallurgical Engineering, University of the Witwatersrand, Johannesburg, South Africa.

‡ Centre of Excellence in Strong Materials, University of the Witwatersrand, Johannesburg, South Africa.

© The Southern African Institute of Mining and Metallurgy, 2016. ISSN 2225-6253. This paper was first presented at the AMI Ferrous and Base Metals Development Network Conference 2016 19–21 October 2016, Southern Sun Elangeni Maharani, KwaZulu-Natal, South Africa.

Cold-spray coating of an Fe-40 at.% Al alloy with additions of ruthenium

microstructure originating from the low diffusivity of Fe in Al (Nayak *et al.*, 2010). However, the Fe-Al alloys are difficult to fabricate in bulk, due to their poor castability and workability (Zhu *et al.*, 2009); this was confirmed by Kuc *et al.* (2009) who found that Fe-Al alloys have an activation energy for deformation of 484.9 kJ/mol compared to 392 kJ/mol for austenitic steel. The region of interest in the current study is the Fe-Al intermetallic compound at around 60 at.% Fe (Figure 1), which is a single-phase bcc region (Eelman *et al.*, 1998).

Mechanical alloying

During mechanical alloying, fine particles are cold-welded together to form larger particles. Once the particles become too large, the milling process breaks them into smaller particles. These two processes continue until the powder has a single uniform composition.

Several studies exist on the processing of Fe-Al alloys by mechanical alloying and mostly the conditions of the milling were different. Nayak *et al.* (2010) used toluene as a process control agent (PCA) and full solid solution of Fe in Al was found after 20 hours' milling at 300 r/min. It was also found that the hardness had improved, due to the nanocrystalline $\text{Fe}_4\text{Al}_{13}$ intermetallic compound formed, the absence of the soft Al phase and the large number of defects induced during mechanical alloying. Skoglund *et al.* (2004) produced an Fe-40 at.% Al alloy by milling with a stearic acid PCA for 4 hours at 360 r/min and created an alloy containing mostly FeAl with some Fe_3Al . Song *et al.* (2009) worked on a nearly equiatomic Fe-Al alloy and milled the powders for 3 to 12 hours at 304 r/min with ethanol as the PCA. After milling, the powder was annealed at 1100°C in a vacuum. Their results indicated that FeAl had not formed by the end of the 12 hours of milling, but that FeAl was formed in the powder after annealing. Abhik *et al.* (2008) found that it was possible to produce FeAl after 10 hours of milling with toluene as a PCA. Shi *et al.* (2008) investigated the stages in

which the alloy forms during the mechanical alloying process. They milled the powders for a total of 50 hours and found that initially the powder formed a solid solution of Al in Fe and as milling time increased, the phase changed to the B2 FeAl phase. After 30 hours of milling the powder consisted of only B2 FeAl.

Another critical parameter that was varied greatly in these studies was the ball to powder ratio. Ratios from as low as 4:1 (Skoglund *et al.*, 2003) to as high as 15:1 (Kezrane *et al.*, 2012), 20:1 (Cheng *et al.*, 2006), 30:1 (Ko, 2010) and 50:1 (Haghghi *et al.*, 2010) were used, although most researchers used a ball-to-powder ratio of 8:1 (Krasnowski *et al.*, 2002, 2006; D'Angelo *et al.*, 2009; Abhik *et al.*, 2008).

Research has already been done on the production of a nanocrystalline coating of the Fe-40Al alloy using spray coating (Grosdidier, 2001), which successfully created a coating with a nanocrystalline grain structure with the milling structure of the feed powders retained in the final coating. There was a problem with the presence of some oxides and depletion of the aluminium content as a result of the thermal spraying. Valdrè *et al.* (1999) and Skoglund *et al.* (2003) found that there was oxygen in the final compacts after mechanical alloying and this was attributed to oxygen present in the aluminium feed powder. Several research teams have successfully created nanocrystalline FeAl materials through mechanical alloying, with crystallite sizes of 10 nm (Valdrè *et al.*, 1999) and 23 nm (D'Angelo *et al.*, 2009; Krasnowski and Kulik, 2007a, 2007b).

Oxidation of Fe-Al alloys

During oxidation testing of Fe-Al alloys a 'wrinkling' of the oxide layer has been observed. All binary Fe-Al alloys experience this effect when subjected to oxidation at temperatures of 900–1100°C (Yang *et al.*, 2005). This wrinkling effect has been attributed to high thermal stresses during cooling of the alloy (Montealegre *et al.*, 2000) and it was

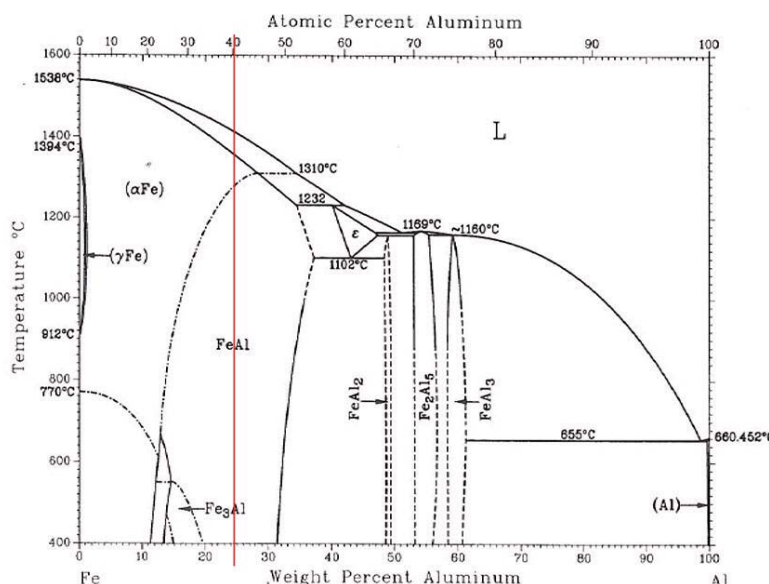


Figure 1—Fe-Al phase diagram (Massalski, 1990)

Cold-spray coating of an Fe-40 at.% Al alloy with additions of ruthenium

suggested that slow cooling retarded, or even completely prevented, the effect. Xu *et al.* (2001) found that adding Y to the Fe-Al alloys can reduce or prevent the wrinkling and spallation of the oxide layer. Xu *et al.* (2000) investigated the reasons for the weaker oxidation resistance of Fe-Al alloys in air compared to pure oxygen and found that at 1100°C in air, the Fe-Al alloys produced a mixed layer of Al₂O₃ and AlN between the outer Al₂O₃ layer and the metal.

Guo *et al.* (2011) found that an Fe-Al coating applied to a 316 stainless steel substrate formed a good bond with the substrate and imparted good oxidation resistance to the metal, due to the formation of a dense and adherent oxide film. Nowak and Kupka (2012) investigated the oxidation of an Fe-Al alloy with additions of B, Cr and Zr and found that the stable α -Al₂O₃ oxide layer started forming at around 900°C. Below this temperature, unstable γ - and θ -type oxides formed. Grabke (1999) concluded that although FeAl contains a high percentage of aluminium, it does not have as good an oxidation resistance as would be expected, due to the formation of transient oxide forms at temperatures below 1000°C.

However, Paldey *et al.* (2003) found that an FeAl coating on 440C stainless steel reduced the mass gain during oxidation tests at 800°C by four times and the same coating on a 304 stainless steel reduced the mass gain by an order of magnitude. Airiskallio *et al.* (2010) and Xu *et al.* (2000) found that additions of Cr (Airiskallio *et al.*, 2010) or a combination of Y and Zr (Xu *et al.*, 2000) to the alloy helped the oxidation resistance, although additions of only Zr decreased the oxidation resistance (Xu *et al.*, 2000).

Cold-spray coating

Cold-spray coating is a technique that was first developed in the mid-1980s. This technique utilizes temperatures significantly below the melting point of the metal being coated –

typically below 1000°C (Concustell *et al.*, 2015). In order to achieve deposition of the material it is necessary to use very high impact velocities and as a result, cold-spray systems also use very high gas pressures (Grigoriev *et al.*, 2015). Recently, there has been increased interest shown in cold-spray coatings and numerous materials have been used as coatings. Some of these materials and the conditions for the coating work are shown in Table I.

Several authors found that cold-spraying of the powders maintained the powder microstructure in the sprayed coating (Jan *et al.*, 2015; Luo and Li, 2012). It was also found that cold-spraying was able to produce coatings with less oxidation than thermal spraying processes (Concustell *et al.*, 2015; Aghasibeg *et al.*, 2016). As shown in Table I, the parameters for the spray coating vary significantly, even for the targeted Fe-Al alloys.

Experimental procedures

Mechanical alloying

The milling was done on a Retsch PM100 milling machine with a stainless steel milling pot and stainless steel balls of two sizes (Table II). The milling was done for the entire time

Table II
Mechanical alloying parameters

Parameter	Value	Parameter	Value
Ball to powder ratio	10:1	Process control agent (wt.%)	0.5
Ball mass (g)	500 g (20 mm) + 500 g (10 mm)	Speed (r/min)	300
Powder sample mass (g)	100	Milling time (h)	24

Table I

Cold-spray parameters found in the literature

Material	Pressure (bar)	Temperature (°C)	Standoff distance (mm)	Reference
Fe-Cr-Si-B-C	40	700–900	30–50	Concustell <i>et al.</i> , 2015
304L	23.1–27.9	550	22	Coddet, Verdy, Coddet, Debray, <i>et al.</i> , 2015
Ag-Cu	23–30	500	20	Coddet, Verdy, Coddet and Debray 2015
Fe-40 at.% Al	30–40	800–1000	-	Cinca <i>et al.</i> , 2015
TiO ₂	9	600	-	Buhl <i>et al.</i> , 2015
Ni	30–50	800–1000	25	Aghasibeg <i>et al.</i> , 2016
Ti-Al	15	300	-	Jan <i>et al.</i> , 2015
Ni-Al	15	300	-	Jan <i>et al.</i> , 2015
Fe-Al	15	300	-	Jan <i>et al.</i> , 2015
Cu	40–50	300–600	-	Jakupi <i>et al.</i> , 2015
TiO ₂	30–40	300–900	60	Herrmann-Geppert <i>et al.</i> , 2016
Al	25–40	300–400	10–50	Henaq <i>et al.</i> , 2016
NiCrAlNBN	22	650	20	Luo and Li, 2015
Fe-40 at.% Al	25	550	20	Luo Li, 2012
Al	30	500	-	Kim <i>et al.</i> , 2015
Ni	38–40	650–750	40–50	Koivuluoto <i>et al.</i> , 2015
NiCu	38–40	650–750	40–50	Koivuluoto <i>et al.</i> , 2015
NiCuAl ₂ O ₃	38–40	650–750	40–50	Koivuluoto <i>et al.</i> , 2015
Ti-6Al-4V	28	520	30	Li <i>et al.</i> , 2007
Ti	28	520	30	Li <i>et al.</i> , 2007
Al	28	520	30	Li <i>et al.</i> , 2007
FeAlAl ₂ O ₃	20	500	20	Wang, Li <i>et al.</i> , 2008
FeAl	20–25	350	20	Wang, Li <i>et al.</i> , 2008
FeAl	20–25	510	15	Yang <i>et al.</i> , 2011

Cold-spray coating of an Fe-40 at.% Al alloy with additions of ruthenium

period specified, with no interval. The selected PCA was stearic acid. Powder mixing, as well as the filling and sealing of the milling pots was done in a glovebox under an argon atmosphere to reduce oxygen entrapment.

Annealing

After milling of the powders, an annealing treatment was performed to ensure that the powder was of a single phase. This annealing was done in a horizontal tube furnace under an argon atmosphere to prevent oxidation of the powders. Annealing conditions are shown in Table III.

Cold-spray coating

Cold spraying was done on a Centreline SST™ Series P cold-spray system using compressed air as the carrier gas. Several runs were conducted in order to determine the optimum parameters for the coating. The conditions for the various runs are shown in Table IV. Run 6 was a repeat of run 5 in order to have a second sample prepared in the same way for use in corrosion testing. The Fe-Al alloy was coated onto a mild steel substrate.

After these trial runs were completed, two more samples were coated. These samples were coated on all sides using the conditions in run 6, in order to be used later for conducting oxidation testing on the coatings. The gun was moved over the surface of the substrate blocks to ensure an even coating of the substrate.

Oxidation

Coated samples as well as an uncoated substrate sample were weighed and then placed in a muffle furnace. The furnace was heated at 10°C per minute to a temperature of 1000°C. The temperature was then kept constant for 48 hours, after which the heating was turned off and the samples were allowed to cool in the furnace to room temperature. Samples were then removed, weighed, sectioned and mounted for analysis. The samples were wrapped with copper tape prior to preparation.

Table III

Annealing parameters

Parameter	Ramp rate (°C/min)	Holding temperature (°C)	Holding time (h)	Gas pressure (kPa)
Value	10	550	2	200

Results

Coating characterization

During the characterization of the coatings, it was found that the initial run of powder had been contaminated with nickel and as a result the coatings were a mix of FeAl, NiAl and Ni₃Al. This contaminated material will be referred to as Fe/Ni-Al. The samples were still characterized fully and the oxidation testing was done on the material as well to determine whether the addition of nickel to the mechanically alloyed material had any effect on the properties of the coating. Figure 2 shows the cross-section of the coating from Run 6 of the trial coating runs (two coating passes). The coating was quite thin, in the region of 3 µm and has a slight two-tone contrast in it showing the different phases in the coating material. The cross-section of the sample coated using five passes (run 7) is shown in Figure 3. After five passes the coating has not built up in any significant way, as the thickness was still at around 3 µm. The contrast in the coating showing the different phases was still visible.

A second run of powder was produced and care was taken to ensure that the feed powders were not contaminated. This correct alloy will be referred to as FeAl. This batch was coated onto the substrate using only the conditions for runs 6 and 7. The cross-sections of the sample coated with two and

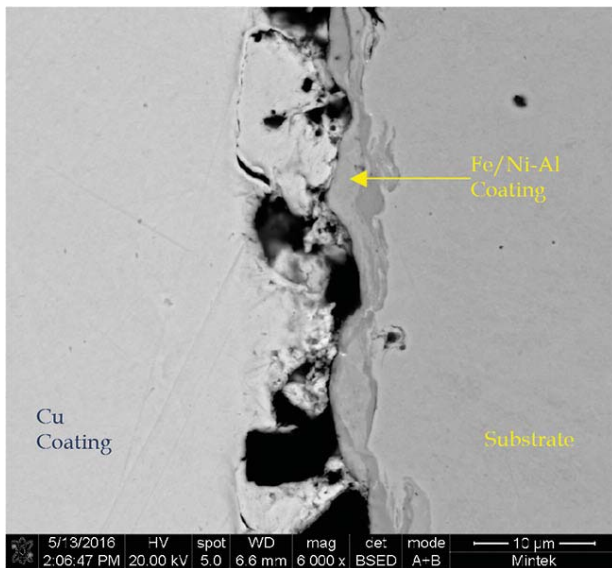


Figure 2—SEM-BSE image of the Fe/Ni-Al coating made with two passes on a mild steel substrate

Table IV

Conditions for cold-spray coating

Condition	Run 1	Run 2	Run 3	Run 4	Run 5	Run 6	Run 7
Temperature (°C)	400	500	500	500	500	500	500
Pressure (bar)	9.65	9.65	9.65	10	10	10	10
Standoff distance (mm)	10	10	10	10	10	10	10
Feed rate (%)	40	40	60	40	40	40	40
No. of passes	1	1	1	1	2	2	5

Cold-spray coating of an Fe-40 at.% Al alloy with additions of ruthenium

five passes are shown in Figures 4 and 5. The coatings did not differ significantly from the Ni-containing coatings in terms of thickness. However, the different contrasts seen in the Ni-containing coatings were not observed.

With both powder lots, the thickness of the coatings obtained is a concern as it would have been preferable to have coatings of at least 10 µm in thickness. There are a number of factors that could be changed to influence this, one being the spray pressure during coating. Unfortunately the system utilized for the spray coating had a maximum pressure limit of 10 bar. Another option would be to increase the temperature used in the spray coating to the upper limit of around 800–1000°C. The third and final option would be to investigate the use of another coating technique such as high-velocity oxy-fuel (HVOF) or plasma-spray coating.

Oxidation trial

The weights of the samples before and after the oxidation treatment as well as the percentage mass increase are shown in Table V. All samples showed an increase in mass, indicating that they were oxidized. The percentage weight gain of all the samples was not significantly different and as such the coatings applied to the samples were not effective in preventing the oxidation of the mild steel.

The oxidized samples were cold-mounted, carbon coated and analysed on the SEM. As expected from the mass gain of the samples during the oxidation trial, all the samples showed significant oxide on the surface of the substrates. The oxides were too thick to be observed in a single SEM image and so only a small portion of each oxide layer is shown in the images. EDX analysis did not reveal any Al in the oxide layer, even at the very edge of the layer. As a result, it could not be determined whether the coating was still intact on top of the oxide layer for the two coated samples (Figure 6–8).

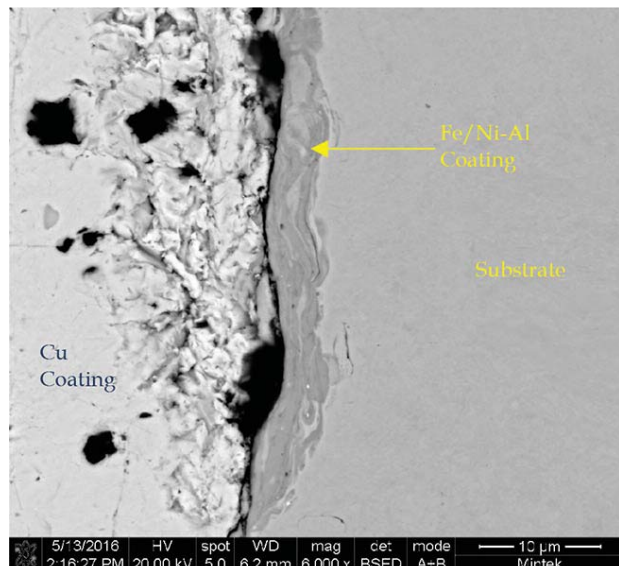


Figure 3—SEM-BSE image of the Fe/Ni-Al coating made with five passes on a mild steel substrate

The compositions of the oxide layers were analysed by SEM-EDX (Table VI). The composition was found to be consistent with the oxidation of the mild steel substrate. The

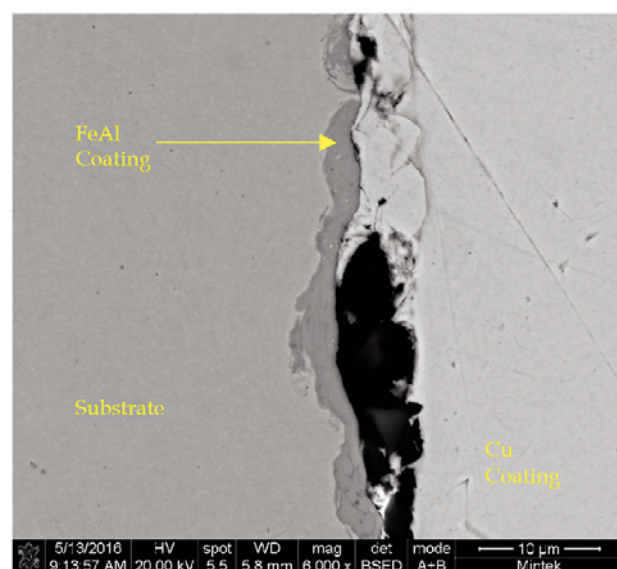


Figure 4—SEM-BSE image of the FeAl coating made with two passes on a mild steel substrate

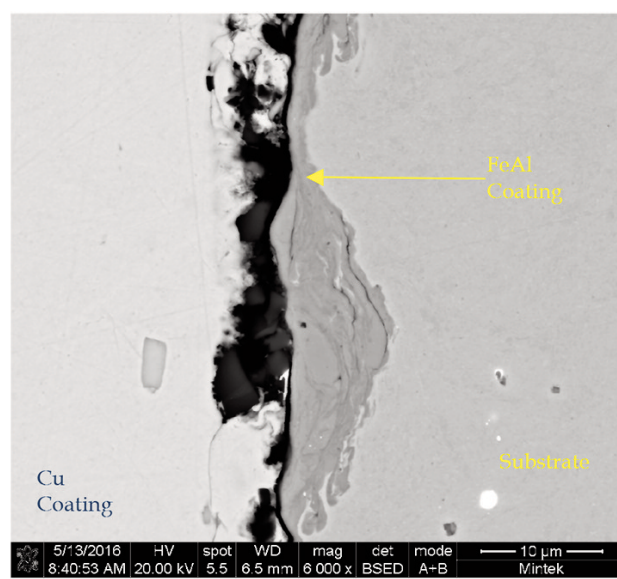


Figure 5—SEM-BSE image of the FeAl coating made with five passes on a mild steel substrate

Table V
Sample weight changes during oxidation treatment

	Mass before oxidation (g)	Mass after oxidation (g)	Weight gain (%)
Mild steel	78.534	84.501	7.6
Fe/Ni-Al	127.919	138.228	8.1
FeAl	122.906	131.452	7.0

Cold-spray coating of an Fe-40 at.% Al alloy with additions of ruthenium

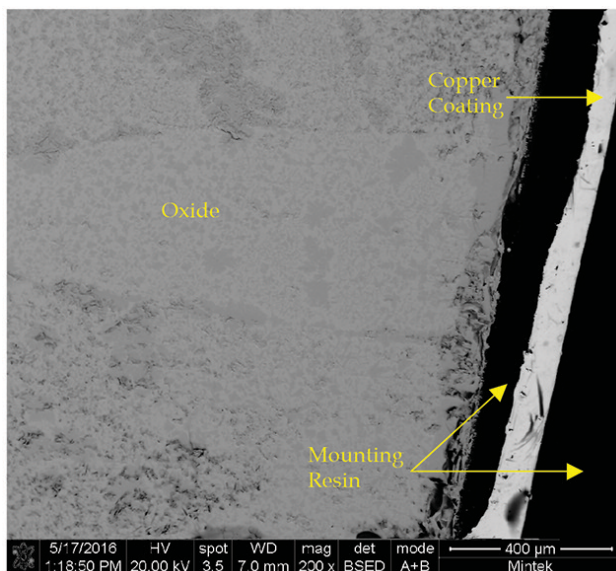


Figure 6—SEM-BSE image of the oxide layer on the uncoated mild steel sample

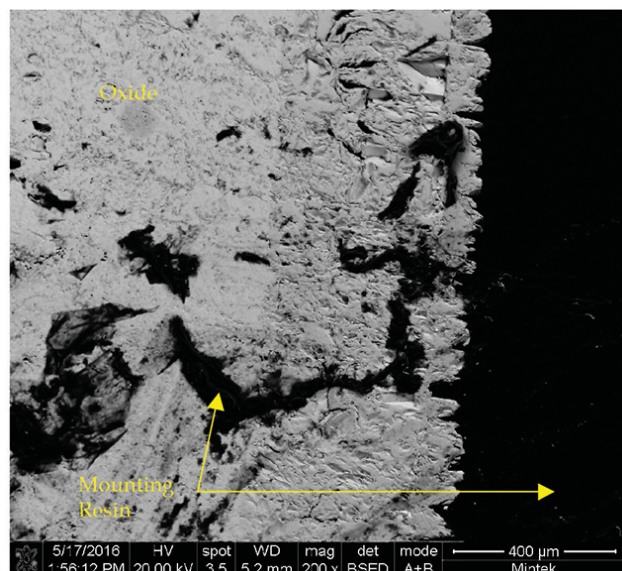


Figure 8—SEM-BSE image of the oxide layer on the sample coated with the FeAl alloy

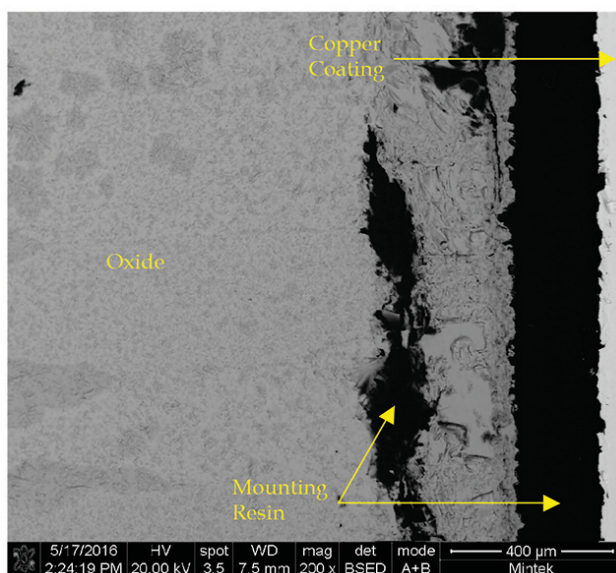


Figure 7—SEM-BSE image of the oxide layer on the sample coated with the Fe/Ni-Al alloy

oxide layers showed two contrasting regions, light and dark and these were analysed on the uncoated sample to determine whether a significant difference existed. It was found that there was a slightly higher oxygen content in the dark regions; however, the difference was not hugely significant. No evidence of the coatings was found on the oxidized samples, indicating that the coatings were ineffective at protecting the substrate.

Discussion

Cold-spray coating of the samples produced very thin coatings on the samples, around 3–5 µm. This is significantly

Table VI
EDX analysis of oxide layers after oxidation trial

At. %	Uncoated mild steel				
	Light	Dark	Overall	Fe/Ni-Al	FeAl
O	42.4±0.6	49.4±0.8	44.9±0.1	44.5±0.4	45.4±0.9
Mn	1.1±0.2	0.6±0.1	0.9±0.1	1.0±0.1	1.0±0.1
Fe	56.5±0.6	48.8±2.0	54.2±0.2	54.5±0.3	53.6±0.9
Cu		1.3±2.2			

thinner than expected and it would be preferable to have a coating thickness of 10 µm or greater. There are a number of options available for improving the deposition efficiency of the cold-spray process. The first and likely most effective option, would be to increase the pressure used during the spraying. Alternatively, it may be necessary to change the coating technique and rather use HVOF, or plasma-spray coating. The oxidation trial of the coated samples confirmed that the coating was not sufficient to protect the substrate from oxidation, as all samples oxidized significantly during the trial. Considering the performance of the coating material in oxidation trials as a bulk sintered material, it is possible that the coating was too thin, not uniform enough, or slightly porous and so allowed oxygen to penetrate to the surface of the substrate.

Conclusions

Cold-spray coating was used successfully to coat the mechanically alloyed powders onto a substrate. However, at the pressures used in this study, the coatings applied to the substrates were very thin. This resulted in a coating that was not effective at preventing the oxidation of the mild steel

Cold-spray coating of an Fe-40 at.% Al alloy with additions of ruthenium

substrates when exposed to high temperatures. As such, it will be necessary to investigate whether a higher pressure can be used in the coating process, as well as the use of alternative coating methods.

References

- ABHIK, N.C., VIVEK, R., UDHAYABANU, V. and MURTY, B.S. 2008. Influence of heat of formation of B2/L12 intermetallic compounds on the milling energy for their formation during mechanical alloying. *Journal of Alloys and Compounds*, vol. 465, no. 1–2. pp. 106–112.
- AGHASIBEIG, M., MONAJATIZADEH, H., BOCHER, P., DOLATABADI, A., WUTHRICH, R. and MOREAU, C. 2016. Cold spray as a novel method for development of nickel electrode coatings for hydrogen production. *International Journal of Hydrogen Energy*, vol. 41, no. 1. pp. 227–238.
- AIRISKALLIO, E., NURMI, E., HEINONEN, M.H., VÄYRYNEN, I.J., KOKKO, K., ROPO, M. and VITOS, L. 2010. High temperature oxidation of Fe-Al and Fe-Cr-Al alloys: The role of Cr as a chemically active element. *Corrosion Science*, vol. 52, no. 10. pp. 3394–3404.
- ARZHNIKOV, A.K., DOBYSHEVA, L.V. and TIMIRGAZIN, M.A. 2008. Formation and ordering of local magnetic moments in Fe-Al alloys. *Journal of Magnetism and Magnetic Materials*, vol. 320, no. 13. pp. 1904–1908.
- BUHL, S., SCHMIDT, K., SAPPOK, D., MERZ, R., GODARD, C., KERSCHER, E. and RIPPERGER, S. 2015. Surface structuring of case hardened chain pins by cold-sprayed microparticles to modify friction and wear properties. *Particuology*, vol. 21. pp. 32–40.
- CHENG, X., OUYANG, Y., SHI, H., ZHONG, X., DU, Y. and TAO, X. 2006. Nano-amorphous (FeAl) $_{1-x}$ Zrx alloys prepared by mechanical alloying. *Journal of Alloys and Compounds*, vol. 421, no. 1–2. pp. 314–318.
- CINCA, N., LIST, A., GÄRTNER, F., GUILEMANY, J.M. and KLASSEN, T. 2015. Influence of spraying parameters on cold gas spraying of iron aluminide intermetallics. *Surface and Coatings Technology*, vol. 268. pp. 99–107.
- CODDET, P., VERDY, C., CODDET, C. and DEBRAY, F. 2015. Effect of cold work, second phase precipitation and heat treatments on the mechanical properties of copper–silver alloys manufactured by cold spray. *Materials Science and Engineering: A*, vol. 637. pp. 40–47.
- CODDET, P., VERDY, C., CODDET, C., DEBRAY, F., and LECOUTURIER, F. 2015. Mechanical properties of thick 304L stainless steel deposits processed by He cold spray. *Surface and Coatings Technology*, vol. 277. pp. 74–80.
- CONCUSTELL, A., HENAO, J., DOSTA, S., CINCA, N., CANO, I.G. and GUILEMANY, J.M. (2015). On the formation of metallic glass coatings by means of Cold Gas Spray technology. *Journal of Alloys and Compounds*, vol. 651. pp. 764–772.
- COUPERTHWAITE, R.A. and MWAMBA I.A. 2013. Effect of platinum group metal additions on the oxidation behaviour of Fe-40at.% Al. *Proceedings of the AMI 2013 Precious Metals Conference*, ISBN 978-1-920410-51-3. pp. 307–316
- COUPERTHWAITE, R.A., CORNISH, L.A., MWAMBA, I.A. and PAPO, M.J. 2015. Effect of Processing Route on the Microstructure and Properties of an Fe-al Alloy with Additions of Precious Metal. *Materials Today: Proceedings*, vol. 2, no. 7. pp. 3932–3942.
- D'ANGELO, L., D'ONOFRIO, L. and GONZALEZ, G. 2009. Nanophase intermetallic FeAl obtained by sintering after mechanical alloying. *Journal of Alloys and Compounds*, vol. 483, no. 1–2. pp. 154–158.
- EELMAN, D., DAHN, J., MACKAY, G. and DUNLAP, R. 1998. An investigation of mechanically alloyed Fe-Al. *Journal of Alloys and Compounds*, vol. 266, no. 1–2. pp. 234–240.
- EHTEMAM HAGHIGHI, S., JANGHORBAN, K. and IZADI, S. 2010. Order-sintering of mechanically alloyed FeAl nanostructures. *Journal of Alloys and Compounds*, vol. 503, no. 2. pp. 375–379.
- GRABKE, H. 1999. Oxidation of NiAl and FeAl. *Intermetallics*, vol. 7, no. 10. pp. 1153–1158.
- GRIGORIEV, S., OKUNKOVA, A., SOVA, A., BERTRAND, P. and SMUROV, I. 2015. Cold spraying: From process fundamentals towards advanced applications. *Surface and Coatings Technology*, vol. 268. pp. 77–84.
- GROS DIDIER, T., TIDU, A. and LIAO, H.-L. 2001. Nanocrystalline Fe-40Al coating processed by thermal spraying of milled powder. *Scripta Materialia*, vol. 44, no. 3. pp. 387–393.
- GUO, P., SHAO, Y., ZENG, C., WU, M. and LI, W. 2011. Oxidation characterization of FeAl coated 316 stainless steel interconnects by high-energy micro-arc alloying technique for SOFC. *Materials Letters*, vol. 65, no. 19–20. pp. 3180–3183.
- HENAO, J., CONCUSTELL, A., G.CANO, I., DOSTA, S., CINCA, N., GUILEMANY, J.M. and SUHONEN, T. 2016. Novel Al-based metallic glass coatings by Cold Gas Spray. *Materials & Design*, vol. 94. pp. 253–261.
- HERRMANN-GEPPERT, I., BOGDANOFF, P., EMMLER, T., DITTRICH, T., RADNIK, J., KLASSEN, T. and SCHIEDA, M. 2016. Cold gas spraying – A promising technique for photoelectrodes. *Catalysis Today*, vol. 260. pp. 140–147.
- JAKUPI, P., KEECH, P.G., BARKER, I., RAMAMURTHY, S., JACKLIN, R.L., SHOESMITH, D.W. and MOSER, D.E. 2015. Characterization of commercially cold sprayed copper coatings and determination of the effects of impacting copper powder velocities. *Journal of Nuclear Materials*, vol. 466. pp. 1–11.
- JAN, V., ČUPERA, J. and CIZEK, J. 2015. On the search for producing intermetallics by diffusion reaction of cold spray bulk deposits. *Surface and Coatings Technology*, vol. 268. pp. 216–223.
- JI, G., GORAN, D., BERNARD, F., GROS DIDIER, T., GAFFET, E. and MUNIR, Z.A. 2006. Structure and composition heterogeneity of a FeAl alloy prepared by one-step synthesis and consolidation processing and their influence on grain size characterization. *Journal of Alloys and Compounds*, vol. 420, no. 1–2. pp. 158–164.
- KEZRANE, M., GUITTOUM, A., BOUKHERROUB, N., LAMRANI, S., and SAHRAOUI, T. 2012. Mössbauer and X-ray diffraction studies of nanostructured Fe70Al30 powders elaborated by mechanical alloying. *Journal of Alloys and Compounds*, vol. 536. pp. S304–S307.

Cold-spray coating of an Fe-40 at.% Al alloy with additions of ruthenium

- KIM, K., LI, W. and GUO, X. 2015. Detection of oxygen at the interface and its effect on strain, stress, and temperature at the interface between cold sprayed aluminum and steel substrate. *Applied Surface Science*, vol. 357. pp. 1720–1726.
- KO, I.-Y., JO, S.-H., DOH, J.-M., YOON, J.-K. and SHON, I.-J. 2010. Rapid consolidation of nanostructured FeAl compound by high frequency induction heating and its mechanical properties. *Journal of Alloys and Compounds*, vol. 496, no. 1–2. pp. L1–L3.
- KOIVULUOTO, H., BOLELLI, G., MILANTI, A., LUSVARGHI, L. and VUORISTO, P. 2015. Microstructural analysis of high-pressure cold-sprayed Ni, NiCu and NiCu+Al₂O₃ coatings. *Surface and Coatings Technology*, vol. 268. pp. 224–229.
- KRASNOWSKI, M., GRABIAS, A. and KULIK, T. 2006. Phase transformations during mechanical alloying of Fe-50% Al and subsequent heating of the milling product. *Journal of Alloys and Compounds*, vol. 424, no. 1–2. pp. 119–127.
- KRASNOWSKI, M. and KULIK, T. 2007a. Nanocrystalline FeAl intermetallic produced by mechanical alloying followed by hot-pressing consolidation. *Intermetallics*, vol. 15, no. 2. pp. 201–205.
- KRASNOWSKI, M. and KULIK, T. 2007b. Nanocrystalline FeAl matrix composites reinforced with TiC obtained by hot-pressing consolidation of mechanically alloyed powders. *Intermetallics*, vol. 15, no. 10. pp. 1377–1383.
- KRASNOWSKI, M., WITEK, A. and KULIK, T. 2002. The FeAl-30%TiC nanocomposite produced by mechanical alloying and hot-pressing consolidation. *Intermetallics*, vol. 10, no. 4. pp. 371–376.
- KUC, D., NIEWIELSKI, G. and BEDNARCZYK, I. 2009. Structure and plasticity in hot deformed FeAl intermetallic phase base alloy. *Materials Characterization*, vol. 60, no. 10. pp. 1185–1189.
- LI, W.-Y., ZHANG, C., WANG, H.-T., GUO, X.P., LIAO, H.L., LI, C.-J. and CODDET, C. 2007. Significant influences of metal reactivity and oxide films at particle surfaces on coating microstructure in cold spraying. *Applied Surface Science*, vol. 253, no. 7. pp. 3557–3562.
- LUO, X.-T. and LI, C.-J. 2012. Dual-scale oxide dispersoids reinforcement of Fe-40at.%Al intermetallic coating for both high hardness and high fracture toughness. *Materials Science and Engineering: A*, vol. 555. pp. 85–92.
- LUO, X.-T. and LI, C.-J. 2015. Large sized cubic BN reinforced nanocomposite with improved abrasive wear resistance deposited by cold spray. *Materials and Design*, vol. 83. pp. 249–256.
- MASSALSKI, T.B. 1990. *Binary Alloy Phase Diagrams*, 2nd edn. vol. 1, ASM International. pp. 148–149.
- MONTEALEGRE, M.A., GONZÁLEZ-CARRASCO, J.L., MORRIS-MUÑOZ, M.A., CHAO, J. and MORRIS, D.G. 2000. The high temperature oxidation behaviour of an ODS FeAl alloy. *Intermetallics*, vol. 8, no. 4. pp. 439–446.
- NAYAK, S.S., WOLLGARTEN, M., BANHART, J., PABI, S.K. and MURTY, B.S. 2010. Nanocomposites and an extremely hard nanocrystalline intermetallic of Al-Fe alloys prepared by mechanical alloying. *Materials Science and Engineering: A*, vol. 527, no. 9. pp. 2370–2378.
- PALDEY, S. and DEEVI, S.C. 2003. Cathodic arc deposited FeAl coatings: properties and oxidation characteristics. *Materials Science and Engineering: A*, vol. 355, no. 1–2. pp. 208–215.
- SHI, H., GUO, D. and OUYANG, Y. 2008. Structural evolution of mechanically alloyed nanocrystalline FeAl intermetallics. *Journal of Alloys and Compounds*, vol. 455, no. 1–2. pp. 207–209.
- SKOGLUND, H., KNUTSON WEDEL, M. and KARLSSON, B. 2003. The role of oxygen in powder processing of FeAl. *Intermetallics*, vol. 11, no. 5. pp. 475–482.
- SKOGLUND, H., WEDEL, M.K. and KARLSSON, B. 2004. Processing of fine-grained mechanically alloyed FeAl. *Intermetallics*, vol. 12, no. 7–9. pp. 977–983.
- SONG, H., WU, Y., TANG, C., YUAN, S., GONG, Q. and LIANG, J. 2009. Microstructure and mechanical properties of FeAl intermetallics prepared by mechanical alloying and hot-pressing. *Tsinghua Science and Technology*, vol. 14, no. 3. pp. 300–306.
- VALDRÉ, G., BOTTON, G. and BROWN, L. 1999. High spatial resolution PEELS characterization of FeAl nanograins prepared by mechanical alloying. *Acta Materialia*, vol. 47, no. 7. pp. 2303–2311.
- WANG, H.-T., LI, C.-J., YANG, G.-J. and LI, C.-X. 2008a. Effect of heat treatment on the microstructure and property of cold-sprayed nanostructured FeAl/Al₂O₃ intermetallic composite coating. *Vacuum*, vol. 83, no. 1. pp. 146–152.
- WANG, H.-T., LI, C.-J., YANG, G.-J. and LI, C.-X. 2008b. Cold spraying of Fe/Al powder mixture: Coating characteristics and influence of heat treatment on the phase structure. *Applied Surface Science*, vol. 255, no. 5. pp. 2538–2544.
- XU, C., GAO, W. and GONG, H. 2000. Oxidation behaviour of FeAl intermetallics. The effects of Y and/or Zr on isothermal oxidation kinetics. *Intermetallics*, vol. 8, no. 7. pp. 769–779.
- XU, C.-H., GAO, W. and HE, Y.-D. 2000. High temperature oxidation behaviour of FeAl intermetallics—oxide scales formed in ambient atmosphere. *Scripta Materialia*, vol. 42, no. 10. pp. 975–980.
- XU, C.-H., GAO, W. and LI, S. 2001. Oxidation behaviour of FeAl intermetallics – the effect of Y on the scale spallation resistance. *Corrosion Science*, vol. 43, no. 4. pp. 671–688.
- YANG, G.-J., WANG, H.-T., LI, C.-J. and LI, C.-X. 2011. Effect of annealing on the microstructure and erosion performance of cold-sprayed FeAl intermetallic coatings. *Surface and Coatings Technology*, vol. 205, no. 23–24. pp. 5502–5509.
- YANG, Z.-G. and HOU, P.Y. 2005. Wrinkling behavior of alumina scales formed during isothermal oxidation of Fe-Al binary alloys. *Materials Science and Engineering: A*, vol. 391, no. 1–2. pp. 1–9.
- ZHU, X., YAO, Z., GU, X., CONG, W. and ZHANG, P. 2009. Microstructure and corrosion resistance of Fe-Al intermetallic coating on 45 steel synthesized by double glow plasma surface alloying technology. *Transactions of Nonferrous Metals Society of China*, vol. 19, no. 1. pp. 143–148. ◆



The influence of particle size distribution on the properties of metal-injection-moulded 17-4 PH stainless steel

by M. Seerane*, P. Ndlangamandla† and R. Machaka*

Synopsis

Metal injection moulding (MIM) is a near-net-shaping powder metallurgy technique suitable for the cost-effective mass production of small and complex components. In this paper, the effects of the metal powder particle size on the final properties of 17-4 PH stainless steel are reported. Three different particle sizes (d_{50} 33.0, 7.91 and 4.04 μm) were used to prepare the injectable MIM feedstocks using a CSIR-developed wax-based binder system at a fixed solids loading of 60 vol.%. The distribution slope parameter and the rheological flow index behaviour were used to predict the flowability of the feedstocks. The effects of the particle size on MIM products were established. The results are discussed in terms of the subsequent microstructural and mechanical properties of MIM 17-4 PH stainless steel against the established MPIF Standard 35.

Keywords

metal injection moulding, MIM, particle size distribution, 17-4 PH stainless steel, densification, properties.

Introduction

Metal injection moulding (MIM) is a near-net-shape manufacturing process established as an alternative to produce complex small-to-medium shaped components that were previously fabricated by conventional methods at higher costs (Attia and Alcock, 2011; Todd and Sidambe, 2013).

Although recent advances in micro-manufacturing (mainly machining and electrodeposition-based) have enabled the fabrication of complex micro-size geometries directly into miniaturized parts, these processes are generally neither routine nor easily accessible at present (Attia and Alcock, 2011).

Typically, the MIM process consists of four steps: mixing, injection moulding, debinding and sintering. Mixing involves blending of the desired metal powder composition with carefully selected multicomponent organic binders at the right proportion. This mixture, which is called feedstock, is then injected into a mould of a required shape to form a 'green part'. Debinding is the removal of the binders by chemical, thermal, or catalytic means while maintaining the shape of the part. Finally, the debound part is sintered to a full or near-full density part (Sotomayor, Varez and Levenfeld, 2010). The MIM process is essentially a

combination of plastic injection moulding with conventional powder metallurgy technologies.

According to the literature (German and Rose, 1997; Khakbiz, Simchi and Bagheri, 2005; Seerane *et al.*, 2013), the mechanical properties of the final MIM-produced components are certainly influenced in the fabrication stages in the MIM processing, as well as by the selection of the starting powder and binder materials. Therefore, understanding the powder characteristics is critical for the success of the MIM process.

Powder particle sizes (German and Rose, 1997; German, 2005) play a significant role in realizing a dense sintered part at the minimum shrinkage (Ma *et al.*, 2014; Sotomayor *et al.*, 2010). Finer powder particles result in smaller moulding defects, increase melt viscosity, higher sintering rates and shrinkage and better surface finish. However, some of the disadvantages encountered with the use of finer particles include agglomeration, which adversely affects the homogeneity of the feedstock, necessitating longer debinding times and higher powder procurement cost. Coarser powder particles, in contrast, give higher packing efficiency, reduced sintering shrinkage rates, shorter debinding times and are typically cheap and easy to handle, but the product quality is often inferior (Bose *et al.*, 2008; German, 1992; Hausnerova, Kitano and Saha, 2010).

The influence of particle size distribution on mouldability of the feedstock is also a crucial factor in the chain of the MIM process (Amin, Jamaludin and Muhamad, 2009). Two

* Light Metals, Materials Science and Manufacturing, Council for Scientific and Industrial Research, Pretoria, South Africa.

† Department of Materials Science and Metallurgical Engineering, University of Pretoria, South Africa.

© The Southern African Institute of Mining and Metallurgy, 2016. ISSN 2225-6253. This paper was first presented at the AMI Ferrous and Base Metals Development Network Conference 2016 19–21 October 2016, Southern Sun Elangeni Maharani, KwaZulu-Natal, South Africa.

The influence of particle size distribution on the properties of metal-injection

parameters that are used to predict the mouldability of the feedstock are the *distribution slope parameter (Sw)* and *flow behaviour index (n)*. The former parameter represents the measure of particle size range and is defined as (German and Bose, 1997):

$$S_w = \frac{2.56}{\log(\frac{d_{90}}{d_{10}})} \quad [1]$$

where the numerator represents the fact that d_{10} and d_{90} are 2.56 standard deviations apart on a Gaussian distribution; however, powders usually follow a lognormal distribution and the logarithmic size is appropriate for obtaining Gaussian behaviour. The average particle size, d_{50} and S_w are important measures of a powder. The parameter S_w is the slope of the lognormal cumulative distribution and is similar to a coefficient of variation or standard deviation. A narrow particle size distribution is implied by larger values of S_w and a wider distribution corresponds to small values of S_w . Powders that exhibit a S_w of 2 (very broad distributions) are easier to mould, while some more difficult powders to mould exhibit S_w values between 4 and 5. A very narrow particle size distribution with S_w greater than 7 is the most difficult to mould.

The flow behaviour index (n value) indicates the sensitivity of the feedstock's viscosity to shear rate variations (Ahn *et al.*, 2009); smaller values (typically less than 1) indicating higher shear sensitivity and more pseudo-plasticity of the feedstock and hence better viscosity response to shear rate changes. For such feedstocks, mould filling is therefore easier, especially at higher shear rates. Amin *et al.* (2009) concluded that fine particles exhibit low n values and thus greater pseudo-plastic behaviour of the feedstock. It is important that the n value for each feedstock is calculated in order to predict the mouldability. The following rheology equation is used to estimate the values of n (Huang, Liang and Qu, 2003):

$$\eta = K \dot{\gamma}^{n-1} \quad [2]$$

where η is the viscosity of the feedstock and K a constant. The slope of the $\log \eta$ versus $\log \dot{\gamma}$ graph is $n - 1$, from which n can be deduced.

There has been a limited amount of work on the effects of particle size and particle size distribution on the mouldability and sinterability of MIM powders. Most work available (Bricout *et al.*, 2013; González-Gutiérrez, Stringari and Emri, 2012; Mannschatz, Muller and Moritz, 2011; Schwartzwalder, 1949) puts considerable emphasis on the influence of particle shape, tailored particle size distribution

and powder loading on the flowability of MIM feedstock and hence the final mechanical properties of the sintered parts.

Mamen *et al.* (2015), however, studied the effect of particle size on the sintering behaviour of tungsten parts produced by MIM, but failed to report on the mechanical properties of their sintered parts. The present work is a study of the influence of the starting powder particle size on the mechanical properties (tensile strength, hardness and density and shrinkage factors) of metal-injection-moulded 17-4 PH stainless steel parts.

Experimental

Materials

The 17-4 PH stainless steel powder materials: -45 µm Grade 630 (Praxair Surface Technologies), -15 µm and -5 µm (Epson Atmix Corp., JP) were used for this study. Figure 1 shows the sizes and spherical morphologies of the metal powders as observed under the JEOL JSM-6510 scanning electron microscope (SEM).

Table I summarizes the size distributions of the metal particles obtained using a laser-scattering particle size analyser (Microtrac Bluewave). The material codes PS-45, PS-15 and PS-5 represent the particle sizes -45 µm, -15 µm and -5 µm respectively.

Table II shows the chemical compositions of the metal powders obtained from the supplier's materials data specification sheets.

Table I
Size distributions of 17-4 PH stainless steel powders

Material code	d_{10} (µm)	d_{50} (µm)	d_{90} (µm)
PS-45	12.3	33.0	50.3
PS-15	2.65	7.91	23.1
PS-5	1.98	4.04	7.90

Table II
Chemical compositions (wt%) of the starting powder materials

	Si	Mn	Ni	Cr	Cu	Nb	Fe
FE-276-3 17-4 PH	1.0 ≤ 0.5	≤ 0.3	4.0 3.0–5.0	16.0 15.5–17.5	3.0 3.0–5.0	0.25 0.15–0.45	Bal. Bal.

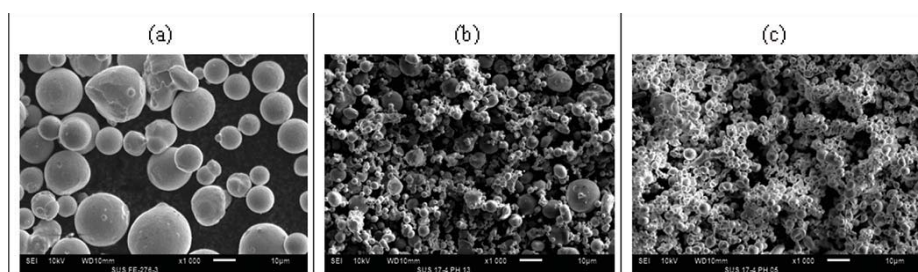


Figure 1—SEM images of 17-4 PH stainless steel powder at 1000x magnification. (a) -45 µm, (b) -15 µm, (c) -5 µm

The influence of particle size distribution on the properties of metal-injection

Feedstock preparation and injection moulding

We prepared three feedstocks by mixing metallic powder materials with a custom wax-polymer binder system developed at CSIR. The binder system consists of paraffin wax, low-density polyethylene, polypropylene and stearic acid. The solids loading, which is the volume ratio of the solid powder to the total volume of the powder and binder, was kept constant at 60 vol.%. The feedstocks were labelled on the basis of powder size and solids loading; the nomenclature is presented in Table III.

The feedstocks were prepared by means of a sigma-type blade mixer (4223 Jones Industrial mixer) using a rotation frequency of 90 r/min for at least 1 hour at 140°C in air. Upon cooling, all feedstocks were appropriately granulated after mixing and were re-mixed for a further 30 minutes to improve homogeneity.

The feedstocks were injection-moulded using a 40 t ARBURG Allrounder 270U 400-70 injection moulding machine. The feedstocks were injection-moulded into MPIF standard 'dogbone' shape tensile specimens of dimensions 89 mm (overall length), 40 mm (gauge length), 14.8 mm (grip section diameter) and 5 mm (gauge section diameter). The product of injection moulding is called a 'green component'. The injection moulding process parameters (injection temperature, speed and pressure and mould temperature) were optimized in previous work (Seerane, Chikwanda and Machaka, 2015).

Debinding and sintering

The debinding of the injection-moulded components was performed using two techniques: solvent extraction and thermal debinding, in that order. Solvent debinding involves the immersion of the green component in *n*-heptane at 60°C for 24 hours to extract the solvent-soluble wax and stearic acid binder fractions. The samples were then dried overnight to reject residual solvent. In order to avoid breakage of the fragile debound parts, the thermal debinding precedes the sintering stage; both were carried out in a Carbolite tube furnace under a controlled flowing argon atmosphere. The solvent-debound samples were placed in an alumina crucible, loaded into the furnace and heated from room temperature to 550°C at 1.0°C/min. The samples were held at 550°C for 1 hour to completely remove the remaining binder components. The furnace temperature was then ramped up to 1300°C at 10 °C/min for sintering. Sintering was performed for 4 hours, then the furnace was cooled. The argon gas flow was maintained at 1.0 L/min. The debinding process parameters were investigated in previous work (Machaka and Chikwanda, 2014; Machaka, Seerane and Chikwanda, 2014; Seerane *et al.*, 2015).

Post-sintering analysis

Sintered samples were evaluated for density and shrinkage level and tested for mechanical properties like apparent hardness and tensile strength. The linear shrinkage level of the sintered samples was measured against the as-moulded green parts using a high-precision Vernier calliper. Sintered density measurement was performed on a precision analytical balance (OHAUS) based on the Archimedes principle. The apparent hardness measurements were carried out by using Vicker's scale through the application of 500 g load for 10

seconds, according to ASTM-E384 standard, on an automated microhardness tester (FM-700). Tensile testing was done on an INSTRON™ Servo Hydraulic 1342 test instrument at the constant rate of 0.5 mm/min.

Microstructural analysis was done using a Leica DMI500 M optical microscope.

Results and discussion

Mouldability

The evaluation of the feedstock mouldability was based on the distribution slope parameter and the flow behaviour index. Table IV summarizes the estimated values of S_w and n . The S_w values for feedstocks PS-45-60 and PS-5-60 indicate that the powders (PS-45 and PS-5) used to prepare the feedstocks are likely to be difficult to mould. The data for feedstock PS-15-60 indicates that the powder (PS-15) used to prepare the feedstock has a wider particle size distribution and hence better mouldability due to the lower S_w value of 2.72. On the other hand, feedstock PS-15-60 has the lowest n value of 0.331 and therefore a higher shear sensitivity and better viscosity response to shear rate variations. From these observations it can be deduced that feedstock PS-15-60 is expected to be mouldable during injection moulding.

Shrinkage

Figure 2 depicts the shrinkage difference between the as-moulded green, solvent-debound and sintered components. Surface appearance of specimens (a) – (c) gives an indication of the binder lost from the green state to the sintered state and this equates to the level of shrinkage that occurred. Specimen (b) underwent solvent debinding and no significant shrinkage difference is observed relative to the as-moulded part.

Figure 3 shows the shrinkage levels of the specimens at different particle sizes. It can be clearly seen that the shrinkage behaviour is sensitive to the feedstock particle size. The PS-45-60 specimen (larger starting particle size) shows a relatively lower shrinkage level and this is advantageous for controlled dimensional tolerance. As

Table III
Formulation of the feedstocks used in this study

Feedstock ID	Feedstock details
PS-45-60	60 vol.%, powder: -45 µm
PS-15-60	60 vol.%, powder: -15 µm
PS-5-60	60 vol.%, powder: -5 µm

Table IV
The parameters representing the mouldability of the feedstocks

Material code	S_w	n
PS-45-60	4.18	0.563
PS-15-60	2.72	0.331
PS-5-60	4.26	0.390

The influence of particle size distribution on the properties of metal-injection



Figure 2—MIM parts of 17-4 PH stainless steel showing shrinkage differentiation: (a) as-moulded, (b) solvent-debound, (c) sintered

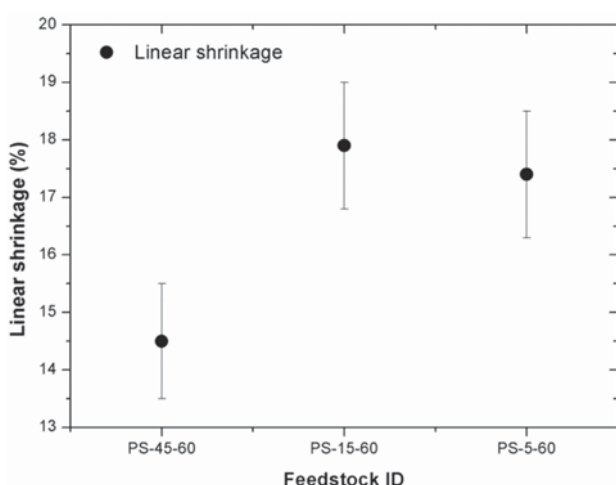


Figure 3—Linear shrinkage of sintered parts at different particle sizes and a fixed starting powder loading of 60 vol.-%

expected, the PS-15-60 and PS-5-60 specimens (smaller particle size) exhibit higher shrinkage levels. The latter result is expected, since smaller particles have a larger specific surface area, necessitating a larger amount of binder which therefore increases the shrinkage level during sintering (Hartwig *et al.*, 1998). PS-15-60 and PS-5-60 specimens do not show a significant difference in their shrinkage levels; however, the PS-5-60 specimen indicates a slightly lower average shrinkage level and this can be attributed to the presence of an oxidation film on the surface of the particles that delays sintering rate and hence shrinkage.

Sintering density and microstructure

Sintered MIM parts are expected to have some residual porosity and usually have densities ranging from 95–99% of the theoretical density (Todd and Sidambe, 2013). It is known in powder metallurgy that finer starting powder particles have better sinterability and therefore tend to achieve relatively higher sintered densities. However, against expectations, the data in Figure 4 seems to indicate that an optimal sintered density is between 94% and 97% of the theoretical density. Specimen PS-15-60 has the highest density of 97%, which conforms to the range quoted in the literature. According to German(1992), for example, the lower density of the specimen PS-5-60 may be the result of particle agglomeration that leads to poor packing density and non-homogeneous feedstock; and hence deteriorated sinterability. In addition, finer powder particles are more prone to surface oxidation (Ye, Liu and Hong, 2008) and this may hinder the sinterability of the localized particles. The higher sintered density of the specimen PS-15-60 can be attributed to a combination of the best mouldability of PS-15-60 feedstock (as shown in Table IV) and the finer starting powder particles to drive sintering.

To complement the sintered density observation, Figure 5 shows the microstructures of the sintered specimens. It can be seen that the finer the starting powder particle size the finer the observed pores are, in general. Specimen PS-45-60 shows, as expected, relatively larger pores that are not particularly uniformly distributed. Specimens PS-15-60 and PS-5-60, on the other hand, shows abundant and uniformly

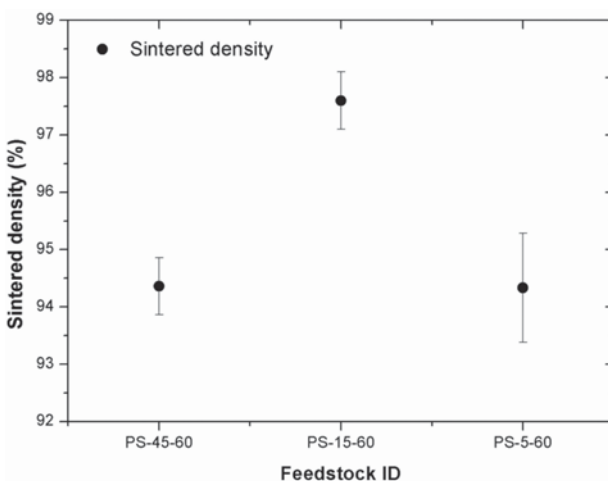


Figure 4—The effect of particle size on the density of sintered parts

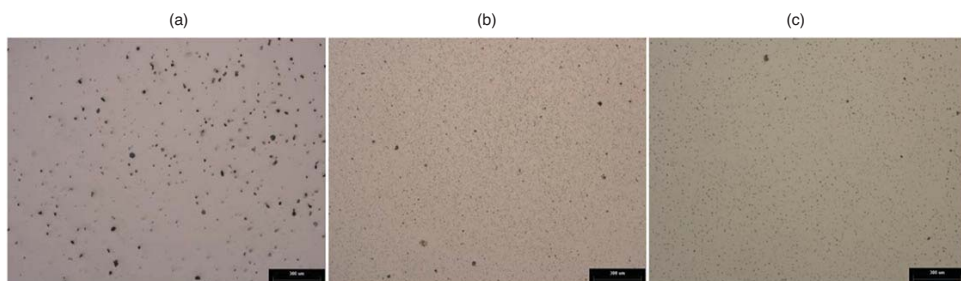


Figure 5—Optical micrographs of the as-sintered parts: (a) PS-45-60, (b) PS-15-60, (c) PS-5-60. Scale bar 300 µm at 5x magnification)

The influence of particle size distribution on the properties of metal-injection

distributed fine pores. However, a few large pores on specimen PS-15-60 can be seen. It is possible that the sum of uniformly distributed fine pores in the PS-5-60 specimen compromises sinterability.

Mechanical properties

Figure 6 summarizes the measured mechanical properties of the sintered parts and the respective as-sintered 17-4PH stainless steel minimum MPIF Standard 35 specifications (MPIF, 2007).

The experimentally measured properties of the PS-45-60 specimen, as presented in Figure 6, are consistently inferior to the minimum tensile property values outlined in the MPIF Standard 35. The PS-5-60 and the PS-15-60 specimens meet most of the minimum standards for density, yield strength, ultimate tensile strength, hardness and elongation. However, the PS-15-60 specimen fails to meet the minimum standard for elongation.

The tensile properties generally improve with a decreasing particle size. This can be attributed to the increasing hardness as the particle size becomes finer. A correlation between hardness and tensile strength is in conformance with the findings in Gülsøy, Özgün and Bilketay (2016) and this relationship is also known to be common (Gaško and Rosenberg, 2011; Shen and Chawla, 2001).

It is apparent therefore that the yield strength, ultimate tensile strength and hardness generally increase as the particle size becomes finer. The influence of particle size on hardness is consistent with the work reported by Srivatsan *et al.* (2002). The lower hardness values of the PS-45-60 and PS-5-60 specimens can be attributed to the considerably larger pore volumes (Figure 5).

Conclusions

Feedstocks of fixed metal powder loading of 60 vol.% and different metal powder particle sizes of -45, -15 and -5 µm were successfully prepared and evaluated for metal injection moulding.

- All the feedstocks exhibited a pseudo-plastic flow property, indicating their general suitability for injection moulding. The starting powder particle size appears to affect the feedstock mouldability; rheological parameters of specimen PS-5-60 indicate moulding difficulty, while PS-15-60 is expected to have superior mouldability during injection
- The effect of the starting powder particle size distribution on the sintered density and shrinkage levels was investigated. A larger particle size yielded minimum shrinkage levels and inferior final sintered densities. Particle agglomeration, poor packing efficiency and non-homogeneous feedstock pseudo-plastic flow properties were identified as reasons for the inferior mouldability of the PS-5-60 feedstocks
- The PS-5-60 material has generally superior mechanical properties and meets the standard in all respects.

Acknowledgements

The contributions of NM, HKC, Ntate SP and PR are duly recognized. The authors are grateful to the DST and the CSIR for financial support. The authors are also indebted to Atmix Corp. (JP) for the supply of powder materials used in this study.

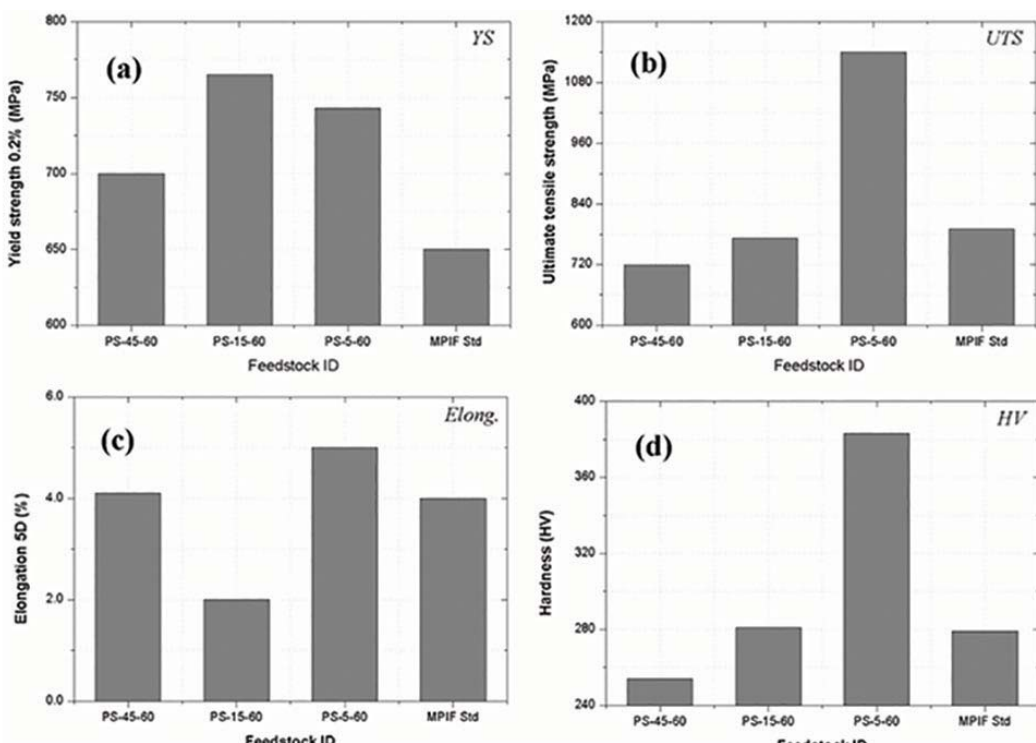


Figure 6—As-sintered MIM parts compared with MPIF Standard 35 (Materials Standard for Metal Injection Moulded Parts)

The influence of particle size distribution on the properties of metal-injection

References

- AHN, S., PARK, S.J., LEE, S., ATRE, S.V. and GERMAN, R.M. 2009. Effect of powders and binders on material properties and molding parameters in iron and stainless steel powder injection molding process. *Powder Technology*, vol. 193, no. 2. pp. 162–169.
- AMIN, S.Y.M., JAMALUDIN, K.R. and MUHAMAD, N. 2009. Rheological properties of Ss316L Mim feedstock prepared with different particle sizes and powder loadings. *Journal of the Institution of Engineers, Malaysia*, vol. 7, no. 2. pp. 59–63.
- ATTIA, U.M. and ALCOCK, J.R. 2011. A review of micro-powder injection moulding as a microfabrication technique. *Journal of Micromechanics and Microengineering*, vol. 21, no. 4. pp. 43001–43001.
- BOSE, A., OTSUKA, I., YOSHIDA, T. and TOYOSHIMA, H. 2008. Faster sintering and lower costs with ultra-fine MIM powders. *Metal Powder Report*, vol. 63, no. 5. pp. 25–30.
- BRICOUT, J., GELIN, J., ABLITZER, C., MATHERON, P. and BROTHIER, M. 2013. Influence of powder characteristics on the behaviour of PIM feedstock. *Chemical Engineering Research and Design*, vol. 91. pp. 2484–2490.
- GASKO, M. and ROSENBERG, G. 2011. Correlation between hardness and tensile properties in ultra-high strength dual phase steels. *Materials Engineering*, vol. 18. pp. 155–159.
- GERMAN, R.M. 1992. Prediction of sintered density for bimodal powder mixtures. *Metallurgical and Materials Transactions A*, vol. 23A, May. pp. 1455–1465.
- GERMAN, R.M. 2005. Powder Metallurgy and Particulate Materials Processing. Metal Powder Industries Federation, Princeton, NJ, USA.
- GERMAN, R.M. and BOSE, A. 1997. Injection Molding of Metals and Ceramics. Metal Powder Industries Federation, Princeton, NJ, USA.
- GONZÁLEZ-GUTIÉRREZ, J., STRINGARI, G.B. and EMRI, I. 2012. Powder Injection molding of metal and ceramic parts. *Intech*. pp. 65–88.
- GÜLSOY, H.Ö., ÖZGÜN, Ö. and BILKETAY, S. (2016). A powder injection molding of Stellite 6 powder : sintering , microstructural and mechanical properties. *Materials Science and Engineering A*, vol. 651. pp. 914–924.
- HARTWIG, T., VELTL, G., PETZOLDT, F., KUNZE, H., SCHOLL, R. and KIEBACK, B. (1998). Powders for metal injection molding. *Journal of the European Ceramic Society*, vol. 18. pp. 1211–1216.
- HAUSNEROVA, B., KITANO, T. and SAHA, P. 2010. Effect of particle size distribution on the flow behaviour of powder injection moulding materials. *Proceedings of the 3rd WSEAS International Conference on Engineering Mechanics, Structures and Engineering Geology*, Corfu. Martin, O. and Zheng, X. (eds.). pp. 192–194.
- HUANG, B., LIANG, S. and QU, X. 2003. The rheology of metal injection molding. *Materials Processing Technology*, vol. 13. pp. 132–137.
- KHAKBIZ, M., SIMCHI, A. and BAGHERI, R. 2005. Analysis of the rheological behavior and stability of 316L stainless steel-TiC powder injection molding feedstock. *Materials Science and Engineering A*, vol. 407, no. 1–2. pp. 105–113.
- MA, J., QIN, M., ZHANG, L., TIAN, L., LI, R., CHEN, P. and QU, X. 2014. Effect of ball milling on the rheology and particle characteristics of Fe-50%Ni powder injection molding feedstock. *Journal of Alloys and Compounds*, vol. 590. pp. 41–45.
- MACHAKA, R. and CHIKWANDA, H.K. 2014. Kinetics of titanium metal injection moulding feedstock thermal debinding. *Proceedings of Light Metals Technologies 2015*, Port Elizabeth. Chikwanda, H.K. and Chikosha, S. (eds.). pp. 1–6.
- MACHAKA, R., SEERANE, M. and CHIKWANDA, H.K. 2014. Binder development for metal injection moulding: a CSIR perspective. *Advances in Powder Metallurgy and Particulate Materials - 2014, Proceedings of the 2014 World Congress on Powder Metallurgy and Particulate Materials, PM 2014*. Metal Powder Industries Federation Princeton, NJ. pp. 443–458.
- MAMEN, B., SONG, J., BARRIERE, T. and GELIN, J. 2015. Experimental and numerical analysis of the particle size effect on the densification behaviour of metal injection moulded tungsten parts during sintering. *Powder Technology*, vol. 270. pp. 230–243.
- MANNSCHATZ, A., MULLER, A. and MORITZ, T. (2011). Influence of powder morphology on properties of ceramic injection moulding feedstocks. *Journal of the European Ceramic Society*, vol. 31, no. 14. pp. 2551–2558.
- MPIF. 2007. Materials standard for metal injection molded parts. MPIF Standard 35, (2007 edn.) Metal Powder Industries Federation, Princeton, NJ. pp. 19–19.
- SCHWARTZWALDER, K. 1949. Injection molding of ceramic materials. *Bulletin of the American Ceramic Society*, vol. 28, no. 11. pp. 459–461.
- SEERANE, M., CHIKWANDA, H. and MACHAKA, R. 2015. Determination of optimum process for thermal debinding and sintering using Taguchi method. *Materials Science Forum*, vol. 829. pp. 138–144.
- SEERANE, M.N., CHIKWANDA, H.K., FOCKE, W. and MACHAKA, R. 2013. Investigating the powder loading of gas atomised Ti6Al4V powder using an 'in-house' binder for MIM. *Advanced Metals Initiative: Precious Metals 2013*. Southern African Institute of Mining and Metallurgy, Johannesburg.
- SHEN, Y. and CHAWLA, N. 2001. On the correlation between hardness and tensile strength in particle reinforced metal matrix composites. *Materials Science and Engineering A*, vol. 297. pp. 44–47.
- SOTOMAYOR, M.E., VAREZ, A. and LEVENFELD, B. 2010. Influence of powder particle size distribution on rheological properties of 316L powder injection moulding feedstocks. *Powder Technology*, vol. 200, no. 1–2. pp. 30–36.
- SRIVATSAN, T.S., WOODS, R., PETRAROLI, M. and SUDARSHAN, T.S. 2002. An investigation of the influence of powder particle size on microstructure and hardness of bulk samples of tungsten carbide. *Powder Technology*, vol. 122. pp. 54–60.
- TODD, I. and SIDAMBE, A.T. 2013. Developments in metal injection moulding (MIM). *Advances in Powder Metallurgy: Properties, Processing and Applications*. Chang, I and Zhao, Y. (eds.). Woodhead, Sheffield. pp. 109–146.
- YE, H., LIU, X.Y. and HONG, H. 2008. Sintering of 17-4PH stainless steel feedstock for metal injection molding. *Materials Letters*, vol. 62, no. 19. pp. 3334–3336. ◆



Spheroidisation of iron powder in a microwave plasma reactor

by J.H. van Laar*† I.J. van der Walt*, H. Bissett*,
J.C. Barry* and P.L. Crouse†

Synopsis

Plasma-assisted spheroidisation of metal powders offers several technical advantages with respect to both the ease of materials handling and powder-metallurgical item manufacturing. Advantages include improved flowability, increased powder packing density, elimination of internal component cavities and fractures, changes in morphology resulting in decreased friction between particles and contamination during pneumatic transport and enhanced particle purity. In this empirical study, spherical iron particles were produced using a microwave plasma operating at atmospheric pressure and characterized using optical microscopy and SEM techniques. Iron powders were fed into the system at fixed operating conditions, resulting in particles with spherical structures. The theoretical estimate of the time required for melting to occur is 1.6 ms, an order of magnitude smaller than the actual residence time.

Keywords

iron powder, spheroidisation, microwave plasma.

Introduction

Particle design and functionalization has become an increasingly popular aspect of materials synthesis and powder-metallurgical item manufacturing. One such technique involves the spheroidisation and densification of feed materials, typically in the form of chemical powders with wide particle size distributions. The major benefits of powder spheroidisation include improved powder flowability, increased powder packing density and powder purity, reductions in internal voids and defects, as well as the ability to manipulate the particles surface morphologies (Boulos, 2004). Thermal plasma processing has the potential for scale-up and for producing industrial quantities of spheroidised powder.

Thermal plasma technologies offer a wide spectrum of material synthesis and treatment options, amongst others the synthesis and spheroidisation of nano-sized ceramic and metal particles (Kumar and Selvarajan, 2006). The spheroidisation process occurs within the plasma discharge via in-flight heating and melting of the powder feed material, given high enough plasma temperatures (Fridman, 2008, p. 495). Surface tension in the molten droplets results in spherical, or nearly

spherical, powder particles being formed upon exiting the plasma discharge where the droplet undergoes rapid cooling and freezes. Quite often, the bulk density of these spherical particles is higher than that of the starting material (Boulos, Fauchais and Pfender, 2013, p. 42). The different plasma spheroidisation techniques reported include radio frequency (RF) induction thermal plasmas (Jiang and Boulos, 2006; Károly and Szépvölgyi, 2005; Yuming, Junjie and Yanwei, 2013), non-transferred direct current (DC) thermal plasmas (Chaturvedi *et al.*, 2014; Kumar and Selvarajan, 2008; Suresh, Selvarajan and Vijay., 2008) and microwave-assisted plasma processing methods (Chen, Gleiman and Phillips, 2001; Vanamu *et al.*, 2004; Weigle *et al.*, 2004).

In this work, a microwave plasma system, similar to that reported in an earlier paper (van Laar *et al.*, 2015b), was used to investigate the potential for spheroidisation of iron powders. Argon served as the carrier gas and the system operated at atmospheric pressure.

Experimental

Apparatus

The experimental set-up consisted of a quartz tube placed perpendicular through a metallic waveguide, connected to a microwave generator operating at 2.45 GHz. The magnetron was powered by a 1.5 kW power supply. The quartz tube, with internal diameter

* Applied Chemistry Division, South African Nuclear Energy Corporation (NECSA) SOC Ltd., Pelindaba, North West Province, South Africa.

† Fluoro-materials Group, Department of Chemical Engineering, Faculty of Engineering, Built Environment and Information Technology, University of Pretoria, Pretoria, South Africa.

© The Southern African Institute of Mining and Metallurgy, 2016. ISSN 2225-6253. This paper was first presented at the AMI Ferrous and Base Metals Development Network Conference 2016 19–21 October 2016, Southern Sun Elangeni Maharani, KwaZulu-Natal, South Africa.

Spheroidisation of iron powder in a microwave plasma reactor

of 2 cm and a length of 30 cm, served as the reaction zone and support flanges at the top and bottom of the tube also served as gas inlets. Argon flow rates were controlled using calibrated Aalborg rotameters. This set-up was similar to that described previously (van Laar *et al.*, 2015a) with the addition of a powder feeder positioned above the reactor inlet, as well as a zirconium wool filter at the bottom of the quartz reactor. A schematic representation of the experimental set-up is shown in Figure 1. A T-connection and valve assembly subsequent to the reactor set-up allowed for easy shifting between vacuum and atmospheric operating pressures.

Characterization of the particles was performed using equipment at the South African Nuclear Energy Corporation (Necsa), as well as the University of Pretoria (UP). Scanning electron microscopy (SEM) was performed on the particles with a high-resolution (0.6 nm) JEOL 6000 system using secondary electron (SE) signals.

Method

At the start of each experimental run, the argon plasma was initiated under vacuum at approximately 15 kPa (Figure 2a), using an Alcatel 2010I dual-stage rotary vane pump. The pressure was then gradually increased by closing the outlet valves, until the pressure reached ambient atmospheric conditions. At this pressure, the plasma became highly filamentary (Cardoso *et al.*, 2009) as shown in Figure 2b. The iron powder was then fed through the plasma zone. During experiments, a dark grey powder deposited on the inner walls of the quartz tubes, as well as on the zirconium wool filter at the bottom of the reactor. After each experimental run, the grey powders were collected from the zirconium wool and the tubes were removed and flushed using acetone. The acetone wash was collected and evaporated in a drying oven operating at 50°C, after which the powders were collected.

The spheroidisation of the iron powders was investigated at constant conditions, given in Table I. The argon flow rates are reported in standard cubic centimetres per minute (sccm). Four runs were completed and all results obtained were

similar. The results presented in this paper are representative of all product powders. During these runs, the reflected power varied between 100 W and 200 W. The reflected power is defined as the total power reflected back towards the magnetron, rather than coupling with the gas in the reactor.

Results and discussion

Optical Microscopy

The presence of spherical particles within the iron product samples was evident. The initial feed powder showed no

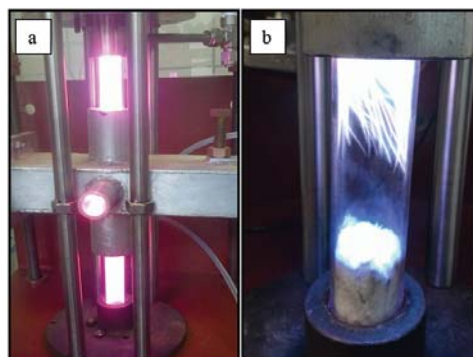


Figure 2—Argon microwave plasma (a) under vacuum and (b) at atmospheric pressure

Table I
Experimental parameters of the spheroidisation experiments

Parameter	Value
Power	1500 W
Ar flow	150 sccm
Pressure	1 atm.
Feed rate	10 g/h

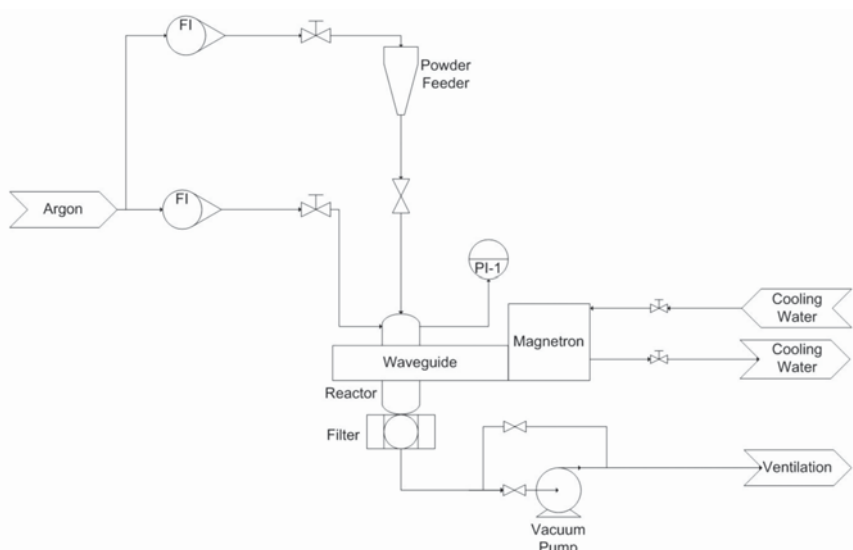


Figure 1—Schematic diagram of the experimental set-up

Spheroidisation of iron powder in a microwave plasma reactor

evidence of large spherical particles at the same magnification settings. After the runs, a definite increase in the amount of spherical particles was found, as shown in Figure 3. The degree of conversion to large spherical morphologies appears to be quite low from these images, implying that a large amount of powder passed through the system without undergoing spheroidisation. This was undoubtedly due to the filamentary nature of the plasma, which decreased the total contact area and time of the particles with the high-energy plasma filaments.

Scanning electron microscopy

SEM images of the iron product are shown in Figure 4. Particle sizes ranged between 20 µm and 100 µm and the surfaces of the particles were either smooth (Figure 4a) or had shallow grooves on the surface (Figure 4b), despite identical operating conditions. The formation of an oxide layer around the particles was also evident from the loosening flakes on the surface, as well as the large white mark, shown in Figure 4b. The different surface morphologies are related to the different flow paths of particles moving through the plasma, resulting in different heating and solidification histories. Li and Ishigaki (2001) hypothesize that the particles with grooved surfaces experience relatively high cooling rates, resulting in the nucleation of polycrystalline particles.

Smaller deposits were also present on the surface of the spheres. These deposits consisted of agglomerated particles ranging between 100 nm and 200 nm. Their presence was attributed to partial evaporation of the iron feed material within the hot plasma filaments, followed by recondensation (Ishigaki *et al.*, 1995).

The iron feed material was also analysed using SEM micrographs and was shown to consist of much smaller spherical particles with sizes 2–6 µm, seen in Figure 5a. These particles were agglomerates of nanosized particles (Figure 5b) and were much smaller than the newly-formed spherical particles in the product powders and hence not visible on the optical images shown in Figure 3.

Other interesting structures seen on the particle surfaces include stacked disc-like, rippled structures, shown in Figure 6(a), similar to the spherical particles reported by Che and Norimasa (2006). The cause and mechanism behind these structures are linked to crystal formation. A variety of nanostructures assume icosahedral shapes at scales where the surface forces exceed the bulk forces. However, some

forms persist into micro-scales, such as certain face-centred cubic (Fcc) metal colloid clusters (de Nijs *et al.*, 2015). The circular discs, magnified in Figure 6(c), are explained through a similar mechanism, by way of body-centred cubic (bcc) cells with (111) hexagonal projections, illustrated in Figure 7, growing radially outward, resulting in the observed ripples and step edges.

In addition, it is well known that crystal plane orientations of materials can be determined and interpreted as spherical representations using Kikuchi patterns, which are obtained using electron backscatter diffraction (EBSD) techniques (Zhou and Wang, 2007, p. 41). Coincidentally, the physical symmetry of the iron particle, highlighted in Figure 6b, bears a remarkable similarity to that of a ferrite spherical Kikuchi map (SKM) shown in Figure 6d (Day, 2008) with a cubic lattice structure viewed along the (111) orientation.

Also present were nanosized cubic and spherical particles, either from the unmelted feed material or subsequently spheroidised. Another phenomenon is shown in Figure 8, where most of the particle surface was covered

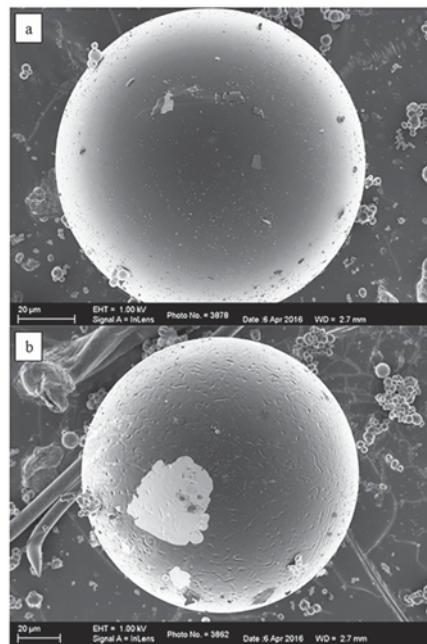


Figure 4—SEM SE images illustrating (a) smooth and (b) rough surfaces

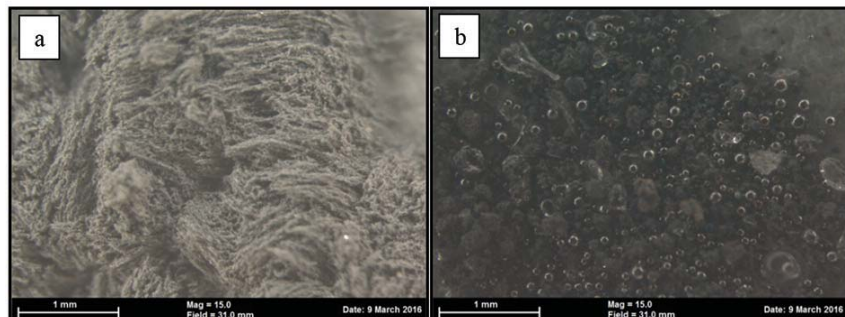


Figure 3—Optical image comparison of the iron powder (a) before and (b) after passing through the microwave plasma

Spheroidisation of iron powder in a microwave plasma reactor

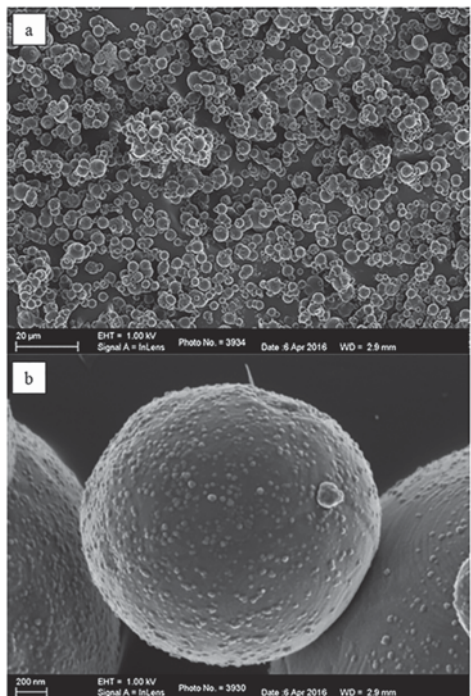


Figure 5—SEM SE images of the iron feed material consisting of (a) smaller spherical agglomerates that were comprised of (b) nanosized particles

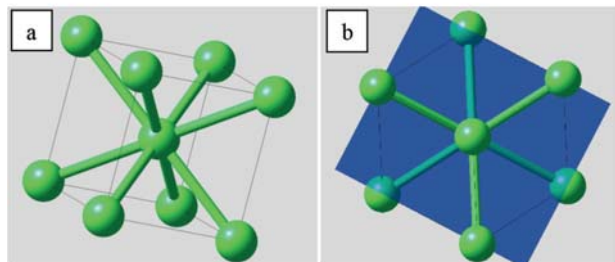


Figure 7—(a) The bcc cell unit with (b) hexagonal projection perpendicular to the (111) plane

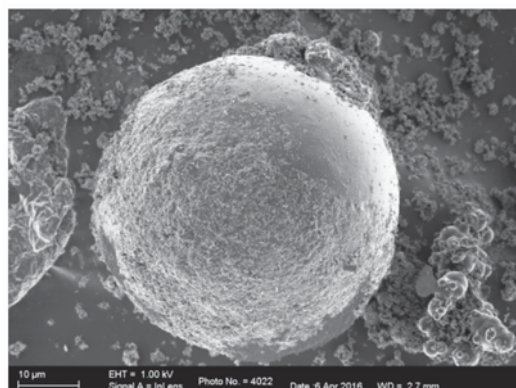


Figure 8—Particles indicative of incomplete melting

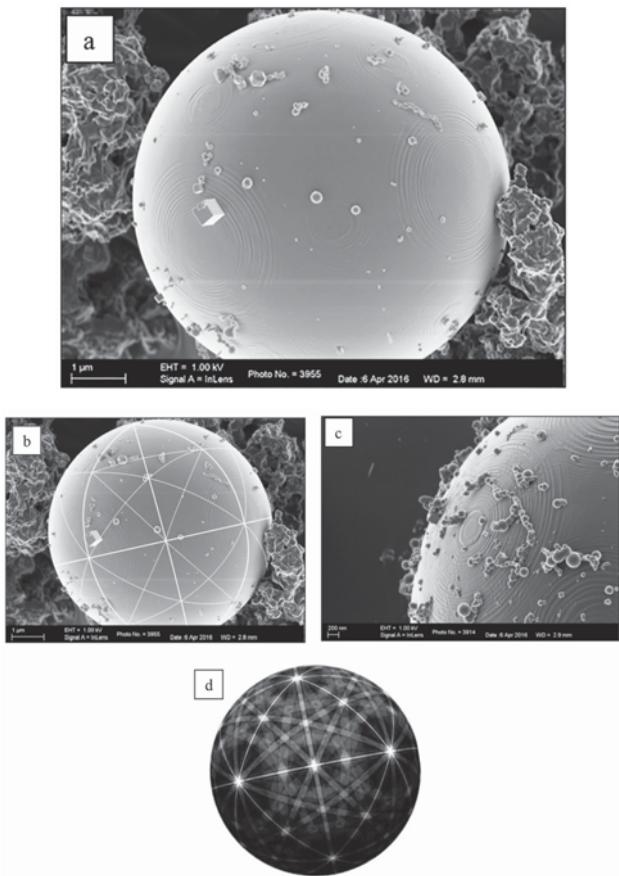


Figure 6—SEM SE morphology of (a) circular discs with (b) highlighted symmetry patterns. The circular discs are magnified (c) and the corresponding Kikuchi pattern (d) is given for ferrite (Day, 2008)

with agglomerates consisting of nanosized particles, similar to the feed material. It is possible that these particles did not experience sufficient heating time for uniform melting and solidification to occur.

The internal structures of the particles were also investigated by embedding the particles in an organic resin, followed by grinding and polishing. The polished surface was then viewed using SEM in order to compare internal morphologies. The internal structure of the feed particles is shown in Figure 9d. These particles appeared to contain minor voids and were non-uniform throughout the entire surface area and were easily damaged due to the aggregated nature of the particles, as indicated in Figure 5b.

The internal structures of the product particles appeared to be quite diverse, with some particles presenting uniform density throughout the particle (Figure 9a and b), while others displayed larger defects and voids (Figure 9c). The straight lines that appeared on some cross-sections, such as those of Figure 9c, were likely due to the grinder pushing too hard on the surface. An alternative explanation entails a different formation mechanism. Regardless, micro-defects and voids were distinguishable within the structure, especially close to the outer perimeter. It is expected that these internal defects were linked to the outer groove formations in Figure 4b. Li and Ishigaki (2001) speculated that these internal defects are a result of a variation in localized cooling rates, where higher cooling rates impeded the nucleation rate for uniform solidification.

Spheroidisation of iron powder in a microwave plasma reactor

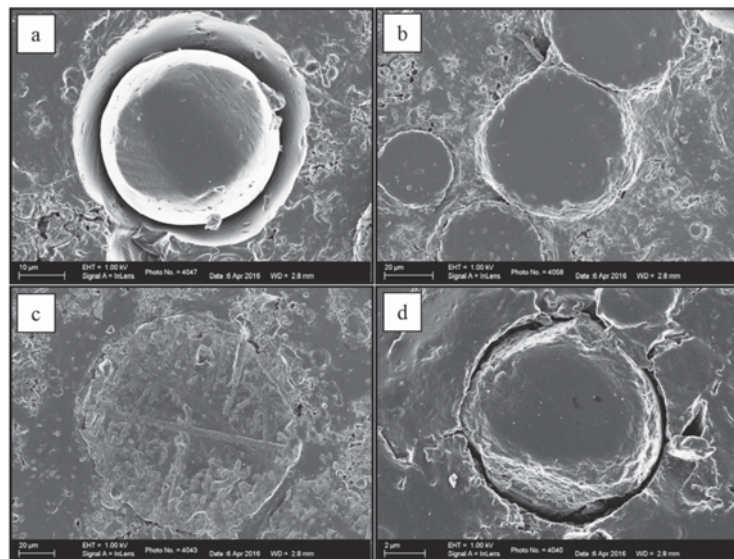


Figure 9—SEM SE images showing the internal cross-section morphologies of spherical iron particles after passing through the microwave plasma

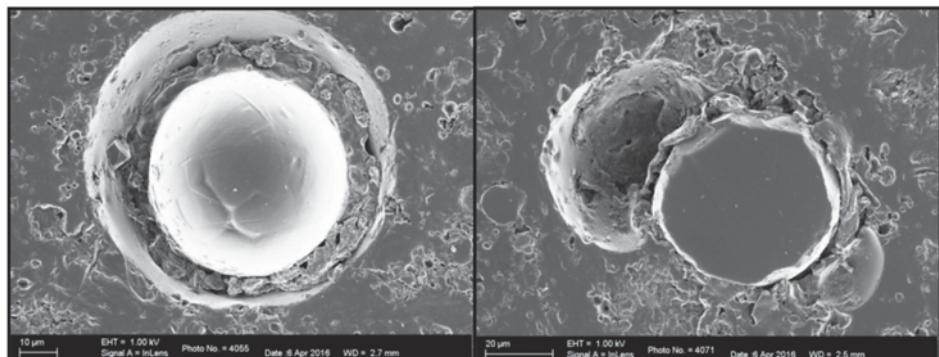


Figure 10—SEM SE micrographs of uniform particles surrounded by a shell consisting of different morphologies

Some particles appeared to possess an outer shell with a different structure from that of the core. Figure 10 presents the cross-sections of particles consisting of a uniformly dense core surrounded by a softer shell. Further investigation revealed the shell to consist of agglomerated structures similar to those of the feed material. The mechanism behind the formation of this shell-and-core structure is unclear; however, one possibility entails the hardening of the organic resin around the particles as they settled to the bottom of the sample during sample sedimentation in the preparation phase.

Heating model

The experimental results showed that a portion of the iron powders underwent spheroidisation in the argon plasma reactor. Theoretical models (Chen and Pfender, 1982) predict the potential for spheroidisation by first considering the heating time of the material, followed by the melting time. The total time needed is then compared to the residence time of the particles inside the hot plasma environment. These models take into account both the melting point and the thermal conduction of the material, as well as the enthalpy of

the plasma gas. Following the model set out by Chen and Pfender (1982) and applied by Li and Ishigaki (2001) for titanium carbide, the heating time, t_h , is given by

$$t_h = \frac{\rho_p}{3} r_w^2 \int_{T_0}^{T_m} \frac{C_p dT_p}{S_\infty - S_w} \quad [1]$$

where ρ_p is the density of the solid particles, r_w the radius of the particles, C_p the heat capacity, T_0 and T_m the starting and melting temperatures respectively and S_∞ and S_w the thermal conduction potentials of the surrounding gas at plasma temperature and the particle surface, respectively.

The thermal conduction potentials are given by

$$S = \int_{T_0}^T k dT \quad [2]$$

where k is the thermal conductivity of the plasma gas. Melting temperature, t_m , is then determined by

$$t_m = \frac{r_w^2 \rho_p L_m}{3(S_\infty - S_m)} \quad [3]$$

Spheroidisation of iron powder in a microwave plasma reactor

where L_m is the heat of fusion of the material and S_m the thermal conductivity potential of the plasma at the melting point, T_m , of the material. For an argon plasma at approximately 2000°C and using the properties of iron (Chase, 1998), the heating and melting times were calculated and are reported in Table II.

The residence time of the powder was assumed to be the time for which the particles fell through the reactor under the influence of gravity only. It was also assumed that due to the filamentary nature of the plasma, only half of the reactor volume was filled with a plasma discharge. With this assumption, the residence times were approximately 175 ms, orders of magnitude higher than those needed according to the model described above.

Conclusions and recommendations

A microwave-induced argon plasma was successfully used for the spheroidisation of iron powders. The feed material (2–6 µm) underwent melting and droplet formation, followed by rapid cooling and solidification. This resulted in larger spherical particles ranging from 20 µm to 100 µm, often with patterns indicative of the underlying crystallinity mechanisms. SEM confirmed the morphological changes brought about by the process and presented various different particle morphologies. Theoretical models were in relative agreement with regards to the potential for spheroidisation, which was confirmed experimentally.

The use of microwave-assisted plasma shows promise for the spheroidisation of metal powders. However, further experimental work is needed to determine the effect of various operating parameters (such as carrier gas composition and flow rates) on the conversion and spheroidisation ratios. Pending these results, it is recommended that the use of microwave plasma systems be considered for further spheroidisation investigations.

Acknowledgements

The authors acknowledge the South African National Research Foundation for financial support and the South African Nuclear Energy Corporation for use of their equipment.

References

- BOULOS, M. 2004. Plasma power can make better powders. *Metal Powder Report*, vol. 59. pp. 16–21.
- BOULOS, M.I., FAUCHAIS, P. and PFENDER, E. 2013. Thermal Plasmas: Fundamentals and Applications. Springer, New York.
- CARDOSO, R.P., BELMONTE, T., NOËL, C., KOSIOR, F. and HENRION, G. 2009. Filamentation in argon microwave plasma at atmospheric pressure. *Journal of Applied Physics*, vol. 105. p. 093306.
- CHASE, M.W.J. 1998. NIST-JANAF Thermochemical Tables. 4th edn. *Journal of Physical Chemistry Ref. Data, Monograph 9*. <http://webbook.nist.gov>
- CHATURVEDI, V., ANANTHAPADMANABHAN, P.V., CHAKRAVARTHY, Y., BHANDARI, S., TIWARI, N., PRAGATHEESWARAN, A. and DAS, A.K. 2014. Thermal plasma spheroidization of aluminum oxide and characterization of the spheroidized alumina powder. *Ceramics International*, vol. 40. pp. 8273–8279.
- CHE, S. and NORIMASA, S. 2006. Preparation and formation mechanism of micrometer-sized spherical single crystal particles of perovskite oxides by flame fusion. *Key Engineering Materials*, vol. 320. pp. 201–204.
- CHEN, C.-K., GLEIMAN, S. and PHILLIPS, J. 2001. Low-power plasma torch method for the production of crystalline spherical ceramic particles. *Journal of Materials Research*, vol. 16. pp. 1256–1265.
- CHEN, X. and PFENDER, E. 1982. Unsteady heating and radiation effects of small particles in a thermal plasma. *Plasma Chemistry and Plasma Processing*, vol. 2. pp. 293–316.
- DAY, A.P. 2008. Spherical EBSD. *Journal of Microscopy*, vol. 230. pp. 472–86.
- DE NIJS, B., DUSSI, S., SMALLenburg, F., MEELDIJK, J.D., GROENENDIJK, D.J., FILION, L., IMHOF, A., VAN BLAADEREN, A. and DIJKSTRA, M. 2015. Entropy-driven formation of large icosahedral colloidal clusters by spherical confinement. *Nature Materials*, vol. 14. pp. 56–60.
- FRIDMAN, A. 2008. Plasma Chemistry. Cambridge University Press.
- ISHIGAKI, T., JUREWICZ, J., TANAKA, J., MORIYOSHI, Y. and BOULOS, M.I. 1995. Compositional modification of titanium carbide powders by induction plasma treatment. *Journal of Materials Science*, vol. 30. pp. 883–890.
- JIANG, X.-L. and BOULOS, M. 2006. Induction plasma spheroidization of tungsten and molybdenum powders. *Transactions of Nonferrous Metals Society of China*, vol. 16. pp. 13–17.
- KÁROLY, Z. and SZÉPVÖLGYI, J. 2005. Plasma spheroidization of ceramic particles. *Chemical Engineering and Processing: Process Intensification*, vol. 44. pp. 221–224.
- KUMAR, S. and SELVARAJAN, V. 2006. Spheroidization of metal and ceramic powders in thermal plasma jet. *Computational Materials Science*, vol. 36. pp. 451–456.
- KUMAR, S. and SELVARAJAN, V. 2008. Plasma spheroidization of iron powders in a non-transferred DC thermal plasma jet. *Materials Characterization*, vol. 59. pp. 781–785.
- LI, Y.-L. and ISHIGAKI, T. 2001. Spheroidization of titanium carbide powders by induction thermal plasma processing. *Journal of the American Ceramic Society*, vol. 84. pp. 1929–1936.
- SURESH, K., SELVARAJAN, V. and VIJAY, M. 2008. Synthesis of nanophasic alumina, and spheroidization of alumina particles, and phase transition studies through DC thermal plasma processing. *Vacuum*, vol. 82. pp. 814–820.
- VAN LAAR, J.H., SLABBERT, J.F.M., MEYER, J.P., VAN DER WALT, I.J., PUTS, G.J. and CROUSE, P.L. 2015a. Microwave-plasma synthesis of nano-sized silicon carbide at atmospheric pressure. *Ceramics International*, vol. 41. pp. 4326–4333.
- VAN LAAR, J.H., VAN DER WALT, I.J., BISSETT, H., PUTS, G.J. and CROUSE, P.L. 2015b. Synthesis and deposition of silicon carbide nanopowders in a microwave-induced plasma operating at low to atmospheric pressures. *Journal of the Southern African Institute of Mining and Metallurgy*, vol. 115. pp. 949–955.
- VANAMU, G., LESTER, K., DATYE, A.K., WEIGLE, J.C., CHEN, C.-K., KELLY, D. and PHILLIPS, J. 2004. Modifying irregular titania powders in a low power microwave plasma torch. *AIChE Journal*, vol. 50. pp. 2090–2100.
- WEIGLE, J.C., LUHRS, C.C., CHEN, C.K., PERRY, W.L., MANG, J.T., NEMER, M.B., LOPEZ, G.P. and PHILLIPS, J. 2004. Generation of aluminum nanoparticles using an atmospheric pressure plasma torch. *Journal of Physical Chemistry B*, vol. 108. pp. 18601–18607.
- YUMING, W., JUNJIE, H. and YANWEI, S. 2013. Spheroidization of Nd-Fe-B powders by RF induction plasma processing. *Rare Metal Materials and Engineering*, vol. 42. pp. 1810–1813.
- ZHOU, W. and WANG, Z.L. 2007. Scanning Microscopy for Nanotechnology: Techniques and Applications. Springer, New York. ◆

Table II

Predicted heating and melting times of Fe in the plasma

Element	t_h (ms)	t_m (ms)	Total time (ms)	Residence time (ms)
Fe	1.31	0.295	1.60	175



Effect of yield strength on wear rates of railway wheels

by V.J. Matjeke*† J.W. van der Merwe†‡, M.J. Phasha*, A.S. Bolokang* and C. Moopanar*

Synopsis

Excessive wear rates on railway wheels can result in rolling-stock derailments. If wear is detected early the possible derailments can be prevented by prematurely replacing wheelsets, although the inventory cost and maintenance downtime remain a challenge. In the current study, wheels were introduced and monitored in-service for two years to investigate the cause of excessive wear rates. The wear rates and stresses were calculated for the wheels suitable for a maximum load of 26 t per axle. Microstructural and mechanical properties were analysed. As expected, the general microstructure of all the wheels tested was pearlitic. Although all the wheels complied with the tensile strength requirements, stress calculations confirmed material distortion on excessively worn wheels whereas trial wheels revealed yield strength exceeding the yield criterion. High wear rates observed on the wheels were a result of low yield strength relative to the load per axle. The typical wear mechanism found was due to a combination of rolling contact fatigue and abrasive brake wear. Despite compliance of the wheels with existing requirements regarding material and mechanical properties (hardness, ultimate tensile strength), it is recommended that the yield strength must also be taken into consideration as a critical parameter.

Keywords

railway wheels, wear rate, yield strength, wear mechanism, rolling contact fatigue.

Introduction

Railway wheels are used to support the wagon mass and guide the wagon along the tracks (Park, 1974). The wheels and rails must be able to tolerate the applied tangential forces in order to effect wagon dynamic performance and reduce material deformation (Ghidini *et al.*, 1994; RSE_TE_SPC_0045, 2011; AAR M107/M 208 Specification, 2011). Over the past ten years, the South African coal wagon maintenance depot has experienced excessive hollow wheel wear rates on the heavy haul line wheels. The maximum load of Jumbo wagons on the coal line is 104 t, or 26 t per axle. Although the maintenance intervention cycle for wheelsets was two years, between February 2011 and August 2012 some wheels experienced excessive hollow wear. Hollow wear is regarded as wear exceeding 2 mm on the central portion of the wheel tread (RSE_TE_SPC_0045, 2011). This happened despite the fact that these wheels were manufactured and certified according to the

requirements of AAR M107/208 standard for carbon steel wheels (AAR M107/M 208 Specification, 2011) and the local wheel RS/ME/SP 021 standard specification (RS / ME / SP / 021 REV 5 (2013)). The AAR standard only specifies a minimum hardness as a required mechanical property and the local standard specifies hardness and minimum tensile strength only. In general, an increase in hardness will improve the rolling/sliding wear resistance of steel. This relationship of hardness and wear resistance was found to be true only in a situation where solid and similar alloys are in contact (Singh, Khatirkar and Sapate, 2015). The sliding wear resistance of a material is usually estimated using Archard's equation (Liu and Li, 2001). This wear mechanism may manifest by crack initiation at the surface and propagation until macroscopic wheel material detachment occurs (Johnson, 1989). Fatigue crack initiation occurs as a result of local plastic deformation (Johnson, 1989; Ekberg, 2001). This plastic deformation and fatigue crack-related detachment forms hollow wear within the wheel/rail interface and progresses over many rolling contact cycles. Lewis and Olofsson (2009) stated that 'severe wear results in a rough, deep torn surface – much rougher than the original metallic wear debris, typical of up to 10 µm'. It was further indicated that there is a

* Transnet Engineering, Research & Development, Kilner Park, Pretoria, South Africa.

† School of Chemical and Metallurgical Engineering, University of the Witwatersrand, Johannesburg, South Africa.

‡ DST-NRF Centre of Excellence in Strong Materials, School of Chemical and Metallurgical Engineering, University of the Witwatersrand, Johannesburg, South Africa.

© The Southern African Institute of Mining and Metallurgy, 2016. ISSN 2225-6253. This paper was first presented at the AMI Ferrous and Base Metals Development Network Conference 2016 19–21 October 2016, Southern Sun Elangeni Maharani, KwaZulu-Natal, South Africa.

Effect of yield strength on wear rates of railway wheels

relationship between crack truncation and wear rate; if the wear rate is high, cracks will probably be worn away before progressing beyond stage A in Figure 1, otherwise the crack becomes unsafe when it reaches point C.

Heat treatment is the most important process for improving wheel rim hardness and subsequently wear resistance (Ekberg, 2001). Residual compressive stresses are introduced in the wheel rim by a rim quenching process during heat treatment that refines the grain structure and as a result improves the wear resistance as well as the resistance to crack initiation (Johnson, 1989). Excessive hollow wear can affect the dynamic behaviour of the railway vehicle and will lead to the increased likelihood of derailments (Lewis *et al.*, 2003). Although the main focus of this paper is on excessive wear rates, wheel-rail interaction is also important. When the contact area between the wheel and rail is small, there is a corresponding high contact stress. Typical contact is made over a quasi-elliptical area with an average diameter of approximately 13 mm (Harris *et al.*, 2001).

This research study was initiated to deepen the understanding of the wear mechanism experienced on the coal line. This will aid efforts to identify and abate the wear rates, as well as in determining combative measures to reduce the wear of the wheels. In order to investigate this, an enhanced understanding of the current operating conditions, wheel mechanical properties, metallographic properties, wear mechanisms and wear regimes is essential.

Background and experimental procedure

Excessively worn wheels

Initially, two batches of wheels that showed high wear rates in-service were declared unroadworthy and were removed from service. Three wheelsets from the two batches were selected for further analysis. The chemistry and tensile properties of these batches were provided by the supplier. Both batches were manufactured by Supplier A (wheel A). The degree of wear was measured using the miniprof wheel rim measurement technique. In addition, microstructural analysis around the excessively worn area on the wheel tread was conducted using optical and scanning electron microscopy (SEM). The hardness results related to the excessively worn wheel test batch were not available. In addition, no further comparative hardness testing could be carried out on the worn wheels due to their condition and profile. However, according to Zang, Li and Zhang, (2011) and Dieter (1988) the hardness of materials often obeys the three times empirical strength relationship of work-hardening

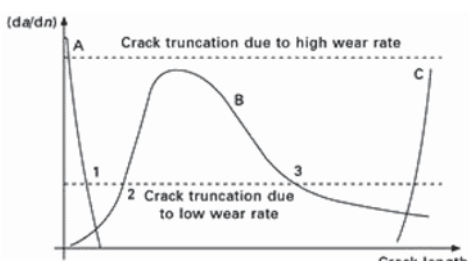


Figure 1—Interaction of fatigue and wear by crack truncation (Lewis and Olofsson 2009)

metals, therefore an extrapolation of material hardness was carried out using the material yield strength.

Ring-fenced wheels

In an effort to further understand the wear mechanism, thirty-two brand-new wheelsets were ring-fenced for trials and monitored for a period of two years on the coal Jumbo wagons. These new wheelsets were supplied by two different companies. The wheels were profiled to the nominal diameter and put in service for wear monitoring. The operating conditions were similar to the conditions that existed in 2011. Sixteen of the 32 wheelsets were manufactured by 'Supplier A' (wheel A) and the other 16 were manufactured by 'Supplier B' (wheel B). Each bogie of the wagon was paired with wheelsets made up of a combination of both wheels A and B. Unfortunately, four wagons were removed due to operational demand and therefore could not complete the trial; and as a result they were excluded from the study. The remaining 16 wheelsets that completed the trial were measured bi-annually.

In addition, a wheel from each supplier was tested to determine the chemistry, microstructural analysis and mechanical properties.

Loading conditions analysis

The wear rate of the tread surface depends on loading conditions, therefore the loading conditions were analysed according to compliance criteria from UIC Code 510-5 (2007) and EN 13103 standards. The applied forces were calculated and the main goal of the two-body contact interface analysis was to determine the magnitude of stresses and deformations.

Results

Excessively worn wheels

The three wheelsets that were removed from service were identified as 8JS6699/024, 8US6855/003 and 8SU6085/046. Wheelset 8JS6699/024 was in service for 9 months while 8US6855/003 and 8SU6085/046 were in service for 18 months.

Chemical composition

The chemical composition of the excessively (abnormal) worn wheels from supplier A is shown in Table I. The chemical composition and mechanical properties were found to be in accordance with the requirements of AAR M107/M 208 and RS/ME/SP 021 specifications, respectively.

Tensile test

The tensile tests results of the quality test batch related to the excessively worn wheels are shown in Table II. These results were found to be satisfactory and compliant with the local specification. The material hardnesses that were extrapolated were found to be approximately 310 HV and 329 HV, (290 HB and 309 HB when converted to Brinell hardness) respectively (Dieter, 1988).

Miniprof wheel measurement of the rim profiles

The rim profile was measured and evaluated according to the requirements of RSE/TE/SPC/0045 (2013). The total average

Effect of yield strength on wear rates of railway wheels

Table I

Chemical composition of the excessively worn wheels, in wt%

	C	Mn	Si	S	P	Al	Ni	Cr	Mo	Cu	Sn	W	Nb	As
Wheel A1	0.68	0.78	0.39	0.01	0.01	0.02	0.13	0.13	0.04	0.16	0.01	0.04	0.01	0.03
Wheel A2	0.69	0.79	0.35	0.01	0.01	0.03	0.11	0.12	0.03	0.20	0.01	0.04	0.01	0.03
AAR M107/208 Grade C Standard	0.67–0.77	0.6–0.9	0.15–1.00	0.005–0.040	0.03*	0.06*	0.25*	0.25*	0.10*	0.35*	0.06*		0.05*	

*Maximum

Table II

Tensile test results of the test batch related to excessive worn wheels

Tensile properties	Wheel A1	Wheel A2	RS/ME/SP 021 grade C specification
Ultimate tensile strength (MPa)	1054	1119	1050 minimum
0.2% yield strength (MPa)	642	660	Not specified
YS:UTS	0.61	0.59	Not specified
% Elongation	15	17	8 minimum
Strain	0.158	0.171	Not applicable
% Reduction area	31	39	Not specified

Table III

Wheelset information and rim profile measurements

Vehicle number	Wheel number	Lifting date	Flange height (mm)	Flange thickness (mm)	Hollow wear (mm)	Flange tip radius (mm)	Flange angle (°)
63655292	T/003 side A	02/2011	34.46	22.74	5.36	7.41	12.53
63655292	T/003 side B	02/2011	32.81	25.57	3.20	7.81	24.22
63655292	U/046 side A	02/2011	32.91	25.54	3.69	7.88	23.79
63655292	U/046 side B	02/2011	32.08	25.27	3.69	8.33	12.88
63655497	G/024 side A	11/2011	35.71	26.33	4.88	8.75	28.28
63655497	G/024 side B	11/2011	34.90	25.12	4.77	7.90	19.27

wear rate was found to be 0.33 mm/month according to the rim profile measurements in Table III. The wear rates were found to be excessive considering that the wheels were in service for a period of 9–18 months.

Figure 2 shows the excessive hollow wear on the wheel rim profiles.

Wheel tread analysis

The treads of the wheels that experienced excessive wear were examined with a stereoscope and optical microscope. The treads revealed fine microscopic cracks, as shown in Figure 3 and Figure 4. The cracking mechanism is similar to that discussed by Lewis and Olofsson (2009); where the wheel surface experiences deformations as a result of cyclic loading, leading to crack initiation which ultimately results in the loss of particles from the surface. Lewis *et al.* (2003) described this phenomenon as ‘ratcheting’.

The general microstructure of the wheel was pearlitic with ferrite embedded on the grain boundaries. The microstructure observed during metallographic examination showed wheel tread plastic deformation of approximately 75 µm (see Figure 5). The wheel tread surface shows a breakage classified as severe wear.

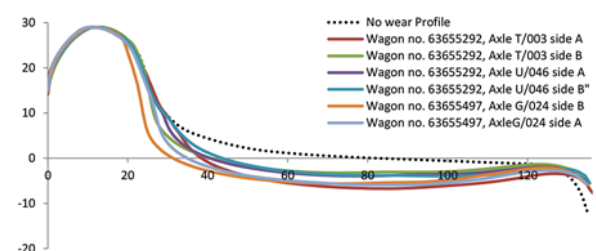


Figure 2—Excessive wheel wear profile



Figure 3—Fine cracks observed on the wheel tread

Effect of yield strength on wear rates of railway wheels



Figure 4—Optical micrograph of cross-section of the un-etched wheel tread showing fatigue cracks

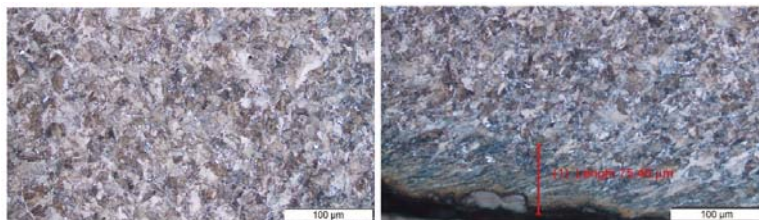


Figure 5—Optical micrograph of the etched wheel tread: (a) pearlite-ferrite microstructure on the wheel rim, (b) the pearlite-ferrite microstructure of the tread

Table IV

Chemical compositions of the wheels related to the wheels on trial, in wt%

Element	C	Mn	Si	S	P	Al	Ni	Cr	Mo	Cu	Sn	W	Nb	As
Wheel A	0.69	0.78	0.33	0.01	0.01	0.02	0.15	0.18	0.04	0.09	0.01	0.04	0.01	0.03
Wheel B	0.73	0.78	0.26	0.01	0.01	0.02	0.10	0.24	0.03	0.21	0.01	0.04	0.01	0.03
AAR M107/208 Grade C Standard	0.67–0.77	0.6–0.9	0.15–1.00	0.005–0.040	0.03*	0.06*	0.25*	0.25*	0.10*	0.35*	0.06*		0.05*	

*Maximum

Figure 6 shows a SEM micrograph detailing the fatigue micro-cracks on the excessively worn wheel.

Analysis of ring-fenced wheels

The metallurgical and mechanical testing results of the two wheels sampled from supplier A and B are presented below.

Chemical composition

Chemical compositions of the trial wheels examined are given in Table IV. The chemical compositions of both wheels conformed to the AAR M107/208 specification. The carbon content of wheel A was 5.5% lower than that of wheel B; this difference is significant given the importance of carbon as an element that influences hardenability.

Tensile strength

The tensile test results are shown in Table V. Results of both wheels complied with the requirements of RS/ME/SP021. The ultimate tensile strength and yield strength of the trial wheels were significantly better than the values for the wheels that experienced excessive wear.

Metallography

Transverse sections of the two wheels sampled from the ring-fenced wheels were prepared for metallographic examination. The general microstructure of the two wheels was pearlitic with ferrite embedded on the grain boundaries (Figure 7).

Hardness testing

A microslice from the rim on the wheels identified for destructive testing was sectioned and prepared for Brinell

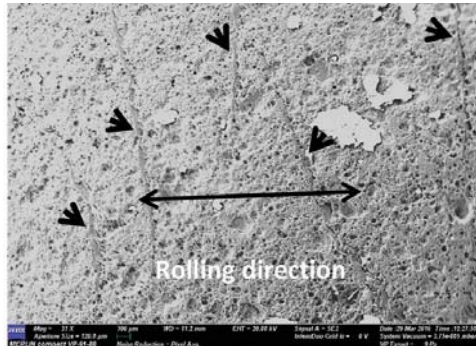


Figure 6—SEM micrograph of the wheel tread showing cracks

Table V

Tensile test results of wheels sampled from ring-fenced wheels

Tensile properties	Wheel A	Wheel B	RS/ME/SP 021 grade C specification
Ultimate tensile strength (MPa)	1223	1185	1050 minimum
0.2% yield strength (MPa)	924	910	Not specified
YS:UTS	0.76	0.77	Not specified
% Elongation	17	16	8 minimum
% Reduction area	35	33	Not applicable

Effect of yield strength on wear rates of railway wheels

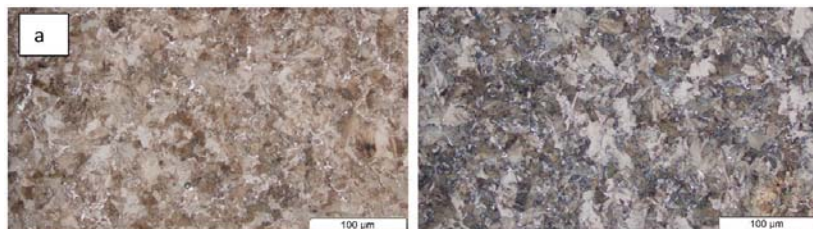


Figure 7—Pearlitic microstructure observed on the rim of (a) wheel A and (b) wheel B, etched with 4% picral

hardness testing. The wheel rim hardness tests were conducted at the positions indicated in Figure 8 and the results are presented in Table VI. All wheels complied with the minimum and maximum hardness requirements of specification RS/ME/SP021 grade C alloy. The hardness measurements were comparable and did not show the effect of the 5.5% carbon variation.

Ring-fenced wheels

Only 16 of the 32 ring-fenced wheelsets were analysed, as mentioned, and the results are discussed below. All the wheels used in the test were manufactured through a forging process.

Miniprof measurements

The results listed in Table VII are the rim profile measurements for the last cycle measurements over a 24-month period.

Of the 16 wheelsets shown in Table VII, 14 of the left-hand side wheels on the wagons were worn more than those on the right-hand side. Only two of the right-hand wheels showed pronounced wear. The hollow wear on trial wheels was satisfactory considering that the average wear rate was 0.06 mm/month and the maximum variation was 0.42 mm per wheelset. Figures 9–12 show the wheel rim profiles per wagon. The wear rates of the trial wheels are significantly lower than the wear rates in Table III.

The asymmetrical hollow wear that was observed on the excessively worn wheels, as originally detected in 2011 and 2012, was indicative of a batch with inferior mechanical properties. The asymmetrical wear on the trial wheels was not as pronounced and as such was deemed normal and acceptable. The high wear rates of the excessively worn wheels also indicate that there is a possibility that the wheel material was of inferior mechanical properties with reference to the trial (ring-fenced) wheels. In general, excessive wear was predominant on wheels identified as wheel type A in 2011 and 2012.

Wheel tread analysis

The tread of the trial wheel shown in Figure 13 was smooth, without signs of the cracks observed on the excessively worn wheels seen in Figure 3. Furthermore, microscopic examination of the wheel tread did not reveal any operation-related defects, except for random micro-spalling seen in Figure 13 and 14. The wear mode was characterized as mild wear. The wheel with high wear rates in Figure 6 showed larger spall marks than the trial wheels in Figure 14 at the same magnification.

Loading conditions and compliance criteria from UIC Code 510-5

This section focuses on wheel load and compliance criteria from UIC Code 510-5 (2007) and BS EN 13103 (2009) standards. The applied forces were calculated on the basis of the value of load Q_g . Load Q_g is defined in the EN 13103 standard as half the vertical force per wheelset on the rail (BS EN 13103, 2009). The main goal of the two-body contact interface analysis was to calculate the magnitude of stresses and deformations. UIC Code 510-5 recommends that for design purposes, three load cases must be considered, namely Load case 1: straight track, Load case 2: curve and Load case 3: negotiation of points and crossings. However, for the purpose of investigating hollow wear only Load case 1 is applicable.

Load case 1

This load case is for a centred wheelset on a straight track as represented by 1 (highlighted) in Figure 15. Equation [1] was used to calculate the loads tabulated in Table VIII.

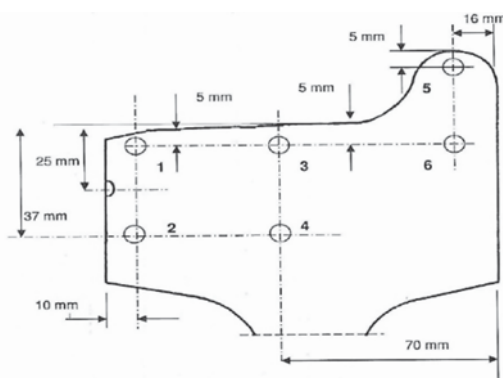


Figure 8—Wheel rim hardness profile

Table VI

Hardness test results

Hardness/ position	Wheel A	Wheel B	Specification RS/ME/SP021 Grade C
1	341	344	
2	347	351	
3	351	341	
4	333	329	321–363
5	341	336	
6	338	321	

Effect of yield strength on wear rates of railway wheels

Table VII

Ring-fenced trial wheel information and rim profile as measured on the last cycle

Wagon no.	Wheel type	Wheel ID	Flange height (mm)	Flange tip radius (mm)	Flange width (mm)	Hollow wear (mm)	Variation	Orientation
63634325	Wheel B	1	30.447	11.105	25.947	1.338	0.00	Left
		2	30.879	11.385	25.831	1.639	0.30	Right
	Wheel A	3	30.148	10.815	26.153	1.274	0.00	Left
		4	30.166	10.881	26.008	1.282	0.01	Right
	Wheel B	5	30.244	11.288	25.897	1.222	0.00	Left
		6	30.599	11.408	25.883	1.559	0.34	Right
	Wheel A	7	30.546	11.254	25.832	1.331	0.00	Left
		8	30.346	10.907	25.713	1.565	0.23	Right
63634317	Wheel B	1	30.246	11.403	25.688	1.535	0.00	Left
		2	30.263	11.299	25.680	1.583	0.05	Right
	Wheel A	3	29.705	10.075	25.794	1.087	0.00	Left
		4	30.569	11.169	25.877	1.390	0.30	Right
	Wheel B	5	30.585	11.528	26.031	1.537	0.00	Left
		6	30.765	11.427	26.041	1.576	0.04	Right
	Wheel A	7	29.934	10.557	26.040	1.168	0.00	Left
		8	31.335	12.092	25.611	1.585	0.42	Right
63634309	Wheel B	1	30.474	11.148	26.025	1.188	0.00	Left
		2	30.455	11.464	26.017	1.452	0.26	Right
	Wheel A	3	30.418	11.198	25.777	1.251	0.00	Left
		4	30.069	11.119	26.180	1.357	0.11	Right
	Wheel B	5	30.116	11.135	25.901	1.119	0.00	Left
		6	30.245	10.673	25.775	1.111	-0.01	Right
	Wheel A	7	30.629	11.449	25.756	1.484	0.00	Left
		8	30.104	11.018	25.983	1.184	-0.30	Right
63634295	Wheel B	1	30.761	11.555	25.961	1.363	0.00	Left
		2	30.458	11.071	25.946	1.588	0.22	Right
	Wheel A	3	30.318	11.145	26.189	1.269	0.00	Left
		4	30.008	11.183	26.092	1.369	0.10	Right
	Wheel B	5	30.302	11.378	25.802	1.255	0.00	Left
		6	30.457	10.989	25.823	1.375	0.12	Right
	Wheel A	7	30.604	11.359	25.981	1.293	0.00	Left
		8	30.366	11.146	25.869	1.557	0.26	Right

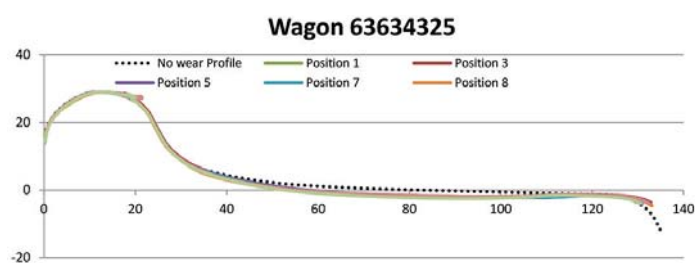


Figure 9—Wear profiles of all wheels on wagon 63634325

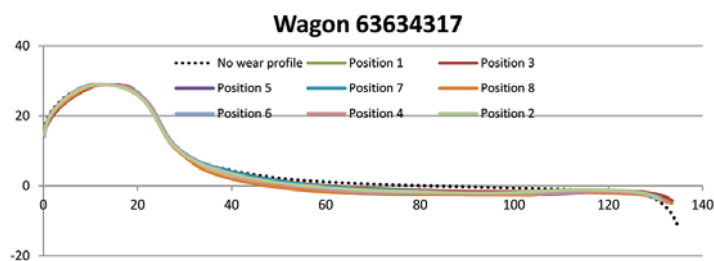


Figure 10—Wear profiles of all wheels on wagon 63634317

Effect of yield strength on wear rates of railway wheels

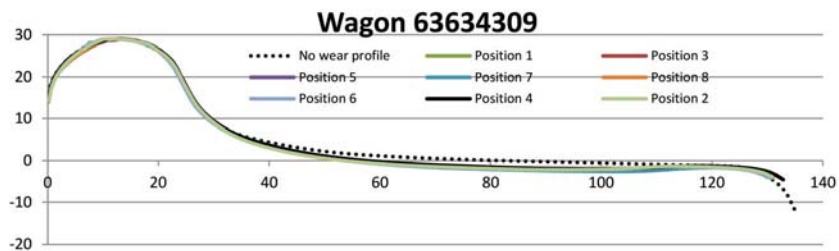


Figure 11 – Wear profiles of all wheels on wagon 63634309

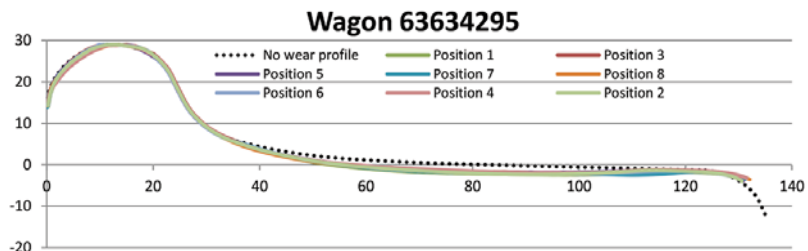


Figure 12 – Wear profiles of all wheels on wagon 63634395

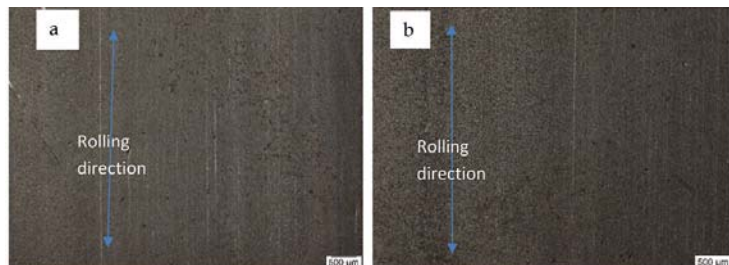


Figure 13 – Typical wheel tread on the trial wheels: (a) wheel A and (b) wheel B

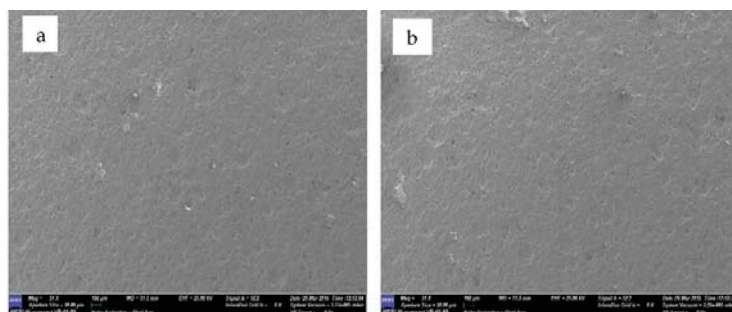


Figure 14 – Trial wheel SEM micrographs: (a) wheel A (b) wheel B

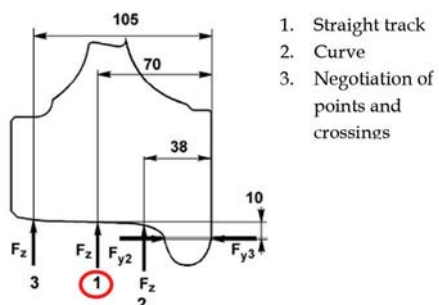


Figure 15 – Load case scenario

Table VIII
Calculated load case forces for 26 t axle load

Description	Value	Unit
Q (per axle)	26	t
Q (per wheel)	13	t
g	9.81	m/s^2
F_{z1}	159 413	N

$$F_{z1} = 1.25Qg$$

$$F_{y1} = 0$$

[1]

Effect of yield strength on wear rates of railway wheels

Hertzian contact stress theory

Hertz (Johnson, 1985) developed a theory to calculate the contact area and pressure between two surfaces and predicted the resulting compression and stress induced on the objects. The principal stresses acting along the x , y , z axes at or below the contact area are σ_x , σ_y and σ_z . The shear stresses acting along the axes at or below the contact area are zero. The current manufacturing specification does not specify the minimum yield strength; however, according to the distortion energy theory, the yield strength is an important property. Harris *et al.* (2001) found that the wheel/rail interaction contact is made over a quasi-elliptical contact patch the size of a small coin of about 13 mm (½ inch) diameter. A minimum diameter of 13 mm was used to calculate the yielding criterion strength for a 26 t per axle load wagon (see Table IX). The results for the excessively worn wheels presented in Table IX show that the yielding criterion exceeded the uniaxial yield strength of wheel A at a contact patch of 13 mm diameter. The elasto-plastic response shown in Figure 16 was extensively analysed by Johnson (1989). The load factor of the excessively worn wheels and the ring-fenced wheels at a maximum contact stress of 1812 MPa are summarized in Table X. Given the interpretation of elasto-plastic behaviour of the wheels at approximately 0.3 coefficient of friction, it is expected that excessively worn wheel A will distort and be more susceptible to both surface fatigue and development of hollow wear in service than the ring-fenced wheels A and B, which showed high yield strength values compared to the values determined by the Von Mises and Tresca criteria.

Discussion

Shear flow on the excessively worn wheels and fatigue micro-cracks suggest a great amount of shear deformation of material on the tread surface. Olofsson *et al.* (2013) found that cyclic loading that leads to wheel surface deformation results in crack nucleation and subsequently removal of material. The excessively worn wheels revealed plastic deformation on the tread that resulted in the initiation of cracks. The wear on the wheels most likely occurred by a form of material detachment at the intersection of cracks. The wear observed in this research occurred by rolling contact fatigue that progressed by the shedding of small particles. The ring-fenced wheels did not exhibit any unusual wear-

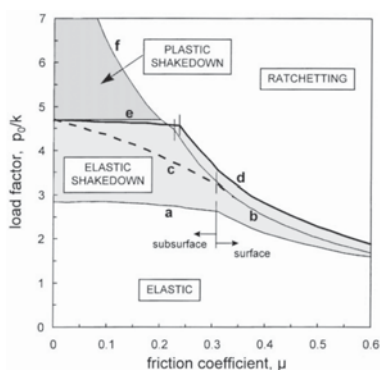


Figure 16—Elasto-plastic limits in sphere contact under repeated sliding condition

Table IX

Yield distortion energy at different contact patch diameters

Average contact diameter (mm)	Area (mm ²)	Stress (MPa)	Max. contact stress	σ_z	σ_x	σ_y	Von Mises yield criterion (MPa)
9	63	2537	3806	3806	2284	2284	1522
11	94	1691	2537	2537	1523	1522	1015
13	132	1208	1812	1812	1088	1088	725
15	176	906	1359	1359	816	816	543
17	226	705	1057	1057	634	634	423
19	283	564	846	846	508	508	338
21	346	461	692	692	415	415	277
23	415	384	577	577	346	346	230
25	490	325	488	488	293	293	195
27	572	279	418	418	251	251	167
29	660	242	362	362	218	218	145
31	754	211	317	317	190	190	127

Table X

Shakedown load factor

Wheel	Maximum contact stress (MPa)	Yield strength (MPa)	Shear Stress (MPa)	Load factor
Wheel A1	1812	660	381	4.8
Wheel A2	1812	642	371	4.9
Wheel A	1812	924	534	3.4
Wheel B	1812	910	525	3.5

Effect of yield strength on wear rates of railway wheels

related defects and since the only difference between the wheels is strength, it is therefore concluded that the wear mechanism is related to the material strength. The tension/shear forces are complicit in the formation of fatigue cracks and material shear deformation.

The test certificate of the wheels showing initial excessive wear revealed a significantly lower yield strength compared to the ring-fenced wheels, although only the ring-fenced wheels satisfied the minimum AAR and local specifications. However, it is worth noting that the yield strength is not a requirement for both specifications. Hardness testing of the excessively worn wheels could not be carried out due to deformations and high wear rates; however, Dieter (1988) reported that empirically the yield strength is three times the hardness of work-hardening materials, therefore the hardnesses of the wheels were extrapolated using the empirical relationship. The converted hardness results did not conform to the minimum requirement of AAR M107/208 and local specification requirements. On the other hand, the Archard wear equation shows that the material surface hardness is inversely proportional to wear resistance and therefore, the likelihood of wear increases with lower hardness (Liu and Li, 2001; Barwell, 1974).

Based on Hertz's theory, the calculated contact area and pressure between wheel and rail predicts plastic deformation on the wheels that ultimately resulted in excessive wheel wear (Barwell, 1974). Stress calculations suggest that the excessively worn wheelsets were exposed to heavy loading, *i.e.* high normal and tangential forces. The ring-fenced wheels' yield strength exceeded the calculated Von Mises and Tresca stresses. The high stress in this instance was determined using a contact patch with an average 13 mm (long diagonal) elliptical diameter.

The ring-fenced wheels showed endurance performance by exhibiting lower wear rates compared to the excessively worn wheels. The lasting performance in the ring-fenced wheels is largely related to the higher yield strength in comparison to the excessively worn wheels.

Conclusion

The high wear rates observed on the excessively worn wheels from supplier A were as a result of low yield strength relative to the load per axle. The typical wear mechanism found here is a combination of rolling contact fatigue and abrasive brake wear. It is recommended that local and AAR specifications should consider minimum yield strength to determine axle load. Furthermore, the development of an optimized heat treatment process aimed at increasing the hardness and yield strength of AAR class C wheel rims will result in a considerable increased wheel life.

Acknowledgements

The wheel profiles used in this report were measured by Georg Hettasch and Victor Ngobeni, who are gratefully acknowledged by the authors.

References

AAR M107/M 208 specification. 2011. Wheels, carbon steel. Association of American Railroads. pp. 1–40.

BARWELL, F. 1974. The tribology of wheel on rail. *Tribology International*, vol. 7. pp. 146–50.

BS EN 13103. 2009. Railway applications — Wheelsets and bogies — Non-powered axles — Design method.

DIETER, G.E. 1988. Mechanical Metallurgy. McGraw-Hill. 243–6, 331.

EKBERG, A. 2001. Anisotropy and rolling contact fatigue of railway wheels. *International Journal of Fatigue*, vol. 23. pp. 29–43.

GHIDINI, A., BELOTTI, G., PATRIOLI, L. et al. 2004. Starting of an innovative line for heat treatment of railways solid wheels and tyres. *Proceedings of the International Wheelset Congress*, University of Illinois, Chicago.

HARRIS, W.J., TOURNAY, H., EBERSÖHN, W. and ZAKHAROV, S.D.L.J. 2001.

Guidelines to best practices for heavy haul railway operations: management of the wheel and rail interface issues. *International Heavy Haul Association*, Virginia Beach, VA. 484 pp.

JOHNSON, K.L. 1989. The strength of surfaces in rolling contact. *Mechanical Engineering Science*, vol. 203, no. 33. pp. 151–163.

JOHNSON, K.L. 1985. *Contact Mechanics*. Cambridge University Press, Cambridge, UK.

LEWIS, R. and OLOFSSON, U. 2009. *Wheel-Rail Interface Handbook*. CRC Press, UK.

LEWIS, R., BRAGHIN, F., WARD, A., BRUNI, S., DWYER-JOYCE, R.S., BEL KNANI, K. and BOLOGNA, P. 2003. Integrating dynamics and wear modelling to predict railway wheel profile evolution. *Proceedings of the 6th International Conference on Contact Mechanics and Wear of Rail/Wheel Systems (CM2003)*, Gothenburg, Sweden, 10–13 June. pp. 7–16.

LIU, R. and LI, D.Y. 2001. Modification of Archard's equation by taking account of elastic / pseudoelastic properties of materials. *Wear*, vol. 251. pp. 956–64.

OLOFSSON, U., ZHU, Y., ABBASI, S., LEWIS, R. and LEWIS, S. 2013. Tribology of the wheel-rail contact – aspects of wear, particle emission and adhesion. *Vehicle System Dynamics*, vol. 51, no. 7. pp. 1091–1120.

PARK, S. 1974. The tribology of wheel on rail. *Tribology International*, vol. 2. pp. 146–50.

RSE_TE_SPC_0045. 2011. Geometric requirements for new, reprofiled and in-service wheelsets.

RS / ME / SP / 021 REV 5. 2013. Transnet freight rail specification for the supply of wrought wheels for tractive and trailing stock.

SINGH, K., KHATIRKAR, R.K. and SAPATE, S.G. 2015. Microstructure evolution and abrasive wear behavior of D2 steel. *Wear*, vol. 328. pp. 206–216.

UIC 510-5. 2007. Technical approval of monoblock wheels.

ZHANG, P., LI, S.X. and ZHANG, Z.F. 2011. General relationship between strength and hardness. *Material Science and Engineering A*, vol. 529. pp. 62–73.◆



KEYNOTE SPEAKERS AND TOPICS

Leadership

Davis Cook, CEO,
Research Institute for
Innovation and Sustainability

Innovation

Gary Lane, Co-founder
and Group CEO, NXGN

Professional Development

Nosipho Siwisa-Damasane, CEO
- Richards Bay Coal Terminal
Thabile Makgala, Vice President -
Gold Fields

BACKGROUND

It is recognised that we live in an era characterised by accelerated change, overwhelming complexities and tremendous competition, all of which result in considerable uncertainty about the future. The challenge for young professionals in this time is to create a vision for mining in Africa that will inspire confidence for the future. Young professionals must create a roadmap that describes the steps necessary to realise the vision. In setting the strategic direction to achieve the vision, these are a few of the questions that must be answered:

- What are the policies that should be developed and implemented to transform the status quo to the envisioned mining environment?
- What are the technical solutions that need to be pursued?
- What are the human capital needs that must be satisfied?
- What are the economic conditions required?

This conference will provide a platform for young professionals to interact with peers and industry thought leaders to drive the dialogue towards unlocking the future of the African minerals industry.

HOW TO REGISTER

Complete the registration form and return to
anna@saimm.co.za or camielah@saimm.co.za

Take advantage of the Early Bird registration discount.
Book before 2 February 2017 to qualify.

WHO SHOULD ATTEND

This conference should be of value to all professionals across the entire minerals industry value chain, including:

- Exploration
- Geology
- Mining
- Mineralogy
- Geotechnical engineering
- All metallurgical fields
- SHE practitioners
- Industrial relations and community involvement

EXHIBITION/SPONSORSHIP

Sponsorship opportunities are available. Companies wishing to sponsor or exhibit should contact the Conference Co-ordinator.



Premature failure of re-sulphurized steel studs

by E. Molobi*

Synopsis

Studs are rods threaded on both ends and are used as mechanical fasteners for two or more components. Stud finds usage in industries such as automotive, construction and aviation. The advantage of studs is that they allow for disassembly of components during maintenance. Studs are continuously subjected to both tensile and shear stresses, depending on the application, therefore they should be manufactured from suitable materials that are capable of withstanding all these external forces. Studs are sometimes manufactured from re-sulphurized steel due to its improved machinability; however, there is a certain limit on the amount of sulphur, above which failure may occur. Premature failure of studs has been a common problem, but failed studs are commonly replaced with new ones without conducting failure investigations. The present work investigates the premature failure of two re-sulphurized steel studs used on a rocker arm assembly and recommends alternative materials. The investigation was carried out by conducting visual examination, microstructural analysis, hardness measurements, chemical analysis and a detailed scanning electron microscopy (SEM) investigation on the fracture surface.

Keywords

re-sulphurized steel, threaded fasteners, failure analysis, fatigue failure, manganese sulphide.

Introduction

Two rocker arm studs used on a 16-cylinder diesel locomotive engine failed prematurely after being in service for less than 5 months. The rocker arm studs had a life-cycle of 5 years. The studs were manufactured from re-sulphurized steel. The paper aims to establish whether re-sulphurized steel is applicable for the manufacture of studs in the automotive industry.

Background

Locomotives are classified as either electric or fuel-powered. Diesel locomotives are an example of fuel-powered locomotives. This type of locomotive uses a diesel engine as a means for propulsion. An engine converts chemical energy into mechanical energy required for traction. In an internal combustion engine a rocker arm is an oscillating lever that conveys radial movement from the cam lobe into linear movement to open and close poppet valves of cylinders (Husain and Sheikh, 2013). The rocker arms are secured on to the cylinder head by rocker arm studs.

During operation of the engine, stresses and vibrations are encountered leading to rocker arm stud deflection (Ridgeway, 1975). The deflection of rocker arm studs causes inefficiency in engine operation and gradually leads to metal fatigue and hence stud breakage or disengagement of the stud from the cylinder head due to loosening (Ridgeway, 1975). However, the latest designs incorporate a housing or adapter cover as a restraining means to prevent stud deflection (Ridgeway, 1975).

Incorrect torqueing of a rocker arm stud can lead to premature failure due to uneven stresses on the component (Roberts, 1997). Torqueing below the minimum requirements would lead to deflection and vibration of the stud, thus leading to fatigue damage and over-torqueing would lead to loss of compression and warpage of the stud (Roberts, 1997). However, the material of the stud also plays a vital role in sustaining the deflection, vibrations and stresses acting on the studs during operational service.

Re-sulphurized steel has found usage in the production of threaded components such as studs, bolts and screws, mainly to enhance machinability and in applications that require low tensile strength material.

Literature review

A stud is a relatively long rod that is threaded on both ends (Wikipedia, 2016), that is designed to be used in tension. Studs are used for joining parts to cast components. The tensile strength of cast iron is very low and excessive tightening of a set screw into a cast

* Transnet Engineering, Product Development, Rotating Machines.

© The Southern African Institute of Mining and Metallurgy, 2016. ISSN 2225-6253. This paper was first presented at the AMI Ferrous and Base Metals Development Network Conference 2016 19–21 October 2016, Southern Sun Elangeni Maharani, KwaZulu-Natal, South Africa.

Premature failure of re-sulphurized steel studs

iron thread may cause the thread to crumble, thus permanently damaging the casting (Jayendran, 2007). Studs are first screwed into the casting and tightening is done using mild steel nuts. Any damage due to excessive tightening will be to the stud or nut and not the casting. Studs are used to ensure gas-tight and watertight joints in applications where heavy pressures are encountered (Jayendran, 2007). A typical stud connection is shown in Figure 1.

In many cases, threaded fastener joints are the weakest elements in a structure or mechanism (Toribo *et al.*, 2010). This is because threads act as stress raisers and lead to easy crack initiation. The failure modes of threaded fasteners such as studs are: (i) overload, (ii) lack of locking mechanism, which cause the studs to become loose, (iii) fatigue failure, (iv) improper torque, (v) improper design, (vi) improper manufacture and (vii) corrosion failure (Roberts, 1997). Fatigue seems to be one of the most common problems and this can be due to insufficient pre-load, loosening, inadequate design considerations and material problems (Toribo *et al.*, 2010).

Threaded fasteners are generally made from low- to medium-carbon steel, but other tough inexpensive metals may be substituted such as stainless steel, brass, nickel alloys, or aluminium alloy. The quality of the metal used is important in order to avoid cracking. Stud threads may be machined or rolled; in cases where machining is used the materials machinability becomes of utmost importance. Free-cutting steels are normally used in applications that require good machinability. Machinability of steels is dependent on hardness, chemistry, microstructure and the mechanical state of the metal (Stephenson and Agapiou, 2006).

Sulphur, phosphorus and lead are added to steel to enhance machinability. Sulphur does not alloy with the iron in steel but combines with the manganese to form sulphide inclusions (Bramfitt and Benscoter, 2002), as sulphur cannot form a solid solution with steel and thus remains as insoluble inclusions in the matrix. Manganese sulphide behaves as a solid lubricant, by coating and lubricating the rake face of the machining tool, hence reduces friction, tool chip temperature and tool wear (Bramfitt and Benscoter, 2002).

Although re-sulphurized steels are beneficial for machinability, the addition of sulphur adversely affects other mechanical properties such as corrosion resistance, ductility, toughness, formability and weldability (Stephenson and Agapiou, 2006).

The stresses acting on threaded fasteners include both a tensile and a shear component (Grove, 2007). Once a threaded fastener is tightened, it is loaded in tension and the fastened parts in compression. In addition, the forces acting on the fastened parts may be acting in opposite directions, resulting in a shear stress on the threaded fastener cross-section. Figure 2 shows typical forces acting on a threaded fastener.

Experimental method

The fracture surfaces of studs A and B were examined visually. The condition of the stud threads was also examined. Magnetic particle inspection was carried out by use of a magnetic yoke and magnetic particles on a white background for crack detection. Chemical analysis was carried out by mass spectrometry. Hardness measurements were conducted using a Brinell hardness meter under a load of 3000 kg and with a 10 mm ball indenter. Metallographic samples were sectioned from studs A and B and mounted in a resin for easy handling. Following mounting, the sectioned samples were ground and polished and etched with 2% nital for microstructural analysis. The fractography of studs A and B was analysed by scanning electron microscopy (SEM) using energy dispersive X-ray (EDX) spectrometry to quantify and identify the inclusions present.

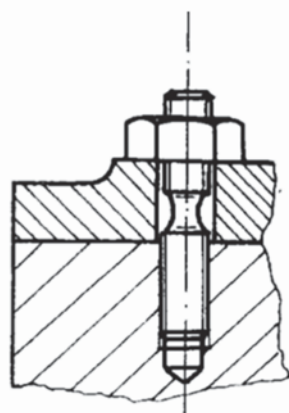


Figure 1—Stud connection (Jayendran, 2007)

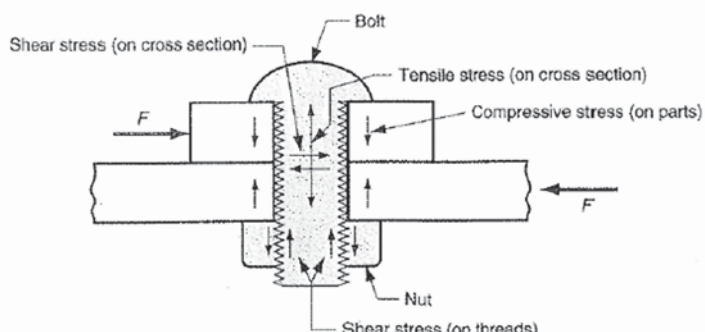


Figure 2—Typical stress acting on a threaded fastener (Grove, 2007)

Premature failure of re-sulphurized steel studs

Results and discussion

Visual examination

Visual examination entailed examination of the stud threads and fracture surface. Contact marks were observed on both studs A and B (Figures 3 and 4); these contact marks could have been formed either before or after stud fracture and could be due to loosening or under-torqueing of the studs. Necking in the longitudinal axis of the studs was not evident and no thread wear or thread mechanical damage was visible. Lack of necking shows that stud over-torqueing was unlikely to be the cause of failure.

The fracture surface of stud A (Figure 5) was perpendicular to the stud axis. Mechanical damage and metal smearing was observed close to the stud peripheral, hence the failure origin could not be established. The roughness of the fracture surface was not uniform and the overload region displayed material tearing. The change in roughness of the fracture surface is one of the indications of fatigue failure. Progression marks were not observed on the fracture surface and final fracture occurred in approximately the 5 o'clock to 7 o'clock position. Lack of progression marks indicates that the load did not vary during the life of the crack. Cracking and material tearing was also observed. The final fracture displayed a ductile mode of failure.

The fracture surface of stud B (Figure 6) was perpendicular to the stud axis. Ratchet marks were observed in the 10 o'clock to 1 o'clock position (Figure 6 and 7); these are



Figure 3—Failed rocker arm, stud A, 0.5 \times

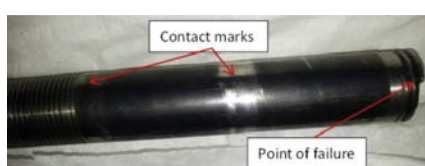


Figure 4—Fracture plane of stud B perpendicular to stud length, 0.8 \times

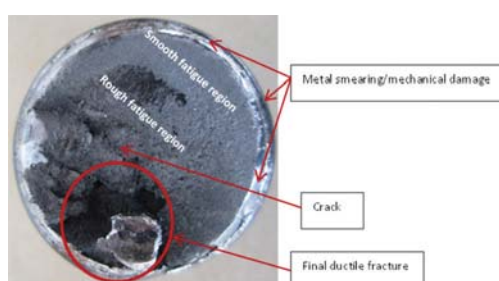


Figure 5—Fracture surface of stud A, 2.4 \times

indicative of fatigue failure. Progression marks were not evident. A shear lip was evident in the 4 o'clock to 7 o'clock position, which is the point of final fracture and cracks were also observed on the fracture surface. The presence of a shear lip may indicate a ductile failure mode. Mechanical damage was also present in areas of the fracture surface, hence the difference in surface roughness of the fracture surface could not be observed.

The threads of both stud A and B showed no evidence of mechanical damage except for the thread in which failure occurred. No progression marks were observed on either stud; hence it is unlikely that the failure was due to stud under-torqueing. The stress level during crack growth did not vary, which is unexpected of a loose stud. The presence of ratchet marks on stud B is evidence of multiple crack origins; however, the final fracture was less than 50% of the surface area of the fracture, hence it is evident that the stress at the time of failure was low. Ratchet marks indicate the presence of stress raisers.

Magnetic particle inspection (MPI)

Magnetic particle inspection revealed cracks on stud B (Figure 8). The crack observed on the fracture surface of stud B (Figure 6) was continuous in the longitudinal direction of the stud.



Figure 6—Fracture surface of stud B, 0.92 \times



Figure 7—Ratchet marks on stud B, 0.64 \times

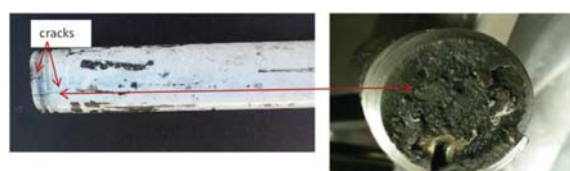


Figure 8—Cracks revealed in stud B following magnetic particle inspection, 1.2 \times

Premature failure of re-sulphurized steel studs

Chemical analysis and hardness properties

Samples were sectioned from studs A and B for spectrometric analysis. Mass spectrometry was used to analyse the chemical composition of the studs. The analysis is shown in Table I. The elemental analysis complied with the requirements of a re-sulphurized steel according to specification SAE 1144. Re-sulphurized steels contain significant quantities of sulphide stringers, which reduce their resistance to fatigue (Bramfitt and Benscoter, 2002) and are not acceptable for use in high-stress and high-cycle vibration fatigue applications, such as studs (Grove, 2007).

The Brinell hardness of stud A and stud B was measured to be 257 and 259, respectively.

Re-sulphurized steels contain particulate phases that reduce their resistance to fatigue (ASTM E45, 2013) and are not acceptable for use in high-stress and high-cycle vibration fatigue life, such as stud fasteners (Smith, 1994). These steels can safely be used in low-ductility applications.

Table I

Chemical analysis and hardness properties of the studs

Element/property	Stud A	Stud B	Specification SAE 1144
Carbon	0.44	0.40	0.40–0.48
Manganese	1.61	1.54	1.35–1.65
Silicon	0.19	0.32	—
Sulphur	0.31	0.32	0.24–0.33
Phosphorus	0.012	0.014	0.04 max.
Chromium	0.09	0.09	—
Copper	0.11	0.12	—
Nickel	0.08	0.04	—
Hardness (10/3000HB)	257	259	217 min

Metallographic examination

The microstructural analysis showed both studs to be composed of pearlite in a ferritic matrix. Level 5 sulphide inclusions were present throughout the ferritic matrix in accordance with specification ASTM E45 (2013). The presence of sulphide stringers indicates that the studs were hot-rolled. Figures 9 to 11 show optical micrographs of studs A and B.

Scanning electron microscopy

The fracture surface of stud A was cleaned using acetone and dried before examination under SEM. The fractography displayed material tearing with numerous cracks, which is characteristic of a ductile dimple fracture mode (Figure 12).

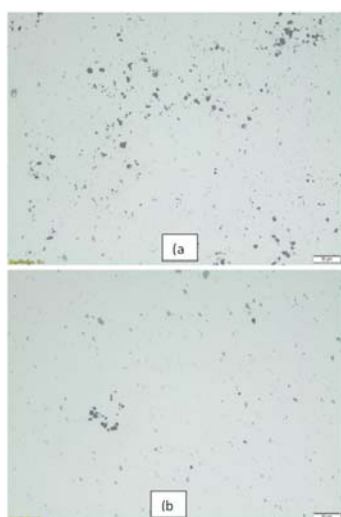


Figure 9—Inclusions in the transverse view: (a) stud A, (b) stud B



Figure 10—Inclusions in the longitudinal view: (a) stud A, (b) stud B



Figure 11—Ferrite pearlite microstructure: (a) stud A, (b) stud B

Premature failure of re-sulphurized steel studs

The cracks and tearing originated from inclusions, which were also present close to the stud surface (Figure 13 and Figure 14a). EDX analysis was conducted to identify and quantify the elemental composition of the inclusions; the EDX positions are shown in Figure 14b. The analysis revealed the inclusions to be MnS (manganese sulphide); results are shown in Table II.

The crack observed on the fracture surface of stud B (Figure 6) was opened (Figure 15) and the crack fracture surface was analysed using SEM. Elongated inclusion stringers were present in the longitudinal direction of the stud (Figure 16) and the fracture surface had a 'woody' appearance, as shown in Figure 15. EDX analysis was conducted on the inclusion stringers to determine and quantify the chemical composition; the EDX positions are shown in Figure 17. EDX revealed the stringers of inclusions to be MnS (Table III). The MnS stringers were elongated in the stud rolling direction; which indicates that the studs were hot-rolled and confirms the pearlitic structure in the ferrite matrix. Sulphur is deformable at high temperatures and

becomes elongated during forming processes such as rolling (Cyril, Fatemi and Cryderman, 2008).

Stringers of MnS inclusions are known to have adverse effects on the mechanical properties of a component, provided that the inclusions are not aligned with the loading direction (Cyril, Fatemi and Cryderman, 2008). Shear stress

Element	Spectrum			
	1	2	3	5
Oxygen	1.07	1.03	2.31	3.44
Aluminium	-	-	0.19	-
Silicon	-	-	0.22	-
Sulphur	34.30	30.87	14.07	22.59
Manganese	57.58	61.84	22.27	33.06
Iron	7.05	6.26	60.95	40.90

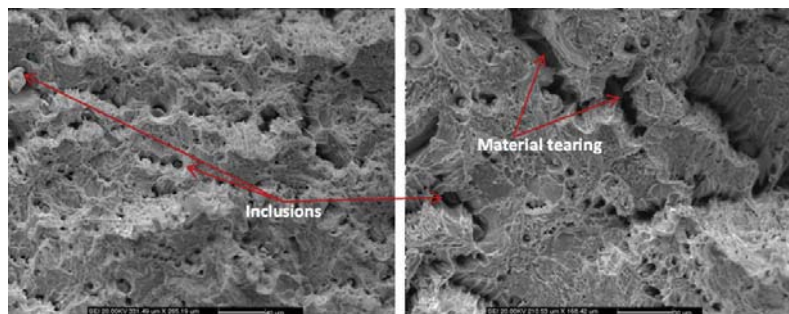


Figure 12—Fractography showing material tearing and inclusions in stud A

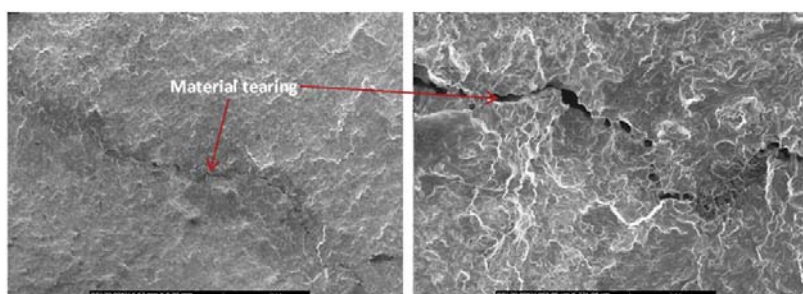


Figure 13—Internal cracking in stud A

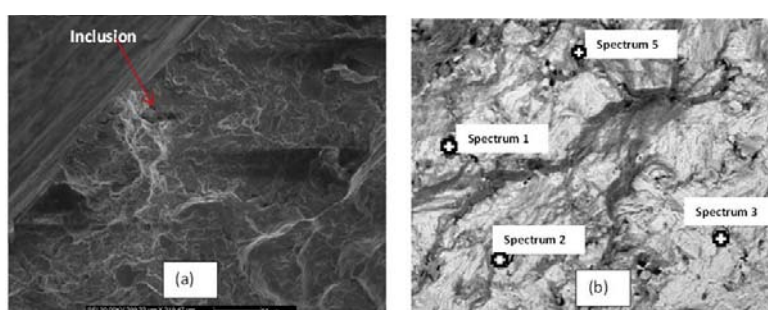


Figure 14—(a) Inclusion close to the surface in stud A, (b) EDX positions

Premature failure of re-sulphurized steel studs

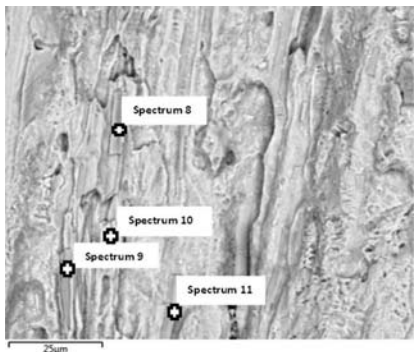


Figure 17—Point locations for EDX analysis

Table III

EDX analysis (mass %) of the inclusion stringers in stud B

Element	Spectrum			
	8	9	10	11
Oxygen	2.15	1.27	1.36	1.50
Sulphur	27.01	31.99	22.69	30.09
Manganese	49.60	53.92	41.67	49.21
Iron	21.24	12.82	34.28	19.21

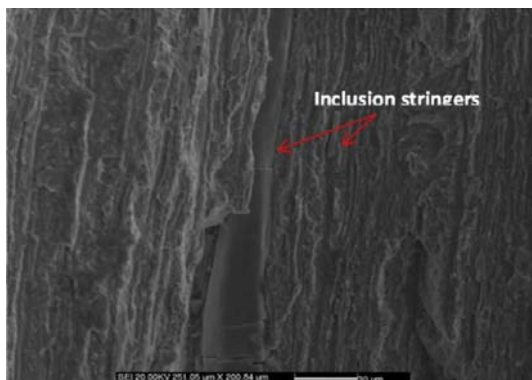


Figure 16—SEM image of opened crack fracture surface with inclusion stringers

perpendicular to the stud axis is present due to the components being joined. It is thus expected that the fatigue properties in the transverse direction of the stud will deteriorate as compared to those in the longitudinal direction. It is probable that the studs failed from fatigue loading caused by the transverse shear stresses, with MnS inclusions as the initiation points, which reduced the fatigue strength of the studs.

Conclusions and recommendations

- The presence of MnS (manganese sulphide) inclusions reduces resistance to fatigue in the transverse direction
- The lack of necking proved that over-torqueing could not have been the cause of failure

- The lack of progression marks and mechanical damage on the rest of the threads suggests that under-torqueing is unlikely to be the cause of failure
- The most probable cause of failure is the presence of large MnS inclusions, which acted as initiation points for fatigue failure. Both transverse shear forces and longitudinal tensile forces could have led to failure
- Re-sulphurized steels are used for applications such as screws, which are subjected to low loads, but are not suitable for high-load application components such as these studs
- It is recommended that studs be manufactured from materials with good strength, hardness and impact properties regardless of anisotropy. These include chromium-nickel steels, which have increased toughness and strength.

References

- ASTM E45. 2013. Standard Test Methods for Determining the Inclusion Content of Steel. Vol. 03.01. Materials Park, OH. pp. 1–19.
- BRAMFITT, B.L. and BENSCOTER, A.O. 2002. Metallographer's Guide: Practice and Procedures for Irons and Steel. 4th edn. ASM International, Materials Park, OH.
- CYRIL, N., FATEMI, A. and CRYDERMAN, B. 2008. Effects of sulfur level and anisotropy of sulfide inclusions on tensile, impact and fatigue properties of SAE 4140 steel. *SAE International Journal of Materials and Manufacturing*, vol. 1, no. 1. pp. 218–227.
- GROOVE, M.P. 2007. Fundamentals of Modern Manufacturing. 3rd edn. Wiley.
- HUSAIN, S.M. and SHEIKH, S. 2013. Rocker arm: a review. *International Journal of Innovative Research in Science*, vol. 2, no. 4. pp. 1120–1126.
- JAYENDRAN, A. 2007. Joining of Metals by Mechanical Methods. 1st edn. Springer.
- RIDGEWAY, R.H. 1975. Rocker arm stud support device. US patent 3870024.
- ROBERTS, C. 1997. The consequences of bolt failures. <http://www.crobers.com/bolt.htm> [accessed 23 May 2016].
- SCHMIDT, F.E., HINEMAN, M.A. and SCHMIDT, B.F. 2014. Improper materials selection in motorcycle stud bolt. *Microscopy and Microanalysis*, vol. 20, no. S3. pp. 1856–1857.
- SMITH, E.H. 1994. Mechanical Engineer's Reference Book. 12th edn. Butterworth-Heinemann.
- STEPHENSON, D.A. and AGAPIOU, J.S. 2006. Metal Cutting Theory and Practice. 2nd Edn. Taylor and Francis.
- TORIBO, J., GONZALEZ, B., MATOS, J.C. and AYASO, F.J. 2010. *Analysis of Failure Paths in Steel Bolted Connections*. University of Salamanca. pp. 521–528.
- WIKIPEDIA. 2016. Studs. https://en.wikipedia.org/wiki/threaded_rod [accessed 23 May 2016]. ◆



Deformation behaviour of aluminium low-micron MMCs and MMNCs at warm working temperatures (0.3–0.5 T_m)

by Z. Gxowa*†‡, L.H. Chown†‡, G. Govender* and U. Curle*

Synopsis

This work evaluates the deformation behaviour, at warm working temperatures, of green particle-reinforced aluminium composites produced by powder blending in a high-energy ball mill. The work focuses on metal matrix composites (MMCs) based on the 2124-Al alloy, reinforced with 10 or 15 vol.% SiC and metal matrix nanocomposites (MMNCs) based on the 2124-Al alloy, reinforced with 5 or 10 vol.% Al₂O₃. Three batches for each powder were blended and powder properties such as particle size distribution (PSD) and shape were consistent after blending. It was observed that a more uniform distribution of the reinforcement phase in the aluminium alloy matrix was achieved in 2124-Al/Al₂O₃ than in 2124-Al/SiC composites. The powders (unreinforced 2124-Al and blended) were initially over-aged at 350°C for 2 hours to reverse any natural ageing that may have occurred prior to use. The over-ageing was incorporated to improve compressibility of the powders with the aim of achieving green compacts with higher integrity. Uniaxial compression tests performed at ambient temperature on a Gleeble® 3500 thermomechanical simulator were unsuccessful as the green compacts fragmented. Engineering stress-strain curves showed that green compacts of unreinforced 2124-Al, 10%SiC MMC and 5%Al₂O₃ MMNC deformed in a similar manner at ambient temperature and had the same compressive fracture stress of approximately 170 MPa. When the deformation temperature was increased from ambient to warm working temperatures (170–280°C) it was observed that electrical resistance heating (the heating mode of the Gleeble®) of unreinforced Al alloy, MMC and MMNC green compacts did not occur. This was attributed to the high electrical conductivity of aluminium, which resulted in poor heat generation due to the low electrical resistance in the samples. It was presumed that the small sample size ($d=8$ mm, $h=12$ mm) also caused rapid heat loss. After further experimentation, the green compacts were heated successfully by insulating the samples to retain heat. It was found that at 280°C, increasing the soaking time from 6 to 20 minutes decreased flow stress and improved plastic flow in the 2124-Al/10%SiC green compact.

Keywords

metal matrix composites, metal matrix nanocomposites, 2124-Al alloy.

Introduction

The automotive and aerospace industries have been interested in metal matrix composites (MMCs) and metal matrix nanocomposites (MMNCs) due to the growing demand for lightweight, high-performance materials (Mazen and Emara, 2004). MMCs and MMNCs have been considered as replacements for conventional metals and alloys because they have higher stability at elevated temperatures, good strength-to-mass ratios and superior wear resistance, along with high stiffness and strength (Zhou *et al.*, 1999).

The mechanical properties of composite products are influenced mainly by the distribution of reinforcing particles in the matrix and the strength of the interfacial bonds between reinforcing particles and the matrix (Liang *et al.*, 1992). The ideal composite has an even distribution of the reinforcement phase throughout the matrix (Ferry, 2005), but generating this is a challenge when fabricating both MMCs and MMNCs. In MMCs, the micrometre-sized reinforcing particles tend to settle on the grain boundaries and in MMNCs the nano-sized reinforcing particles form agglomerates (Borgonovo and Apelian, 2011; Casati and Vedani, 2014).

Secondary deformation processes such as extrusion, forging, rolling and drawing may be used to improve the reinforcing particle distribution, thereby enhancing mechanical properties such as hardness and strength (Hirianiah *et al.*, 2012). These deformation processes are usually carried out at high temperatures since more deformation can be achieved due to the increased plastic flow (Saravanan and Senthilvelan, 2015). However, operating at high temperatures has the disadvantages of high energy costs, reduced equipment and tool life, poor surface finish and low dimensional accuracy (Rajput, 2007). These disadvantages mean that hot-worked MMC and MMNC components are expensive and thus are unattractive to industry.

* Materials Science and Manufacturing, Council for Scientific and Industrial Research (CSIR).

† School of Chemical and Metallurgical Engineering, University of the Witwatersrand, Johannesburg, South Africa.

‡ DST-NRF Centre of Excellence in Strong Materials, hosted by University of the Witwatersrand, Johannesburg, South Africa.

© The Southern African Institute of Mining and Metallurgy, 2016. ISSN 2225-6253. This paper was first presented at the AMI Ferrous and Base Metals Development Network Conference 2016 19–21 October 2016, Southern Sun Elangeni Maharani, KwaZulu-Natal, South Africa.

Deformation behaviour of aluminium low-micron MMCs and MMNCs

Warm working has been shown to have some advantages over both cold and hot working (Rao *et al.*, 1999).

Advantages of warm working over cold working include (Cavaliere, 2002):

- Less strain hardening – fewer annealing operations
- Increased plastic flow – lower loads are required
- Higher metal ductility.

Warm working has lower processing costs than hot working due to the lower energy requirement, longer equipment and tool life and better dimensional accuracy and surface finish (Cavaliere, 2002). Operating at warm working temperatures may thus decrease processing costs while still producing high-quality products (Jensrud, 1998).

In this work, the deformation behaviour, at warm working temperatures, of particle-reinforced aluminium composites produced by powder blending in a high-energy ball mill was evaluated through uniaxial compression tests performed on a Gleeble® 3500 thermomechanical simulator.

Experimental procedure

A Simoloyer CM-01® 2L horizontal high-energy ball mill was used to blend 2124 aluminium alloy (45–90 µm) powder (the matrix material) with reinforcing powders to form:

- *Low-micron aluminium metal matrix composites* with 10 or 15 vol.% SiC (1–10 µm) as the low-micron reinforcement
- *Metal matrix nanocomposites* with 5 or 10 vol.% Al₂O₃ (40–70nm) as the nano-sized reinforcing phase.

Three batches of 2124 aluminium alloy powder with Al₂O₃ (MMNC) and three with SiC (MMC) powder were blended to assess the consistency of blending. The powders were characterized by particle size and shape analysis using a Microtrac Bluewave® and were visually assessed by scanning electron microscopy (SEM) on a JEOL JSM 6510®. The unreinforced aluminium alloy powder and the blended powders were then cold-compacted, *i.e.* at ambient temperature, into cylindrical green compacts with a diameter of 8 mm and height of 12 mm in preparation for the uniaxial compression tests.

The initial cold compaction trials of both the unreinforced aluminium alloy powder and blended powders were challenging as the green compacts fractured into horizontal slices. This was attributed to natural ageing of the Al alloy powder due to long-term storage. The powders (unreinforced 2124-Al and blended) were then over-aged at 350°C for 2 hours, which improved their compressibility and resulted in green compacts with better consolidation and no surface cracks. The deformation behaviour of the unreinforced 2124 aluminium alloy, MMC and MMNC green compacts was evaluated by performing uniaxial compression tests on a Gleeble 3500® thermomechanical simulator at approximately 25°C and 280°C, a total strain of 0.1 and a strain rate of 0.01 s⁻¹. The green compacts were soaked for 6 minutes before compression. The soaking time was then increased to 20 minutes for the MMC green compact with 10 vol.% SiC to evaluate the effect of soaking time on deformation behaviour.

Results and discussion

Three batches (referred to as batch 1, 2 and 3) of each powder were blended, which helped to assess if the properties that were obtained after blending were consistent.

Blending

5 vol.% Al₂O₃

SEM micrographs of MMNC blended powders with 5 vol.% Al₂O₃ from three batches at 500× magnification are shown in Figure 1. From these images it can be observed that there are lighter, finer Al₂O₃ particles on the surface of the coarser, spherical 2124-Al alloy powder particles. The three batches have a relatively uniform distribution of Al₂O₃ particles on the aluminium alloy particles. Figure 1a shows that some of the aluminium alloy particles have changed shape and some have fractured into smaller particles. The change in particle shape can be attributed to plastic deformation that occurred during blending.

10 vol.% Al₂O₃

Figure 2 shows a similarly uniform distribution of Al₂O₃ nano-sized particles on the 2124-Al powder particles, despite the 5 to 10 vol.% increase in Al₂O₃. This finding contradicts results found in liquid-state processing, where Borgonovo and Apelian (2011) found that the tendency of nanoparticles to form agglomerates increased as their volume fraction in the matrix increased. The even distribution found in this work (Figure 2) can be attributed to good blending parameters, as well as the fact that any particle clusters that may have formed were ground as the blending process progressed. This positive result is an indication that the problems of agglomeration encountered in liquid-state processes could be averted by using solid-state techniques.

10 vol.% SiC

The micrographs in Figure 3 show that all three 10% SiC batches contained spherical 2124-Al alloy particles surrounded by small, irregularly shaped SiC particles. As only a small amount of the SiC particles coated the 2124-Al alloy particles and a large amount of the SiC particles were loose, it can be inferred that the SiC powder did not blend fully with the aluminium alloy powder. This poor blending was attributed to poor surface interaction between SiC and the 2124-Al alloy particles.

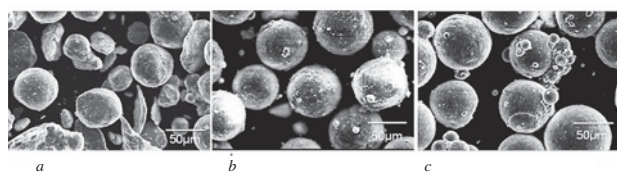


Figure 1—MMNC blended powders with 5 vol.% Al₂O₃ from (a) batch 1, (b) batch 2 and (c) batch 3

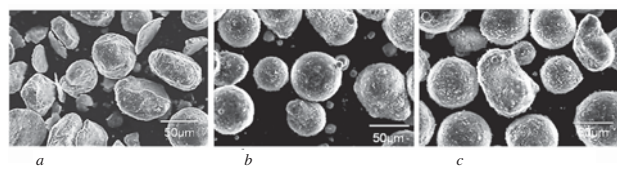


Figure 2—MMNC blended powders with 10 vol.% Al₂O₃ from (a) batch 1, (b) batch 2 and (c) batch 3

Deformation behaviour of aluminium low-micron MMCs and MMNCs

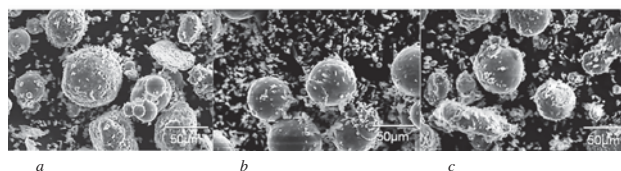


Figure 3—MMC blended powders with 10 vol.% SiC from (a) batch 1, (b) batch 2 and (c) batch 3

Powder characterization

The mode of the particle size distribution (PSD) for the unreinforced 2124-Al alloy powder was 74 µm. Figure 4a shows that the addition of 5 vol.% Al₂O₃ to the 2124-Al powder caused no difference to the shape or mode of the PSD curves for batches 2 and 3 (mode of 74 µm), but the mode of batch 1 was 62.23 µm, indicating breakage of some 2124-Al particles. There was less scatter with 10 vol.% Al₂O₃ addition (Figure 4b) with PSD modes of batches 2 and 3 between 62 and 74 µm and the mode of batch 1 at 62 µm.

The 2124-Al/SiC powder batches had bimodal size distributions (Figure 5), shown by two peaks on the PSD curves, with the major peaks very close to that of the pure 2124-Al powder. The minor peaks at approximately 5.5 µm (Figures 5a and 5b) correspond with loose SiC particles that did not adhere to the 2124-Al powder. However, there was no minor peak for 10% SiC batch 1, as the sizes ranged from 2.75 to 37 µm, showing agglomeration of the SiC particles. All batches with 10% and 15% SiC powders had major peak modes of 62 to 74 µm, showing slight attrition of the 2124-Al powder particles. The bimodal nature of the SiC-added PSD curves show a much lower adherence of SiC to the 2124-Al particles (Figure 5) than the Al₂O₃-added powder particles (Figure 4), indicating poorer blending behaviour of SiC.

Compaction

During cold compaction, the green compacts of the unreinforced and blended powders fractured into thin, nearly horizontal slices, as shown in Figure 6. This was attributed to natural ageing of the 2124-Al alloy powder due to long-term storage (Nazarenko *et al.*, 2014). The powders were then exposed to an over-ageing heat treatment at 350°C for 2 hours in order to reverse the effects of ageing. Figure 7 shows a green compact that was successfully compacted using the over-aged powder.

Optical microscopy of the green compact (Figure 7) revealed a non-uniform density distribution in the uniaxial green compact, with high density at the surface (Figure 8a) and low density at the core (Figure 8b). German (1994) showed how density varies in green compacts from both single- and double-action pressing (Figure 9). In the current work, double-action pressing was used. From Figure 9 it can be observed that green compacts produced from double-action pressing have lower densities at the mid-height surface (Hofmann and Bowen, 2011).

Pressure gradients, caused by the friction between the powder and the die walls, lead to non-uniform density distribution in green compacts (Glass and Ewsuk, 1995). The frictional force opposes the applied force and decreases the amount of pressure transmitted to the powder for consolidation (Turenne *et al.*, 1999), so high pressures result in high green densities (Tiwari, Rajput and Srivastava 2012). Thus the lower densification observed at the core of the sample (Figure 8b) is an indication of a non-uniform density distribution in the sample.

The technique of over-ageing the powders before cold compaction worked for the unreinforced and reinforced powders, except for the powder reinforced with 10 vol.% Al₂O₃. The poor compressibility of the 2124-Al/10%Al₂O₃

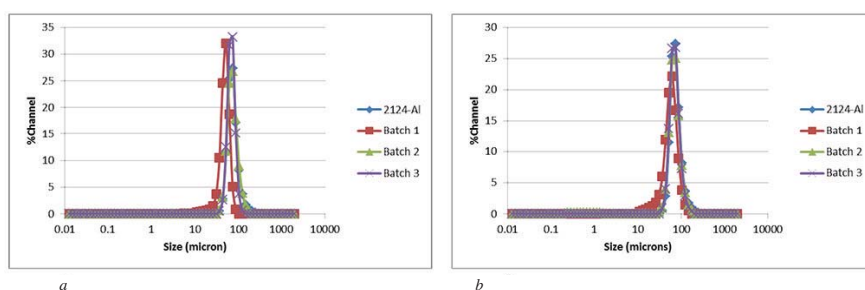


Figure 4—PSD curves for 2124-Al with (a) 5%Al₂O₃ and (b) 10%Al₂O₃ powders

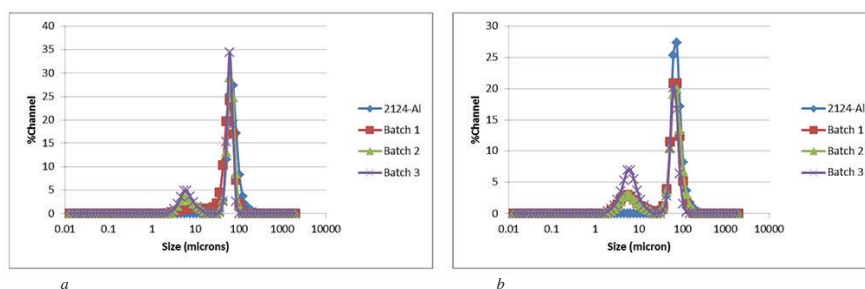


Figure 5—PSD curves for 2124-Al with (a) 10%SiC and (b) 15%SiC powders

Deformation behaviour of aluminium low-micron MMCs and MMNCs



Figure 6—Fractured green compact



Figure 7—Green compact successfully compacted from over-aged powder

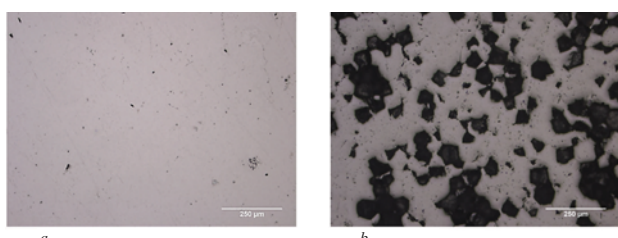


Figure 8—Difference in consolidation at (a) surface and (b) core of a green compact (shown in Figure 7) made with over-aged powder

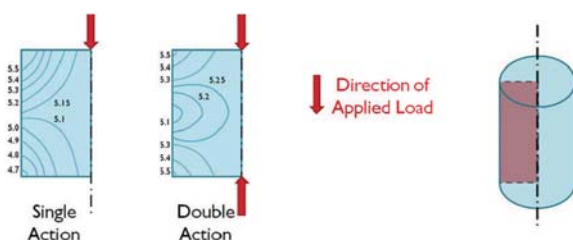


Figure 9—Diagrams illustrating non-uniform density distribution in green compacts produced by single- and double-action pressing (German, 1994, redrawn by Selig, 2012)

powder could have been due to the higher amount of Al_2O_3 on the surface of the 2124-Al particles, thus limiting the effect of over-ageing and preventing plastic deformation and bonding. Al_2O_3 has a high heat resistance, so the Al_2O_3 coating could have acted as a barrier to heat transfer thus limiting the effect of over-ageing, which meant that the hardness of the 2124-Al/10% Al_2O_3 powder was not changed dramatically by the over-ageing process (Pham, Maruoka and Nanko, 2016). The presence of more Al_2O_3 particles on the

aluminium alloy particle surfaces, due to a higher vol.% Al_2O_3 added, could have increased the hardness of the reinforced powder even further, since Al_2O_3 has a higher hardness than the Al alloy (Auerkari, 1996).

Poor consolidation and very little plastic deformation or bonding occurred in the 2124-Al/10% Al_2O_3 composite, as shown in the polished section in Figure 10. Figure 10 shows that there are nano- Al_2O_3 particles situated on the Al alloy grain boundaries. The micrograph supports the notion that plastic deformation and bonding were limited by the presence of Al_2O_3 particles on Al alloy particle surfaces.

Micrographs of the compacted 2124-Al/10%SiC powder are shown in Figures 11(a) and 11(b). These images show that consolidation was achieved by localized deformation at grain boundaries where there were few or no SiC particles. The same result was obtained for 2124-Al/15%SiC composite (not shown). This shows that in composite powders where reinforcing particles have settled on grain boundaries, consolidation is achieved by localized deformation at small contact points between matrix grains.

Uniaxial compression tests

The uniaxial compression tests performed in the Gleeble 3500® at ambient temperature were unsuccessful, as the green compacts fractured immediately under the compressive load, as shown in Figure 12.

Engineering stress-strain curves from uniaxial compression tests performed at ambient temperature (Figure 13) show the deformation behaviour of 2124-Al alloy, 2124-Al with 5% Al_2O_3 and 2124-Al with 10%SiC at ambient temperature. The three materials behaved in a similar manner during deformation since their stress-strain

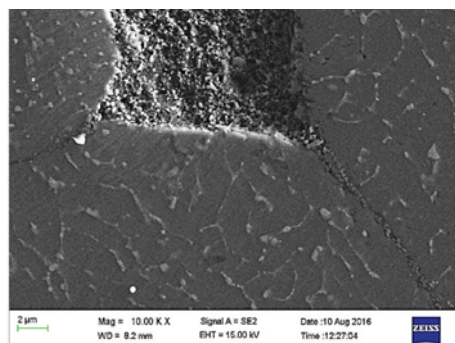


Figure 10—SEM micrograph showing polished section of MMNC green compact with 10 vol.% Al_2O_3

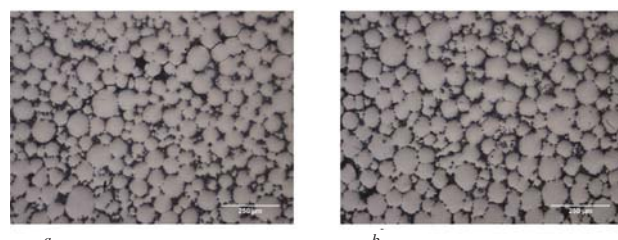


Figure 11—Optical micrographs showing consolidation at (a) surface and (b) core of a MMC green compact with 10 vol.%SiC produced from over-aged powder

Deformation behaviour of aluminium low-micron MMCs and MMNCs



Figure 12—Image showing a green compact fracturing during compression test at ambient temperature

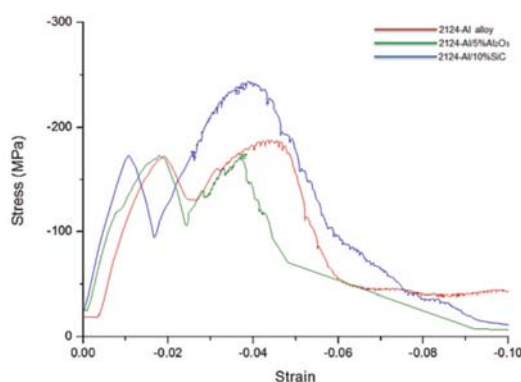


Figure 13—Engineering stress-strain curves showing deformation behaviour of 2124-Al alloy, and 2124-Al with 5% Al_2O_3 and 10% SiC green compacts at ambient temperature (6 minutes soak time and 0.01 s^{-1} strain rate)

curves follow the same trend. The compressive fracture stresses of the 2124-Al, 10% SiC MMC and 5% Al_2O_3 MMNC green compacts were similar at approximately 170 MPa. The peculiar shape of the stress-strain curves shows that the green compacts initially compressed and elastically deformed to a stress of approximately 170 MPa and then started to fracture as the plastic region was approached, leading to a sharp decrease in stress.

In initial testing at a programmed temperature of 280°C, electrical resistance heating of the green compacts did not occur, which was attributed to the high electrical conductivity and low resistance of aluminium. High electrical conductivity resulted in poor heat generation because electrical resistance in the samples was low (Ozturk *et al.*, 2016). It was presumed that the small sample size ($d=8 \text{ mm}$, $h=12 \text{ mm}$) also caused rapid heat loss. After further experimentation, the green compacts were heated successfully by using fibre optic wool and a conductive foil wrapped around the samples as insulation in order to retain heat.

The deformation behaviour of 2124-Al with 5% Al_2O_3 , 10% SiC and 15% SiC at 280°C is shown in Figure 14. The peaks of the curves represent the maximum flow stress. It is interesting to see that the 10% SiC sample showed a higher flow stress (200 MPa) than the 15% SiC sample (170 MPa). This could be a result of improved consolidation during compaction of 2124-Al with 10% SiC compared with 15% SiC.

The higher temperature improved the shape of the compression curves, removing the sudden drop in stress after elastic deformation that was seen in the ambient temperature tests. This indicates that the deformation was more uniform, which can be attributed to improved plastic flow due to an increase in temperature (Osakada, 1997).

The soaking time was increased from 6 to 20 minutes for the MMC green compact with 10 vol.% SiC to assess the effect of soaking time on deformation behaviour, as shown in Figure 15. The shape of the flow stress curve improved and it looks more like a standard compressive stress-strain curve. The various points and regions (elastic region, plastic region, maximum flow stress and final fracture point) on the curve can easily be identified. This shows that an increase in soaking time improved plastic flow in the material and improved the deformation behaviour.

Increasing the soaking time from 6 to 20 minutes decreased the maximum flow stress from 200 to approximately 170 MPa. Holding the sample at an elevated temperature for an increased time leads to more atoms gaining energy, thus the flow of particles in the material is improved (Arya *et al.*, 2016). Deforming the material became easier and a lower load was required to deform the material. As the soaking time did have an effect on the deformation behaviour it should be carefully selected.

Conclusions

The deformation behaviour, at warm working temperatures, of green particle-reinforced aluminium composites produced

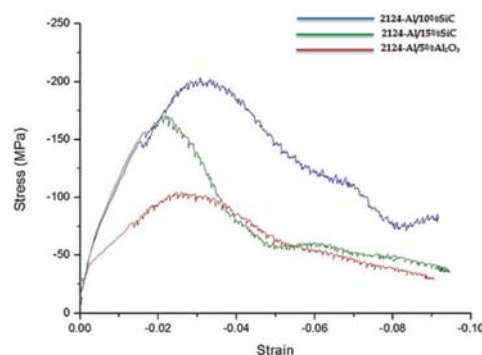


Figure 14—Engineering stress-strain curves showing deformation behaviour of 2124-Al with 5% Al_2O_3 , 10%SiC and 15%SiC at 280°C (6 minutes soak time, 0.01 s^{-1} strain rate)

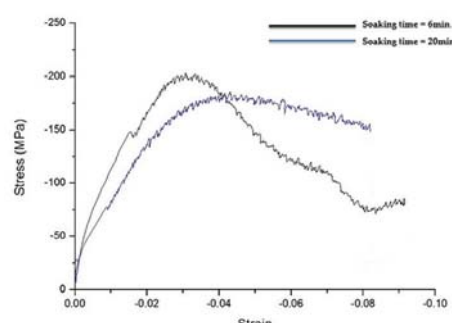


Figure 15—Engineering stress-strain curves showing the influence of soaking time (6 or 20 minutes) on deformation behaviour of MMC green compacts with 10 vol. %SiC at 280°C

Deformation behaviour of aluminium low-micron MMCs and MMNCs

by powder blending in a high-energy ball mill was investigated by performing uniaxial compression tests in a Gleeble 3500® thermomechanical simulator.

1. After blending, the morphology and size of the 2124-Al powder and the distribution of the SiC or Al₂O₃ reinforcing phase on the aluminium alloy particles were consistent over three batches
2. A more uniform distribution of the reinforcement phase was achieved in 2124-Al composites with nano-Al₂O₃ than with micro-SiC
3. Long-term storage of the age-hardenable aluminium alloy powders caused ageing, which results in a change in the powder characteristics such as hardness. Ageing was reversed by heat treatment of the unreinforced and blended powders into the over-aged condition
4. Electrical resistance heating of green compacts of aluminium alloy 2124, its MMC composites with SiC and MMNC composites with Al₂O₃ can be improved by insulating the samples with fibre optic wool and a conductive foil
5. The deformation of the 2124-Al alloy, 10% SiC MMC and 5% Al₂O₃ MMNC green compacts was poor at ambient temperature and the compacts had similar compressive fracture stresses. Improved deformation behaviour was observed at 280°C and the MMC with 10%SiC had the highest maximum flow stress (approx. 200 MPa)
6. Increasing the soaking time at 280°C from 6 to 20 minutes decreased the maximum flow stress from 200 MPa to approximately 170 MPa and improved the compressive deformation behaviour of the 2124-Al/10%SiC green compact.

References

- ARYA, V., PADAP, A.K., KUMAR, M. and HIWARKAR, A.D. 2016. Mechanical properties and electroconductivity of aluminum alloys processed using uniaxial compression. *Proceedings of the 3rd International Conference on Science, Technology and Management (ICSTM-16)*, New Delhi. pp. 749–754. <http://doi.org/978-81-932074-0-6>
- AUERKARI, P. 1996. Mechanical and physical properties of engineering alumina ceramics. *Mechanical and physical properties of engineering alumina ceramics. Research Notes 1792*. VTT Technical Research Centre of Finland.
- BORGONOVO, C. and APELIAN, D. 2011. Manufacture of aluminum nanocomposites: a critical review. *Materials Science Forum*, vol. 678. pp. 1–22. <http://doi.org/10.4028/www.scientific.net/MSF.678.1>
- CASATI, R. and VEDANI, M. 2014. Metal matrix composites reinforced by nanoparticles—a review. *Metals*, vol. 4, no. 1. pp. 65–83. <http://doi.org/10.3390/met4010065>
- CAVALIERE, P. 2002. Hot and warm forming of 2618 aluminium alloy. *Journal of Light Metals*, vol. 2, no. 4. pp. 247–252. [http://doi.org/10.1016/S1471-5317\(03\)00008-7](http://doi.org/10.1016/S1471-5317(03)00008-7)
- FERRY, M. 2005. Discontinuously reinforced metal matrix composites. *The Deformation and Processing of Structural Materials*. Guo, X.Z. (ed.), Woodhead Publishing, UK. p. 203. <https://books.google.co.za/books?hl=en&lr=&id=QbukAgAAQBAJ&oi=fnd&pg=PA203&dq=discontinuously+reinforced+metal+matrix+composite&ots=LqdU3ZDaei&sig=CseonOY467mV9ggRLwo+v5CScyw#v=onepage&q=discontinuously reinforced metal matrix composite&f=false>
- GERMAN, R.M. 1994. *Powder Metallurgy Science*. (2nd edn). Metal Powder Industries Federation, New Jersey.
- GLASS, S.J. and EWSUK, K.G. 1995. Ceramic powder compaction. *American Ceramic Society International Symposium on Manufacturing Practices and Technology*. <http://doi.org/10.1557/S0883769400034709>
- HIRANIAH, C.S.R.A., HARISHANAD, K.S. and NORONHA, N.P. 2012. A review on hot extrusion of metal matrix composites. *RESEARCH INVENTY: International Journal of Engineering and Science*, vol. 1, no. 10. pp. 30–35.
- HOFMANN, H. and BOWEN, P. 2011. Powder Technology. Part II: Compaction. *Laboratory of Powder Technology, École Polytechnique Fédérale de Lausanne*.
- JENSRUD, O. 1998. Warm-deformation and the age hardening response in two aluminium alloys. *Advanced Light Alloys and Composites*. Springer, Dordrecht. pp. 415–420. http://doi.org/10.1007/978-94-015-9068-6_54
- LIANG, X., EARTHMAN, J.C., WOLFNSTINE, J. and LAVERNIA, E.J. 1992. A comparison of techniques for determining the volume fraction of particulates in metal matrix composites. *Materials Characterization*, vol. 28, no. 4. pp. 173–178. [http://doi.org/10.1016/1044-5803\(92\)90079-W](http://doi.org/10.1016/1044-5803(92)90079-W)
- MAZEN, A.A. and EMARA, M.M. 2004. Effect of particle cracking on the strength and ductility of Al-SiCp powder metallurgy metal matrix composites. *Journal of Materials Engineering and Performance*, vol. 13, no. 1. pp. 39–46. <http://doi.org/10.1361/10599490417579>
- NAZARENKO, O.B., AMELKOVICH, Y.A. and SECHIN, A.I. 2014. Characterization of aluminum nanopowders after long-term storage. *Applied Surface Science*, vol. 321. pp. 475–480. <http://doi.org/10.1016/j.apsusc.2014.10.034>
- OSAKADA, K. 1997. Effects of strain rate and temperature in forming processes of metals. *Le Journal de Physique IV*, vol. 7. pp. 37–44. <http://doi.org/10.1051/jp4:1997502>
- OZTURK, F., ECE, R.E., POLAT, N., KOKSAL, A., EVIS, Z. and SHEIKH-AHMAD, J.Y. 2016. Application of electric resistance heating method on titanium hot forming at industrial scale. *Arabian Journal for Science and Engineering*. <http://doi.org/10.1007/s13369-016-2159-6>
- PHAM, H.V., MARUOKA, D. and NANKO, M. 2016. Influences of Al₂O₃ grain size on high-temperature oxidation of nano-Ni/Al₂O₃ composites. *Journal of Asian Ceramic Societies*, vol. 4, no. 1. pp. 120–123. <http://doi.org/10.1016/j.jascer.2016.01.003>
- RAJPUT, R.K. 2007. Metal forming processes. *A Textbook of Manufacturing Technology: Manufacturing Processes* (1st edn). Laxmi, New Delhi. pp. 142–143. <https://books.google.co.za/books?id=6wFuw6wufTMC&pg=PA140&lpg=PA140&dq=journals+on+disadvantages+of+hot+working+metals&source=bl&ots=7F-q942-wt&sig=9loky-tAxuqmF9XBscLgjLcyRGc&hl=en&sa=X&ved=0ahUKEwiRybafuprNAhXhB8AKHZRjAOY4ChDoAQgbMAE#v=onepage&q=journal>
- RAO, B.K., KHADAR, M.S.A. and SRINIVASAN, K. 1999. High temperature compression testing and determination of warm working temperature for commercial purity aluminium. *Bulletin of Materials Science*, vol. 22, no. 1. pp. 17–20. <http://doi.org/10.1007/BF02745670>
- SARAVANAN, L. and SENTHILVELAN, T. 2015. Investigations on the hot workability characteristics and deformation mechanisms of aluminium alloy-Al₂O₃ nanocomposite. *Materials & Design*, vol. 79. pp. 6–14. <http://doi.org/10.1016/j.matdes.2015.04.024>
- SELIG, S.G. 2012. Finite element simulation of the compaction and springback of an aluminium powder metallurgy alloy. Dalhousie University.
- TIWARI, S., RAJPUT, P. and SRIVASTAVA, S. 2012. Densification behaviour in the fabrication of Al-Fe metal matrix composite using powder metallurgy route. *ISRN Metallurgy*, 2012, pp. 1–8. <http://doi.org/10.5402/2012/195654>
- TURENNE, S., GODERE, C., THOMAS, Y. and MONGEON, P.E. 1999. Evaluation of friction conditions in powder compaction for admixed and die wall lubrication. *Powder Metallurgy*, vol. 42, no. 3. pp. 263–268. <http://doi.org/10.1179/003258999665611>
- ZHOU, J., DRUZDZEL, A. and DUSZCZYK, J. 1999. The effect of extrusion parameters on the fretting wear resistance of Al-based composites produced via powder metallurgy. *Journal of Materials Science*, vol. 34, no. 20. pp. 5089–5097. ◆



Grain refinement of 25 wt% high-chromium white cast iron by addition of vanadium

by L.A. Mampuru*, M.G. Maruma* and J.S. Moema*

Synopsis

Mill liner wear is a major cost item in the mining industry and there is continuous research to prolong the life of the liners. Over the years it has become apparent that even though high-chromium white cast irons are highly efficient as abrasion-resistant materials, a combination of wear resistance and fracture strength remains difficult to achieve. Increasing the hardness of the high-chrome white cast iron (HCWCI), which improves the resistance to abrasion wear, is often accompanied by a deterioration in fracture strength. Operational conditions inside the mill require that the liner should be made of highly wear-resistant material with some fracture strength. Vanadium additions ranging from 0.2 to 3 wt% were made to HCWCI in an attempt to refine the microstructure. It was found that an increase in vanadium content promotes grain refinement. A content of 1.5–3 wt% gave the best results as measured by the maximum breaking strength.

Keywords

HCWCI, mill liners, grain refinement, hardness.

Introduction

Over the years it has become apparent that even though high-chromium white cast irons are highly efficient abrasion-resistant material, a combination of excellent wear resistance and fracture strength remains difficult to achieve. The exceptional wear resistance of high-chromium white cast iron (HCWCI) is attributed to hard chromium carbides embedded in an austenitic/martensitic/pearlitic matrix. When the chromium contents exceed 12 wt%, interconnected MC_3 -type carbides of conventional cast irons are replaced by rod-shaped and isolated M_7C_3 carbides (Powell, 1980), leading to an improvement in the impact toughness, ductility and fatigue resistance. However, the main M_7C_3 carbides in HCWCI are hard and brittle and can provide an easy path for crack propagation. This limits the applications of HCWCI, particularly in severe impact conditions. Most operations involving HCWCI are in crushing and grinding and the life of a part/liner is limited by its wear resistance. However, improving the wear resistance of HWCI comes at the cost of a significant reduction in fracture strength. Concerns about premature failure of HCWCI

mill liners in the mining industries prompted a study to improve the wear resistance and mechanical properties of HCWCI.

Addition of alloying elements to HCWCI can significantly change the microstructure, which may result in adequate combinations of wear resistance and fracture strength (Powell, 1980; Filipovic *et al.*, 2013). Most studies have shown that eutectic carbides influence the fracture strength of the white cast iron and by controlling the morphology of the carbides and the matrix structure, can lead to major improvements in the fracture strength (Filipovic *et al.*, 2013, 2014; Filipovic, 2013). Research and development is ongoing on the effect of microalloying, heat treatments and different casting techniques on the properties of HCWCI. This is aimed at widening the application of these alloys by extending their service life and minimizing the maintenance cost through addition of strong carbide formers such as vanadium, tungsten, niobium and titanium (Liu *et al.*, 2005; Radulovic *et al.*, 1994; Sawamoto, Ogi and Matsuda, 1986; Anijdan *et al.*, 2007; Chung *et al.*, 2009; Lu, Soda and Mclean, 2003). Strong carbide-forming elements like vanadium, tungsten, niobium and titanium may also be added to improve the mechanical properties (Filipovic, 2013; Liu *et al.*, 2005; Radulovic *et al.*, 1994).

Addition of vanadium to HCWCI can form vanadium carbides, which are much harder than M_7C_3 carbides and may lead to strengthening of the austenitic matrix and improve the fracture strength of the HCWCI (Liu *et al.*, 2005). The hardness of vanadium carbides differs with composition; their round morphology reduces splitting to the matrix and

* Advanced Materials Division, Mintek, Randburg, South Africa.

© The Southern African Institute of Mining and Metallurgy, 2016. ISSN 2225-6253. This paper was first presented at the AMI Ferrous and Base Metals Development Network Conference 2016 19–21 October 2016, Southern Sun Elangeni Maharani, KwaZulu-Natal, South Africa.

Grain refinement of 25 wt% high-chromium white cast iron by addition of vanadium

improves the fracture strength due to formation of a fine-grained microstructure (Nelson, 2010; Liu *et al.*, 2005). Dupin and Schissler (1984), as quoted by Filipovic (2013), indicated that the addition of as little as 1% vanadium does not produce any vanadium carbides, but refines the eutectic carbides. This conclusion is supported by Bedolla-Jacuinde (2001), who indicated that even the addition of 2 wt.% vanadium did not form any vanadium carbides but increased the volume fraction of the M_7C_3 carbides (Filipovic, Kamberovic and Korac, 2011).

Most of the work to date has been aimed at improving the tough of HCWCI, mostly on the hypereutectic alloys. The research was centred on modifying the shape of carbides but there has been no breakthrough. The work in this current study focuses on improving the fracture strength of hypoeutectic white cast iron by the addition of vanadium.

Experimental procedure

Melting and casting

Melting of the HCWCI alloy was accomplished in a medium frequency induction furnace with a capacity of about 150 kg. The molten metal was poured into a sand mould and allowed to cool to room temperature. The chemical compositions of the alloys produced are given in Table I. The test materials produced for this project consisted of HCWCI in the form of $50 \times 100 \times 500$ mm flat rectangular test bars (*i.e.* thickness \times width \times length) as shown in Figure 1a.

The alloys were examined for surface defects before proceeding with testing and there was no indication of defects (Figure 1b). The specimens were then polished and etched with 3% Nital. The microstructural analysis was carried out using an Olympus PGM optical microscope equipped with Analysis Image software and a scanning electron microscope.

Brinell hardness measurements were performed through the cross-sections of the as-cast test samples, using a load of 750 kg. The measurements were taken from the surface to the centre of the rectangular test sample to ascertain if there were any hardness gradient changes within the test sample. It was found that the difference was minimal. Bending tests are intended for brittle materials when the scope of test is to determine the strength of material. To determine the bending strength Q_{max} , the beam must be so proportioned that it will not fail in shear or by lateral deflection before reaching its ultimate flexural strength. Hence, for a rectangular part in a three-point bending test, bending strength is the highest stress at the moment of rupture. Usually, long specimens with higher length to depth ratio ($L/h > 10$) are recommended.

Table I

Alloy compositions

Alloy ID	Composition
Reference	ASTM A 532 Class III
Alloy 1	ASTM A 532 Class III + 0.2-0.8V
Alloy 2	ASTM A 532 Class III+ 0.8-1.5V
Alloy 3	ASTM A 532 Class III+1.5-3.0V

Results and discussion

Effect of vanadium on the microstructural evolution

The microstructure of the as-cast reference alloy is shown in Figure 2a. The microstructure consists of primary austenite dendrites surrounded by a eutectic mixture of carbide particles and austenite. In hypoeutectic cast iron, solidification proceeds with austenite, eutectic vanadium carbides (VC) and finally M_7C_3 carbides. It can be seen from Figure 2a that the M_7C_3 carbides are of a rod and needle type of morphology and that the stress concentration factor will play a larger role when the material is exposed to an impact. Addition of vanadium to HCWCI has changed the needle-shaped M_7C_3 to an isotropic morphology. This change in the carbide morphology may play a critical role in determining the fracture strength of the HCWCI.

The scanning electron microscope analysis of the alloy in the as-cast condition and corresponding EDS composition maps are shown in Figures 3 to 5. One can see that the element distributions are consistent with the identified phases in the microstructure. The microanalysis of the phases shown in Table II reveals that V substituted Cr and Fe in M_7C_3 up to about 2.5 wt% V. V was also dissolved into the austenitic matrix, reaching a maximum of about 0.3 wt%. The presence of vanadium carbide particles in M_7C_3 , which would result in significant refinement of the M_7C_3 carbides by acting as the heterogeneous substrates of M_7C_3 carbides, was

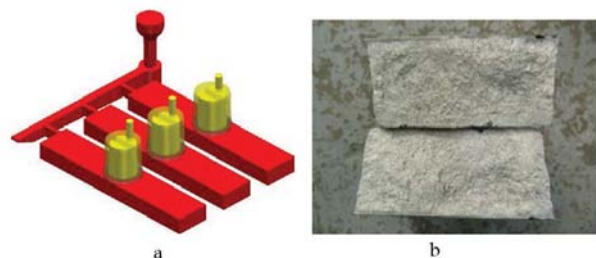


Figure 1—Pattern design that was used to produce test bars: (a) simulated pattern, (b) actual casting with no defects

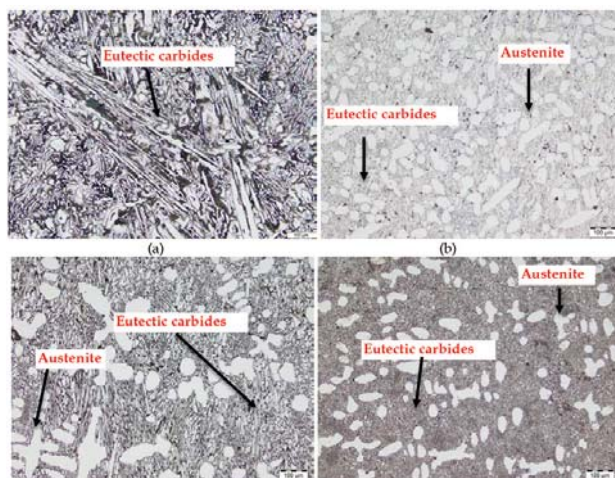


Figure 2—Micrograph of the (a) Reference alloy, (b) 0.2-0.8%V, (c) 0.8-1.5%V and (d) 1.5-3%V showing M_7C_3 carbides in an austenite matrix

Grain refinement of 25 wt% high-chromium white cast iron by addition of vanadium

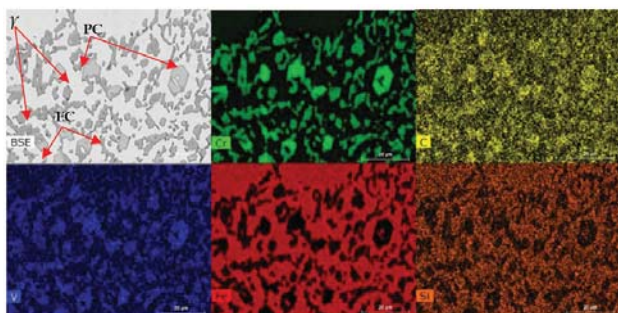


Figure 3—SEM-EDX mapping of the as-cast HCWCI with addition of 0.2-0.8%V. PC = primary carbides, EC, eutectic carbides and γ = austenite

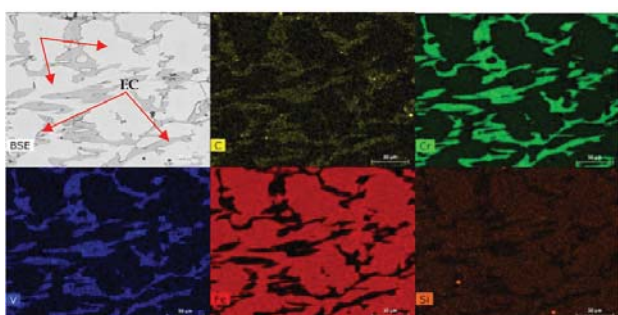


Figure 4—SEM-EDX mapping of the as-cast HCWCI with addition of 0.8-1.5%V. EC, eutectic carbides and γ = austenite

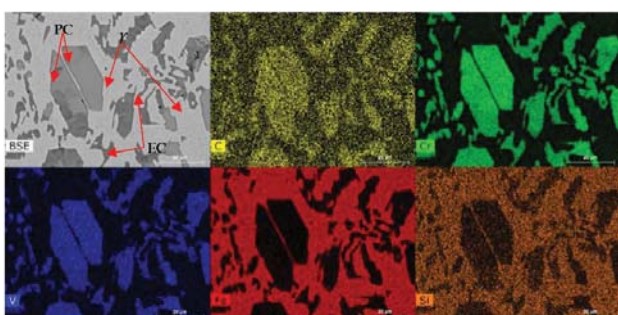


Figure 5—SEM-EDX mapping of the as-cast HCWCI with addition of 1.5-3%V. PC = primary carbides, EC, eutectic carbides and γ = austenite

Table II Composition (in wt%) of HCWCI-V phases determined by EDS					
Alloy	Phases	C	V	Cr	Fe
ASTM A 532 Class III + 0.2-0.8%V	M_7C_3	1.2	0.6	67.7	30.5
	Matrix	1.1	0.1	16.5	81.4
ASTM A 532 Class III+ 0.8-1.5%V	M_7C_3	1.5	0.3	68.4	29.6
	Matrix	0.2	0.25	19.4	79.2
ASTM A 532 Class III+1.5-3.0%V	M_7C_3	2.6	2.5	60.3	34.1
	Matrix	1.0	0.3	13.4	83.5

Trace elements: 0.5% V (Matrix 0.9), 1% V (Matrix 0.9) (M_7C_3 0.2) and 2% V (Matrix 1.8) (M_7C_3 3.0.5)

not observed. The results are in agreement with those of Dupin and Schissler (1984), who did not detect vanadium carbide formation in HCWCI with 1% V additions. This may be due to the lower vanadium content as reported by Sawamoto *et al.* and the literature has indicated that vanadium carbide can form when the V content exceeds 5% (Sawamoto, Ogi and Matsuda, 1986). This is in contradiction to the work by Filipovic (2013), which indicated that vanadium-rich carbides are found in Fe-Cr-C-V irons containing 1.19–4.73% V.

However, the grain refinement effect of M_7C_3 carbides with an increase in vanadium content can be explained by their influence on the eutectic solidification temperature. Filipovic, Kamberovic and Korac (2011) indicated that the addition of V decreased the liquidus temperature and increased the eutectic temperature, thus the eutectic solidification temperature interval was decreased. It has been previously reported that the carbides' spacing increases with the increase in the eutectic temperature range, so the decreasing eutectic temperature interval effectively reduced the carbides' spacing due to the addition of V (Ogi, Matsubara and Matsuda, 1982).

Effect of vanadium on hardness

Effect of vanadium on the hardness of the HCWCI is shown in Table III. The hardness of the material is directly proportional to the wear resistance, *i.e.* an increase in hardness will lead to improved wear resistance. It can be seen from Table III that the bulk hardness increased and then decreased with increasing vanadium addition

The variation in hardness is attributed to two factors. Firstly, vanadium dissolves in the austenite and improves austenite hardness by solid solution strengthening. Secondly, from the microstructural analysis using SEM, vanadium existed in M_7C_3 carbides and this may have increased the hardness of M_7C_3 carbides as Ma *et al.* (2013) indicated. The results in Table III indicate that addition of vanadium led to improved wear resistance while retaining the fracture strength.

Effect of vanadium on fracture strength

Table IV shows the experimental results of the fracture strength. Vanadium contributes to the improvement of fracture strength of Fe-Cr-C-V alloys in the as-cast condition as measured by the stress required to fracture the HCWCI. This increase in fracture strength indicates that the vanadium addition had a beneficial effect on the properties of HCWCI. Figures 3 to 5 show a clear dispersion of the vanadium in the matrix, and this might have led to matrix hardening/strengthening and hence improved the fracture strength.

Table III The effect of vanadium on the hardness of HCWCI	
Alloy	Brinell hardness (BHN)
ASTM A 532 Class III	432
ASTM A 532 Class III + 0.2-0.8%V	555
ASTM A 532 Class III+ 0.8-1.5%V	485
ASTM A 532 Class III+1.5-3.0%V	514

Grain refinement of 25 wt% high-chromium white cast iron by addition of vanadium

Table IV

The effect of vanadium on fracture strength of HCWCI

Alloy	Fracture load average (N)	Stress (σ_{max}) (MPa)
ASTM A 532 Class III	184 400	332
ASTM A 532 Class III + 0.2-0.8%V	192 000	346
ASTM A 532 Class III+ 0.8-1.5%V	212 700	383
ASTM A 532 Class III+1.5-3%V	306 400	552

Morphology of the particles also plays a role. It can be seen from Figure 2 that in the reference HCWCI, the M_7C_3 carbides are of the rod and needle type and therefore the stress concentration factor will play a bigger role when the material is exposed to an impact. The tip of the needle type carbides will act as a stress riser and thus lead to reduction in fracture strength. The increase in fracture strength brought about by increasing the vanadium content is also in agreement with the results of Liu *et al.* (2005), who attributed the increase in fracture strength to the finer primary austenite dendrites. Changing the morphology from rod to isotropic therefore leads to a significant increase in fracture strength.

Conclusions

The main aim of this project is to improve the mechanical properties of high-chromium white cast iron (HCWCI) for mill liners with special emphasis on improving the fracture strength of these alloys. The influence of vanadium on the grain refinement of HCWCI was investigated. The addition of vanadium was found to change the morphology of eutectic carbides from plate- and rod-like shapes to isotropic shapes. Addition of vanadium led to an increase in fracture strength in the cast structure. This was due to the fine-grained microstructure and increased matrix strength through a dispersion-hardening effect of vanadium – the fine secondary carbides can increase the mechanical support offered by the eutectic carbides.

References

- ANJIDAN, S.H.M., BAHRAMI, A., VARAHRAM, N. and DAVAMI, P. 2007. Effects of tungsten on erosion-corrosion behaviour of high chromium white cast iron. *Materials Science and Engineering A*, vol. 454–455. pp. 623–628.
- BEDOLLA-JACUNDE, A. 2001. Microstructure of vanadium, niobium and titanium-alloyed high-chromium white cast irons. *International Journal of Cast Metals Research*, vol. 13. pp. 343–361.
- CHUNG, R.J., TANG, A., LI, D.Y., HINCKLEY, B. and DOLMAN, K. 2009. Effects of titanium addition on microstructure and wear resistance of hypereutectic high chromium cast iron Fe-25wt. %Cr-4wt. %C. *Wear*, vol. 267, no. 1–4. pp. 356–351.
- DUPIN, P. and SCHISSLER, J.M. 1984. A structural study of chromium white cast iron. *American Foundry Society Transactions*, vol. 92. pp. 355–360.
- FILIPOVIC, M. 2013. Fe-Cr-C-V white cast iron - the microstructure and properties. Faculty of Technology and Metallurgy, University of Belgrade, Belgrade, Serbia.
- FILIPOVIC, M., KAMBEROVIC, Z. and KORAC, M. 2011. Solidification of high chromium white cast iron alloyed with vanadium. *Materials Transactions*, vol. 52. pp. 386–390.
- FILIPOVIC, M., KAMBEROVIC, Z., KORAC, M. and GAVRILOVSKI, M. 2013. Correlation of microstructure with the wear resistance and fracture toughness of white cast iron alloys. *Metals and Materials International*, vol. 19, no. 3. pp. 473–481.
- FILIPOVIC, M., KORAC, M. and KAMBEROVIC, Z. 2014. The effect of vanadium content and heat treatment on wear resistance and fracture toughness of Fe-Cr-C-V alloy. *Metallurgical and Materials Engineering*, vol. 20, no. 1. pp. 1–13.
- LIU, K., WANG, F., LI, C. and SU, L. 2005. Influence of vanadium on microstructure and properties of medium-chromium white cast iron. *Iron and Steel*, vol. 10 (Supplement). pp. 207–211.
- LIU, K., WANG, F., LI, C. and SU, L. (2005). Influence of vanadium on microstructure and properties of medium-chromium white cast iron. *Iron and Steel*, vol. 40 (Supplement). pp. 207–211.
- LU, L., SODA, H. and MCLEAN, A. 2003. Microstructure and mechanical properties of Fe-Cr-C eutectic composites. *Materials Science and Engineering A*, vol. 347. pp. 214–222.
- MA, Y., LI, X., LIU, Y., ZHOU, S. and DANG, X. 2013. Microstructure and properties of Ti-Nb-V-Mo-alloyed high chromium cast iron. *Bulletin of Materials Science*, vol. 36, no. 5. pp. 839–844.
- NELSON, G.D. 2010. The influence of microstructure on the corrosion and wear mechanisms of high chromium white irons in highly caustic solutions. School of Mechanical Engineering, University of Adelaide, South Australia.
- OGI, K., MATSUBARA, Y. and MATSUDA, K. 1982. Eutectic solidification of high chromium cast iron - mechanism of eutectic growth. *AFS Transactions*, vol. 89. pp. 197–204.
- POWELL, G.L.F. 1980. Morphology of eutectic M_3C and M_7C_3 in white iron castings. *Materials Forum*, vol. 3. pp. 37–40.
- RADULOVIC, M., FISSET, M., PEEV, K. and TOMOVIC, M. 1994. Influence of vanadium on fracture toughness and abrasion resistance in high chromium white cast iron. *Journal of Material Science*, vol. 29, no. 19. pp. 5085–5094.
- SAWAMOTO, A., OGI, K. and MATSUDA, K. 1986. Solidification structure of Fe-C-Cr-(V-Nb-W) alloys. *AFS Transactions*, vol. 72. pp. 403–416.
- SAWAMOTO, A., OGI, K. and MATSUDA, K. 1986. Solidification structures of Fe-C-Cr-(V-Nb-W) alloys. *AFS Transactions*, vol. 94, no. 86–72. pp. 403–416.
- ZHI, X., XING, J., FU, H. and XIAO, B. 2008. Effect of niobium on the as-cast microstructure of hypereutectic high chromium cast iron. *Materials Letters*, vol. 62. pp. 857–860. ♦



X-ray computed microtomography studies of MIM and DPR parts

by N.S. Muchavi*, L. Bam†, F.C. De Beer†, S. Chikosha* and R. Machaka*

Synopsis

Parts manufactured through power metallurgy (PM) typically contain pores that can be detrimental to the final mechanical properties. This paper explores the merits of 3D X-ray computed tomography over traditional microscopy for the characterization of the evolution of porosity in metal injection moulding (MIM) and direct powder rolling (DPR) products. 17-4 PH stainless steel (as-moulded, as-debound and sintered) dog-bone samples produced via MIM and Ti-HDH strips (as-rolled and sintered) produced via DPR and were analysed for porosity. 3D micro-focus X-ray tomography (XCT) analysis on specimens from both processes revealed spatial variations in densities and the existence of characteristic moulding and roll compaction defects in agreement with traditional microscopic microstructural analysis. It was concluded that micro-focus XCT scanning can be used to study MIM and DPR parts for the characterization of the amount, position and distribution of porosity and other defects. However, the majority of the sub-micron sized pores could not be clearly resolved even at the highest possible instrument resolution. Higher-resolution scans such as nano-focus XCT could be utilized in order to fully study the porosity in MIM and DPR parts.

Keywords

X-ray tomography, metal injection moulding, direct powder rolling, 17-4 PH stainless steel, titanium.

Introduction

Metal injection moulding (MIM) is a novel process, which combines the advantages of powder metallurgy (PM) and plastic injection moulding. MIM has found widespread applications in the cost-effective production of high-sintered density small parts with complicated shapes and mechanical properties equivalent to those of wrought materials (German and Bose, 1977; Machaka and Chikwanda, 2015; German, 2013). There are four basic processing steps involved in MIM, namely; feedstock preparation, injection moulding, debinding and sintering. These steps are discussed in greater detail elsewhere (Machaka, Seerane and Chikwanda, 2014; German and Bose, 1977; Machaka and Chikwanda, 2015; German, 2013).

Feedstock preparation involves mixing metal powder with a carefully selected composition of polymeric binder materials at a specific temperature. The feedstock is then granulated and injected into a predefined mould die with the desired shape. The part

produced during the moulding step is referred to as a 'green' component. The green component typically contains no porosity since the spaces between adjacent powder particles are readily filled with the binder materials (German and Bose, 1977; Li, Li and Khalil, 2007). Debinding is the systemic removal of the binder components by chemical, catalytic, or/and thermal means while maintaining the shape of the component. The part produced after the debinding step is referred to as a 'brown' component. Debinding is known to be the source of porosity in brown components (Ji *et al.*, 2001; Tsai and Cen, 1995). Finally, the brown debound part is sintered to full or near-full density (Sotomayor, Várez and Levenfeld, 2010). The sintering step and associated densification closes up the majority of the pores. Sintered MIM parts are typically sintered to high density (95–99%) and retain an irreducible amount of residual porosity (Barriere, Liu and Gelin, 2003; German, 1990).

Direct powder rolling (DPR) of metal powders is a fairly new process (Cantin and Gibson, 2015). The DPR process consists of (i) roll compaction, sintering, mechanical working and/or heat treatment (Ro, Toaz and Moxson, 1983) or (ii) roll compaction, hot rolling, mechanical working and/or heat treatment (Cantin *et al.*, 2011). The rolling mill consolidates the powders into green compacts (Park *et al.*, 2012; Chikosha, Shabalala and Chikwanda, 2014; Cantin *et al.*, 2010; Peterson, 2010). The green compacts produced via DPR contain pores between the consolidated powder particles. Sintering or hot rolling

* Light Metals, Materials Science and Manufacturing, Council for Scientific and Industrial Research, Pretoria, South Africa.

† Radiography/Tomography Section, Necsa, Radiation Science Department, Pretoria, South Africa.

© The Southern African Institute of Mining and Metallurgy, 2016. ISSN 2225-6253. This paper was first presented at the AMI Ferrous and Base Metals Development Network Conference 2016 19–21 October 2016, Southern Sun Elangeni Maharani, KwaZulu-Natal, South Africa.

X-ray computed microtomography studies of MIM and DPR parts

followed by mechanical working and/or heat treatment is performed to reduce the pores, resulting in a highly densified part (Qian, 2010; Froes *et al.*, 2004). The number, distribution and evolution of pores throughout the DPR stages are derived from the measured densities. The methods used for density studies of powder metallurgy parts such as dimensional measurements and the hydrostatic Archimedes method can be labour-intensive and time-consuming as they can involve sectioning and infiltrating specimens (Bateni, Parvin and Ahmadi, 2011; Martin *et al.*, 2003). As such, nondestructive material testing such as gamma radiology, ultrasonic tomography, eddy current measurements and micro-focus X-ray computed tomography (μ XCT) become attractive alternative ways of identifying and characterizing porosity and other flaws in a material (Bateni, Parvin and Ahmadi, 2011; Kohn, 1972).

Recent developments have seen a growing interest in μ XCT analysis both as a characterization and quality inspection technique in material science; it has been successfully applied to many different materials (Heldele *et al.*, 2006; Kara and Matula, 2015; O'Brien and James, 1988; Yang, Zhang and Qu, 2015a; Lunel, 2013; Mutina and Koroteev, 2012; Tammas-Williams *et al.*, 2015; du Plessis *et al.*, 2016; Alcica *et al.*, 2010) to show the resolvable microstructural features such as second-phase particulates as well as defects such as inclusions, pores and cracks (Maire *et al.*, 2001). To date, the application of μ XCT analysis in powder metallurgy has been explored by several groups: de Chiffre *et al.* surveyed existing systems, scanning capabilities and technological advances on a variety of μ XCT scanning technologies while reviewing the state of the industrial applications of XCT methods in general. Bateni, Parvin and Ahmadi (2011) conducted *in situ* density measurements on porous PM compacts using XCT techniques. O'Brien and James (1988), Yang, Zang and Qu (2015a) and Kara and Matula (2015) reviewed the application of XCT techniques to issues relating to powder compaction and compact ejection for PM components. Ma, Li and Tang (2016) applied XCT technique in characterizing the microstructural evolution and densification mechanisms during the sintering of steel powders. Aldica *et al.* (2010) used XCT in the characterization of mechanically alloyed MgB₂ superconductor materials consolidated by spark plasma sintering. Heldele *et al.* (2006), Weber *et al.* (2011), Yang, Zhang and Qu (2015b) and Fang *et al.* (2014) investigated various aspects of MIM parts using XCT. No literature sources currently available

report on the application of XCT techniques to study the powder rolling process or intermediate MIM debinding stages. However, available literature shows that XCT techniques have found widespread quality inspection application in studying porosity formation in additive manufactured metal components and the formation of porosity therein (Tammas-Williams *et al.*, 2015; du Plessis *et al.*, 2016).

This paper explores the merits of 3D XCT over traditional microscopy and inspection techniques for the characterization of the evolution of 3D pore distribution, concentration and size in MIM and DPR products. This technique will offer more detailed results than the traditional microscopy technique, which provides only 2D surface information of the specimen.

Experimental background

MIM sample preparation

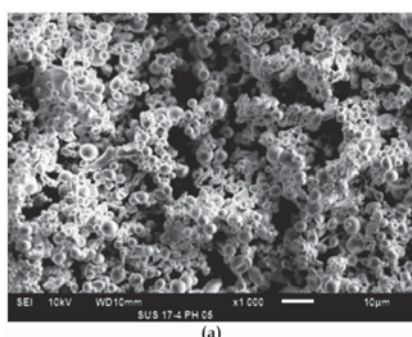
A bimodal 17-4 PH stainless steel powder material was prepared for this work. It consisted of -15 μ m and -5 μ m powder materials blended in a 75:25 weight ratio, respectively; both materials were supplied by Atmix Corp. JP. Figure 1 shows the representative powder particle sizes and spherical morphologies as observed under a JEOL JSM - 6510 scanning electron microscope (SEM).

Table I summarizes the starting metal powder particle sizes measured using a laser scattering particle size analyser (Microtrac Bluewave). The material identification codes PS-15 and PS-5 represent the particle sizes -15 μ m and -5 μ m, respectively. Table II shows the typical chemical compositions of the metal powder materials as obtained from the supplier's data specification sheets.

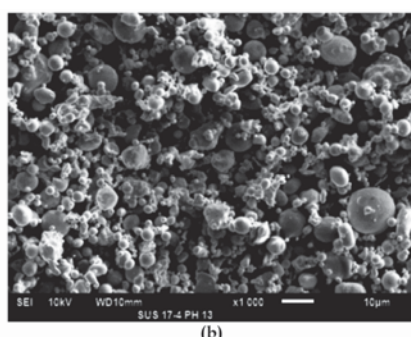
An injection-ready MIM feedstock was prepared by compounding the bimodal 17-4 PH stainless steel powder material with a proprietary wax-polymer binder system developed at the CSIR (Machaka and Chikwanda, 2015). The binder system consists of a major fraction of paraffin wax, a

Table I
Size distribution of 17-4 PH stainless steel powder

Material ID	d_{10} (μ m)	d_{50} (μ m)	d_{90} (μ m)
PS-15	2.65	7.91	23.1
PS-5	1.98	4.04	7.90



(a)



(b)

Figure 1—Scanning electron micrographs of 17-4 PH stainless steel powder at 1000x magnification (a) -5 μ m and (b) -15 μ m

X-ray computed microtomography studies of MIM and DPR parts

Table II

Chemical composition (by weight) of the starting powder materials, %

	Si	Mn	Ni	Cr	Cu	Nb	Fe
17-4 PH	≤ 0.5	≤ 0.3	3.0–5.0	15.5–17.5	3.0–5.0	0.15–0.45	Bal.

blend of low-density polyethylene, polypropylene and a stearic acid surfactant of less than 1 wt.% of the binder system composition. The feedstock was prepared in a sigma-type blade mixer for at least 1 hour at 140°C in air.

Upon cooling, the feedstock was appropriately granulated and injection-moulded into standard MPIF 'dogbone' tensile specimens. The injection moulding was done at 140°C using an ARBURG Allrounder 270U 400-70 injection moulding machine.

Debinding of green parts was performed in two steps. The first step was solvent extraction of the low-molecular-weight solvent-soluble binder components in n-heptane (Merck) at 60°C for up to 24 hours. The sample was subsequently dried before being weighed to obtain the percentage weight loss of the binder. The second step was thermal decomposition of the backbone binder during the pre-sintering cycle. This was accomplished in a Carbolite tube furnace under a controlled flowing argon atmosphere at 550°C. The mechanism of this thermal debinding procedure has been reported elsewhere (Machaka and Chikwanda, 2015; Machaka, Seerane and Chikwanda, 2014; Seerane, Chikwanda and Machaka, 2015).

The thermally debound components were sintered at 1300°C for 4 hours followed by furnace cooling. The argon gas flow was maintained at 1.0 L/min. The microstructure, density, microhardness and tensile properties of the sintered components were investigated accordingly.

DPR sample preparation

Ti-HDH 100 mesh (-150 µm) powders supplied by Chengdu Huarui Industrial in China were used. The powders were rolled in a modified Schwabenthal Polymix 150T rubber mill with a roll diameter of 170 mm. The rolling speed was set at 10 r/min with a roll gap of 0.3 mm. The set strip width was varied at 20, 50 and 100 mm.

The masses of the strips were measured using an Ohaus Explorer balance, the length and width were measured using a Vernier caliper and the thickness was measured using a TA micrometer screw gauge. Five measurements were taken for each parameter and an average value used. The green density of each strip was calculated using the measured mass, length, width and thickness of the compact strips.

Sintering was carried out in a Carbolite tube furnace at 1300°C for 3 hours followed by furnace cooling. Argon was used as an inert atmosphere at 1 L/min. After sintering, the density of each strip was measured using an Ohaus Explorer density determination kit based on the Archimedes principle according to ASTM standard B311. The sintered compacts were sectioned into several pieces, mounted, ground and polished according to standard metallography procedures. The microstructures of the polished samples were recorded using a DM5000 optical microscope with Image Pro-AMS 603 software for recording the micrographs.

X-ray computed tomography scanning

Representative as-moulded green component, dried brown components and final sintered components were probed by means of XCT to investigate the evolution of the pores throughout the stages of MIM processing (injection moulding, debinding and sintering). For the DPR process, sintered samples that were 20, 50 and 100 mm wide were probed to investigate the residual porosity in terms of the position and distribution.

The X-ray computed tomography scans were conducted at the Micro-focus X-ray Radiography/Tomography (MIXRAD) laboratory using the NIKON XTH 225ST system based at the South Africa Nuclear Energy Corporation (Necsa) (Hoffman and Beer, 2012). The high-resolution system consists of a tungsten target with a 3.7 µm spot size with a variable energy potential of approximately 25 to 225 kV. The maximum resolution achievable at the detector is 200 µm. Each sample was scanned at a potential of 115 kV and beam current of 100 A to obtain beam penetration > 10% from background. During the scan the sample rotated in equal angular steps through 360° to produce 1000 radiographs at each step angle, which were then reconstructed using the CT-Pro 3D-reconstruction software (Hoffman and Beer, 2012). The reconstruction process transforms the acquired 2D radiographs into a virtual 3D volume that is an exact digital copy of the sample. This virtual 3D volume was analysed using VGStudioMAX (ver. 2.2) rendering software, which allows rendering of the sample in 3D. The background is represented by darker grey values, whereas the sample has lighter/bright grey values. This grey value difference was used to determine porosity distribution within the samples.

Results and discussion

MIM parts and properties

Figure 2 depicts the differences between the as-moulded green, solvent-debound and sintered components. The surface appearance of specimens (a–c) gives an indication of the binder lost from the green state to the sintered state and this equates to the level of shrinkage that occurred. Specimen (b) underwent solvent debinding and no significant shrinkage difference was observed relative to the as-moulded part. The linear shrinkage of the sintered sample (Figure 2 (c)) was calculated to be 12.5%.

The as-sintered dogbone specimens were used for tensile tests without any preparation. The mechanical properties of unimodal 17-4 PH stainless steel feedstock specimens are



Figure 2—Standard MIM 'dogbone' component as observed during MIM processing – (a) as-moulded, (b) solvent-debound and (c) sintered at 1300°C

X-ray computed microtomography studies of MIM and DPR parts

reported elsewhere (Seerane, Ndlangamandla and Machaka, 2016). Table III summarizes the mechanical properties of metal-injection-moulded 17-4 PH stainless steel obtained in this study. The values are well above minimum standard stipulated values (MPIF, 2016; ASTM International, 2005).

The densities of the sintered specimens were determined according to ASTM B311 (Archimedes method). Specimen hardness was determined at room temperature using the Vickers hardness testing procedure.

MicroCT scanning of MIM parts

Unless purposely intended (Chen *et al.*, 2016), sintered MIM parts are typically sintered to high density (95–99%); a small amount of residual porosity may arise from (a combination of) poorly formulated feedstock, the debinding process, gas entrapment during sintering and/or incomplete sintering of metal particles (German and Bose, 1977; German, 2013; Machaka, Seerane and Chikwanda, 2014).

Figure 3 to Figure 5 illustrate the XCT 3D analysis of reconstructed green, solvent-debound and sintered MIM parts. The three steps conducted in each case involved (a) reconstructing the 3D surface from raw data, (b) histogram segmentation and identification of the open pores and interior pores and inclusions from the background and (c) separating the various individual components identified in Figure 2 for structural properties such as relative volume, spatial distribution, domain size and shape distributions, specific area, interconnectedness and spatial orientation.

The reconstructed surface in Figure 3a shows the holistic surface integrity of the green part and can also be used as a versatile inspection tool (for obvious moulding defects and resolvable surface porosity) and for dimensional measurements. In Figure 3b, the 3D distribution surface and interior pores in the green part volume are determined, while in Figure 3c the identified defects are analysed in isolation. The results aid the visualisation of the size and spatial distribution of injection moulding defects. A maximum defect volume of approximately 0.05 mm³ was identified; however, no MIM-specific standards have been developed to determine if such defect volumes are repairable in subsequent steps. It is has been shown that some defects do occur in green parts and these defects can be avoided or controlled by adopting good tooling design and optimizing injection moulding parameters (see Nor *et al.*, 2009).

Figure 4a shows a reconstructed 3D surface image of the solvent-debound part that shows no evidence of surface porosity. From Figure 3a, it is also apparent that the shape form and dimensions of the green part are largely retained in the brown part. The visualization of the debinding defects and resulting surface porosity shows a two-fold increase in the relative pore density to approximately 0.10 mm³ in Figures 4b and 4c. This observation is expected since the extraction of the soluble binder during solvent debinding is known to be the source of porosity in the brown part (Ji *et al.*, 2001; Tsai and Chen, 1995). Hwang, Shu and Lee (2005) have also demonstrated that pore channels develop and the average pore size increases as solvent debinding proceeds.

Figure 4b shows remarkable differences between the surface regions and the interior due to varying material density. This difference can be used to determine porosity distribution towards the sample surfaces arising from the development of pore channels and increasing average pore size during solvent debinding (Hwang, Shu and Lee, 2005).

Perhaps the most compelling evidence for the use of tomographical probing techniques to non-destructively investigate the 3D internal structure of MIM-prepared 17-4 PH stainless steel is shown in the analysis of the sintered part illustrated in Figure 5. Figure 5a shows a reconstructed 3D surface image of a selected sintered part exhibiting only some occurrences of open pores. Figure 5b and Figure 5c however reveal the existence of an uncharacteristically large irregular subsurface feature with a maximum defect volume of approximately 1.00 mm³.

Table III
Properties of as-sintered parts 17-4 PH stainless steel against MPIF and ASTM standards (MPIF, 2016; ASTM International, 2005)

Material	Density (g/cm ³)	YS (MPa)	UTS (MPa)	Elongation (%)	Hardness (HV)
This study	7.6	661	838	6.4	308#
Standards	7.5	650	790	4.0	279

indicates that the hardness values were converted from HRC to HV in accordance with ASTM A370 – 03A (ASTM International, 2003)

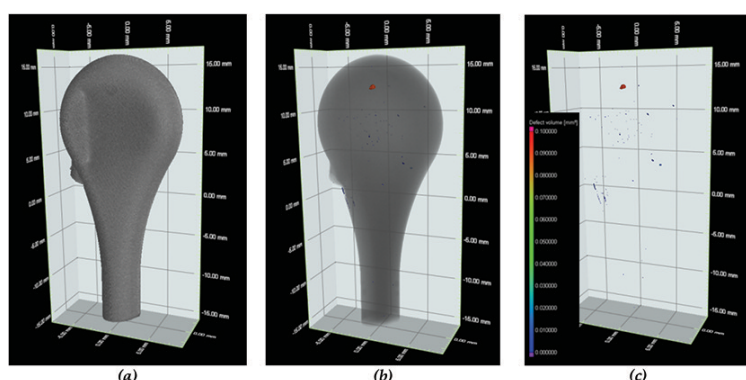


Figure 3—(a) Reconstructed as-molded green part μXCT surface model, (b) 3D μXCT showing the part's defect volume and (c) the size and spatial distribution of the porosity and inclusions as obtained after segmentation – the figure legend applies to the entire figure. Resolution: 14.6 µm

X-ray computed microtomography studies of MIM and DPR parts

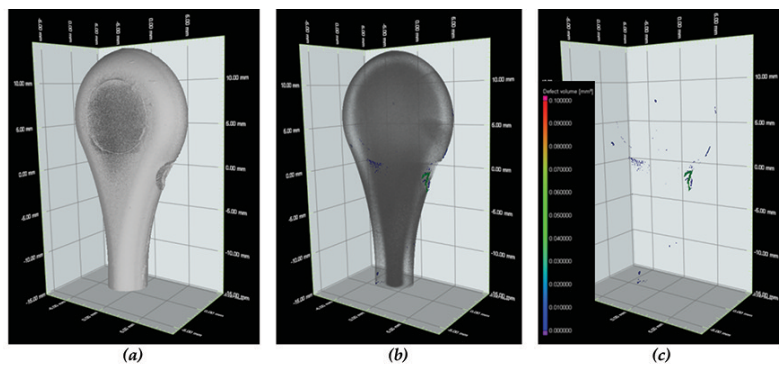


Figure 4—(a) Reconstructed µXCT surface model of a solvent-debound part, (b) 3D µXCT showing the part's defect volume and (c) the size and spatial distribution of the porosity and inclusions as obtained after segmentation – the figure legend applies to the entire figure

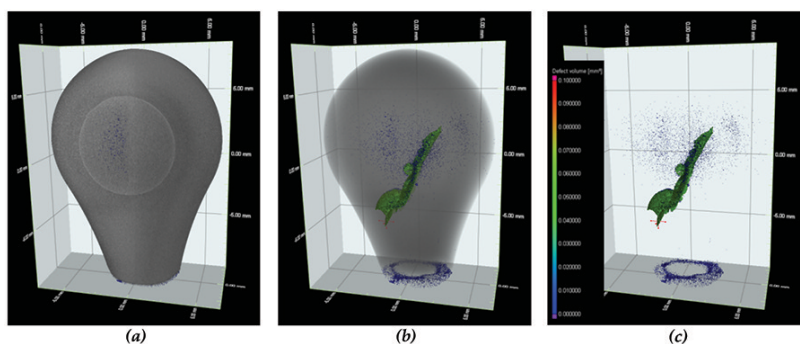


Figure 5—(a) Reconstructed as-moulded green part µXCT surface model, (b) 3D µXCT showing the part's defect volume and (c) the size and spatial distribution of the porosity and inclusions as obtained after segmentation – the figure legend applies to the entire figure

MIM-fabricated 17-4 PH stainless steel parts are intrinsically susceptible to porosity (Murray *et al.*, 2011; James, 2015) which arises from innumerable sources during MIM processing. However, after sintering, the pores are typically near-spherical in morphology; see Figure 6a for example. The origin of the ‘uncharacteristically large irregular pore’ feature is attributed to either incomplete die cavity filling during the injection moulding stage or (most probably) a combination of pore formation due to gas entrapment (thermal debinding evolved products) during sintering (German and Bose, 1977) and the shrinkage porosity, since it is located in the thickest section of the part. Such features are uncommon and are therefore seldom reported. The observed open surface pores after sintering can be attributed to either the residual porosity from solvent debinding, voids remaining after thermal debinding, or the evaporation of alloy elements (chromium and manganese) due to their high vapour pressure during high-temperature sintering (Murray *et al.*, 2011).

Microscopy of MIM parts

A typical secondary electron SEM micrograph of the as-polished 17-4 PH sintered specimen is presented in Figure 6a. The pores are evenly distributed and primarily spherical in morphology; indicating that at 1300°C, sintering progressed to its final possible stages.

The pore sizes and distribution were determined by evaluating the SEM micrographs using ImageJ software (Schindelin *et al.*, 2015). The pore size distribution

histogram obtained from comprehensive image analysis is presented in Figure 6b. The pore sizes observed exhibit a lognormal peak (distribution mode approx. 1.0 µm) with the largest pores typically less than 4.5 µm in diameter. The largest pore sizes obtained from the image analysis are much smaller than those detected by the lowest resolution of 10 µm that can be achieved by the µXCT machine even after having compromised on the size of the piece to be analysed.

DPR parts and properties

Ti-HDH 100 mesh (-150 µm) powders were supplied by Chengdu Huarui Industrial Co., Ltd in China. The powder particle sizes and morphology are reported elsewhere (Motsai, 2016). The powders were roll compacted. Figure 7 shows photographs of rolled strips that are 20, 50 and 100 mm wide. By observation, the rolled strips demonstrate

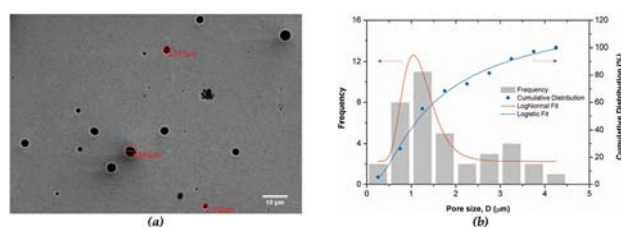


Figure 6—(a) As-polished SE-SEM micrographs of the sintered specimen and (b) pore size distribution histogram obtained from comprehensive image analysis

X-ray computed microtomography studies of MIM and DPR parts

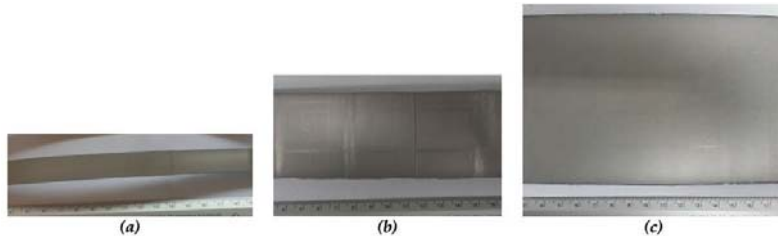


Figure 7—Photographs of Ti HDH 100 mesh strips rolled at 0.3 mm roll gap and (a) 20 mm, (b) 50 mm and (c) 100 mm set widths

good densification without exhibiting obvious signs of warping, cracking and alligatoring, which are typical rolling defects (Park *et al.*, 2012; Joo *et al.*, 2005).

Table IV summarizes the properties of the green (rolled) and brown (sintered) Ti-HDH strips. The hardness values for the higher density 20 mm strips were closer to the commercially pure Ti grade 4. The hardness values were reduced for the lower density 50 mm and 100 mm strips. A reduction in hardness has been observed in powder metallurgy components and is due to the amount of pores in the components (Dutta and Bose, 2012). The density results show an increase after sintering. However, full density was not achieved by sintering for all the strips.

Microscopy of DPR parts

Sintering of the strips in Figure 7 was carried out. Results of the sintering studies showed that full density was not achieved at the selected sintering condition used. These measured densities do not provide any information regarding the position and distribution of the pores within the strips. Therefore, microscopy was carried out to determine the distribution of porosity within the strips. The 20 mm strip was cut in half along the rolling direction, mounted and polished. Figure 8a shows a micrograph taken to include the edge of the strip. It can be seen that the strip had a lower density at the edge (right side of the micrograph) which increased towards the centre (left side of micrograph) of the strip. For samples larger than 20 mm, several samples were cut from the edge, midway between edge and centre and centre of the strips. Figure 9b and 9c show the micrographs of the 100 mm wide strip from the centre and the edge of the strips respectively. It is clear from the micrographs that the porosity pattern is similar to that of the 20 mm strips was observed, with the density being higher at the centre and lower at the edge of the compact.

It was also observed that after sintering, warping of the strips occurred. The microscopy studies showed that the sintered strips had non-uniform density across the width, which implies non-uniform density in the green strips as well. Density variations within the green strip are known to create residual stresses and cause different densification rates during sintering, which ultimately cause the dimensional distortions (Khoei, 1995). It is therefore plausible that the observed dimensional distortions (warping) of the sintered strips in this study are a consequence of the non-uniform density within the strips.

MicroCT scanning of DPR parts

In order to understand the extent of density variations in the DPR strips, an alternative XCT scanning technique was used.

The XCT scanning technique was evaluated for use as a non-destructive test for detecting non-uniform densities, with the additional benefit of elimination of the tedious microscopy studies required to map DPR strips that are long and wide.

By way of illustration, Figure 9 shows the visualization of 3D XCT data on a section of the 20 mm wide sintered rolled strip. Similarly to the MIM XCT results shown in Figure 3, three analysis steps were conducted in each case involving (a) reconstructing the 3D surface, (b) the identification of the open pores, interior pores and inclusions and (c) isolating the open pores, interior pores and inclusions identified in (b) for structural properties and visualisation

The reconstructed surface in Figure 9a shows the surface defects such as chipping of the strip at the edges and the different grey levels characteristic of the varying densities. No other rolling defects are detected in the strip. Figure 9b shows the 3D distribution of pores in the sintered volume while Figure 9c shows the pores in isolation. The result confirms the presence of density variations in the sintered DPR strips as shown by the microscopy studies. Furthermore, XCT was able to show that the pores are concentrated at the edges of the strips, with some detected in the transverse direction to rolling as is typical of compacts produced by non-optimal rolling conditions. Using traditional techniques to detect these density changes, sections of the strips are cut up, mounted and polished to look for porosity differences in the compacts. This process is destructive and tedious. In this study the

Table IV
Properties of green and brown Ti-HDH strips

Material	Green density (g/cm ³)	Brown density (g/cm ³)	Macro hardness (HV5kg)
20 mm wide strip	3.7	4.3	268
50 mm wide strip	3.2	4.0	185
100 mm wide strip	3.2	4.0	180
ASTM CP Grade 4 Ti		4.51	280

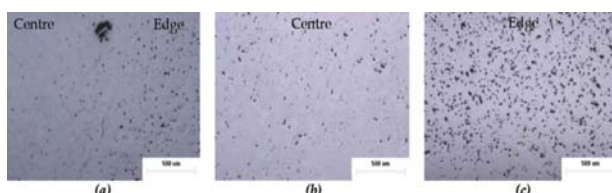


Figure 8—SEM micrographs of (a) 20 mm, (b) centre of 100 mm and (c) edge of 100 mm samples

X-ray computed microtomography studies of MIM and DPR parts

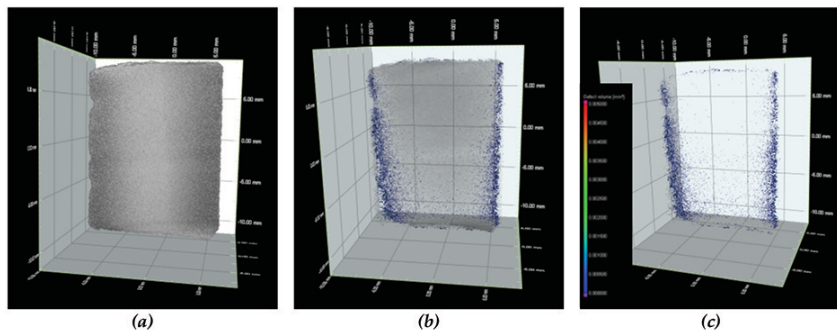


Figure 9—µXCT visualization of portions of the 20 mm strips. The results show that the strips are dense at the centre and less dense at the edges

visualization of the density variation and edge porosity is made clear in Figure 9b and 9c.

Results from this study show that µXCT scanning is suitable for characterizing small-sized samples such as the 20 mm wide strip shown in Figure 9. However, when the examination of bigger samples such as the 50 and 100 mm wide strips was attempted, the overall instrument resolution was compromised, making it difficult to resolve the pore structures. Owing to the size effects, it was necessary to section wider or longer strips to small sections, requiring a large number of scans to map out a significant size of the compacts. This diminished the benefit of non-destructive testing and ability to map out the densities for wider and longer strips.

Conclusions

An important advantage of the µXCT method is that no specific sample preparation is needed. Detailed quantitative and qualitative information obtained in this study relating to the 3D internal structure of MIM-prepared 17-4 PH stainless steel and DPR-prepared parts shows that XCT is a powerful non-invasive and non-destructive measurement technique that can be very useful for research purposes. Structural parameters such as relative volume, spatial distribution, size and shape distributions, specific area, connectivity and orientation are resolved with the benefit of colour-coded visualization of individual pores and inclusions according to volume.

Analysis of MIM and DPR parts demonstrated:

- i. µXCT scanning conducted in this study demonstrated the capabilities by detecting the amount, position, and distribution of the pores in MIM and DPR parts, as well as detecting sub-surface features such as shrinkage pores as seen on the sintered MIM parts
- ii. Comparative µXCT and SE-SEM shows that the spatial resolution of the µXCT will limit the smallest detectable variations in the as-produced porous samples. Features smaller than the resolution will not be measured correctly. Based on the findings, it is therefore, concluded that a higher resolution scan such as X-ray nano-tomography has to be used to study porosity evolution in these parts
- iii. The examination of different pore structures in wider or longer rolled strip samples (such as the 50 and 100 mm) with µXCT was not successfully achieved

with the required resolution, without the need to section the wider or longer strips into small sections, thus requiring a large number of scans.

Acknowledgements

The contributions of Ntate Sam Papo, Mandy Seerane, Hilda Chikwanda and Pierre Rossouw are duly recognized. This work is funded by the DST and the CSIR. NSM acknowledges the NRF for financial support through the DST-NRF Internship Programme. The authors are also indebted to Atmix Corp. (JP) for the supply of powder materials used in the preparation of MIM components.

References

- ALDICU, G., TISEANU, I., BADICA, P., CRACIUNESCU, T. and RINDFLEISCH, M. 2010. X-ray micro-tomography as a new and powerful tool for characterization of MgB₂. *Superconductor*. Juiz, A.M. (ed.). Scyo.
- ASTM INTERNATIONAL. 2005. ASTM B883-05, Standard Specification for Metal Injection Molding (MIM) Ferrous Materials. West Conshohocken, PA.
- ASTM INTERNATIONAL. 2003. ASTM A370-03a, Standard Test Methods and Definitions for Mechanical Testing of Steel Products. West Conshohocken, PA.
- BARRIERE, T., LIU, B. and GELIN, J.C. 2003. Determination of the optimal process parameters in metal injection molding from experiments and numerical modeling. *Journal of Materials Processing Technology*, vol. 143–144, pp. 636–644.
- BATENI, A., PARVIN, N. and AHMADI, M. 2011. Density evaluation of powder metallurgy compacts using *in situ* X-ray radiography. *Powder Metallurgy*, vol. 54, no. 4, pp. 533–536.
- CANTIN, M.A. and GIBSON, G.M.D. 2015. Titanium sheet fabrication from powder titanium. *Powder Metallurgy*. Qian, M. and Froes, F.H. (eds.). Elsevier, pp. 383–403.
- CANTIN, G.M.D., KEAN, P.L., STONE, N.A., WILSON, R., GIBSON, M.A., YOUSUFF, M., RITCHIE, D. and RAJAKUMAR, R. 2011. Innovative consolidation of titanium and titanium alloy powders by direct rolling. *Powder Metallurgy*, vol. 54, pp. 188–192.
- CANTIN, D., KEAN, P., STONE, N.A., WILSON, R., GIBSON, M.A., RITCHIE, D. and RAJAKUMAR, R. 2010. Direct powder rolling of titanium. *Proceedings of Titanium 2010*, Orlando, Florida, 3–6 October 2010. International Titanium Association, Northglenn, CO.
- CHEN, J., CHEN, L., CHANG, C.-C., ZHANG, Z., LI, W., SWAIN, M.V. and LI, Q. 2016. Micro CT based modelling for characterising injection moulded porous titanium implants. *International Journal for Numerical Methods in Biomedical Engineering*. [DOI: 10.1002/cnm.2779].
- CHIKOSHA, S., SHABALALA, T.C. and CHIKWANDA, H.K. 2014. Effect of particle morphology and size on roll compaction of Ti-based powders. *Powder Technology*, vol. 264, pp. 310–319.
- DE CHIFFRE, L., CARMIGNATO, S., KRUTH, J.P., SCHMITT, R. and WECKENMANN, A. (2014). Industrial applications of computed tomography. *CIRP Annals - Manufacturing Technology*, vol. 63, no. 2, pp. 655–667.

X-ray computed microtomography studies of MIM and DPR parts

- DU PLESSIS, A., LE ROUX, S.G., BOOYSEN, G. and ELS, J. 2016. Directionality of cavities and porosity formation in powder-bed laser additive manufacturing of metal components investigated using X-ray tomography. *3D Printing and Additive Manufacturing*, vol. 3, no. 1. pp. 48–55.
- DUTTA, G. and BOSE, D. 2012. Effect of sintering temperature on density, porosity and hardness of a powder metallurgy component. *International Journal of Emerging Technology and Advanced Engineering*, vol. 2, no. 8. pp. 121–123.
- FANG, W., HE, X., ZHANG, R., YANG, S. and QU, X. 2014. The effects of filling patterns on the powder–binder separation in powder injection molding. *Powder Technology*, vol. 256. pp. 367–376.
- FROES, F.H., MASHI, S.J., HEBEISEN, J.C., MOXSON, V.S. and DUZ, V.A. 2004. The technologies of titanium powder metallurgy. *JOM*, vol. 56. pp. 46–48.
- GERMAN, R. 2013. Progress in titanium metal powder injection molding. *Materials*, vol. 6. pp. 3641–3662.
- GERMAN, R.M. 1990. Powder injection molding. Metal Powder Industries Federation, Princeton, NJ.
- GERMAN, R.M. and BOSE, A. 1977. *Injection Molding of Metals and Ceramics*. Metal Powder Industries Federation Princeton, NJ.
- HELDELE, R., RATH, S., MERZ, L., BUTZBACH, R., HAGELSTEIN, M. and HAUSSET, J. 2006. X-ray tomography of powder injection moulded micro parts using synchrotron radiation. *Nuclear Instruments and Methods in Physics Research Section B: Beam Interactions with Materials and Atoms*, vol. 246, no. 1. pp. 211–216.
- HOFFMAN, J.W. and BEER, F.C.D.E. 2012. Characteristics of the micro-focus X-ray tomography system at the MIXRAD facility at NECSA in South Africa. *Proceedings of the 18th World Conference on Nondestructive Testing*, Durban, South Africa, 16–20 April 2012. South African Institute for Non-Destructive Testing. http://www.ndt.net/article/wcndt2012/papers/37_wcndtfinal00037.pdf
- HWHWANG, P.S.K.S., SHU, G.J. and LEE, H.J. 2005. Solvent debinding behavior of powder injection molded components prepared from powders with different particle sizes. *Metallurgical and Materials Transactions*, vol. 36 no. 1. pp. 161–167.
- JAMES, W.B. 2015. *ASM Handbook*, vol. 7. 922 p.
- JOO, S.H., CHANG, H.J., BANG, W.H., HAN, H.N. and OH, K.H. 2005. Analysis of alligatoring behavior during roll pressing of DRI powder with flat roller and indentation-type roller. *Materials Science Forum*, vol. 475–479. pp. 3223–3226.
- KARA, E. and MATULA, G. 2015. Review of innovation in using X-ray tomography for non-destructive analysing of the green parts. *Journal of Achievements in Materials and Manufacturing Engineering*, vol. 73, no. 2. 139 p.
- KHOEI, A. 2005. Computational Plasticity in Powder Forming Processes. Elsevier, Tehran.
- KOHN, H.W. 1972. Non-destructive testing. *Journal of General Education*, vol. 24. pp. 176–178.
- LI, Y., LI, L. and KHALIL, K.A. 2007. Effect of powder loading on metal injection molding stainless steels. *Journal of Materials Processing Technology*, vol. 183. 432 p.
- JI, C.H., LOH, N.H., KHOR, K.A. and TOR, S.B. 2001. Sintering study of 316L stainless steel metal injection molding parts using Taguchi method: final density. *Materials: Science and Engineering A*, vol. 311. pp. 74–82.
- LUNEL, M. 2013. Structure Characterisation of catalysts using X-ray micro-computed tomography, PhD thesis, University of Birmingham, United Kingdom.
- MA, J., LI, A. and TANG, H. 2016. Study on sintering mechanism of stainless steel fiber felts by X-ray computed tomography. *Metals*, vol. 6, no. 1. 18 p.
- MACHAKA, R. and CHIKWANDA, H.K. 2015. Kinetics of titanium metal injection moulding feedstock thermal debinding. *Proceedings of the Seventh International Light Metals Technology Conference*, (LMT 2015), Port Elizabeth, South Africa, 27–29 July 2015. Chikwanda, H.K. and Chikosha, S. (eds.). pp. 1–6.
- MACHAKA, R., SEERANE, M. and CHIKWANDA, H.K. 2014. Binder development for metal injection moulding: a CSIR perspective. *Advances in Powder Metallurgy and Particulate Materials - 2014. Proceedings of the 2014 World Congress on Powder Metallurgy and Particulate Materials, PM 2014*, Orlando, Florida, 18–22 May. Metal Powder Industries Federation. pp. 43–58.
- MAIRE, E., BUFFIÈRE, J.Y., SALVO, L., BLANDIN, J.J., LUDWIG, W. and LÉTANG, J.M. 2001. X-ray micro-tomography an attractive characterisation technique in materials science. *Advanced Engineering Materials*, vol. 3, no. 8. pp. 539–546.
- MARTIN, P., HASKINS, J., THOMAS, G. and DOLAN, K. 2003. Advanced NDE techniques for powder metal components. *Proceedings of the International Conference on Powder Metallurgy and Particulate Materials (PM2TEC 2003)*, Las Vegas, Nevada, 8–12 June 2003. Metal Powder Industries Federation, Princeton, NJ.
- MOTSAI, T.M., CHIKOSHA, S., BHERO, S. and CHIKWANDA, H.K. 2016. Investigation of pressing and sintering of Ti-HDH powder. *Proceedings of Ferrous 2016, Ferrous and Base Metals Development Network (FMDN)*, (In Press).
- MPIF. 2016. *MPIF Standard 35*, Materials Standards for Metal Injection Molded Parts. 2016 edn. Metal Powder Industries Federation (MPIF), Princeton, NJ.
- MURRAY, K., COLEMAN, A.J., TINGSKOG, T.A. and WHYCHELL D.T. SR. 2011. Effect of particle size distribution on processing and properties of MIM 17-4PH. *International Journal of Powder Metallurgy*, vol. 47, no. 4. pp. 21–28.
- MUTINA, A. and KOROTEV, D. 2012. Using X-ray microtomography for the three dimensional mapping of minerals. *Microscopy and Analysis*, vol. 26, no. 2. pp. 7–12.
- NOR, N.H.M., MUHAMAD, N., ISMAIL, M.H., JAMALUDIN, K.R., AHMAD, S. and IBRAHIM, M.H.I. 2009. Flow behaviour to determine the defects of green part in metal injection molding. *International Journal of Mechanical and Materials Engineering*, vol. 4. pp. 70–75.
- O'BRIEN, R.C. and JAMES, W.B. 1988. A review of nondestructive testing methods and their applicability to powder metallurgy processing. *MPIF Seminar on Prevention and Detection of Cracks in Ferrous P/M Pads, International Powder Metallurgy Conference and Exhibition*. pp. 1–17.
- PARK, N.K., LEE, C.H., KIM, J.H. and HONG, J.K. 2012. Characteristics of powder-rolled and sintered sheets made from HDH Ti powders. *Key Engineering Materials*, vol. 520. pp. 281–288.
- PETERSON, S. 2010. Investigation of the Hot deformation of Sintered Titanium Compacts Produced from Direct reduction Powder. Masters thesis, University of Cape Town, South Africa.
- QIAN, MN. 2010. Cold compaction and sintering of titanium and its alloys for near-net- shape or preform fabrication. *International Journal of Powder Metallurgy*, vol. 46, no. 5. pp. 29–44.
- RO, D.H., TOAZ, M.W. and MOXSON, V.S. 1983. The direct powder-rolling process for producing thin metal strip. *JOM*, vol. 35, no. 1. pp. 34–39.
- SCHINDELIN, J., RUEDEN, C.T., HINER, M.C. and ELICEIRI, K.W. 2015. The ImageJ ecosystem: An open platform for biomedical image analysis. *Molecular Reproduction and Development*, vol. 82, nos. 7–8. pp. 518–529.
- SEERANE, M., CHIKWANDA, H. and MACHAKA, R. 2015. Determination of optimum process for thermal debinding and sintering using Taguchi method. *Materials Science Forum*, vol. 828–829. 138 pp.
- SEERANE, M., ND LANGAMANDLA, P. and MACHAKA, R. 2016. The influence of particle size distribution on the properties of metal-injection-moulded 17-4 PH stainless steel. *Proceedings of Ferrous 2016, Ferrous and Base Metals Development Network (FMDN)*, (In Press).
- SOTOMAYOR, M.E., VÁREZ, A. and LEVENFELD, B. 2010. Influence of powder size distribution on rheological properties of 316L powder injection moulding feedstocks. *Powder Technology*, vol. 200, nos. 1–2. pp. 30–36.
- TAMMAS-WILLIAMS, S., ZHAO, H., LÉONARD, F., DERGUTI, F., TODD, I. and PRANGNELL, P.B. 2015. XCT analysis of the influence of melt strategies on defect population in Ti-6Al-4V components manufactured by selective electron beam melting. *Materials Characterization*, vol. 102. pp. 47–61.
- TSAI, D.S. and CHEN, W.W. 1995. Solvent debinding kinetics of alumina green bodies by powder injection molding. *Ceramics International*, vol. 21, no. 4. pp. 257–264.
- WEBER, O., RACK, A., REDENBACH, C., SCHULZ, M. and WIRJADI, O. 2011. Micropowder injection molding: investigation of powder–binder separation using synchrotron-based microtomography and 3D image analysis. *Journal of Materials Science*, vol. 46, no. 10. pp. 3568–3573.
- YANG, S.-D., ZHANG, R.-J. and QU, X.-H. (2015a). X-ray tomography analysis of aluminum alloy powder compaction. *Rare Metals*. pp. 1–7.
- YANG, S., ZHANG, R. and QU, X. 2015b. Optimization and evaluation of metal injection molding by using X-ray tomography. *Materials Characterization*, vol. 104. pp. 107–114. ◆



Effect of niobium on the solidification structure and properties of hypoeutectic high-chromium white cast irons

by M.E. Maja*†, M.G. Maruma*, L.A. Mampuru* and S.J. Moema*

Synopsis

The most commonly used high-chromium white cast iron (HCWCI) is the hypoeutectic white cast iron that contains 2–3.5 wt.% C and 10–30% Cr. This type of material relies on hard, brittle M_7C_3 carbides to impart good wear resistance. Due to its good wear resistance, this material has found application in the mining industry and cement industry. However, it has low fracture strength and this challenge led to research aimed at refining the microstructure. This was done by the addition of niobium in the range between 0.1 and 0.6 wt.%. In the as-cast condition, the addition of niobium was found to increase the fracture strength due to the finer eutectic microstructure. The hardness was also found to have increased slightly compared to the reference alloy with no niobium additions. Low fracture strength after heat treatment was observed in the Nb-added HCWCI, which is believed to have been caused by the precipitation of secondary carbides and the transformation of the matrix from austenite to martensitic.

Keywords

HCWCI, niobium, grain refinement, fracture strength.

Introduction

For the past few years Mintek has been involved in a project in which a number of alloys have been identified for grinding media applications. The high-chromium white cast iron (HCWCI) alloys were among the alloys researched for this application. The knowledge acquired from the grinding ball media research has now been extended to mill liners, which have traditionally been made of manganese-, chromium- and chrome-molybdenum steels. The replacement of worn mill liners costs the mining industry a significant amount of money and this has led to a need for continuous research to prolong the life of the liners. During milling operations, liner wear has an adverse effect on the capacity of the mill, the energy efficiency and milling efficiency and finally leads to relining, to replace worn liners.

The mill efficiency depends on the charge motion, which in turn is largely influenced by the liner profiles and performance. The choice of a liner requires a holistic approach that examines the compatibility with the mill conditions, the mechanical performance and the cost-effectiveness. The operating conditions in a fine grinding mill require that the liner should be made of highly wear-

resistant material with some fracture strength such as (HCWCI).

HCWCI contains a minimum of 2% C with a chromium content ranging from 15% to 35%. The term 'white cast iron' refers to the appearance of a white fractured surface in the material after damage, due to the presence of white cementite. This material has been proven to be effective for applications in aggressive environments where wear and erosion resistance are required. The high wear resistance of HCWCI is attributed to the microstructural constituents such as hard primary and/or eutectic carbides of M_7C_3 (where M is iron, chromium and other strong carbide formers) and a relatively ductile ferrous matrix (Bedolla-Jacuinde *et al.*, 2005, 2007; Adler and Dogan, 1999; Dogan, Hawk and Laird, 1997; Stevenson and Hutchings, 1995; Radzikowska, 2004). Austenitizing at a temperature above 1100°C leads to the precipitation M_7C_3 carbides while below 1100°C the precipitation of both M_7C_3 and $M_{23}C_6$ carbides, which are rich in alloying elements, occurs (Kootsookos and Gates, 2008). The precipitation of secondary carbides lowers the alloy content in the dendritic austenite and thus raises the martensite start temperature, hence the formation of martensite upon cooling (Cetinkaya, 2006).

The hardness of M_7C_3 is in the range of 1200 HV (Stevenson and Hutchings, 1995), which may vary with the composition and the ferrous matrix binds the hard M_7C_3 carbides and provides the material with certain fracture strength that is vital for handling high impact forces (Bedolla-Jacuinde *et al.*, 2005;

* Advanced Materials Division, Mintek Randburg, Johannesburg, South Africa.

† Tshwane University of Technology, Pretoria, South Africa.

© The Southern African Institute of Mining and Metallurgy, 2016. ISSN 2225-6253. This paper was first presented at the AMI Ferrous and Base Metals Development Network Conference 2016 19–21 October 2016, Southern Sun Elangeni Maharani, KwaZulu-Natal, South Africa.

Effect of niobium on the solidification structure and properties of hypoeutectic

Cetinkaya, 2006; Lewellyn *et al.*, 2004). Through appropriate heat treatment and alloying, different structures of the matrix can be formed. Pearlite, martensite and austenite are among the typical microstructures of the matrix (Radzikowska, 2004; Cetinkaya, 2006; Lewellyn *et al.*, 2004; Correa *et al.*, 2007; Thorpe and Chicco, 1985; Dolman, 2005). HCWCIs thus typically have high strength and hardness.

However, HCWCIs have low fracture strength. The objective of this project is to improve the life and mechanical properties of the current HCWCI alloys through grain refinement. Grain refinement is the only strengthening method that also improves the fracture strength of iron. Many researchers (Zhang *et al.*, 2014; Zhi *et al.*, 2008a, 2008b) have attempted to improve the mechanical properties of HCWCI through grain refinement, especially in hypereutectic HCWCI. However, their work focused more on improving the wear resistance by increasing the hardness. This work focuses more on improving the fracture strength of the materials by the addition of niobium as a grain refiner. Increasing the fracture strength of HCWCI will open doors for other application outside of the mining industry.

Experimental procedure

Casting of alloys

Three HCWCI alloys were melted in a medium-frequency induction furnace with a capacity of about 150 kg. Charge material was prepared to give the targeted chemistry as shown in Table I.

The test materials produced for this project consisted of HCWCI in the form of 50 mm × 100 mm × 500 mm rectangular flat test bars (thickness × width × length) as shown in Figure 1. The alloys were examined for surface defects before proceeding with testing. Cast iron mould boxes (0.5 m length, 0.38 m width and 0.14 m depth) were used to

accommodate both the drag (bottom) and cope (top) parts of the pattern.

Heat treatment

The alloys were austenitized at 875°C for 3 hours and force air-quenched. Force air-quenching was chosen for an increased cooling rate to avoid the formation of a pearlitic microstructure. The samples were then tempered at 450°C for 3 hours then air-cooled to room temperature. This was employed to transform all the retained austenite.

Microstructural analysis

Specimens were removed from the heat-treated samples, polished and etched with Murakami and 3% nital. The microstructural analysis was carried out using an Olympus PGM optical microscope equipped with Analysis Image software and by scanning electron microscopy.

Hardness

Brinell hardness measurements were performed through the cross-sections of the as-cast and heat-treated test samples, using a load of 750 kg. The measurements were taken from the surface to the centre of the rectangular test pieces to evaluate whether there were any hardness changes within the test sample.

Bending tests

Bending tests are intended for brittle materials when the scope of test is to determine the strength of material. Specimens with dimensions of 50 × 100 × 500 mm were used. The cast blocks were placed in the specially designed mandrel and the load applied to break them without any preparation to the samples (*i.e.* machining). The specimen is placed on two supports that are 300 mm apart (L) and the force applied in the exact middle of the two supports ($L/2$). To determine the bending strength Q_{\max} , the beam must be so proportioned that it will not fail in shear or by lateral deflection before reaching its ultimate flexural strength. Hence, for a rectangular part in a three-point bending test, the bending strength is the highest stress at the moment of rupture. Usually, long specimens with higher length to depth ratio ($L/h > 10$) are recommended.

Results and discussion

Microstructural analysis

As-cast alloys

The microstructures of the as-cast alloys, depicted in Figure 2, consist of primary austenite dendrites surrounded by a eutectic mixture of carbide particles and austenite. It can be seen from Figure 2 that the M_7C_3 carbides are rod- and needle-like in morphology and that the stress concentration at the tips of the needle-type carbides will play a major role when the material is subjected to impact loading. Addition of niobium to HCWCI has changed the morphology of the rod-shaped M_7C_3 to isotropic. This change in carbide morphology plays a critical role determining the fracture strength of the HCWCI.

Etching with 3% nital revealed the presence of a thin dark layer surrounding the eutectic carbides. This layer was found

Table I

Actual chemical composition of tested alloys

Alloy	Composition
Alloy 1	ASTM A 532 Class III
Alloy 2	ASTM A 532 Class III + 0.1-0.4Nb
Alloy 3	ASTM A 532 Class III+ 0.4-0.6Nb

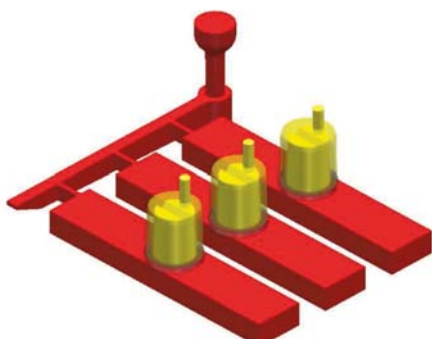


Figure 1—Pattern that was used to produce the alloys

Effect of niobium on the solidification structure and properties of hypoeutectic

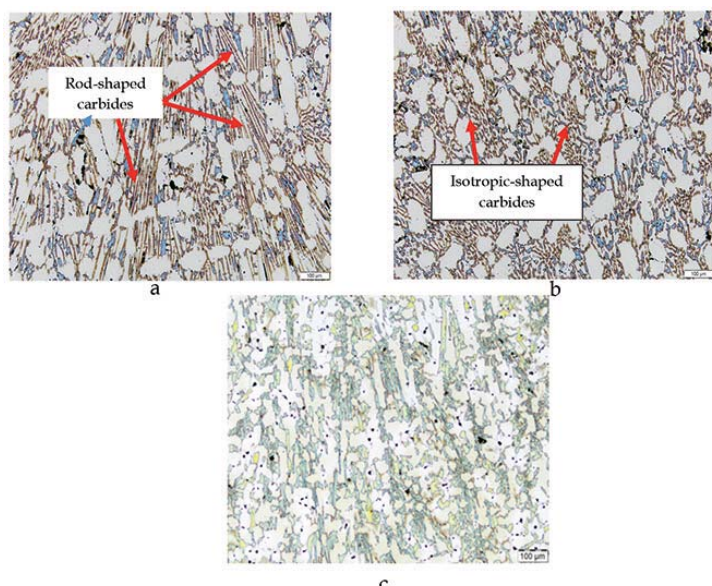


Figure 2—Effect of niobium on the microstructure of HCWCI (a) 0%Nb, (b) 0.1–0.4% and Nb (c) (0.4–0.6%Nb)

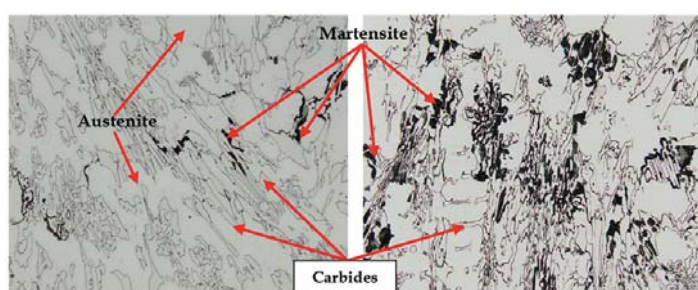


Figure 3—Microstructures of HCWCI with 0.1–0.4% and 0.4–0.6% Nb showing the presence of martensite at the carbide interface

to be martensite (Figure 3). According to the literature (Zum Gahr and Eldis, 1980; Matsubara *et al.*, 2001; Turenne *et al.*, 1989; Tabrette and Sare, 1998, 1997, 2000; Tabrette *et al.*, 1996) the formation of the eutectic carbides in contact with the primary austenitic phase leads to excessive consumption of carbon and chromium in the interfacial region, depleting these elements in the interface and increasing the M_s temperature. As a result, martensite forms at the periphery of the primary carbide particles.

The role of the Nb in grain refinement can be explained as follows. The formation of the first precipitated NbC reduces the carbon available to form primary M_7C_3 carbides and as a result the volume fraction and the size of the primary M_7C_3 carbides decreases (Zhi *et al.*, 2008b). The concentration of Nb in the matrix and M_7C_3 is very low as this element tends to partition into NbC in the Fe-Cr-Cr (Zhi *et al.*, 2008b; Hannes and Gates, 1997; Coelho *et al.*, 2003; Baik and Loper, 1998). This results in niobium enrichment at the grain boundaries of the carbides during solidification until NbC precipitates due to solubility of Nb at the grain boundaries being exceeded. The precipitated NbC impedes the preferential directional growth of the M_7C_3 carbides and result in finer, isotropic carbides (Fiset *et al.*, 1993; Zhi *et al.*, 2008b).

Heat-treated alloys

Figure 4 shows the microstructural analysis of the HCWCI after heat treatment. It is evident that the morphology of the microstructure has changed significantly from the as-cast condition. After heat treatment the microstructures reveals the presence of primary and eutectic carbides in a martensitic matrix. Precipitation of secondary carbides during austenitising resulted in the depletion of carbon in the austenite and during quenching the austenite partially transformed to martensite (see Figure 5). Addition of niobium resulted in grain refinement of the HCWCI.

The presence of NbC was also evident from SEM-EDX mapping as shown by the dark spots in Figures 6 and 7. Niobium is a strong carbide-forming element and it has been found that NbC particles are formed before the precipitation of primary carbides when niobium is added into the melts (Fiset *et al.*, 1993).

Effect of niobium on hardness

The effect of niobium on the hardness of HCWCI is also given in Table II. It can be seen that the as-cast hardness firstly increases with the addition of Nb and then decreases with a further increase in niobium.

Effect of niobium on the solidification structure and properties of hypoeutectic

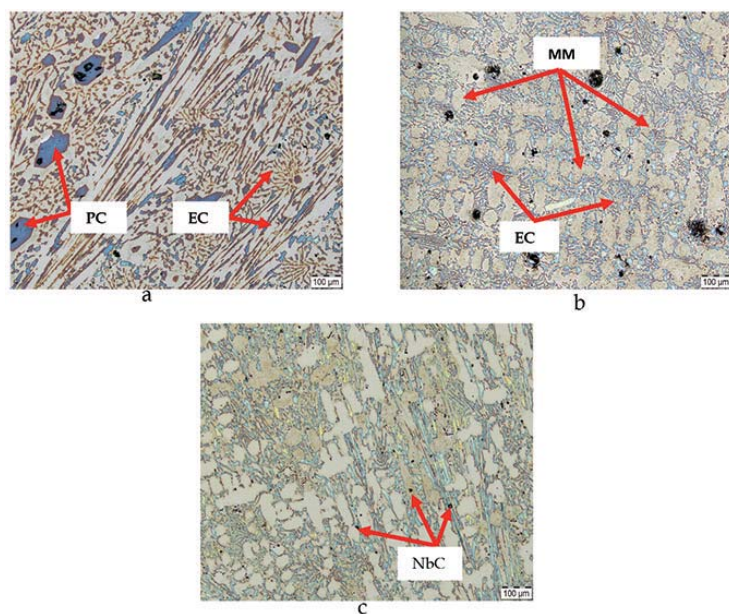


Figure 4—Effect of niobium on the microstructure of HCWCI (a) 0%Nb, (b) 0.1–0.4% Nb and (c) (0.4–0.6%Nb). PC=primary carbides, EC=eutectic carbides, MM=martensitic matrix

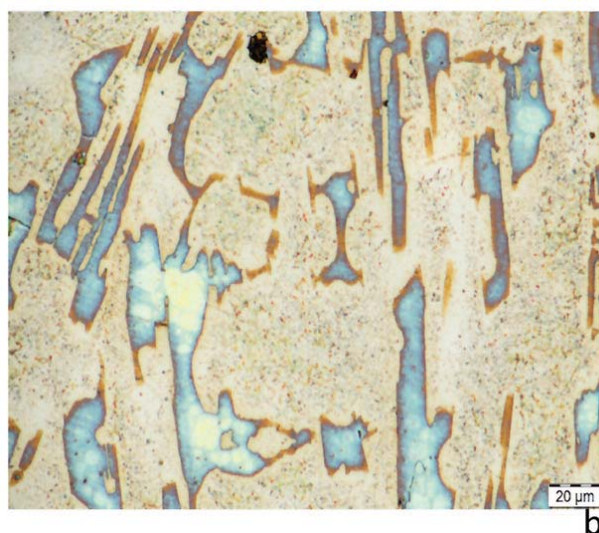


Figure 5—High-magnification microstructure of HCWCI with 0.1–0.4% Nb showing the presence of secondary carbides (dark spots within the matrix)

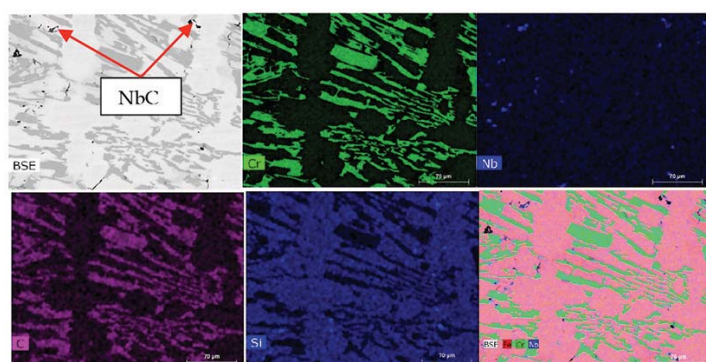


Figure 6—SEM-EDX mapping of the as-cast HCWCI with addition of 0.1–0.4% Nb

Effect of niobium on the solidification structure and properties of hypoeutectic

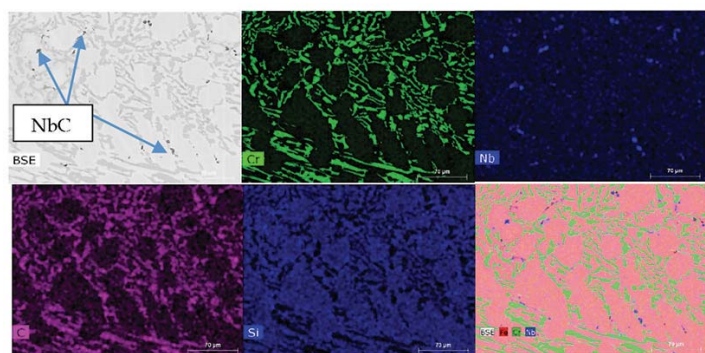


Figure 7—EDS mapping of the as-cast HCWCI with addition of 0.4–0.6% Nb

Table II

The effect of niobium on the hardness of HCWCI

Alloy	Brinell hardness average (BHN)
Reference	432
0.1–0.4%Nb alloy	485
0.4–0.6%Nb alloy	438
Reference (HT)	457
0.1–0.4%Nb alloy (HT)	354
0.4–0.6% Nb alloy (HT)	426

The decrease in hardness can be attributed to a decrease in the carbide volume fraction. The formation of the first precipitated carbides consumed carbon in the alloy, so the total volume fraction of M_7C_3 was reduced. The relationship between total carbide volume fraction and carbon content (weight fraction) is described as follows (Zhou and Su, 1986, as quoted in Matsubara *et al.*, 2001):

$$V_{\text{total}} = 12.33C + 0.55Cr - 15.2 \quad [1]$$

Decreasing carbon and chromium lead to a decrease in the total volume fraction of carbides and hence to a decrease in bulk hardness.

Effect of niobium on fracture strength

The effect of niobium content on the maximum stress required to break the HCWCI is indicated in Table III. It can be seen from the results that niobium has a more positive effect on the fracture strength than on the hardness. It should be mentioned that the impact strength does not depend only on the matrix but also on the volume fraction, distribution, morphology and size of the carbides.

The stress concentration factor plays a bigger role when the material is exposed to impact forces. The micro-cracks of carbides propagate quickly along the direction of minimum resistance. Rod- and needle-like carbides provide an environment for high stress concentration and an easy path for crack propagation, hence they have low fracture strength. Increasing the niobium content led to a finer eutectic microstructure, which was beneficial to the mechanical behaviour of the alloy. Finer, isotropic carbides weaken the stress concentration factor compared to rod-and needle-like carbides (Ma *et al.*, 2013). This will lead to a decrease in the

crack propagation rate and when the alloy is subjected to impact, the stress on the carbides can be rapidly transferred to the soft austenite.

As-cast specimens show better fracture strength compared to the heat-treated samples. This can be attributed to the austenite matrix acting as a cushion/arrester of crack propagation by preventing brittle cracks from propagating directly from one carbide grain to another (Ma *et al.*, 2013). Low fracture strength after heat treatment can also be due to the precipitation of secondary carbides and the transformation of the matrix from austenite to martensite. However, on the other hand the martensitic matrix is also recommended for greater hardness and better wear properties at the expense of fracture strength.

Conclusions

The aim of the project was to improve the mechanical properties of the current high-chromium white cast iron (HCWCI) mill liner material by applying grain refinement. The addition of niobium was found to change the morphology of the eutectic carbides from a plate- and rod-like shape to an isotropic shape. The change in morphology was due the precipitation of niobium carbides (NbC) at the grain boundaries, which impedes the directional growth of the M_7C_3 carbides and result in finer, isotropic carbides. Initial addition of niobium led to an increase in hardness and further increase in niobium lead to decrease in hardness of the HCWCI. This trend was attributed to the decrease in carbon content available to form chromium carbides, due to formation of NbC.

Table III

The effect of niobium on the fracture strength of HCWCI

Alloy	Fracture load (N)	Stress (σ_{\max}) MPa
Reference	184 400	332
0.1–0.4%Nb alloy	314 450	566
0.4–0.6%Nb alloy	425 400	767
Reference (HT)	223 500	402
0.1–0.4%Nb alloy (HT)	201 200	362
0.4–0.6%Nb alloy (HT)	372 650	671

Effect of niobium on the solidification structure and properties of hypoeutectic

The addition of Nb led to a significant improvement in the fracture strength of both the as-cast and heat-treated alloys. This increase in fracture strength was due to the finer eutectic microstructure. There was a general decrease in the fracture strength after heat treatment, which is attributed to the precipitation of secondary carbides and the transformation of the matrix from soft austenite in as-cast condition to hard and brittle martensite after heat treatment. Austenite has a higher intrinsic fracture strength compared to martensite, but strain-induced martensite from impact forces may further enhance the fracture strength.

Future work

Industrial liners will be produced using the optimized chemistry. This will be done to validate the laboratory results and for ease of comparison with what is currently in the market.

Acknowledgements

The authors thank Mintek for financial support and for permission to publish this article.

References

- ADLER, T.A. and DOGAN, O.N. 1999. Erosive wear and impact damage of high-chromium white cast irons. *Wear*, vol. 229. pp. 174–180.
- BAIK, H.K. and LOPER, C.R. 1998. The influence of niobium on the solidification structure of Fe-C-Cr alloys. *American Foundry Society Transactions*, vol. 96. pp. 405–412.
- BEDOLLA-JACUINDE, A., CORREA, R.I. MEJIAA, I., QUEZADA, J.G. and RAINFORTH, W.M. 2007. The effect of titanium on the wear behaviour of a 16%Cr white cast iron under pure sliding. *Wear*, vol. 263. pp. 808–820.
- BEDOLLA-JACUINDE, A., CORREA, R., QUEZADA, J.G. and MALDONADO, C. 2005. Effect of titanium on the as-cast microstructure of a 16% chromium white iron. *Materials Science and Engineering A*, vol. 398. pp. 297–308.
- CETINKAYA, C. 2006. An investigation of the wear behaviours of white cast irons under different compositions. *Materials and Design*, vol. 27. pp. 437–445.
- COELHO, G.C., GOLCZEWSKI, J.A. and FISCHMEISTER, H.F. 2003. Thermodynamic calculations for Nb-containing high-speed steels and white-cast-iron alloys. *Metallurgical and Materials Transaction A*, vol. 34. pp. 1748–1758.
- CORREA, E.O., GUEDES DE ALCÁNTARA, N., TECCO, D. and KUMAR, R.V. 2007. The relationship between the microstructure and abrasive resistance of a hardfacing alloy in the Fe-Cr-C-Nb-V system. *Metallurgical and Materials Transactions A*, vol. 38. pp. 1671–1680.
- DOGAN, O.N., HAWK, J.A. and LAIRD, G. 1997. Solidification structure and abrasion resistance of high chromium white irons. *Metallurgical and Materials Transactions A*, vol. 28. pp. 1315–1328.
- DOLMAN, K.F. 2005. Metallurgy of white cast irons: effect of alloying elements and heat treatment. *Proceedings of the 36th Australian Foundry Institute National Conference*, Sydney.
- FISSET, M., PEEV, K. and RADULOVIC, M. 1993. The influence of niobium on fracture toughness and abrasion resistance in high-chromium white cast irons. *Materials Science Letters*, vol. 12. pp. 615–617.
- HANNES, S.K. and GATES, J.D. 1997. A transformation toughening white cast iron. *Journal of Materials Science*, vol. 32. pp. 1249–1259.
- KOOTSOOKOS, A. and GATES, J.D. 2008. The role of secondary carbide precipitation on the fracture toughness of a reduced carbon white iron. *Materials Science and Engineering A*, vol. 490. pp. 313–318.
- LLEWELLYN, R.J., YICK, S.K. and DOLMAN, K. 2004. Scouring erosion resistance of metallic materials used in slurry pump service. *Wear*, 256. pp. 592–599.
- MA, Y., LI, X., LIU, Y. and DANG, X. 2013. Microstructure and properties of Ti-Nb-V-Mo-alloyed high chromium cast iron. *Bulletin of Materials Science*, vol. 36, no. 5. pp. 839–844.
- MATSUBARA, Y., SASAGURI, N., SHIMIZU, K., YU, S. and YU, K. 2001. Solidification and abrasion wear of white cast irons alloyed with 20% carbide forming elements. *Wear*, vol. 250. pp. 502–510.
- RADZIKOWSKA, J.M. 2004. Metallography and microstructures of cast iron. *ASM Handbook: Metallography and Microstructures*. ASM International, Materials Park, Ohio. pp. 565–587.
- STEVENSON, A.N.J. and HUTCHINGS, I.M. 1995. Wear of hardfacing white cast irons by solid particle erosion. *Wear*, vol. 186. pp. 150–158.
- TABRETT, C.P. and SARE, I.R. 1997. The effect of heat treatment on the abrasion resistance of alloy white irons. *Wear*, vol. 203–204. pp. 206–219.
- TABRETT, C.P. and SARE, I.R. 1998. Effect of high temperature and sub-ambient treatments on the matrix structure and abrasion resistance of a high chromium white iron. *Scripta Materialia*, vol. 38, no. 12. pp. 1747–1753.
- TABRETT, C.P. and SARE, I.R. 2000. Fracture toughness of high chromium white irons: influence of cast structure. *Journal of Materials Science*, vol. 35. pp. 2069–2077.
- TABRETT, C.P., SARE, R. and GHOMASHCHI, M.R. 1996. Microstructure-property relationships in high chromium white iron alloys. *International Materials Reviews*, vol. 41, no. 2. pp. 52–89.
- THORPE, W.R. and CHICCO, B. 1985. The Fe-rich corner of the metastable C-Cr-Fe liquidus surface. *Metallurgical Transactions A*, vol. 16. pp. 1541–1549.
- TURENNE, S., LAVALLÉE, F. and MASOUNAVE, J. 1989. Matrix microstructure effect in the abrasion resistance of high chromium white cast iron. *Journal of Materials Science*, vol. 24. pp. 3021–3028.
- ZHANG, Z., YANG, C., ZHANG, P. and LI, W. 2014. Microstructure and wear resistance of high chromium cast iron containing niobium. *China Foundry*, vol. 11, no. 3. pp. 179–184.
- ZHI, X., XING, J., FU, H. and GAO, Y. 2008a. Effect of titanium on the as-cast microstructure of hypereutectic high chromium cast iron. *Materials Characterisation*, vol. 58. pp. 1221–1226.
- ZHI, X., XING, J., FU, H. and XIAO, B. 2008b. Effect of niobium on the as-cast microstructure of hypereutectic high chromium cast iron. *Materials Letters*, vol. 62. pp. 857–860.
- ZHOU, Q. and SU, J. 1986. Chromium family of wear resistant cast iron. *Xi'an Jiaotong University Press*. pp. 111–112. [In Chinese].
- ZUM GAHR K.-H and ELDIS, G.T. 1980. Abrasive wear of white cast irons, *Wear*, vol. 64. pp. 175–194. ◆

INTERNATIONAL ACTIVITIES

2016

25 October 2016 — 14th Annual Student Colloquium

Mintek, Randburg
Contact: Raymond van der Berg
Tel: +27 11 834-1273/7
Fax: +27 11 838-5923/833-8156
E-mail: raymond@saimm.co.za
Website: <http://www.saimm.co.za>

2017

9–10 March 2017 — 3rd Young Professionals Conference

Innovation Hub, Pretoria, South Africa
Contact: Camielah Jardine
Tel: +27 11 834-1273/7
Fax: +27 11 838-5923/833-8156
E-mail: camielah@saimm.co.za
Website: <http://www.saimm.co.za>

9–12 May 2017 — 6th Sulphur and Sulphuric Acid 2017 Conference

Cape Town, South Africa
Contact: Camielah Jardine
Tel: +27 11 834-1273/7
Fax: +27 11 838-5923/833-8156
E-mail: camielah@saimm.co.za
Website: <http://www.saimm.co.za>

25–28 June 2017 — Emc 2017: European Metallurgical Conference

Leipzig, Germany
Contact: Paul-Ernst-Straße
Tel: +49 5323 9379-0
Fax: +49 5323 9379-37
E-mail: EMC@gdmg.de
Website: <http://emc.gdmb.de>

6–7 June 2017 — Mine Planning School 2017

Gauteng
Contact: Camielah Jardine
Tel: +27 11 834-1273/7
Fax: +27 11 838-5923/833-8156
E-mail: camielah@saimm.co.za
Website: <http://www.saimm.co.za>

27–29 June 2017 — 4th Mineral Project Valuation Colloquium

Mine Design Lab, Chamber of Mines Building,
The University of the Witwatersrand, Johannesburg
Contact: Raymond van der Berg
Tel: +27 11 834-1273/7
Fax: +27 11 838-5923/833-8156
E-mail: raymond@saimm.co.za
Website: <http://www.saimm.co.za>

10–11 July 2017 — Chrome School 2017

Gauteng
Contact: Camielah Jardine
Tel: +27 11 834-1273/7
Fax: +27 11 838-5923/833-8156
E-mail: camielah@saimm.co.za
Website: <http://www.saimm.co.za>

7–8 August 2017 — Rapid Underground Mine & Civil Access 2017 Conference

Gauteng
Contact: Camielah Jardine
Tel: +27 11 834-1273/7
Fax: +27 11 838-5923/833-8156
E-mail: camielah@saimm.co.za
Website: <http://www.saimm.co.za>

30 August–1 September 2017 — MINESafe Conference 2017

Emperors Palace, Hotel Casino Convention Resort
Contact: Raymond van der Berg
Tel: +27 11 834-1273/7, Fax: +27 11 838-5923/833-8156
E-mail: raymond@saimm.co.za,
Website: <http://www.saimm.co.za>

11–13 September 2017 — Uranium 2017 International Conference

Swakopmund, Namibia
Contact: Raymond van der Berg
Tel: +27 11 834-1273/7
Fax: +27 11 838-5923/833-8156
E-mail: raymond@saimm.co.za
Website: <http://www.saimm.co.za>

2–7 October 2017 — AfriRock 2017: ISRM International Symposium ‘Rock Mechanics for Africa’

Cape Town Convention Centre, Cape Town
Contact: Raymond van der Berg
Tel: +27 11 834-1273/7
Fax: +27 11 838-5923/833-8156
E-mail: raymond@saimm.co.za
Website: <http://www.saimm.co.za>

20–24 November 2017 — AMI Precious Metals 2017 ‘The Precious Metals Development Network (PMDN)’

North West Province, South Africa
Contact: Raymond van der Berg
Tel: +27 11 834-1273/7
Fax: +27 11 838-5923/833-8156
E-mail: raymond@saimm.co.za,
Website: <http://www.saimm.co.za>

Company Affiliates

The following organizations have been admitted to the Institute as Company Affiliates

3M South Africa (Pty) Limited	Expectra 2004 (Pty) Ltd	Ncamiso Trading (Pty) Ltd
AECOM SA (Pty) Ltd	Exxaro Coal (Pty) Ltd	New Concept Mining (Pty) Limited
AEL Mining Services Limited	Exxaro Resources Limited	Northam Platinum Ltd - Zondereinde
Air Liquide (PTY) Ltd	Filtaquip (Pty) Ltd	PANalytical (Pty) Ltd
AMEC Foster Wheeler	FLSmidth Minerals (Pty) Ltd	Paterson and Cooke Consulting Engineers (Pty) Ltd
AMIRA International Africa (Pty) Ltd	Fluor Daniel SA (Pty) Ltd	Polysius A Division Of Thyssenkrupp Industrial Sol
ANDRITZ Delkor (Pty) Ltd	Franki Africa (Pty) Ltd-JHB	Precious Metals Refiners
Anglo Operations (Pty) Ltd	Fraser Alexander Group	Rand Refinery Limited
Arcus Gibb (Pty) Ltd	Geobrugg Southern Africa (Pty) Ltd	Redpath Mining (South Africa) (Pty) Ltd
Aurecon South Africa (Pty) Ltd	Glencore	Rocbolt Technologies
Aveng Engineering	Goba (Pty) Ltd	Rosond (Pty) Ltd
Aveng Mining Shafts and Underground	Hall Core Drilling (Pty) Ltd	Royal Bafokeng Platinum
Axis House Pty Ltd	Hatch (Pty) Ltd	Roytec Global Pty Ltd
Bafokeng Rasimone Platinum Mine	Herrenknecht AG	RungePincockMinarco Limited
Barloworld Equipment -Mining	HPE Hydro Power Equipment (Pty) Ltd	Rustenburg Platinum Mines Limited
BASF Holdings SA (Pty) Ltd	IMS Engineering (Pty) Ltd	SAIMM Company Affiliates
BCL Limited	Ivanhoe Mines SA	Salene Mining (Pty) Ltd
Becker Mining (Pty) Ltd	Joy Global Inc.(Africa)	Sandvik Mining and Construction Delmas (Pty) Ltd
BedRock Mining Support Pty Ltd	Kudumane Manganese Resources	Sandvik Mining and Construction RSA(Pty) Ltd
Bell Equipment Limited	Leco Africa (Pty) Limited	SANIRE
Blue Cube Systems (Pty) Ltd	Longyear South Africa (Pty) Ltd	SENET (Pty) Ltd
CDM Group	Lonmin Plc	Senmin International (Pty) Ltd
CGG Services SA	Magotteaux (Pty) Ltd	Smec South Africa
Concor Mining	MBE Minerals SA Pty Ltd	SMS group Technical Services South Africa (Pty) Ltd
Concor Technicrete	MCC Contracts (Pty) Ltd	Sound Mining Solution (Pty) Ltd
Cornerstone Minerals Pty Ltd	MD Mineral Technologies SA (Pty) Ltd	South 32
Council for Geoscience Library	MDM Technical Africa (Pty) Ltd	SRK Consulting SA (Pty) Ltd
Cronimet Mining Processing SA (Pty) Ltd	Metalock Engineering RSA (Pty) Ltd	Technology Innovation Agency
CSIR Natural Resources and the Environment (NRE)	Metorex Limited	Time Mining and Processing (Pty) Ltd
Data Mine SA	Metso Minerals (South Africa) Pty Ltd	Tomra (Pty) Ltd
Department of Water Affairs and Forestry	MineRP Holding (Pty) Ltd	Ukwazi Mining Solutions (Pty) Ltd
Digby Wells and Associates	Mintek	Umgeni Water
DRA Mineral Projects (Pty) Ltd	MIP Process Technologies	Webber Wentzel
DTP Mining - Bouygues Construction	MSA Group (Pty) Ltd	Weir Minerals Africa
Duraset	Multotec (Pty) Ltd	WorleyParsons RSA (Pty) Ltd
Elbroc Mining Products (Pty) Ltd	Murray and Roberts Cementation	
eThekweni Municipality	Nalco Africa (Pty) Ltd	
	Namakwa Sands (Pty) Ltd	

Forthcoming SAIMM events...

EXHIBITS/SPONSORSHIP

Companies wishing to sponsor and/or exhibit at any of these events should contact the conference co-ordinator as soon as possible

SAIMM DIARY

2016

- ◆ COLLOQUIUM
14th Annual Student Colloquium
25 October 2016, Mintek, Randburg

2017

- ◆ CONFERENCE
3rd Young Professionals Conference
9–10 March 2017, Innovation Hub, Pretoria
- ◆ CONFERENCE
6th Sulphur and Sulphuric Acid 2017 Conference
9–12 May 2017, Cape Town
- ◆ SCHOOL
Mine Planning School 2017
6–7 June 2017, Gauteng
- ◆ COLLOQUIUM
4th Mineral Project Valuation Colloquium
27–29 June 2017, Mine Design Lab, Chamber of Mines Building, The University of the Witwatersrand, Johannesburg
- ◆ SCHOOL
Chrome School 2017
10–11 July 2017, Gauteng
- ◆ CONFERENCE
Rapid Underground Mine & Civil Access 2017
7–8 August 2017, Gauteng
- ◆ CONFERENCE
MINESafe Conference 2017
30 August–1 September 2017, Emperors Palace, Hotel Casino Convention Resort
- ◆ CONFERENCE
Uranium 2017 International Conference
11–13 September 2017, Swakopmund, Namibia
- ◆ SYMPOSIUM
AfriRock 2017: ISRM International Symposium '*Rock Mechanics for Africa*'
2–7 October 2017, Cape Town Convention Centre, Cape Town
- ◆ CONFERENCE
AMI Precious Metals 2017 'The Precious Metals Development Network (PMDN)'
20–24 November 2017, North West Province, South Africa



SAIMM
THE SOUTHERN AFRICAN INSTITUTE
OF MINING AND METALLURGY

For further information contact:

Conferencing, SAIMM
P O Box 61127, Marshalltown 2107
Tel: (011) 834-1273/7
Fax: (011) 833-8156 or (011) 838-5923
E-mail: raymond@saimm.co.za



About LMDN and TiCoC

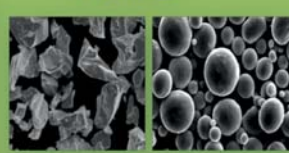
The CSIR Light Metals (LM) Competence Area hosts the Light Metals Development Network (LMDN) and Titanium Centre of Competence (TiCoC). Both TiCoC and LMDN are supported by The DST via AMI. This is in response to the mineral beneficiation plan of SA, the second largest producer of Titanium minerals with a share of 23 % of the world deposits. The CSIR, various universities, science councils and private companies are collaborating in developing the technology building blocks and R&D platforms towards adding value to SA's mineral resources. The CSIR has specialised facilities and capabilities for materials (metals and composites) design and selection, materials testing and characterisation, structural design and analysis and advanced capabilities in parts/components manufacturing, which benefit key stakeholders, such as universities, new enterprises, SMEs and large enterprises. The CSIR Light Metals Team of highly experienced and qualified researchers is equipped with advanced infrastructure for innovation and manufacturing capabilities.

Technologies and Products

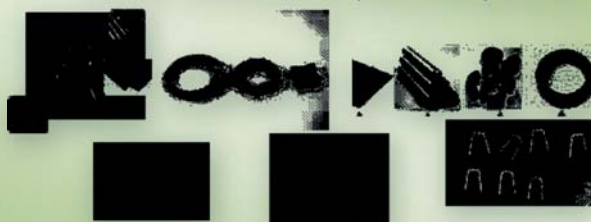
Ti Powder Pilot Plant



Ti Powder



Powder Consolidation parts/components



Casting Technologies



Composites Manufacture



Design and Analysis



Mechanical testing (ISO/IEC 17025)



Major R&D Platforms

Primary Processes

- Ti Powder production
- Process conceptualisation, development and design
- Molten salt electrolysis of alkali metals
- Pilot Plant design and construction

Powder Metallurgy Techs

- Metal Injection Moulding
- Powder Sintering
- Powder Rolling
- Process development
- Alloy development
- Alloy modification

Advanced Casting Techs

- Investment casting
- Thin-walled complex shape castings
- High Pressure die casting
- Semi-solid metal processing
- Vacuum heat treatment
- Ti and Al metallurgy
- Chemical milling
- Materials selection

Design, Analysis & Testing

- Mechanical design and analysis
- Stress and thermal analysis
- CAD and FEM
- Fibrous composite manufacture
- Tool, die and machine design
- Manufacturing
- Mechanical Testing (ISO 17025 accredited)

Contact:

Tel: 012 841 4955; e-mail RTshikhudo@csir.co.za; website: www.csir.co.za